PIECING TOGETHER HUMAN AGING, PAGE 1419

3 September 2004

Science

Vol. 305 No. 5689
Pages 1353–1512 $10

AAAS

Science

Volume 305
3 September 2004
Number 5689

COVER The phenomenon now known as RNA interference (RNAi) was first uncovered as a sequence-specific gene silencing response provoked by the introduction of exogenous multicopy transgenes into petunia. This resulted in flowers with two-toned color patterns, as shown here. The crystal structure of Argonaute, a signature component of the RNAi effector complex, is shown with its PAZ domain in blue and PIWI domain in purple. See pages 1409, 1434, and 1437. [Petunia image, R. Jorgensen; ribbon diagram, L. Joshua-Tor]

SAGE KE AND *SCIENCE* JOINT SPECIAL ISSUE

PIECING TOGETHER HUMAN AGING

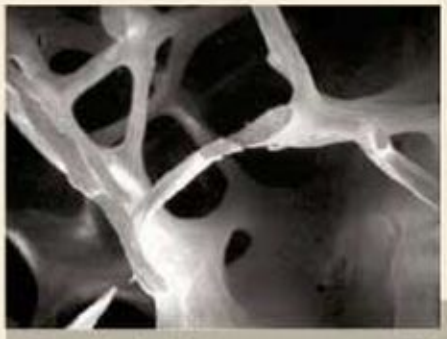

For related online content, see page 1363, or go to www.sciencemag.org/sciext/aging2004

DEPARTMENTS

1390

NEWS OF THE WEEK

1407

NEWS FOCUS

LETTERS

BOOKS *ET AL.*

Contents continued

Science

Essay

Perspectives

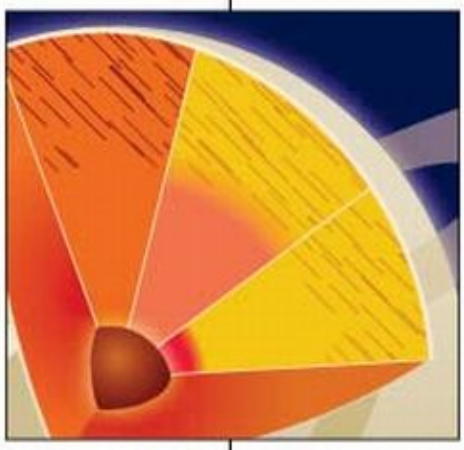

1414

Science Express www.sciencexpress.org

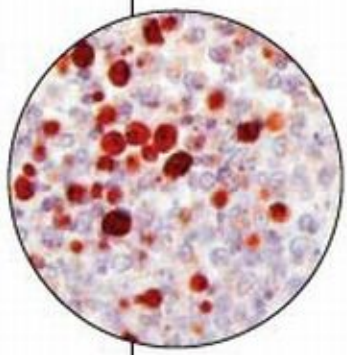

Technical Comment Abstracts

Brevia

Research Articles

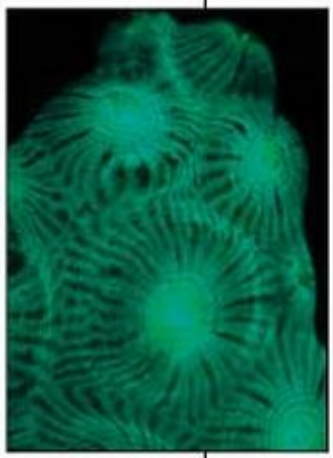

1433

Contents continued

Science

Reports

1447

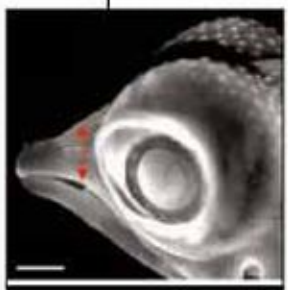

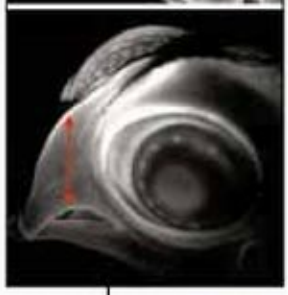

1383, 1462, & 1465

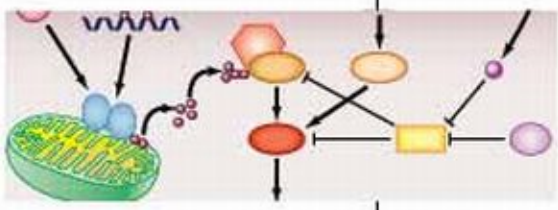

1411, 1466, & 1471

AAAS
ADVANCING SCIENCE. SERVING SOCIETY

SCIENCE (ISSN 0036-8075) is published weekly on Friday, except the last week in December, by the American Association for the Advancement of Science, 1200 New York Avenue, NW, Washington, DC 20005. Periodicals Mail postage (publication No. 484460) paid at Washington, DC, and additional mailing offices. Copyright © 2004 by the American Association for the Advancement of Science. The title SCIENCE is a registered trademark of the AAAS. Domestic individual membership and subscription (51 issues): $130 ($74 allocated to subscription). Domestic institutional subscription (51 issues): $550. Foreign postage extra: Mexico, Caribbean (surface mail) $55; other countries (air assist delivery) $85. First class, airmail, student, and emeritus rates on request. Canadian rates with GST available upon request, GST #125488122. Publications Mail Agreement Number 1069624. Printed in the U.S.A.

Change of address: allow 4 weeks, giving old and new addresses and 8-digit account number. Postmaster: Send change of address to Science, P.O. Box 1811, Danbury, CT 06813–1811. Single copy sales: $10.00 per issue prepaid includes surface postage; bulk rates on request. Authorization to photocopy material for internal or personal use under circumstances not falling within the fair use provisions of the Copyright Act is granted by AAAS to libraries and other users registered with the Copyright Clearance Center (CCC) Transactional Reporting Service, provided that $15.00 per article is paid directly to CCC, 222 Rosewood Drive, Danvers, MA 01923. The identification code for Science is 0036-8075/85 $15.00. Science is indexed in the *Reader's Guide to Periodical Literature* and in several specialized indexes.

Contents continued

sciencenow www.sciencenow.org Daily News Coverage

Carbon Monoxide's Two-Pronged Attack
Delayed immune response explains why brain damage develops weeks after exposure.

The Pleasure of Punishment
Our brains may take special satisfaction in keeping others honest.

Surprising Start for Snail Asymmetry
Development of spiraling shells includes an unexpected twist.

Finding careers in computer software.

science's next wave www.nextwave.org Career Resources for Young Scientists

Global: **Science Careers in Software** *A. Kotok*
Next Wave's September feature highlights career opportunities for scientists in computer software.

Global/UK: **Good Judgment Is the Key to a Successful Career** *C. Adam*
A physics Ph.D. graduate discovered his calling as an information technology architect.

Global/UK: **A Career in e-Science, With a Few Twists and Turns** *A. Fernandes*
An interest in science and a talent for information technology fueled a career in scientific computing.

Postdoc Network: **Visa Rules Still Complicate Postdocs' Lives** *B. Benderly*
Travel difficulties facing noncitizen scientists since September 11 have only begun to ease.

MiSciNet: **Bridging the Gap—Science in Español** *E. Francisco*
A weekly science radio program serves the Hispanic community in Tucson, Arizona.

science's sage ke www.sageke.org Science of Aging Knowledge Environment

Related Piecing Together Human Aging section page 1419

Review: **Aging of the Human Adrenal Cortex** *P. J. Hornsby*
Cell loss and compensatory overgrowth might cause age-related changes.

Perspective: **Not Wisely But Too Well—Aging as a Cost of Neuroendocrine Activity** *C. V. Mobbs*
Does neuroendocrine activity accelerate aging?

Case Study: **Osteoarthritis** *N. Shakoor and R. F. Loeser*
This most common form of arthritis is a major cause of disability in the elderly.

Regeneration magicians reveal their tricks.

News Synthesis: **Regenerating Regeneration** *R. J. Davenport*
Classic models illuminate possible ways to rejuvenate human tissues.

News Synthesis: **Déjà Vu** *I. Chen*
Arguments in the stem cell debate mirror the controversy surrounding the first test tube baby.

News Focus: **Stuck in the Craw** *M. Leslie*
Parkinson's proteins choke cell's recycling system.

News Focus: **Hastening Death to Delay Aging** *R. J. Davenport*
New approach speeds hunt for manipulations that retard fly decrepitude.

Bone, a tissue affected by aging.

science's stke www.stke.org Signal Transduction Knowledge Environment

Review: **Signal Transduction and Mechanical Stress** *M. Hughes-Fulford*
Numerous signaling pathways act to promote osteoblast proliferation in response to mechanical stress.
related Piecing Together Human Aging section page 1419

Events
See the updated list of meetings and conferences of interest to cell signaling researchers.

Separate individual or institutional subscriptions to these products may be required for full-text access.

edited by Stella Hurtley and Phil Szuromi

Clumps and Bumps in a Dusty Disk

Debris disks around young stars are full of dust and gas, created when objects in the disk collide. The young, nearby star Beta Pictoris (β Pic) has a well-studied, dust-rich and relatively large disk, and by studying such disks, astronomers may find evidence of extrasolar planets. Recently, a disk was discovered around the young star, AU Microscopii (AU Mic), which is near to β Pic and about the same age. Using the Keck II 10-meter telescope and adaptive optics, **Liu** (p. 1442, published online 12 August 2004) has now found clumps, an asymmetric variation in disk thickness, and some bending of the inner disk around AU Mic. These substructures may be attributed to perturbations of the disk by extrasolar planets.

Neat Nanotube Fibers

Single-walled carbon nanotubes (SWNTs) can be difficult to process because they are insoluble in most solvents. The addition of surfactants can improve SWNT solubility, but the surfactants tend to poison the outstanding nanotube properties. **Ericson *et al.*** (p. 1447), building on previous work in which they showed that SWNTs can dissolve in fuming sulfuric acid, have developed a process for spinning the SWNTs into highly oriented fibers without having to debundle the as-formed nanotubes. They show how the superacids interact with the nanotubes and nanotube bundles to make them soluble.

Plug-In Photonics

Photonic crystals confine light by the periodicity of their structure. When defects are introduced at specific positions in their lattice, light can be guided out of the structure, and this capability has resulted in optical devices with spatial volumes on the size scale of the wavelength of light. The smaller devices so far, however, have been optically pumped. For practical application and ready integration into optoelectronic technology, electrically driven devices are required. **Park *et al.*** (p. 1444) have developed a defect-mode photonic crystal laser that allows the carriers to be injected electrically. The devices have low current thresholds and operate in pulsed mode at room temperature.

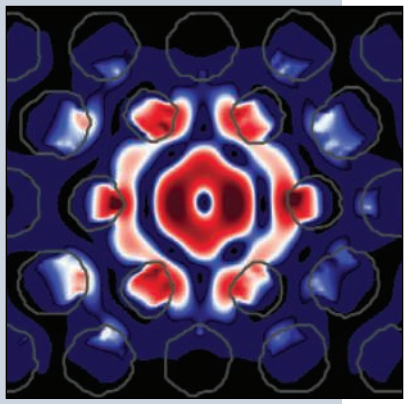

Bone Supports Bipedal Contention

One candidate for an extremely early hominid is *Orronin tugenensis*, found in 2001 in Kenya. The fossils included several limb bone fragments, including several parts of three femora. These fossils were interpreted as representing a bipedal hominid dating to 6 million years ago, although this interpretation has been widely debated and disputed. **Galik *et al.*** (p. 1450) have now used computerized tomography to analyze the internal structure of the most complete left femur. The structure of the femur, which reflects the loads placed on it, matches closely that of humans and is distinct from those of gorillas and chimps, and confirms a bipedal origin.

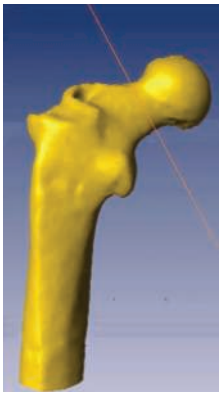

CREDITS: (TOP TO BOTTOM) PARK *ET AL.*; GALIK *ET AL.*

Slicer Steps into the Limelight

During RNA interference, small interfering (si)RNAs generated by Dicer (or provided exogenously) are loaded onto the RNA-induced silencing complex (RISC), which then binds homologous target RNAs, cleaving and inactivating them. The major constituents of RISC are the single-stranded siRNA and any one of a number of different proteins of the Argonaute (Ago) family. Until now, the identity of the nuclease in RISC, nicknamed "Slicer," has remained a mystery (see the Perspective by **Sontheimer and Carthew**). **Song *et al.*** (p. 1434, published online 29 July 2004) present the structure of the Ago protein from *Pyrococcus furiosus*, which consists of four domains; the PAZ and PIWI domains being the defining characteristics of Ago. The PfAgo PIWI domain is homologous to RNase H, including conserved catalytic residues, and the juxtaposition of PAZ and PIWI domains suggests a mechanism by which Ago might load and cleave target RNAs. **Liu *et al.*** (p. 1437, published online 29 July 2004) show that, unlike other mouse Agos, only Ago2 can form a cleavage-competent RISC. Ago2 is also essential in vivo for RNAi, and is required for normal mouse development. Because the conserved catalytic residues in the RNaseH-like PIWI domain are critical for RISC cleavage activity, it is likely that Ago2 is "Slicer."

Methane Counter-Production

The anaerobic oxidation of methane that takes place in anoxic sediments has long been attributed to sulfate-reducing bacteria, but none has been found that oxidize methane. More recently, it has been suggested that the methanogens themselves can consume methane. **Hallam *et al.*** (p. 1457) have discovered methane-oxidizing archaeans that have most of the methanogenesis machinery, and suggest these organisms also consume methane by reversing the methanogenesis pathway. This process is apparently thermodynamically coupled with the activities of sulfate-reducing bacteria in microbial consortia that develop in anoxic sediments.

Molecular Beak Tweaking

Two studies explore the molecular origin of beak variation (see the news story by **Pennisi**). **Abzhanov *et al.*** (p. 1462) examined the genus *Geospiza*, or "Darwin's finches," to explain the molecular events

CONTINUED ON PAGE 1367

Published by AAAS

in specifying the bird beak. The correlation of the morphology of the beak and expression of *bone morphogenic protein 4* (*Bmp4*) among six species of finches supports the hypothesis that the expression of this factor accounts for differences in beak morphology between species. **Wu *et al.*** (p. 1465) looked at differences in chicken and duck beaks and note variations in the respective zones of cell proliferation and *Bmp4* expression.

Sending a Cell-Death Sentence

Cancer cells proliferate because they evade programmed cell-death pathways, and much effort is being devoted to finding ways to activate apoptotic pathways in such cells (see the Perspective by **Denicourt and Dowdy**). Key interactions that determine whether cells live or die are mediated by so-called BH3 (BCL-2 homology 3) domains, which are found in proteins that regulate apoptosis. Such signals can be mimicked or disrupted by peptides that resemble the interaction domains, but such molecules have major shortcomings as experimental or therapeutic agents because of low potency, instability, and inefficient delivery to cells. **Walensky *et al.*** (p. 1466;) now show that these problems could be overcome when a BH3 domain that promotes apoptosis was held in its native α-helical form by a chemical modification they call a hydrocarbon staple. The modified peptide showed increased binding affinity for its target, was relatively protease resistant, and could cross cell membranes. Preliminary studies in animals even showed that the modified peptides could decrease growth of transplanted tumors in mice. The activity of caspases, the cysteine proteases that mediate cell death by apoptosis, is held in check by the inhibitor of apoptosis proteins (IAPs). The protein known as Smac promotes apoptosis by binding to IAPs and relieving inhibition of caspases. **Li *et al.*** (p. 1471) show that the effect of the Smac peptide can be potently mimicked by a small membrane-permeable molecule. Studies with the compound revealed that the well-known requirement for inhibition of protein synthesis to allow apoptotic effects of tumor necrosis factor α (TNFα) likely reflects decreased IAP-mediated inhibition of caspases. The new compound sensitized cancer cells in culture to TNFα-induced cell death.

A Disarming Approach to Predation

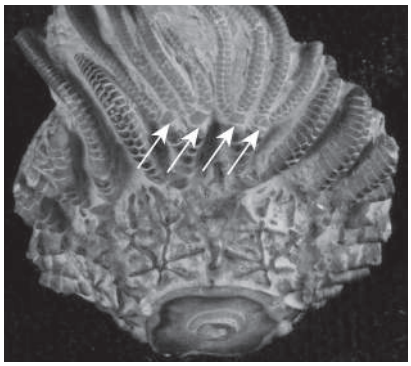

Predation has often been considered to be an important force in driving evolution. Several periods in Earth's history seem to record rapid evolution of both predators and prey; one of these is the Mid-Paleozoic Marine Revolution, about 440 to 360 million years ago. To test whether increased predation might be recorded in the fossil record directly, and whether it might have driven this marine revolution, **Baumiller and Gahn** (p. 1453; see the news story by **Stokstad**) examined the damage to arms of crinoids. Crinoids often sacrifice or shed one or more of their arms to attackers, then regenerate them. The distribution of crinoids with damaged arms jumped abruptly during this revolution, supporting the predation hypothesis.

A Swell Way to Grow

Early self-replicating systems that acquired an encapsulating membrane would presumably have gained vital protection from the environment, but acquisition of a membrane would have also required that the membrane grow and divide in synchrony with the replicator. RNA is a candidate early replicator, and **Chen *et al.*** (p. 1474) have looked at the link between RNA-based replicators and fatty acid–based vesicles. Encapsulated RNA exerts osmotic pressure on the membrane. These swollen, hypertonic vesicles grow by scavenging membrane from isotonic vesicles with low osmotic pressure. Thus, vesicles containing more effective RNA replicators (or, indeed, any replicator that exerts osmotic pressure) would have grown and outcompeted less-effective vesicle-encapsulated replicators.

CREDIT: BAUMILLER AND GAHN

Published by AAAS

Longevity, Quality, and the One-Hoss Shay

This special issue of *Science* is called "Piecing Together Human Aging" and its scientific content, as you will see in the following pages, is devoted mainly to the life and death cycles of the cells and tissues that compose our bodies. The topic ushers in some troubling thoughts about the way we wear out, as well as about the length of life and its quality—two features that are sometimes in conflict with one another. Let's start with the former: longevity. Demographers have always been interested in life expectancy, and in the problem of whether it has a finite, biologically conferred limit. The history of prediction in this area is a trail of busted estimates; proposed limits have been exceeded, one after another, since 1928, and there is no indication that a biological maximum of some kind is being closely approached. Most think such a maximum exists, but evidence from the steady improvement in life expectancy achieved by the best performers shows that it is still at a distance (Oeppen and Vaupel, *Science*, 10 May 2002, p. 1029).

Does that make us all feel better? Well, it depends—and that brings us to the quality-of-life issue, which has a lot to do with how we wear out. Oliver Wendell Holmes provided one metaphor for the perfect life-span in his poem "The Deacon's Masterpiece Or, the Wonderful One-Hoss Shay: A Logical Story." The deacon completes this extraordinary project in 1755, the year of the great Lisbon earthquake. Built of carefully selected parts that the builder thought would wear out but not break down, it lasted exactly a hundred years in good condition. Then, on the centenary of the earthquake, the Wonderful One-Hoss Shay collapsed into a mound of dust, going to pieces "…all at once, and nothing first—just as bubbles do when they burst." Its driver, the parson, was deposited unceremoniously onto the ground, right outside the meeting-house.

The shay's life cycle would be an attractive metaphor for us humans if the span were long enough. Alas, those of us at a Certain Age are all too acutely conscious of differential wear-out. As Roth *et al*. point out (p. 1423) in exploring the similarities between aging in humans and rhesus monkeys, there is a canonical sequence: presbyopia, cataracts, loss of motor activity, decline in memory performance. It would be nice if these things happened all at once instead of sequentially—as long as it wasn't too soon! How would you choose, for example, between the maximum human life-span (around 122 years) and a hundred years of perfect health followed by concurrent wear-out? My Aunt Margaret, like most of you, would choose the latter; she made it to 101, but said she didn't want many more years like the last few. (A sampler on the kitchen wall of her little house in Maine said: "It's hard to be nostalgic when you can't remember anything.")

Alas, we will not be given the chance to trade quality for quantity in life's lottery. Biology is biology, and our different parts wear out on their own different trajectories. The task of aging-related research and geriatric medicine is to improve the quality of life during a period in which some loss of function is the order of the day. And the research reported in this issue, and in *Science*'s two knowledge environments, SAGE (aging) and STKE (signal transduction), is beginning to suggest how cell and tissue death relate to organismal aging. How is replication failure related to cellular senescence? What is the role of telomere shortening and telomerase expression?

At the whole-organism level, we know that caloric restriction has a pronounced effect in promoting longevity. We still don't know how, although a variety of candidate mechanisms are now being proposed—including possible connections to the lowered insulin sensitivity in aging animals and people. Finally, we may well learn something from those genetic changes that produce effects that resemble aging, or progeria, explored in this issue by Kipling *et al*. (p. 1426). Research is unlikely to produce a future with the Holmesian hundred-year rectangular hyperbola, but just the same, we keep extending the human life-span. So we need to learn all we can about the cell biology of our weakest parts, while awaiting the appearance of some bionic deacon who can fix it so that they all last for a century.

Donald Kennedy
Editor-in-Chief

CREDIT: CORBIS

Published by AAAS

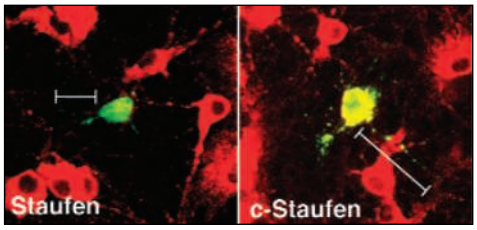

Knockdown (left) of staufen (red) decreases transport of CaMKII mRNA (green) compared to control (right).

CREDIT: KANAI *ET AL.*, *NEURON* **43**, 513 (2004)

CELL BIOLOGY

Moving Supplies to the Front

The decentralized approach to decision-making in neurons, in which synaptic plasticity is locally determined, implies that transcription (which occurs back in the cell body) cannot be relied upon as a means of regulation. Instead, messenger RNAs (mRNAs), quite possibly in an inactive state, are transported along dendrites to postsynaptic regions where they may be translated when protein is needed.

Kanai *et al*. have used a battery of techniques to identify components, including the RNA-binding protein staufen and the mRNA encoding calcium/calmodulin protein kinase II (CaMKII), that are carried by the molecular motor kinesin in the form of large 1000*S* granules. Staufen is already known to participate in the transport and localization of mRNAs in the *Drosophila* embryo, and CaMKII is a central player in activity-dependent phosophorylation at the synapse. The authors propose that core components would assemble on mRNAs to form granules and that cell- or dendrite-specific factors would be added as requisitioned by synaptic events. — GJC

Neuron **43**, 513 (2004).

CANCER

Inflammation Revisited

There has been a resurgence of interest in the concept that inflammatory mechanisms can profoundly affect the pathogenesis of many common human diseases. In the case of cancer, much research has focused on the role of NF-κB, a transcription factor that is normally activated in response to pro-inflammatory cytokines and that regulates the expression of more than 200 genes. Many tumor cell lines show constitutive activation of NF-κB signaling, but there has been conflicting evidence as to whether this promotes or inhibits tumorigenesis.

Three groups have studied mouse models of intestinal (Greten *et al*.), liver (Pikarsky *et al*.), and mammary (Huber *et al*.) tumors; they conclude that activation of the NF-κB pathway enhances tumor development and may act primarily in late stages of tumorigenesis. Inhibition of NF-κB signaling uniformly suppressed tumor development but, depending on the model studied, this salutary effect was attributed to an increase in tumor cell apoptosis, reduced expression of tumor cell growth factors supplied by surrounding stromal cells, or abrogation of a tumor cell dedifferentiation program that is critical for tumor invasion/metastasis. Although collectively these results support the development of NF-κB inhibitors as potential anticancer agents, they illustrate that such inhibitors could have complex physiological effects. — PAK

Cell **118**, 285 (2004); *Nature* 10.1038/nature02924 (2004); *J. Clin. Invest.* **114**, 569 (2004).

HIGHLIGHTED IN *SCIENCE*'S SIGNAL TRANSDUCTION KNOWLEDGE ENVIRONMENT

Science's stke www.stke.org

Arousal Without Anxiety

Xu *et al*. have investigated the physiological function and anatomical localization of a recently deorphanized G protein–coupled receptor (GPCR) and its peptide ligand, named neuropeptide S (NPS). Nanomolar concentrations of human, rat, or mouse NPS increased intracellular calcium concentrations in cultured cell lines stably transfected with the NPS receptor, suggesting that it couples to G_q proteins. The peptide and its receptor were highly expressed in brain, as well as in thyroid, salivary glands, and mammary glands. In situ hybridization for the NPS precursor, tyrosine hydroxylase, and corticotropin-releasing factor (CRF) revealed the existence of a pontine cluster of NPS-producing neurons between the locus coeruleus (norepinephrine-producing neurons) and Barrington's nucleus (CRF-producing neurons). NPS both enhanced locomotor activity in mice and promoted several behaviors that are associated with anxiolytic activity. The authors note that this receptor may also be linked to asthma susceptibility (see Laitinen *et al*., Reports, 9 April 2004, p. 300). — EMA

Neuron **43**, 487 (2004).

EDITORS' CHOICE

edited by Gilbert Chin

ECOLOGY/EVOLUTION

Tear-Away Spots

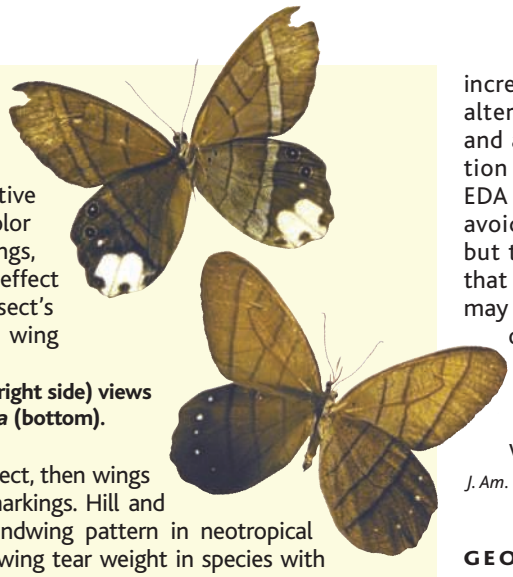

Dorsal (left side) and ventral (right side) views of *P. astyoche* (top) and *P. lamia* (bottom).

Predation is thought to be one of the primary selective factors that influence the frequently conspicuous color patterns on the wings of butterflies. Wing markings, particularly those at the outer margins, may have the effect of deflecting predatory attention away from the insect's vital parts—head and body—to the more expendable wing edges. The century-old deflection hypothesis also suggests that wings would be selected to tear, enabling the butterfly to escape its predator; if correct, then wings would be expected to tear more easily at deflection markings. Hill and Vaca tested whether wing tear weight varied with hindwing pattern in neotropical butterfly species in the genus *Pierella*. They found that wing tear weight in species with conspicuous white wing patches (*P. astyoche*) was significantly lower than in species lacking the patch (*P. lamia* and *P. lena*), providing evidence in favor of the second part of the deflection hypothesis: that deflection markings coincide with mechanically weak areas of wing. — AMS

Biotropica **36**, 362 (2004).

GEOCHEMISTRY

On the Hot Seat

Iceland straddles a plate boundary, the mid-oceanic ridge that separates the North American and Eurasian plates, and a hotspot plume. This placement results in the many volcanoes, geothermal systems, and earthquakes that are all carefully monitored in an attempt to understand subsurface complexity.

Claesson *et al*. have been sampling fluid from a 1.5-km-deep borehole that taps into four aquifers at one end of the Húsavík-Flatey fault. They measured sharp increases in Cu, Zn, Mn, and Cr at 1, 2, 5, and about 10 weeks, respectively, prior to a moment magnitude 5.8 earthquake (16 September 2002) whose epicenter was 90 km north of the borehole. They theorize that the elemental transients were caused by the accumulation of stress that then squeezed the hydrothermal system and allowed fluids that had recently been in contact with hotter basaltic rock to enter the borehole; therefore, these chemical signals may be useful for earthquake prediction. About 2 to 9 days after the earthquake, the chemistry shifted again, even more rapidly, with increases in B, Ca, Na, and S, and with changes in oxygen and hydrogen isotopes. These postseismic shifts imply that the borehole is now tapping a 10,000-year-old aquifer from the last ice age. — LR

Geology **32**, 641 (2004).

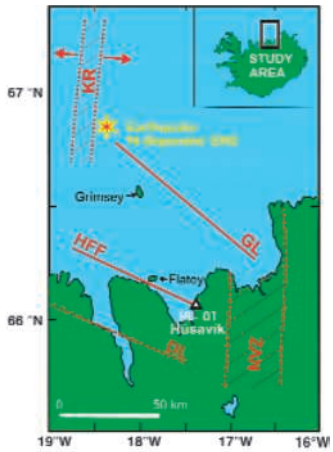

Map of the Húsavík-Flatey fault (HFF) and the borehole (HU-01) on the north coast of Iceland.

CHEMISTRY

One Carbene Helps Another

Homogeneous copper catalysts are widely used to add electrophilic carbenes to organic substrates. In a typical variant of the reaction, the Cu center stabilizes a carbene formed by N_2 loss from an ethyl diazoacetate (EDA) precursor; next, the carbene can transfer from Cu to an olefin to form the desired cyclopropane derivative. Unfortunately, the Cu-carbene complex also tends to react with another EDA molecule, giving undesired carbene dimers.

Fructos *et al*. have prepared a Cu(I) chloride catalyst that effectively eliminates the EDA dimerization pathway, while transferring a carbene to olefins, alcohols, and amines at high rates and efficiencies. It turns out that the key to this catalyst is another carbene, bound to Cu as a ligand. Unlike the electrophilic reagent derived from EDA, the ligand is an electron-rich substituted N-heterocyclic carbene, a class of molecule increasingly used as an alternative to phosphines and amines in coordination compounds. How EDA dimerization is avoided is not yet clear, but the authors speculate that the order of steps may be reversed, with olefin (or alcohol or amine) coordination to the Cu complex preceding reaction with EDA. — JSY

J. Am. Chem. Soc. 10.1021/ja047284y (2004).

GEOLOGY

Refreshing Water

The Everglades is maintained by the slow sheetlike flow of fresh water from a series of control gates in central Florida southward into Florida Bay, and is representative of many other coastal wetlands. The crux of a recent restoration effort is the reengineering of a more natural flow after decades of diversions, levees, and canals, and is complicated by the variable habitats and permeability of the Everglades. Part of the difficulty in monitoring this effort is that the flow is driven by subtle variations in water level that are difficult to capture by scattered gauges (elevation changes of less than 1 m in 10 km). Wdowinski *et al*. show that the large-scale variations in flow, as reflected in water elevation, as well as other details, can be captured by satellite interferometry. Their observations, gathered in 1994, show that flow was sheetlike in the eastern Everglades, but more radial in the western region, and provide an estimate of the diffusivity, an important hydrologic parameter for inferring flow dynamics. — BH

Geophys. Res. Lett. **31**, 10.1029/2004GL20383 (2004).

CONTINUED ON PAGE 1373

CREDITS: (TOP) HILL AND VACA, *BIOTROPICA* **36**, 362 (2004); (BOTTOM) CLAESSON *ET AL*., *GEOLOGY* **32**, 641 (2004)

Published by AAAS

edited by Mitch Leslie

FUN

Science Jukebox

The sun is a mass of incandescent gas
A giant nuclear furnace
Where hydrogen is built into helium
At a temperature of millions of degrees

Yo ho, it's hot, the sun is not
A place where we could live
But here on Earth there'd be no life
Without the light it gives

That's a selection from "Why Does the Sun Shine," an educational ditty by Hy Zaret and Lou Singer, science's answer to Cole Porter. Although solar physics and other technical topics will never surpass romance and heartache as the favorite subjects of songwriters, they figure in a surprising number of compositions, as you'll learn at the entertaining site MASSIVE (Math And Science Song Information, Viewable Everywhere). The database from chemical engineer and occasional songwriter Greg Crowther of the University of Washington, Seattle, lists more than 1600 titles, from "The Song of the Tungara Frog" to "Carbon Is a Girl's Best Friend." Links whisk you to lyric sheets and audio snippets. Most composers and singers are obscure, but a few big names show up, including Monty Python and country singer Clint Black—who perform the same song (separately) about the immensity of the universe. For nonstop science tunes, you can also listen to MASSIVE radio.

www.science-groove.org/MASSIVE

DATABASE

Protein Matchmaking

This collection of more than 50,000 protein structures provides a speedy way to contrast similar molecules. ProteinDBS lets you enter a Protein DataBank ID number or file of coordinates for a molecule such as carbonic anhydrase (left), which helps rid the body of carbon dioxide from metabolism. The search finds the 50 proteins most like your choice and allows you to make visual and statistical comparisons. For instance, you can superimpose three-dimensional portraits of two proteins or parse their sequences amino acid by amino acid. The site comes from computer scientist Chi-Ren Shyu of the University of Missouri, Columbia, and colleagues.

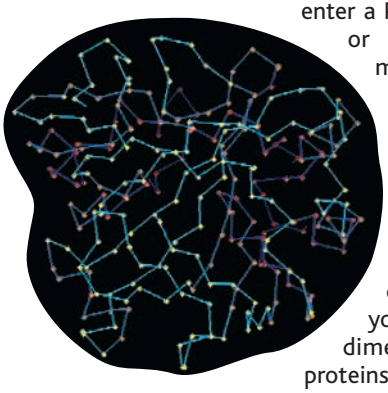

proteindbs.rnet.missouri.edu

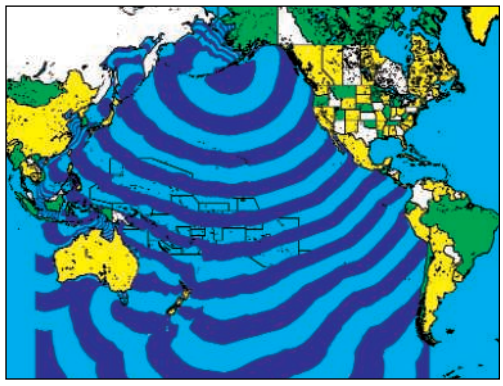

RESOURCES

Waves of Destruction

On 1 April 1946, a strong earthquake hoisted the sea floor near the Aleutian Islands, unleashing 35-meter waves that rolled across the Pacific Ocean (left). The massive ripples were still 12 meters tall when they walloped Hawaii, killing 159 people. To learn more about the causes and consequences of towering waves, visit the International Tsunami Information Center* in Honolulu, Hawaii. Tsunamis—which can result from earthquakes, volcanic eruptions, meteorite strikes, or other upheavals—arise worldwide but are most common in the Pacific because of its size and seismic activity. Along with data on recent events, check out vivid descriptions of tsunamis from the last 60 years and the gallery of devastation. For a quick overview that includes samples of nifty computer simulations, try this tsunami primer from the University of Washington.†

* www.prh.noaa.gov/itic

† www.geophys.washington.edu/tsunami/welcome.html

RESOURCES

All the Fish in the Sea

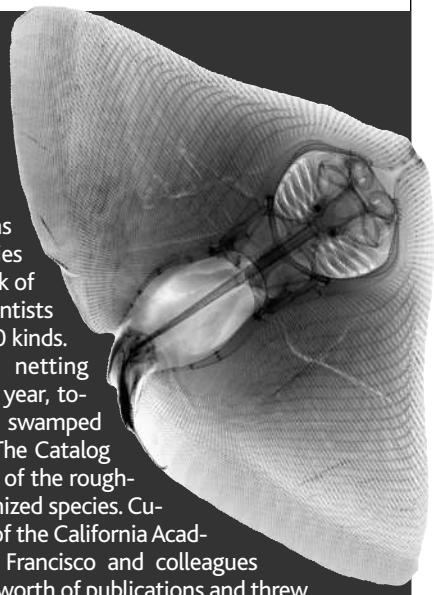

When pioneering taxonomist Carolus Linnaeus was cataloging all known species in the 1750s, keeping track of the fishes was easy; scientists had tallied only about 500 kinds. But with ichthyologists netting some 300 new species a year, today's researchers can get swamped without a guide such as The Catalog of Fishes, which covers all of the roughly 29,000 currently recognized species. Curator William Eschmeyer of the California Academy of Sciences in San Francisco and colleagues trawled nearly 250 years' worth of publications and threw back defunct and dubious species names, creating the first comprehensive compilation of fish taxonomy since Linnaeus. The site also links to other Cal Academy ichthyology resources, such as an image database stocked with photos and x-rays of most of the academy's more than 1600 type specimens (the original examples used to describe the species). Above, the ray *Pteroplatea rava* from Mexico.

www.calacademy.org/research/ichthyology/catalog/fishcatsearch.html

Send site suggestions to netwatch@aaas.org. Archive: www.sciencemag.org/netwatch

CREDITS: (TOP TO BOTTOM) NOAA; CALIFORNIA ACADEMY OF SCIENCES; CHI-REN SHYU/UNIVERSITY OF MISSOURI

Published by AAAS

This Week

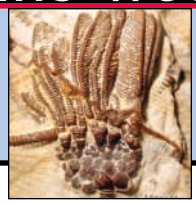

PAGE 1385
Predators' ancient handiwork

1386
EuroScience meeting debut

EXTRASOLAR PLANETS

Planet Hunting Gets Rocky As Teams Clash Over Small Worlds

Three teams of astronomers have found the first Neptune-size planets orbiting stars beyond our solar system, a milestone for the elite community of extrasolar-planet hunters. But the joyful glow over the new worlds—which may be the first rocky bodies known to circle other ordinary stars like the sun—was dimmed by a preemptive announcement that stunned U.S. observers.

Astronomers with the European Southern Observatory (ESO) trumpeted their unreviewed discovery on 25 August, just 5 days after their last observations. In an odd twist, several of the European scientists also are co-authors of one of the two U.S. papers on similar planets, both refereed and originally scheduled for public release in mid-September. "I was shocked," says astronomer Barbara McArthur of the University of Texas, Austin, of the decision by her European co-authors. Privately, a colleague was less kind: "It's outrageous, and everyone sees it that way."

Of about 130 known exoplanets, astronomers think nearly all are vast spheres of gas like Jupiter, which is 318 times as massive as Earth. As a gas giant orbits, its gravity tugs its parent star to and fro. That periodic motion creates wobbles in the starlight, which sensitive telescopes on Earth can detect.

Eager to find smaller, solid bodies that could potentially support water and alien slime, planet hunters have refined their techniques to spot ever-tinier stellar motions. For now, their quarries are planets like Neptune and Uranus, which have 17 times and 14.5 times Earth's mass, respectively. Neptune and Uranus hide major cores of ice and some rock beneath their gaseous mantles. But models show that planets of similar size consisting mostly of rock could coalesce in the warm portions of iron-rich dusty disks.

This summer, a group led by astronomers Paul Butler of the Carnegie Institution of Washington, D.C., and Geoffrey Marcy of the University of California, Berkeley, found a planet with at least 21 Earth masses orbiting the red dwarf star GJ 436. The paper was reviewed and accepted at *Astrophysical Journal*. NASA, which partially funds the search program, scheduled a press conference on 13 September to tout the results.

Marcy soon learned that McArthur's team had evidence for a body of at least 14.2 Earth masses orbiting the star ρ Cancri. He invited McArthur to join NASA's press conference. As the teams talked to theorists, their excitement grew. "For the first time, it's plausible that these are mostly rocky iron balls, with surfaces enabling liquid water to puddle on them," Marcy says. "This is putting us on the doorstep of detecting other Earths."

McArthur originally prepared a submission to *Nature* but later switched to *Astrophysical Journal Letters* out of concern that the *Nature* embargo would delay the reports. Among her co-authors, she included four European astronomers who supplied some data on ρ Cancri's motions. The journal quickly vetted and accepted the paper.

The European team—including veteran planet hunters Michel Mayor and Didier Queloz of the University of Geneva in Switzerland—was seeing tantalizing things as well. The scientists used a new spectrograph on ESO's 3.6-meter telescope at La Silla, Chile, to expose stellar velocities with a striking precision of less than 1 meter per second. In June, colleagues monitoring seismological pulsations of a star called μ Ara realized that the signals oscillated gently on a 9.5-day cycle. Further data in July and August nailed the presence of a planet of at least 14 Earth masses, Mayor says.

The astronomers issued an ESO news release on 25 August—the day Queloz was to deliver a long-scheduled talk at the EuroScience Open Forum 2004 in Stockholm, Sweden (see p. 1387). On the same day, the team submitted a short manuscript to *Astronomy & Astrophysics*. The Europeans refrained from noting that the McArthur team's discovery—on which Mayor and Queloz are co-authors—came first, because they believed the paper was under embargo at *Nature*, Mayor says.

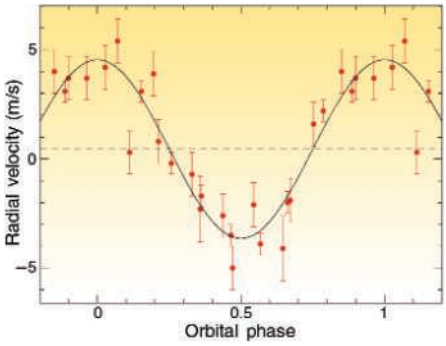

Planetary pull. A Uranus-size body tugs back and forth on the star μ Ara as it orbits.

"This is a … story of convenience," retorts Marcy. "They clearly went immediately to the presses with a quick and dirty analysis, and with one purpose in mind: to lead the world to believe that they found the first [Neptune]." The upset Americans moved their NASA briefing to 31 August to salvage some media attention.

Amid the rancor, theorists are excitedly interpreting the discoveries. "This is a very encouraging sign that we will find a lot of lower-mass rocky planets in the next 10 years or so," says Alan Boss of the Carnegie Institution. But theorist Jack Lissauer of NASA's Ames Research Center in Mountain View, California, cautions that such bodies would require "a huge amount of rock" to coalesce in the young stellar disks. "It's possible that an ice-rock planet like Neptune, with some gas, would migrate close to the star and not evaporate," he says.

Both Boss and Lissauer note that astronomers must find an exo-Neptune that crosses in front of its star to verify its diameter and thus its density. Planet hunters hope this next race will have a more collegial outcome. —ROBERT IRION

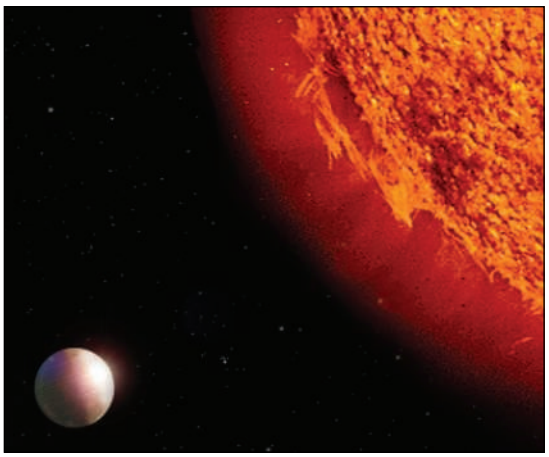

Alien Neptune. A possibly rocky body is the fourth planet circling ρ Cancri, in this illustration.

CREDITS (TOP TO BOTTOM): ESO; MELODY LAMBERT

Published by AAAS

DEVELOPMENTAL BIOLOGY

Bonemaking Protein Shapes Beaks of Darwin's Finches

Darwin's finches are to evolutionary biology what Newton's apple is to physics. After exploring the Galápagos Islands in 1835, Charles Darwin later became intrigued by the varying shapes and sizes of the closely related birds' beaks. Each beak appeared to be specialized for a task, such as cracking seeds or drinking nectar. Once Darwin formulated his ideas about evolution, he realized that these birds exemplified the principles he was proposing. Today, these songbirds are often cited as a perfect example of how new species arise by exploiting ecological niches.

Now developmental biologists have added a new twist to this classic story. Two research teams have discovered that a protein normally associated with the development of the skull and other bones is one of the molecules that tailors the shapes of beaks. Different shapes arise depending on where and when this signaling molecule, called bone morphogenic protein 4 (BMP4), is turned on during development, says Cheng-Ming Chuong, a evolutionary developmental biologist at the University of Southern California (USC) in Los Angeles.

On page 1465, Chuong's team describes BMP4's role in building beaks in chickens and ducks. And on page 1462, developmental biologist Clifford Tabin of Harvard Medical School in Boston and his colleagues show that the expression of BMP4's gene varies, just as the beaks do, in six species of Darwin's finches. Both groups also demonstrated that they can cause birds to develop misshaped beaks by altering BMP4 levels during development.

The two groups' results provide a window into the molecular basis of diversity, says Dolph Schluter, an evolutionary biologist at the University of British Columbia in Vancouver, Canada. He was particularly taken with Tabin's work. "This paper represents a step in answering [how diversity arises] in the most celebrated example of adaptive evolution, the radiation of the Darwin's finches," he notes.

An outgrowth of the jaw, a beak forms as six processes extend from jawbones in a coordinated manner. Chuong's USC research associate Ping Wu followed one of the processes, the frontonasal mass, in developing ducks and chicks and discovered that the growth patterns differ in the two species. Moreover, the actively growing areas contained BMP4. To test the protein's role in shaping beaks, the researchers increased the amount of BMP4 by injecting it or its gene into the tissue that helps form them. The excess BMP4 resulted in longer, wider, and deeper beaks, Wu and his colleagues report. When they did the reverse experiment, adding a gene whose protein counteracts BMP4, the beaks ended up smaller than normal.

The work "is an experimental test that the molecule could be manipulated in a way to [recapitulate] beak shape," says Jeff Podos, a behavioral ecologist at the University of Massachusetts, Amherst. Adds Jill Helms, a developmental biologist at Stanford University, "This work underscores that [morphological] changes do not take much [genetic change]."

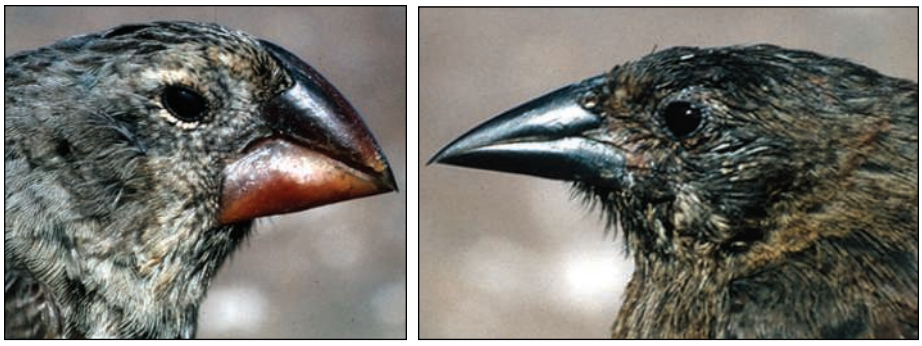

CREDIT: A. ABZHANOV *ET AL*

Pecking away. Researchers now know that a protein is key to the diversity of beaks in Darwin's finches.

Working independently, Tabin and his colleagues actually studied Darwin's famous birds. Aided by Princeton University field biologists Rosemary and Peter Grant—renowned for their studies of these Galápagos birds—Tabin's team collected eggs of six *Geospiza* species. Three species, the ground finches, had stout bills for cracking seeds; the other three, the cactus finches, had the slender, pointed bills needed for retrieving nectar. As such, these beaks are "a wonderful model for understanding the interaction between environment and evolution on speciation," says Chuong.

Tabin's postdoctoral fellow Arhat Abzhanov looked at finch embryos at different points in development, documenting when and where the genes for 10 different growth factors were expressed among the six species. BMP4 was the only growth factor to distinguish ground finches from cactus finches. The two groups of birds differed in both the amount of BMP4 and the timing of BMP4 activity. The ground finches, with larger beaks, make more BMP4 protein at an earlier stage, Tabin explains.

Each ground finch species had its own distinct pattern of BMP4 expression. *G. magnirostris* begins making its BMP4 much earlier than the other ground finches examined, for example. "To see the beaks of the different ground finch species light up with different patterns of BMP4 expression was a thrill," says Schluter.

Tabin's results, coupled with Chuong's, offer convincing evidence that BMP4 shapes beaks, says Podos. Other genes and molecules will also be involved, cautions evolutionary biologist R. Craig Albertson of the Forsyth Institute in Boston, Massachusetts. Indeed, neither group knows what makes the BMP4 gene more active in birds with bigger bills.

Whatever the underlying molecular cause of beak diversification, Podos hopes that further investigations of BMP4 in other bird species will lead to insights into why some birds, such as the finches, rapidly form new species—with the different lifestyles that are possible because of changes in their shapes—while others living in the same place, for example, warblers, do not.

That's the beauty of this work, Podos says: "It translates genetic variation into something we can sink our teeth into. Maybe we are beginning to understand something about [morphological] plasticity."

Darwin would be pleased.

–ELIZABETH PENNISI

Published by AAAS

VIROLOGY

Avian Flu Finds New Mammal Hosts

Worries about the avian influenza strain, H5N1, that's circulating in Asia have ratcheted up another notch. A paper published online by *Science* this week (www.sciencemag.org/cgi/content/abstract/1102287) confirms that the virus can infect cats, and that felines can transmit the virus to other cats as well—and perhaps to humans, according to one of the study's authors, Albert Osterhaus of Erasmus University in Rotterdam, the Netherlands.

Although there's no evidence yet that cats have helped spread the flu anywhere, their vulnerability to H5N1—which comes on the heels of similar findings in pigs—increases concerns that the virus may evolve into a more dangerous strain that could set off an influenza pandemic, says virologist Richard Webby of St. Jude Children's Research Hospital in Memphis, Tennessee.

Species jump. This tiger became infected with the avian influenza virus H5N1. Domestic cats can also contract the deadly strain.

CREDIT: SAEED KHAN/AFP/GETTY IMAGES

H5N1 has ravaged poultry farms in nine Asian nations—Malaysia officially joined the list 2 weeks ago—and has claimed the lives of at least 26 people. The virus was first reported in cats in January, when a clouded leopard at a zoo near Bangkok died from an infection. A month later, a sick white tiger at the same zoo tested positive for H5N1. Three domestic cats that died near a Thai farm were also found to harbor the virus. In each case, eating raw, infected poultry was the likely infection route.

To further investigate cats' susceptibility, Thijs Kuiken, a veterinary pathologist in Osterhaus's lab, inoculated H5N1 isolated from a fatal human case into the tracheas of three young domestic cats. All developed flu symptoms, such as fever and labored breathing, and one died after 6 days. (In contrast, cats inoculated with H3N2, a human flu virus, did not become infected.) Necropsy of the sick cats revealed lung tissue damage similar to that caused by H5N1 in humans. Further experiments showed that two cats living in close contact with an infected animal also became sick, as did three others that each ate an H5N1-infected chick.

The study underscores H5N1's ability to infect multiple mammal species, which is unusual for strains that circulate in birds. That prowess may help the virus acquire the genes necessary to become easily transmissible among humans, a prerequisite for triggering a pandemic. "The more hosts it gets into, the more possibility it has to change," says Webby.

Just 2 weeks ago, director Chen Hualan of China's National Avian Influenza Reference Laboratory in Harbin announced at a meeting in Beijing that H5N1 had also been found to infect pigs as early as last year. The finding was reported in January in a Chinese journal and mentioned in one sentence in a July paper in the *Proceedings of the National Academy of Sciences*, but it went largely unnoticed among Western flu scientists. Those results are especially worrisome, flu experts say, because pigs are believed to be mixing vessels in which avian and human flu viruses can combine into new strains.

Klaus Stöhr, a virologist at the World Health Organization in Geneva, says there's no indication so far that H5N1 has become established in pig populations. The "strongest evidence," he says, comes from Hong Kong, which imports 5000 pigs a day, mostly from south China. Each month since 1999, Hong Kong agriculture ministry officials have tested a couple of hundred nasal swabs from pigs. They have found human flu viruses, but "never, ever was H5N1 isolated," Stöhr says. That's no cause for complacency, however, adds Stöhr, who urges countries where H5N1 has been found to step up surveillance of pigs.

Colleagues also note that there's no reason for the public at large to worry about their pet cats—let alone to dispose of them—but that some precautions would be wise. For example, the practice of feeding dead carcasses to carnivores in zoos and on farms "is clearly a bad idea," warns Malik Peiris, a flu expert at the University of Hong Kong. And cats with access to poultry should be watched for signs of illness, says Stöhr.

–MARTIN ENSERINK AND JOCELYN KAISER

ScienceScope

Japanese Researcher Sues Government Over Detention

TOKYO—A Japanese researcher who faced U.S. charges of economic espionage has sued the Japanese government for detaining him for 57 days. Microbiologist Takashi Okamoto says he was "unjustly" held while a Japanese court considered a U.S. extradition request. He is seeking $390,000 in compensation.

The U.S. Justice Department wants to try Okamoto on charges of stealing genetic materials from the Cleveland Clinic Foundation in Ohio, where he worked as an Alzheimer's researcher. But the Tokyo High Court rejected the extradition request last March (*Science*, 2 April, p. 31).

Meanwhile, Okamoto is fighting another lawsuit. Former friend Hiroaki Serizawa is suing Okamoto for $770,000 in legal fees and damages relating to his entanglement in Okamoto's case. Serizawa, then a research biologist at the University of Kansas Medical Center, temporarily stored Okamoto's samples and later pleaded guilty to U.S. perjury charges. Serizawa says the incident ruined his research career. Okamoto says that "there is no connection between the two cases."

–DENNIS NORMILE

California Acts on Ocean Policy Reports

California has become the first state to pass legislation implementing major ocean policy recommendations made in two recent reports (*Science*, 23 April, p. 496). The state legislature late last month approved the California Ocean Protection Act (COPA), which creates the Cabinet-level Ocean Protection Council to coordinate research and data sharing across agencies and establish a trust fund for marine-related programs.

Those ideas emerged directly from recent reports by the U.S. Commission on Ocean Policy and the private Pew Oceans Commission, notes Andrew Rosenberg, a member of the U.S. commission and a professor of natural resources at the University of New Hampshire in Durham. California is one of the nation's most important coastal states, and COPA "has the potential to be a leading force in ecosystems-based management in the ocean," he says.

California Governor Arnold Schwarzenegger is expected to sign the bill by the end of this month. Analysts predict that the trust fund, which will draw money from state oil and gas royalties, will start life with $10 million.

–ERICA GOLDMAN

Published by AAAS

PALEONTOLOGY

400-Million-Year-Old Wounds Reveal a Time When Predators Romped

Just as swords inspired the invention of chain mail, the history of life hints at many arms races between predators and prey. But with the remnants of the carnage long turned to stone, it can be difficult to prove that the evolution of bigger teeth, for instance, actually did encourage the evolution of defenses like thicker armor.

On page 1453, two paleontologists establish a key part of the argument in a new way. Forest Gahn of the Smithsonian Institution's National Museum of Natural History in Washington, D.C., and Tomasz Baumiller of the University of Michigan, Ann Arbor, show that stalked filter-feeders called crinoids suffered ever fiercer attacks during a period when fish and other major predators were diversifying. Paleontologist Christopher Maples of the Desert Research Institute in Reno and Las Vegas, Nevada, says the case study is "really cool" and could help explain a subsequent explosion in crinoid diversity.

Most studies of predation intensity have focused either on holes that marine snails, which drill into bivalves and brachiopods or on broken fossil shells that show signs of repair. Regrowth indicates the prey survived an attack and could have passed on genes for a thicker shell or other defense, thus ratcheting up the arms race.

Gahn and Baumiller looked at another set of predators and prey during what's called the Middle Paleozoic Marine Revolution. At that time—about 380 million years ago—sharks and fishes were diversifying wildly. Invertebrates in shallow waters were changing, too; crinoids, for example, were evolving thicker armor and spines.

Life and limb. Crinoids fossilized while regrowing damaged arms (arrow) bear witness to ancient dangers.

CREDIT: FOREST J. GAHN

Like their starfish cousins, crinoids excel at regenerating lost body parts. So when a fish chomps off several of the tentacle-like appendages, crinoids grow new ones. Looking at slabs with beautifully preserved crinoids, primarily from eastern North America, Gahn and Baumiller could spot new arms growing from stumps. By counting the stumps, they calculated the rate of predation.

For approximately 100 million years before the Middle Paleozoic Marine Revolution, the researchers found that fewer than 5% of crinoids sported regenerating arms. By the time the predator revolution was in full swing, however, more than 10% were growing replacement arms. The evidence increasing predation is "straightforward and convincing," says paleobiologist Geerat Vermeij of the University of California, Davis, who showed that a later burst of predator evolution called the Mesozoic Marine Revolution spurred prey to respond.

Crinoid arm regeneration could be a useful way to look at predation intensity in other time periods as well, says paleontologist Tatsuo Oji of the University of Tokyo, although he and Vermeij caution that comparing regeneration rates between species and environments can be tricky. Baumiller and Gahn are planning to measure predation intensity throughout the fossil record, including Vermeij's Mesozoic revolution, when a group of crinoids called comatulids hit on a particularly effective defense tactic: the ability to flee.

—ERIK STOKSTAD

SCIENTIFIC PUBLISHING

Zerhouni Plans a Nudge Toward Open Access

Hoping to resolve an escalating debate about public access to biomedical research reports, National Institutes of Health (NIH) Director Elias Zerhouni consulted with scientists this week and said that he is leaning toward a delay of 6 months after publication before posting grantees' papers on NIH's free Web archive. This plan won't satisfy everyone, he acknowledged, but it is "reasonable."

A war of words broke out this summer after Zerhouni responded to a House report urging NIH to come up with a plan to give free access to published papers. In a stern seven-page letter last week, the Association of American Publishers and other groups called NIH's plans a "radical new policy" and an "inappropriate intrusion" on free enterprise; they contend that it could force journals to adopt an "unproven" model in which authors pay publication costs. Lobbying for the plan, 25 Nobel laureates—led by Richard Roberts and including former NIH director Harold Varmus and James Watson—wrote Congress on 26 August expressing "strong support" for posting NIH grantees' papers in PubMedCentral—NIH's free, full-text archive—as soon as they are published. A new coalition of patient and library groups called the Alliance for Taxpayer Access, meanwhile, is backing a 6-month release plan.

On Monday, Zerhouni invited about two dozen grantees and intramural scientists to describe "rank-and-file" views. Some expressed concern about pushing journals toward an author-pays model, saying they feared that young scientists might not be able to pay the charges of journals, which could run to $6000 per paper or more. A major shakeup of journals could also harm the peer-review system, others noted. "One of the losers could easily be the scientists," said Gary Westbrook of Oregon Health & Science University, editor-in-chief of the *Journal of Neuroscience*.

Participants seemed comfortable, however, with a 6-month delay; many of journals already meet that standard, said Zerhouni, who also planned to meet with patient advocacy groups this week. Meanwhile, a staffer for Representative Ernest Istook (R–OK), who inserted the open-access language in the House report, said he plans to hold a colloquy to clarify that NIH should take all views into account.

—JOCELYN KAISER

Published by AAAS

MEETINGS

Europe Clones U.S. Science Festival

STOCKHOLM—Scientists and science groupies gathered here from all quarters last week to mingle and share views at the first pan-European jam session of its kind. In the high-ceilinged classrooms of a beautifully restored 1880 grammar school, they discussed the European baby bust, the commercialization of science, and how to make sense of math for a lay audience. Former President Bill Clinton's science adviser Neal Lane gave an in-depth radio interview about nanotechnology policy, young scientists sat down for one-on-one chats with a career counselor, and a horde of noisy teenagers scoured exhibition stands for free goodies.

It all took place under the umbrella of the EuroScience Open Forum (ESOF), a new general meeting that drew 1800 people—among them more than 300 reporters—from dozens of countries to the Swedish capital, many more than the organization had hoped for.

The 4-day event is the brainchild of Carl Johan Sundberg, a physiologist at the Karolinska Institute in Stockholm with a longtime interest in sharing science with the public. He first proposed the idea in 1999 and served as chair of the steering committee. It's no secret, Sundberg says, that the smorgasbord program was not a Swedish invention but a faithful copy of the format of the annual meeting of AAAS, *Science*'s publisher. Like that meeting, ESOF had multiple goals, from scientific debate to discussing the role of pure science in society and piquing the public's interest in research.

CREDIT: M. ENSERINK

Science on wheels. From the Amazing Profmobil, parked in a busy square, Stockholm University geologist Thomas Andrén explains the draining of the Baltic Ice Lake.

Although ESOF's model may be American, participants stressed that the theme of the gathering was distinctly European, and its multinational audience evidence that a science system long fractured along national lines is beginning to coalesce. Many sessions addressed Europe-wide issues, such as the new European Centre for Disease Prevention and Control, slated to open next May in Stockholm; obstacles to career mobility; and the movement to establish a European Research Council for basic research. Indeed, the backdrop of European integration gave the meeting "tremendous symbolism," says Frank Gannon, an Irish biologist who directs the European Molecular Biology Organization in Heidelberg, Germany.

ESOF also included a few innovations to the AAAS model, such as a daily wrap-up of events during spirited (at times hilarious) cocktail-hour debates led by BBC reporter Quentin Cooper. To get the public involved in events scattered throughout downtown Stockholm, some surprises were deployed. The most eye-catching was a German contraption, the "Amazing Profmobil," a bicycle with a small podium and a computer screen mounted on the back that scientists could wheel into parks and squares to explain their work to the public. (The public appeared mostly dumbfounded.)

Despite the festive atmosphere, some journalists grumbled about the meeting's heavy slant toward policy issues and a dearth of breaking science news. Apart from the announcement of the detection of the smallest known exoplanet (see p. 1382), few research results were presented. "You don't go home with a lot of news stories," says Bruno van Wayenburg, a freelance reporter from the Netherlands. Reporter Angela Grosse of the *Hamburger Abendblatt* says that didn't bother her, because she came—like some other media representatives—primarily to find contacts and inspiration for future stories.

Sundberg counters that it's hard to persuade researchers to announce their findings at a general meeting like ESOF or the AAAS annual meeting; they prefer to inform their colleagues first. But he says the organizers will try harder next time.

Unlike the AAAS meeting, ESOF will be a biennial event; Munich will play host in 2006, and Barcelona has indicated its desire to be next after that. As other cities learn of ESOF's potential to boost their image as a science hub, Sundberg predicts, there may well be an Olympic-style bidding war for the 2008 edition.

–MARTIN ENSERINK

ScienceScope

U.S. Releases Draft Plan for Dealin With Pandemic Flu

Mounting concerns about H5N1 avian flu, which has devastated poultry farms in Asia and killed two dozen people (see p. 1385), spurred the release last week of the United States' first pandemic influenza preparedness plan.

The avian flu outbreak has experts worried that the H5N1 virus could morph into a lethal strain passed from person to person. The draft document from the Department of Health and Human Services (HHS) describes plans to increase surveillance for such potentially deadly flu strains, expand vaccine manufacturing, stockpile antivirals, and coordinate response to any outbreak (www.hhs.gov/nvpo/pandemicplan/index.html). THe plan "draws up on the wealth of experience" that the United States has gained dealing with SARS and other threats, says HHS Secretary Tommy Thiompson.

But the plan leaves open for discussion details such as who should receive limited supplies of flu drugs and vaccines. "There will be some tough choices," says Bruce Gellin, director of HHS'S National Vaccine Program Office. The deadline for comments is 26 October.

–JOCELYN KAISER

In Settlement, Glaxo Agrees to Publicize Drug Trial Data

Just 12 weeks after New York Attorney General Eliot Spitzer charged British drug giant GlaxoSmithKline (GSK) with fraud in selling drugs for children, his office has settled the case out of court. Glaxo, accused of understating the clinically documented risks of suicide among youthful users of its antidepressant Paxil (*Science*, 11 June, p. 1576), last week agreed to pay a $2.5 million fine and provide public Web access to clinical trial results from all of its marketed medicines. In general, GSK pledged to post study results for approved drugs within 10 months of the trial's completion.

The settlement "holds GSK to a new standard of disclosure" that will "set an example for the entire pharmaceutical industry," Spitzer's office crowed in a 26 August announcement. GSK noted in a terse statement that it paid the $2.5 million simply "to avoid the high costs and time required to defend" against Spitzer's charges, and that it was releasing clinical data "voluntarily ... in response to public concern."

–ELIOT MARSHALL

Published by AAAS

PRESIDENTIAL APPOINTMENTS

NSF's Acting Chief Facing Legal Limit on Tenure

Time is running out for Arden Bement, the acting director of the U.S. National Science Foundation (NSF). Unless the White House acts promptly—which it promises to do—Bement could be sent packing later this month because of an obscure law designed to encourage timely presidential appointments.

Countdown. Arden Bement's days at NSF are numbered.

Bement was already serving as the presidentially chosen director of the National Institute of Standards and Technology (NIST) when he was tapped earlier this year as a temporary successor to Rita Colwell, who left NSF before the end of her 6-year term (*Science*, 20 February, p. 1116). The 72-year-old materials engineer took office on 21 February, and that's when the clock started ticking.

Under the 1998 Federal Vacancies Reform Act, a presidentially appointed stand-in cannot serve for more than 210 days. For Bement, time runs out on 18 September. Acting officials can't be reappointed or have their terms extended, according to the law, and any official duties performed after the deadline are null and void.

There is one relevant exception. If the president formally nominates someone, the clock is suspended until the Senate acts on the nomination. A rejection or withdrawal of the nominee restarts the 210-day clock.

Bement said in February that he expected to return to NIST quickly, and presidential science adviser John Marburger said in April that a nomination was imminent. Although no name has surfaced, last week Office of Science and Technology Policy spokesperson Robert Hopkins said that "the Administration intends to nominate a permanent NSF director prior to the end of Bement's temporary appointment."

That silence is making the scientific community increasingly anxious. "We are very concerned," says Warren Washington, chair of the National Science Board, which oversees NSF. He says that Bement "has done an excellent job. Arden is due to leave on the 19th, and it's not clear what will happen after that. You'd think [the White House] would be able to find someone during that [210-day] time."

Federal agencies are occasionally run by acting officers, of course. But the 1998 law is intended to prevent a president from sidestepping the U.S. Constitution with acting officials who don't have to be approved by the Senate.

So far, however, the little-known law is struggling to gain the respect of the Executive Branch. A 2001 study by the Government Accountability Office (GAO), which is responsible for enforcing the law, found that agencies hadn't even reported a quarter of their acting officials.

Once GAO detects a violation, its authority is limited to notifying both the agency and Congress that the law has been broken. GAO's database, for example, shows that Ruth Kirschstein twice exceeded her 210-day authority as acting National Institutes of Health (NIH) director after succeeding Harold Varmus in January 2000. In the first instance, NIH's parent agency, the Department of Health and Human Services, changed Kirschstein's title but said she could continue to act as NIH's boss. The second time, after a new 210-day stint triggered by a change in administration also ran out, Congress added language to an NIH spending bill that gave Kirschstein the right to remain acting director until her successor was in place. Her interim reign finally ended in July 2002, when the Senate confirmed her successor, Elias Zerhouni.

A senior congressional aide says there are no plans to address the situation at NSF when Congress returns next week from its summer recess, and NSF General Counsel Lawrence Rudolph speculated that it would be difficult for legislators to act by the 18th. In the meanwhile, Bement continues to shuttle between NIST and NSF, doing both jobs and waiting for his political bosses to clarify his status.

—JEFFREY MERVIS

ACADEMIC LEADERS

Neuroscientist Named MIT President

A neurobiologist from Yale University has been named president of the Massachusetts Institute of Technology (MIT). The appointment of Susan Hockfield to succeed Charles Vest in December reflects the growing importance of the life sciences at MIT, which for the first time in its 142-year history will be led by a woman.

"I think they are slightly redefining MIT" by choosing Hockfield, says James Watson, a Nobel laureate who hired her as a junior investigator at New York's Cold Spring Harbor Laboratory in 1980. "They haven't chosen someone from the military-academic-industrial complex." Her selection, he adds, "is great for neuroscience at MIT." This year, for example, MIT for the first time will receive more research dollars from the National Institutes of Health than from the Pentagon.

Hockfield is currently provost at Yale, which she joined as a faculty member in 1985. She has also served as dean of the graduate school of arts and sciences. She possesses "a rare combination of scientific achievement, outstanding managerial talent, and an extremely engaging personal style," says James Champy, who chaired the presidential search committee. All of MIT's previous 15 presidents have been male engineers or physicists, and the institution's prominence has made them national spokespersons for the science and engineering communities. Vest, a mechanical engineer, certainly played that role during his 14 years at the helm. Although Hockfield lacks that experience, her boss, Yale president Richard Levin, predicts that she "will take a leading role in shaping national science policy."

New leader. Susan Hockfield's appointment is said to "redefine MIT."

Hockfield's research has focused on brain tumors, and her work using monoclonal antibody technology led to the discovery of a protein that regulates changes in neuron structure. She also found a gene and proteins that may help researchers battle the spread of particularly deadly brain cancers. Yale colleagues cite her efforts to increase the number of women faculty members, a contentious issue at MIT since a 1999 report that was harshly critical of its treatment of women.

—ANDREW LAWLER

CREDITS (TOP TO BOTTOM): RICK KOZAK; DONNA COVENEY/MIT

The causes of this syndrome have long been controversial. Now research is unearthing both genetic and environmental triggers and pointing the way to better treatments

Making Sense of Tourette's

When Purdue University neurobiologist Peter Hollenbeck lectures in front of his 400-student cell biology class, the symptoms of his Tourette syndrome—the up-and-down movements of one arm, the twists of his head, the barely audible sounds—virtually disappear. But, by the time the lecture is finished, the urge to move is unbearable. He quickly retreats to his office to "tic, tic, tic," he says, "until the need subsides."

Hollenbeck has a mild case of Tourette syndrome, whose effects he chooses to endure rather than experience the slight sedation he feels when medicated. Other people are more harshly affected. A small minority exhibits complex behaviors such as imitating others or blurting out profanities. Some are tormented by obsessive thoughts, such as the scientist who had to give up high-energy physics because every time he saw a "Danger—High Voltage" sign, he felt compelled to touch the equipment. Many cases of Tourette's are socially inconspicuous, and people with the syndrome deride the stereotyped depictions that occasionally appear in the media. But severe cases can still provoke, as James Boswell said of Samuel Johnson's Tourette's, "surprise and ridicule."

The cause of Tourette syndrome has been controversial ever since Georges Gilles de la Tourette, a neurologist who shared a mentor with Sigmund Freud at the Salpêtrière Hospital in Paris, first described the condition in 1885. Is the syndrome the result of hysteria (Tourette's hypothesis), repressed sexual conflicts, or oppressive mothers, which were the favored explanations for much of the 20th century? Or is it an organic defect of the brain, as many neuroscientists and physicians now hold? The ability of neuroleptic drugs, beginning with haloperidol in the 1960s, to reduce tics supported the neurologic position. But why then are people with severe cases sometimes drawn toward socially proscribed behaviors?

New findings are beginning to resolve old controversies. Researchers are identifying parts of the brain affected by the syndrome. They are teasing out the genetic and environmental factors that help produce it. New behavioral and pharmacological treatments are improving the quality of life for Tourette's sufferers. Although many features of the syndrome remain baffling, researchers say that the intensified research of recent years has begun to pay off.

Defining the phenotype

The wide range of Tourette's symptoms makes it tough to figure out how many people have the syndrome. Many children exhibit tics such as blinking or shrugging. When researchers observed first- through sixth-grade classrooms in Montgomery County, Maryland, in 1999–2000, they saw single or occasional tics in 18% of children and persistent tics in 6%. But just a fraction of these children would be diagnosed as having Tourette syndrome. Current diagnostic criteria require the presence of multiple motor tics and one or more vocal tics that persist for more than 1 year. Typically, the tics wax and wane over the course of weeks and months, with old tics disappearing and new ones taking their place. Children often show the initial signs of tics at ages 6 or 7, and in many cases the tics diminish significantly in the mid- to late teen years.

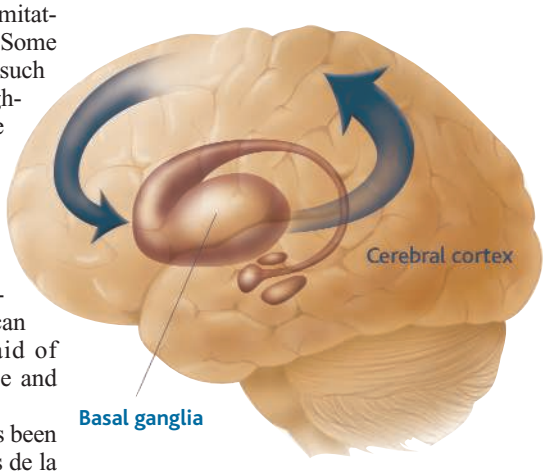

Faulty wiring? Tourette syndrome appears to arise from defects in neural circuits (shown schematically by arrows) passing from the cerebral cortex through the structures constituting the basal ganglia and back to the cerebrum.

"When I'm asked how many people have it," says John Walkup, a child and adolescent psychiatrist at Johns Hopkins University (JHU) School of Medicine in Baltimore, "my response is, 'Have what: mild tics or a severe case?' " According to Lawrence Scahill, who studies neuropsychiatric disorders at the Yale Child Study Center, a plausible lower bound for the syndrome is 1 in 1000 people and a plausible upper bound is 1 in 100. But because many people who would meet the diagnostic criteria for Tourette syndrome never seek treatment, better estimates are elusive.

Comorbid conditions complicate many diagnoses. As many as half of the patients who come to clinics with the symptoms of Tourette syndrome also have other disorders. Obsessive-compulsive disorder (OCD) and attention deficit–hyperactivity disorder (ADHD) are the most common, but Tourette's patients also have elevated rates of depression, anxiety disorders, and social and emotional difficulties. A clinician might have to decide, for example, whether repeatedly lining up a finger with a corner of a room constitutes a tic or a compulsion.

Some researchers see Tourette syndrome as a single discrete disorder that may be accompanied by other syndromes such as OCD or ADHD. Others see Tourette's as part of a spectrum of disorders with common causes and varying manifestations. The distinction is critical when designing studies of Tourette's, says Mary Robertson, a neuropsychiatrist at Royal Free and University College London Medical School. If patients with Tourette's symptoms alone have a different disorder from that of patients with Tourette's and OCD, researchers need to distinguish between the two groups to search for causes. "Unless you define what the phenotype is, studies of Tourette syndrome are nonsense," Robertson says.

Investigators who image the brain have made some progress in detecting patterns of neural activity that might help in making diagnoses. For example, imaging studies show that when ticcing or suppressing tics, people with Tourette syndrome differ from controls in localized brain activity.

CREDIT: K. SUTLIFF/*SCIENCE*

Published by AAAS

But the patterns of activity vary from person to person, so observing and describing tics remains the best way to arrive at a diagnosis.

From phenotypes to causes

Brain imaging has also helped focus attention on the parts of the brain that seem to give rise to the symptoms of Tourette syndrome: the basal ganglia. These are a set of interconnected brain structures positioned beneath the cerebral cortex. Neural circuits run from the cerebrum through the basal ganglia and then back to the cerebral cortex, providing a feedback loop that helps integrate brain functioning. In some ways, the basal ganglia act as an operating system, linking volitional acts initiated in the cerebrum with the nerves and muscles that carry out our wishes.

In Tourette syndrome, that operating system appears to be somewhat buggy, says Jonathan Mink, a neuroscientist at the University of Rochester Medical Center in New York. One function of the basal ganglia is to learn and regulate the expression of discrete chunks of behavior, such as particular movements or thoughts. In this way, says Mink, the basal ganglia help the other parts of the brain perform, combine, and suppress behaviors. "A lot of learning involves enabling the behaviors you want and inhibiting the ones you don't," he says.

Mink suspects that, in Tourette syndrome, groups of neurons in the basal ganglia fail to inhibit particular movements or other unwanted behaviors. As a result, these behaviors surface as tics. Furthermore, circuits from all parts of the cerebral cortex—including those involved in motion, sensation, and emotion—pass through the basal ganglia. Disinhibiting specific parts of the basal ganglia may trigger different manifestations of Tourette's and related disorders. Also, although circuits largely run in parallel through the basal ganglia, some neurons spread across circuits, allowing for crosstalk. This might explain, for example, why tics get stronger when someone is stressed or tired.

Researchers don't know why parts of the basal ganglia may be malfunctioning. But the neurotransmitter dopamine appears to be involved, because many of the drugs that are effective against Tourette syndrome block dopamine receptors. Researchers have looked at dopamine release, dopamine reception, and secondary pathways within postsynaptic neurons, but no obvious culprit has emerged. However, a recent imaging study has revealed an elevated number of dopamine-containing neurons in one part of the basal ganglia of Tourette's patients, and another has shown that abnormal brain function during a memory test can be restored to normal by manipulating dopamine.

Advocates. These athletes and artists with Tourette's are trying to change the image of the syndrome.

Genetic origins?

Several lines of evidence point toward a genetic cause of Tourette syndrome. The disorder tends to run in families and is several times more common in boys than girls. In some families, parents pass the syndrome on to their children as if it were a dominant trait. Even when Tourette's arises anew in a generation, relatives are often more likely to suffer from associated conditions such as OCD or ADHD.

Because of the seemingly simple transmission of the disorder in some families, researchers in the 1990s expected to find a single, relatively rare genetic variant, as in Huntington's disease, that caused at least some cases. But that model proved to be too simple, says David Pauls, a geneticist at the Harvard School of Public Health and Massachusetts General Hospital in Boston. Instead, genetic studies suggested that several chromosomal regions were involved, with the genes in these regions having contrasting effects. According to Matthew State, a geneticist at the Yale Child Study Center and the Center for Genomics and Proteomics, "Studies have pointed to genes with dominant, recessive, and intermediate inheritance, which makes our lives very difficult."

Researchers are eagerly awaiting the fall release of results from an ongoing genetic study of 256 families being conducted by an international consortium. Meanwhile, other studies that can be done with far fewer research subjects are sharpening the focus on suspicious chromosomal regions and identifying new ones. Many geneticists now suspect that Tourette syndrome results from several genetic variants acting in concert. They also believe that, if enough research subjects can be recruited, future genetic studies will uncover the specific variants responsible for the absence or presence of comorbidities with Tourette's.

Environmental complications

But genes are only part of the story: As with other complex diseases, environmental factors influence the syndrome. Although identical twins tend to share Tourette syndrome, in about 20% of cases one has the syndrome and the other does not. And even when both have Tourette's, their experiences with the syndrome can differ markedly, with the lighter-weight twin at birth often having more severe symptoms. Possible environmental factors range from complications during pregnancy, to stressful early-life experiences, to random events during development. But suspicion has focused on an infectious agent.

Since the 18th century, physicians have known that rheumatic fever can lead to

CREDITS: PHOTOS COURTESY OF TOURETTE SYNDROME ASSOCIATION INC.

movement disorders in a subset of those afflicted. This observation led researchers to wonder whether streptococcal infections—the cause of rheumatic fever—might be behind some cases of Tourette syndrome. Some children first show signs of Tourette's after a strep infection, and subsequent infections often seem to exacerbate their tics. In addition, immunologic studies have suggested that in some children the antibodies generated to combat strep misidentify and damage neurons in the basal ganglia. "Parallel lines of research were coming together and showing the same thing: that strep is a factor," says Susan Swedo of the National Institute of Mental Health, who categorizes such cases of Tourette's and related conditions as pediatric autoimmune neuropsychiatric disorders associated with *Streptococcus* (PANDAS).

Swedo and her colleagues have conducted double-blind trials of penicillin and azithromycin prophylaxis to prevent exacerbations of tics in children with Tourette syndrome. They also have experimented with the more invasive process of using plasmaphoresis to remove anti–basal ganglia antibodies from the blood. Although the waxing and waning of the syndrome complicates the interpretation of results, Swedo is convinced that both approaches can significantly reduce the impairment caused by Tourette's and related disorders.

Many researchers are skeptical of the association and of pharmacological efforts to prevent strep infections in children with Tourette syndrome. "It's an intellectually compelling hypothesis that deserves further study, but the data are not all there," says Harvey Singer, a pediatric neurologist at JHU. Singer points out that most children contract multiple strep infections, so an association with tic exacerbations could be coincidental. Many researchers and physicians also worry about prescribing long-term use of antibiotics for children with neuropsychiatric disorders, because such widespread use would likely increase levels of drug resistance. An ongoing large-scale study of penicillin prophylaxis may provide some answers, but the strep connection is likely to remain controversial.

Treating the symptoms

For now, the most common treatment for Tourette syndrome remains what it has been for the past 4 decades: using drugs to alter the activity of dopamine and related neurotransmitters in the basal ganglia. Newer kinds of drugs, known as atypical neuroleptics, are thought to produce fewer unwanted side effects than did earlier treatments. Many physicians practice the "art of medicine," prescribing different drugs until they find one that works for a patient.

Earlier this year, a man suffering from a severe case of Tourette syndrome underwent an experimental procedure in which battery-powered electrodes were placed in his thalamus, which forms part of the circuit connecting the basal ganglia and the cerebral cortex. The electrical stimulation from the electrodes produced an almost complete cessation of his tics. Although the success has generated great excitement among patients, many researchers and physicians are cautious. "This is an experimental procedure that has significant risks," says JHU's Walkup. "We may not like all of the medications all of the time, but many patients find a way to get control of their tics with them."

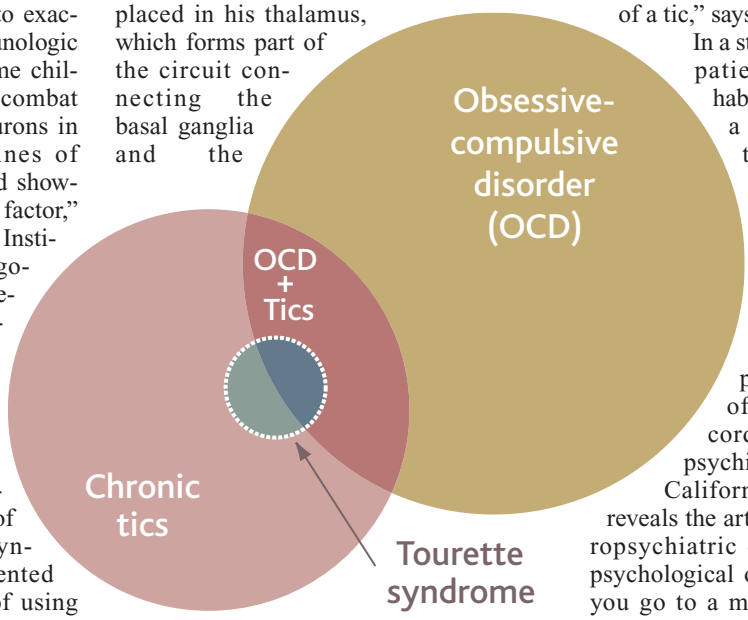

Multifaceted. Not everyone with chronic tics has Tourette syndrome. Sometimes those with the syndrome also exhibit symptoms of obsessive-compulsive disorder (shown in this diagram) or other neuropsychiatric disorders, such as ADHD.

Other nonpharmaceutical interventions hold greater promise. Buoyed by the success of behavioral modification therapy in treating OCD, researchers have been examining similar approaches to Tourette syndrome. One problem with Tourette's, says John Piacentini, a specialist on childhood and teen neuropsychiatric disorders at the University of California, Los Angeles, is that it sets up a positive feedback loop. Patients feel the need to tic and then experience relief when they do, thus reinforcing the neural circuits involved in that behavior. To break the loop, Piacentini and his colleagues have been experimenting with behavioral techniques. People with Tourette syndrome are helped to be made aware of their tics—for example, by watching themselves in a mirror. They then are taught to replace the tic with a competing response. They might replace the tic with a movement that is less apparent, tense the muscle involved in the tic, or strengthen an antagonistic muscle. Such an approach "tries to disrupt the automatic chain of events underlying the expression of a tic," says Piacentini.

In a study conducted with his own patients, Piacentini has seen habit-reversal training produce a 30% reduction in tic severity. Now he is participating in a multicenter study to investigate the therapy more thoroughly.

Unifying mind and brain

The renewed emphasis on behavioral approaches is producing a broader view of Tourette syndrome. According to Neal Swerdlow, a psychiatrist at the University of California, San Diego, Tourette's reveals the artificiality of viewing a neuropsychiatric disorder as either purely psychological or purely neurological: "If you go to a meeting, single-cell neurophysiologists and people studying theories of the mind both have something to contribute to the discussion."

This unified view of Tourette syndrome has important implications in both the clinic and the lab, say physicians and researchers. The goal of treatment is not necessarily to eliminate tics, say clinicians; it is to enable someone with Tourette's to function effectively in society. The Tourette Syndrome Association Inc. (www.tsa-usa.org), an advocacy group founded in 1972 by some of the first patients to benefit from pharmacologic treatments, has worked hard to educate the public and the media about the syndrome. Especially for cases of Tourette's unaccompanied by severe comorbidities, understanding and accommodation can be as important as medications.

Similarly for the research community, an emphasis on the experiences and adaptations of individuals can suggest areas to explore that a narrow biomedical focus might overlook. For example, determining which patients could benefit most from behavioral approaches could provide physicians and their patients with badly needed guidance. Tourette syndrome has biological, psychological, and social dimensions, says Swerdlow, "and you can't separate out one of those without losing the disorder."

–STEVE OLSON

Steve Olson's most recent book is *Count Down: Six Kids Vie for Glory at the World's Toughest Math Competition.*

ADAPTED FROM ADA ZOHAR *ET AL., TOURETTE'S SYNDROME: TICS, OBSESSIONS, COMPULSIONS*

Telescopes Break New Ground In Quest for Cosmic Rays

To trace the origins of mysterious particles from space, researchers are building instruments that reap novel benefits from being planted on terra firma

In 1912, Austrian physicist Victor Hess set out to find the source of a mysterious radiation that was plaguing electrical experiments of the day. Most scientists thought it came from radioactive minerals in the ground. But in a series of daring balloon flights that reached heights of several kilometers, Hess showed that the radiation increased with altitude and did not wane even during the night or a near-total eclipse of the sun. He concluded, controversially, that the radiation came from deep space. The discovery of "cosmic rays" later netted Hess the Nobel Prize in physics. Yet, nearly a century after Hess's experiments, astrophysicists still do not know where in space they come from.

That may be about to change, thanks to powerful new telescopes designed to detect light with the very highest energies: gamma ray photons with energies in the range of 10^{12} electron volts, or tera–electron volts (TeV). Unlike ordinary astronomical telescopes, which try to peer through Earth's distorting blanket of air to view objects beyond, the new instruments—known as imaging air Cerenkov telescopes—use an indirect method: They look for flashes of visible light created high in the atmosphere when the gamma rays hit. Theorists believe that many of these gamma rays share a common origin with cosmic rays and that they should be easier to trace back to their sources.

First-generation Cerenkov telescopes have been scanning the skies for 2 decades. But although they have turned up several promising sources of TeV gamma rays, they cannot yet prove that cosmic rays come from the same place. Researchers expect that the new, more powerful generation of these telescopes, which came on line this year, will cement the connection. At the vanguard is a four-scope array based in Namibia and named the High Energy Spectroscopic System (HESS), in honor of the cosmic ray pioneer. HESS began observing last January and will be officially inaugurated on 28 September. A second array in Australia started up in March; a single scope in the Canary Islands will join the hunt this autumn; and a U.S.-based array is scheduled for completion in 2006.

TeV gamma ray astronomy has always been an oddball in the astronomy world, says Karl Mannheim of the University of Würzburg, Germany: "We use particle physics techniques. The whole culture is different." But thanks to some recent successes with both the old and new Cerenkov telescopes, astronomers are now beginning to "take us seriously," says HESS spokesperson Werner Hofmann of the Max Planck Institute for Nuclear Physics in Heidelberg. That's particularly true because, even though the original motivation for studying TeV gamma rays was to track down the source of cosmic rays, this part of the spectrum shows promise for studying traditional astronomical objects, such as pulsars, blazars, and active galactic nuclei, and perhaps even enigmatic gamma ray bursts and dark matter.

Cosmic rays are small atomic nuclei—mostly hydrogen nuclei, or protons—that whiz through space at close to the speed of light. No ordinary star could boost matter to such unimaginably high speeds; some other high-energy process in deep space must be at work. Researchers suspect supernovas but don't yet have conclusive evidence. The problem is that cosmic rays themselves don't tell you where they've come from. Because the particles carry electric charge, interstellar magnetic fields scramble their trajectories, making it impossible to identify their source. But if theorists are right that the cosmic rays get their initial kick from supernova remnants, then this boost has a byproduct: TeV gamma rays, which, being chargeless, zip through space as straight as an arrow. Find where those gamma rays come from, the theory goes, and you might just find a source of cosmic rays.

Gamma rays don't give up their secrets easily, however, because they cannot penetrate Earth's atmosphere. Astronomers first got a good look at them with the help of orbiting detectors, culminating, between 1991 and 2000, in NASA's enormous Compton Gamma Ray Observatory. But CGRO was not sensitive to TeV photons. To study them, astrophysicists hit on a counterintuitive trick: making the atmosphere part of the detector.

When a gamma ray or a cosmic ray hits the upper atmosphere, it shatters an atom. The fast-moving debris shatters other atoms, and debris from them shatters more. Soon a shower of millions of particles rains down toward Earth's surface. Initially, these particles are traveling faster than the speed of light in air, so to slow down they shed photons of blue light known as Cerenkov radiation. Researchers first detected the Cerenkov light from cosmic rays in the 1950s, but it was not until the 1980s that they figured out how to distinguish the more informative gamma ray air showers from cosmic ray air showers: The two types of showers have slightly different shapes.

The Whipple telescope, a 10-meter-wide optical dish on Arizona's Kitt Peak, was the first instrument to capture the Cerenkov light from an air shower and form it into an image. Such Cerenkov telescopes do not need to be made to the optical perfection of normal astronomical telescopes because they are observing something only 10 kilometers away in the upper atmosphere. But the light from air showers is very faint—just 100 photons per square meter reach the ground—so the telescopes preferably need to be somewhere high, dry, and very dark. The telescope dish focuses this faint signal onto an array of photomultiplier tubes—which can detect single photons—that forms a rough image of the shower.

The image is key. The shape not only distinguishes gamma rays from cosmic rays but also helps researchers calculate the direction the gamma ray came from. And the intensity of the image—the number of photons—tells them its energy. In 1989, the Whipple telescope for the first time traced TeV gamma rays back to a recognizable source: the Crab nebula, the remnant of a supernova thought to have exploded in 1054.

The next breakthrough came in the mid-

Looking up. Two of HESS's four 12-meter dishes in Gamsberg, Namibia.

CREDIT: HESS COLLABORATION

Published by AAAS

1990s from a European collaborative experiment called HEGRA, for High-Energy Gamma Ray Astronomy, based on the island of La Palma in the Canary Islands. HEGRA had a variety of different detectors for TeV gamma rays, but the most successful, says Mannheim, was an array of five imaging Cerenkov telescopes arranged in a square 100 meters across with one scope in the middle. The benefit of having an array of telescopes is that the different views of the air shower can produce a three-dimensional image, giving better discrimination between gamma rays and cosmic rays and a better fix on the direction of the original gamma ray (see figure). "The stereoimaging technique is incredibly powerful," says Rene Ong of the University of California, Los Angeles.

The success of the HEGRA telescopes spawned proposals for several more arrays, with bigger dishes and better electronics. Part of the HEGRA collaboration joined with others and began building HESS in Gamsberg, Namibia. The Whipple team embarked on VERITAS (the Very Energetic Radiation Imaging Telescope Array System), initially to have four scopes, on Kitt Peak. And a Japanese-Australian team that built a first-generation Cerenkov instrument in Woomera, Australia, set about building four new ones, dubbed CANGAROO III, short for Collaboration of Australia and Nippon for a Gamma Ray Observatory in the Outback. Other HEGRA members formed a new team, including Mannheim, to try a different route: building a single, much larger telescope, the 17-meter-wide MAGIC (Major Atmospheric Gamma-ray Imaging Cherenkov [*sic*] telescope) on La Palma, which can detect lower-energy gamma rays from the ground.

HESS began routine operations last January, and CANGAROO III followed suit in March. Both teams announced some of their first results at a meeting on high-energy gamma ray astronomy in Heidelberg in July (*Science*, 6 August, p. 763). VERITAS, which took longer to secure funding, has one prototype scope working and should be up and running in 2006. "We've demonstrated the technology works. Now we just have to replicate it," says VERITAS's spokesperson, Trevor Weekes of the Whipple Observatory. MAGIC hopes to begin routine observing this October.

Researchers are bracing themselves for a flood of new data. "In the past, the main problem was that you were only looking at 18 or 19 [TeV gamma ray] sources," says Hofmann. The new scopes, with their superior ability to pick out gamma rays from the background, should rapidly expand that catalog to 100 or more TeV sources, including both supernova remnants and other more exotic objects in distant galaxies, Hoffman says. That will be "the beginning of 'real' astronomy," says CANGAROO III spokesperson Masaki Mori of the University of Tokyo.

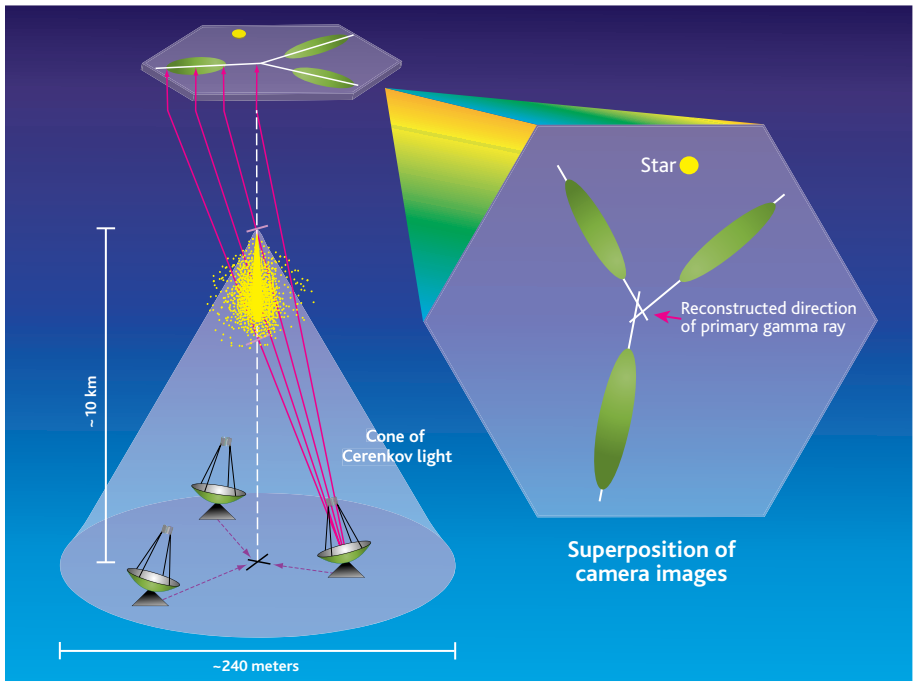

Fresh perspective. Multiple views of air showers help trace the source of gamma rays.

Their first big project, researchers say, is to nail down whether supernovas do produce cosmic rays. When material speeding out from the supernova hits interstellar gas, it creates a shock wave, and particles, usually protons, "ride the shock like a surfer on a wave," says Hofmann. Most of these light-speed surfers glide off into space as cosmic rays, but a few slam into atoms of interstellar gas and are annihilated, each creating a neutral pion that quickly decays into two TeV gamma rays.

But that is not the only process that can produce TeV gamma rays. Accelerated electrons colliding with low-energy photons can also produce them. To discover whether at least some of the gamma rays are produced by protons rather than electrons, researchers will have to try to map out where the gamma rays originate around the supernova remnant, because the two processes would have different distributions. Resolving the cosmic ray mystery "won't happen overnight," says Weekes. "No single observation will solve it." And researchers caution that the result is not a foregone conclusion. "If supernovae are not confirmed as the source [of cosmic rays]," says Hofmann, "we'll really have to rethink our models."

Even if that revolution never comes, Cerenkov telescopes are already unleashing surprises. When the first instruments were built, researchers were focused on the cosmic ray problem. "I wouldn't have been surprised if we'd just seen supernova remnants," says Weekes. But a large chunk of the sources they found were in fact far more distant objects in other galaxies. When researchers managed to identify these extragalactic sources by looking for them at other wavelengths, they were staggered by the sheer variety. The menagerie includes active galactic nuclei, which are believed to have huge accreting black holes at their centers. These black holes often send out jets of particles at relativistic speeds that can produce gamma rays. There are also tight-knit groups of very massive and hot stars, known as OB stars, that produce such an outflow of stellar wind that they create a shock wave when they hit the interstellar medium.

Perhaps the "most fascinating," says Mannheim, is the possibility of identifying dark matter. We know from the way galaxies behave that there must be more matter in them than we can see in the shining stars and glowing dust. Theorists believe that some dark-matter particles cluster around the centers of galaxies or in their haloes. If dark-matter particles and antiparticles are annihilating each other, they will produce TeV gamma rays visible to Cerenkov telescopes. At the Heidelberg meeting, the HESS team reported seeing gamma rays from the center of our galaxy. Hofmann says the energy was wrong for dark matter but adds that they "cannot exclude" that explanation.

Pioneers at this high-energy frontier don't yet know what they will learn from these exotic objects by studying their TeV gamma rays, but they're looking forward to finding out. "We have to be prepared to find something new," says Mannheim. Adds Ong: "The HESS results are just the beginning"

–DANIEL CLERY

ILLUSTRATION: K. BUCKHEIT/*SCIENCE*; SOURCE: G. PUEHLHOFER

Newly Hatched Dinosaur Babies Hit the Ground Running

BOCA RATON, FLORIDA—From 27 July to 1 August, animals with a backbone drew the attention of morphologists, evolutionary biologists, and other researchers.

Therizinosauroid dinosaurs grew up fast. When they chipped their way out of an egg, the animals emerged strong-legged, ready to fend for themselves and find food, according to an analysis of 80-million-year-old fossil dinosaur eggs conducted by a team of paleontologists and developmental biologists.

For the past 6 years, Arthur Cruickshank of the University of Leicester, U.K., Martin Kundrát of Charles University in Prague, Czech Republic, and their colleagues have studied the jumbles of bones and teeth packed into a dozen fossil eggs found in Henan Province, in east-central China. The teeth and bones allowed them to identify the fossils as theizinosauroid, Kundrát reported.

Now, by comparing the dinosaur embryos with embryos of birds and alligators, Kundrát has determined how far along in development each embryo was and has begun to piece together how therizinosauroid young grew to be independent. To do this, Kundrát's team enlisted the help of Terry Manning of Rock Art in Leicester, who spent several years removing the eggshells, etching out the rock inside, and exposing the fossils. The results of Manning's efforts are impressive and provide unprecedented details about dinosaur embryos, says Eric Snively, a paleontologist at the University of Calgary, Canada.

A good egg. This fossil embryo revealed many secrets about one dinosaur's early life.

Manning and Cruickshank first documented the amount of yolk in each egg and the position of each dinosaur embryo. Because the amount of yolk packed around an embryo decreases over time, the degree to which the embryo is squished inside the eggshell is a rough indicator of the embryo's age.

Kundrát got an even better sense of each embryo's developmental age by using the porosity of the fossilized dinosaur skulls, limb bones, and backbones as a guide. A skeleton starts out soft and porous and gradually hardens into bone, so the degree of ossification typically reflects the age of an embryo. Using the known morphology and hardness of alligator bones at different points in embryogenesis, Kundrát was able to sharpen his age estimate for each dinosaur embryo.

Kundrát determined that all the dinosaur embryos were at least two-thirds of the way through their development, and parts of their skeletons were much further along than those of comparably aged alligator embryos. For example, the dinosaur vertebrae were less porous than expected. "They had well-ossified limb bones, so they can walk immediately after hatching," says Kundrát.

As part of their study, Kundrát and his colleagues also gathered the fossilized teeth of the embryos. Those from the youngest embryos resemble the teeth of the other theropods and were well suited for eating meat. In the more mature embryos, although the teeth retained some meat-eating potential, they were more like those seen in adult therizinosauroids, which are presumed to be herbivores. "We could see the transition of the tooth crown and cusp," Kundrát said.

These data suggest that the hatchlings came out of the egg able to chase down prey and consume suitable plants, Kundrát reported. He suggests that these stages of tooth development reflect the evolutionary steps that allowed therizinosauroids to arise from carnivorous ancestors.

"I'm glad to see this [embryo work] done," says Zhe-Xi Luo, a paleontologist at the Carnegie Museum of Natural History in Pittsburgh, Pennsylvania. In addition to their embryos, he notes, the eggs are important in their own right, because they hint at another aspect of the dinosaurs' lives. Until recently, the only adult remains of therizinosauroids in the Far East have been found near Mongolia, about 1,000 kilometers from the site where the eggs were found. This suggests to Luo that these dinosaurs migrated great distances or that they were much more widespread than paleontologists had thought.

Tiny Salamanders Show Their Teeth

For such small animals, salamanders belonging to the *Thorius* genus have posed a big problem: Biodiversity experts can't easily tell different species apart, because many of them look identical. That makes it difficult to count species or understand the animals' evolutionary history. Now, James Hanken of Harvard University has used genetics to classify the animals and place them on a family tree that illuminates the morphological history of the genus. As Hanken reported at the meeting, the tree suggests that a few *Thorius* species have turned back the evolutionary clock, reacquiring traits—including teeth—that their earliest ancestors had lost.

The miniature salamanders, which are native to Mexico, live on moss and inside bromeliads and fallen logs. Hanken, who began studying the animals 30 years ago, has always been fascinated by their size. Although some are much larger, certain *Thorius* species have bodies just 13 mm long, making them the tiniest tailed tetrapods. Packing all the necessary organs into a body that size poses a challenge. "[They] are right up against the edge of vertebrate design," says Hanken. They can't be much smaller, agrees Johan van Leeuwen of Wageningen University in the Netherlands.

Hanken originally thought there were fewer than a dozen *Thorius* species, but by looking for slight genetic differences that readily distinguish one species from another, he and his colleagues quickly identified 14 new species. His group recently added eight more to the list. "Every trip we take, we find one or two new species," says Hanken.

Those results answered one long-standing question: In part because there's little room in those tiny bodies to move parts around, researchers have wondered whether the small size of *Thorius* salamanders would

CREDITS: T. W. MANNING

Published by AAAS

Compact package. The tiny *Thorius* is one-tenth the size of many other salamanders.

limit the animals to splitting into just a few species instead of radiating into many. "Hanken's results show that … these salamanders have been radiating just fine," says Jukka Jernvall, an evolutionary biologist at the University of Helsinki, Finland.

That radiation took some surprising turns, however. The skull bones of the tiniest *Thorius* species are mere slivers compared to those of other salamanders, and they no longer interlock to make a solid skull. Their 3-mm-long heads have just enough room for a brain, eyes, nose, and ears—the majority of muscles and connective tissue is missing or greatly reduced. In most species, the upper teeth are even gone.

Yet four of the salamander species have their upper teeth. Hanken had assumed that these species all descended from a common ancestor that had kept those teeth while other branches of the *Thorius* tree lost them. Yet the family tree he and his colleagues constructed revealed that the four species are not closely enough related to have shared such an ancestor. Instead, each species with upper teeth came from toothless stock. These upper teeth "have been reacquired four times," Hanken reported at the meeting.

Three of the upper-toothed species break the miniaturization trend among *Thorius* salamanders. They're larger and have bigger skulls than other extant species. "The presence of teeth seems to be fluid over time and suggests miniaturization and loss of elements might not always be final," says Jernvall.

Some of Hanken's colleagues question his interpretation, noting that the common wisdom holds that once a trait disappears from a group of organisms, it rarely resurfaces. Hanken's conclusion is "something that's hard to defend," says Ann Huysseune of Ghent University in Belgium. But Hanken argues that these small vertebrates must have had a lot of evolutionary tricks up their sleeves in order to survive tough times. He points to the success that small animals in general have had after mass extinctions and attributes that to their ability to rapidly change and adapt.

Thorius species, he thinks, may have retained the capability of making upper teeth, even if their tooth-building program became short-circuited. The reappearance of upper teeth in the four salamander species, says Hanken, "offers an example of latent developmental potentialities that reside within living species but which may not be manifest or expressed until far into the future."

CREDITS: (TOP) D. B. WAKE/UC BERKELEY; K. JACKSON *ET AL.*

Snake Tartare—Quite a Bodyful

Feasting on everything from ant larvae to mammals seemingly too big to swallow, snakes have eclectic tastes. Some even like to eat other snakes. Such slithering snacks present particular challenges if the snake being consumed is longer than the snake doing the eating. "It's a little like me swallowing you," says Margaret Rubega, a functional morphologist at the University of Connecticut, Storrs.

At the meeting, Kate Jackson, a herpetologist now at the University of Toronto, Canada, described how x-ray scans and old-fashioned dissection revealed that a surprisingly stretchy stomach holds the key to successful snake consumption. The study, says Rubega, is "a wonderful, creative use of a variety of tools."

While at Harvard University, Jackson bought juvenile king snakes, reputed snake eaters, and corn snakes from a pet store. When she and her colleagues put the two species into a cage, the snakes would immediately turn into a writhing ball of whipping heads and tails. After just a few minutes, however, the king snake would typically sink its teeth into the corn snake. The king snake, which is not venomous, would then spend the next 8 hours squeezing its prey to death.

Once it had subdued its meal, the king snake would start with the head of the corn snake.* Swallowing required two motions, Jackson reported. As is typical for some snakes, the left and right sides of the jaw can move independently, and each side alternated between grabbing the prey and pulling it back—a "jaw walk," says Jackson's colleague Elizabeth Brainerd, a functional morphologist at the University of Massachusetts, Amherst.

The king snake eventually switched to a different swallowing technique. It would grab hold of its prey, then kink up its vertebrae, and finally, let go and straighten out. "It slides the body over the prey," says Jackson. Within 2 hours, a corn snake would disappear down a king snake's gullet.

Jackson expected ingestion to come to an abrupt halt once the king snake had swallowed the equivalent of two-thirds of its length; that's the end of its stomach. But the king snake managed to cram in the whole corn snake. A dissection of the newly satiated snake revealed how it achieved this gluttonous feat: "The stomach was stretched to 91% of its body cavity," Jackson reported. All the other organs were squished out of the way. "I am amazed at the way they do it," comments David Wake, a herpetologist at the University of California, Berkeley.

The stomach's stretchiness could only partly explain how the king snake swallowed prey bigger than itself. Telltale bulges down the length of the king snake suggested another trick. When Jackson and her colleagues x-rayed a king snake with its ingested prey, they discovered that the corn snake was, in the words of Brainerd, "compressed like an accordion."

Jackson found that even after a king snake had finished taking a corn snake down its throat, it sometimes spit the whole snake back up, particularly if startled. "That's a big risk," says Wake, because it takes so much energy to procure such a meal in the first place. On the other hand, a yen for snakes has its advantages.

Yum, yum. Snakes use special tricks to eat other snakes. Trace the two tails to see who is eating whom.

For its size, the king snake gets the richest meals of all the nonvenomous snakes. "The king snakes are able to get the energy input of a very large meal without having the large mouth-gape specializations and venom of vipers," says Brainerd. Thus, Jackson proposes, even if a dinner is sometimes wasted, it's worth the effort.

—ELIZABETH PENNISI

* Video: www.bio.umass.edu/biology/brainerd/video-library.php

Published by AAAS

Random Samples

Edited by Constance Holden

Reef Therapy

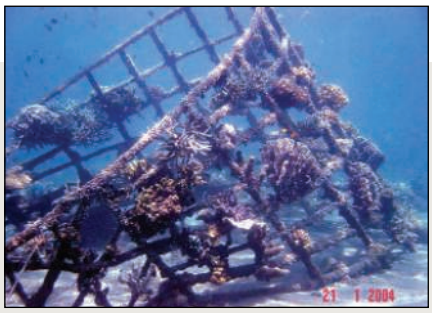

New reef 3 years after getting wired.

Conservationists claim they have developed a system that will cure sick coral reefs through delivery of a mild electric current.

Ecologist Thomas Goreau of the Global Coral Reef Alliance in Cambridge, Massachusetts, and German architect Wolf Hilbertz have been working for decades on the scheme. They're now claiming success in Bali, Indonesia, where they have wires running out to a 300-meter stretch of artificial reefs built with iron construction bars. At the correct voltage, explains Goreau, rising pH causes precipitation of minerals from the supersaturated seawater, forming calcium carbonate that provides the limestone matrix for coral larvae. The limestone accumulates at about 1 to 2 centimeters a year. "This has tremendous applications for habitat restoration," says Goreau.

Goreau says that since the project started in 2000, "we're growing most of the world's main kinds of corals" on the electrified reef. But he hasn't won much interest from funding sources, which are "locked into other conservation strategies."

Robert Buddemeier, an environmental scientist at the University of Kansas, Lawrence, says reef electrotherapy, although not a long-term solution, might serve as intensive care. But even if it works, he says, no one has produced a "rigorous study" showing how.

Turtle Service

Scientists in the United Kingdom are harnessing wide-ranging leatherback turtles—the largest of the sea turtles—to monitor ocean temperatures.

Marine biologist Graeme Hays of the University of Wales, Swansea, and his team have been using satellites to track the giant reptiles as they move from their breeding grounds in the Caribbean to their stomping grounds in the North Atlantic, where they feed on jellyfish. Now the scientists have affixed new satellite tags on seven of the beasts that will relay temperature data for a year or more. Because the leatherbacks range so widely, says Hays, "this system is perfect for effectively monitoring water temperatures across entire ocean basins."

Leatherback girded for climate duty.

The leatherbacks are helping "usher in a new era of ocean monitoring," says Hays. Other animals are being enrolled in the cause, he adds: The largest such effort is an international program called Tagging of Pacific Pelagics, which will be equipping more than 100 turtles and elephant seals with the new tags.

Tibet's Ancient Flood

Geologists say they've found evidence for one of the most powerful "megafloods" ever, in Tibet's Tsangpo Gorge.

The Tsangpo River flows along the southern edge of the Tibetan Plateau before slicing through the mountains toward India, dropping a dizzying 2500 meters through a 200-kilometer-long gorge. Few explorers have visited the forbidding terrain—and paddlers have died trying to run the river.

Intrigued by reports of ancient lakeshore sediments perched high on local mountains, a team led by geomorphologist David Montgomery of the University of Washington, Seattle, this year went to look. It found evidence that glaciers had repeatedly formed rock-and-ice dams along the river over the last 10,000 years, creating enormous lakes and leaving terraced "bathtub rings" on valley walls. One dam appears to have failed catastrophically, suddenly releasing more than 800 cubic kilometers of water, Montgomery's team reports in the

September issue of *Quaternary Research*.

Although scientists have documented bigger ancient megafloods, this one was "one of the most erosive events in recent Earth history," believes Montgomery, because the waters were forced through an extremely steep, narrow valley. The findings confirm that megafloods, although rare, "are an important process in geological evolution," says geomorphologist Vic Baker of the University of Arizona, Tucson, and may help explain how the Tsangpo cut through the region's resistant rock.

Georgia Science Center Closes

SciTrek, the Science and Technology Museum of Georgia in Atlanta, announced late last month that it is suspending operations. The hands-on educational museum, which opened in 1988, suffered from declining attendance and a meager budget.

SciTrek got just 30% of its budget from the government and wasn't able to make ends meet with revenue from visitors. Paul Ohme, director of the Center for Education Integrating Science, Mathematics, and Computing at Georgia Tech, says the center's "exhibits had aged" and that without money for continuous updating, they did not attract many repeat visitors.

The board of the museum said SciTrek may come alive again in the future—as a science education center offering teacher training.

CREDITS: (TOP TO BOTTOM) ARI SPENHOFF; SPACE IMAGING; ANDY MYERS

Published by AAAS

Edited by Yudhijit Bhattacharjee

JOBS

Up the coast. Assisted reproduction pioneer Roger Gosden is packing up after 2 years as head of the Jones Institute for Reproductive Medicine in Norfolk, Virginia, and heading for Cornell's Weill Medical College in New York City.

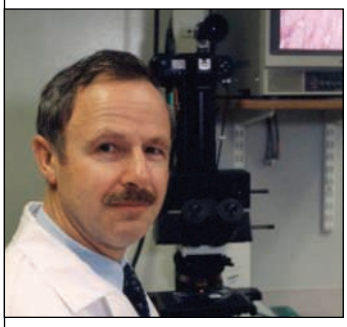

Gosden, 55, is moving for reasons both professional and personal. He recently married Lucinda Veeck, Cornell director of clinical embryology. But he also faced a limited future at Jones, which drew heavy criticism and political hostility for creating a new human embryonic stem cell line in 2001 (*Science*, 25 January 2002, p. 603). The controversy meant that scientists couldn't "effectively do stem cell research" at Jones, says Gosden.

He expects to find a less restrictive environment at Cornell, where he'll also have access to a larger patient population for his ongoing research on identifying markers for top-quality eggs for in vitro fertilization.

Rockefeller chief. Psychologist Judith Rodin, who stepped down as president of the University of Pennsylvania in June, has been named to lead the Rockefeller Foundation in New York City. Rodin, 59, succeeds Gordon Conway, who is retiring at the end of the year. She will take charge of the $3 billion philanthropy in March.

NONPROFIT WORLD

Judicious spender. When Madeleine Jacobs took over as executive director of the American Chemical Society (ACS) in January, she inherited two Cadillac town cars that her predecessor, John Crum, had used for years along with a chauffeur. Within weeks, she let the chauffeur go and had the cars auctioned. "Neither I nor anybody on the board had any use for them," she says.

Those actions have won praise from the society's members, including writers of a letter in *Chemical & Engineering News* last month asking ACS to publish the salaries of employees making more than $150,000 and expressing outrage at Crum's 2002 compensation of $721,000. By cutting back on travel and hotel expenses for herself and her staff, Jacobs has shown that "she has the best interests of the organization at heart," says Robert Bergman, a chemist at the University of California, Berkeley, and a co-signer of the letter. But without greater financial transparency, he says, the system remains open to abuse by senior management.

Jacobs disagrees, saying that executive salaries are determined after studying the market. Although her own salary is "significantly less" than Crum's, she won't reveal it until the fall of 2005, when ACS files its annual report with the government. Listing more than the top five earners, says ACS spokesperson Nancy Blount, would be an invasion of employee privacy.

TWO CULTURES

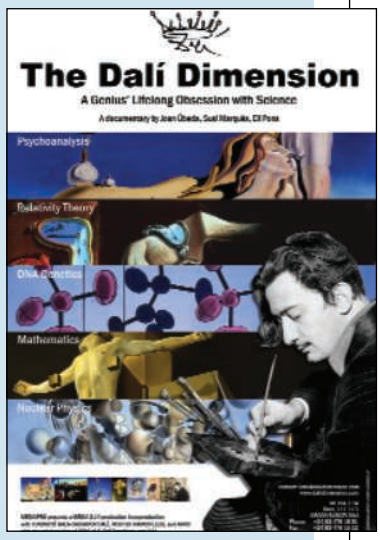

Dalí documented. Science fascinated the eccentric Spanish artist Salvador Dalí (1904–89). He incorporated scientific themes such as psychoanalysis, relativity, and the helical structure of DNA into his paintings and met with illustrious researchers including Sigmund Freud, Ilya Prigogine, and James Watson, who were surprised to discover a keen scientific mind behind his clownish appearance. The Dalí Dimension, produced for European TV by Spanish filmmaker Joan Ubeda, documents the influence that science had on Dalí's work. It premiered at the EuroScience Open Forum in Stockholm last week.

DATAPOINT

A matter of degree. Think you need a bachelor's degree or higher for a career in science and engineering? Think again. A new study by the U.S. National Science Foundation (NSF) has found that 22% of the country's 4.6 million S&E jobs are held by people with no more than a 2-year associate's degree or simply a high school diploma.

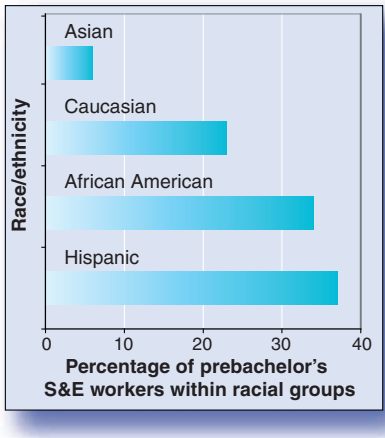

"They're trained, but not necessarily in traditional academic programs," says NSF's John Tsapogas, who extracted the data from the U.S. Census Bureau's monthly *Current Population Survey* for April 2003 and its sample of 10,000 adults. The computer industry and engineering offer the greatest opportunities for non–B.A. degree holders, he notes, but the demographics differ: "The engineers are older and tend to have moved up through the ranks, while the computer scientists are younger, maybe hired during the dot.com boom." And minorities (see graph) represent a disproportionate share of that pool: Some 37% of all Hispanics working in S&E fields, and 34% of all African Americans, hold less than a 4-year degree.

Tsapogas says the size of the non–B.A. work force is more than twice what he would have predicted. NSF's first look at the topic also raises questions about federal training programs that assume the need for advanced S&E degrees.

Got any tips for this page? E-mail people@aaas.org

LETTERS

Letters to the Editor

Letters (~300 words) discuss material published in *Science* in the previous 6 months or issues of general interest. They can be submitted through the Web (www.submit2science.org) or by regular mail (1200 New York Ave., NW, Washington, DC 20005, USA). Letters are not acknowledged upon receipt, nor are authors generally consulted before publication. Whether published in full or in part, letters are subject to editing for clarity and space.

Disclosure of Clinical Trials in Children

AFTER E. MARSHALL'S NEWS STORY ON THE drug industry's burying unfavorable clinical data ("Buried data can be hazardous to a company's health," E. Marshall, News of the Week, 11 June, p. 1576), there have been interesting outcomes. GlaxoSmithKline published full reports of clinical tests on paroxetine in children on its Web site and announced that, in the future, a clinical trial register will be created and made accessible to doctors and the public. In the meantime, another company (Foster Laboratories) was charged with "publication bias" by the *New York Times* for two antidepressant drug trials in children (*1*), suggesting the need for an urgent solution to this lack of transparency.

CREDIT: ALAN STONEBRAKER AND JOSHUA MOGLIA/*SCIENCE*

Many attempts at creating publicly accessible, international clinical trial registries have been made to overcome issues related to the inaccessibility of trial information, such as the *meta*Register of Controlled Trials (http://controlled-trials.com/mrct). The pediatric population, like other subpopulations, is more strongly affected by limits to information, and this led to the creation of an international, pediatric clinical trial register in 2003. The project, the European register of clinical trials on medicines for children—Drug Evaluation in Children (DEC-net; www.dec-net.org)—is the first clinical trial register dealing with a specific population. The project is supported by the European Community as part of its Fifth Framework Programme. The DEC-net register's main objective is to help identify the few pediatric studies being carried out to help researchers and health care workers increase their knowledge on drug therapies derived from them. DEC-net also represents a resource for planning new studies, promoting collaboration between researchers, facilitating patient access to and recruitment into trials, preventing trial duplication and inappropriate funding, and identifying the therapeutic needs of children who remain neglected (*2*). The register will be freely accessible, and the information will be displayed in two interchangeable formats: a simple one for parents/lay public and a more advanced one for health professionals.

MAURIZIO BONATI, CHIARA PANDOLFINI, ANTONIO CLAVENNA
Laboratory for Mother and Child Health, "Mario Negri" Pharmacological Research Institute, Via Eritrea 62, 20157 Milan, Italy.

References
1. B. Meier, "Drug maker acknowledges some negative test results," *N.Y. Times*, 26 June 2004, p. C2.
2. K. Dickersin, D. Rennie, *JAMA* **290**, 516 (2003).

Antidepressants' Use in Anorexic Girls

THE USE OF SELECTIVE SEROTONIN REUPTAKE inhibitor (SSRI) antidepressants in children is debated because of the potential risk of suicide ("Buried data can be hazardous to a company's health," E. Marshall, News of the Week, 11 June, p. 1576; "Volatile chemistry: children and antidepressants," J. Couzin, News Focus, 23 July, p. 468). In our work with adolescent girls suffering from anorexia nervosa, we have noticed that at least 50% are routinely prescribed SSRIs. Yet SSRIs have no effect on the psychiatric symptoms of anorexia, and there is no evidence that they affect outcome favorably (*1*). In addition, we have repeatedly [most recently in (*1*)] pointed out that serotonin, the neurotransmitter system that is stimulated by SSRIs, inhibits food intake, gonadotropin secretion, and sexual behavior; decreases body temperature; and makes learning difficult. These are highly undesirable effects not only in anorexic adolescents but in all developing women. Hence, there are many reasons other than the risk of suicide why SSRIs should not be used in young women.

PER SÖDERSTEN AND CECILIA BERGH
Karolinska Institutet, Section of Applied Neuroendocrinology, AB Mando, Novum, S-141 57 Huddinge, Sweden.

Reference
1. C. Bergh, J. Ejderhamn, P. Södersten, *Curr. Opin. Pediatr.* **15**, 344 (2003).

SSRIs in Children and Suicide

IN HER ARTICLE "VOLATILE CHEMISTRY: CHILDREN and antidepressants" (News Focus, 23 July, p. 468), J. Couzin writes about the complex situation regarding the use of selective serotonin reuptake inhibitors (SSRIs) in children, including the possible initiation of suicidal acts by SSRIs, concealment by industry of negative data, and the problematic state of diagnosis of childhood depression.

I am quoted as dismissing the SSRI fuss as "a tempest in a teapot." My point was that the available data showed that the ambiguous ratings considered putatively suicidal occurred before treatment in less than 1% of the children studied. After SSRI treatment, this approximately doubled, but it is still not clear if this "signal" is statistically significant or clinically meaningful. It is still a very minority "signal." No actual suicides occurred. The furor for immediate action is premature. It should also be noted that much public indignation comes from those who believe that any medical treatment of mental illness should be condemned. Severe depression is a serious illness and close therapeutic monitoring is necessary. This applies to all forms of treatment.

DONALD F. KLEIN
Department of Psychiatry, Columbia University, 1051 Riverside Drive, New York, NY 10032, USA.

Disparities in Cancer Funding

IN HIS EDITORIAL, "PERCEIVED THREATS AND real killers" (14 May, p. 927), R. I. Glass makes important distinctions between the health impact and scientific effort devoted to common and often controllable infectious agents such as influenza and rotaviruses and rare and unpredictable agents such as *Ebola* virus. Similar comparisons between perceived threats, real killers, and scientific emphasis could be made with human cancers. Although the threat of developing common cancers such as breast or prostate cancer is real and not perceived, the cancer that is most proficient at killing humans is lung cancer and the etiologic agent is tobacco. Tobacco is responsible for ~30% of all cancer deaths (*1*), and deaths from lung cancer in the United States exceed those of breast cancer, colorectal cancer, and prostate cancer combined (*2*). Yet the amount of dollars spent per cancer death by funding agencies has

historically favored breast and prostate cancers over lung cancer (sixfold less spent per lung cancer death than per prostate cancer death and ninefold less per lung cancer death than per breast cancer death for National Cancer Institute funding in 2001). The disparity between funding and mortality is consistent with a low level of commitment from the scientific community to study lung cancer: The number of investigators studying rare cancers such as those derived from bone marrow exceeds the number studying the biology of tobacco and lung carcinogenesis. State governments also appear not to perceive tobacco-related illnesses as a real threat because many have opted to use hundreds of millions of dollars in tobacco settlement money to balance skewed budgets and not to address tobacco addiction that fuels these illnesses. Important health issues such as diarrhea, influenza, and lung cancer may not be sexy, but they deserve the public's attention and commitment from policymakers and the scientific community.

PHILLIP A. DENNIS
National Cancer Institute, Bethesda, MD 20889, USA.

References

1. J. Mackay, M. Eriksen, *The Tobacco Atlas* (World Health Organization, Geneva, Switzerland, 2002).
2. A. Jemal *et al.*, *CA Cancer J. Clin.* **54**, 8 (2004).

The Case Against Stem Cell Research

IN HIS LETTER "HUMAN BEING REDUX" (16 April, p. 388), M. S. Gazzaniga constructs his defense of human embryonic stem cell research around his difficulty in thinking of a "miniscule ball of cells in a petri dish, so small that it could rest on the head of a pin" as a human being. This rhetoric may mislead the lay public, but scientists should recognize that the size or the developmental stage does not separate the embryo from the human being. The embryo and the adult are different stages in the development of the human being.

The embryo possesses more than just "the genetic material for a future human being." In ways that we do not yet fully understand, the embryo is organized so that it is capable of executing a developmental program and growing into what Gazzaniga will admit is a human being. This capability distinguishes the embryo from a differentiated cell in culture. Gazzaniga suggests that, because an embryo that is not implanted in the uterus of a woman will not be able to execute this program, the embryo has no moral status. I think he has it backwards. The scientist who destroys an embryo to harvest stem cells commits a wrong, for the scientist has denied that embryo the opportunity to grow into an adult.

My moral objections to human embryonic stem cell research are not assuaged by severing its connection to reproductive cloning. In my judgment, the developmental events leading from fertilized ovum, to blastula, to embryo, to fetus, to fully formed adult constitute a continuum. It is artificial, and even self-serving, to declare the embryo "not yet human" before some point, and to declare that we may do with that embryo as we will.

JOHN T. DURKIN
47 Wellington Road, Ardmore, PA 19003, USA.
E-mail: jtd71220@aol.com

Problems in FBI mtDNA Database

IN HIS EDITORIAL "FORENSIC SCIENCE: oxymoron?" (5 Dec. 2003, p. 1625), D. Kennedy wonders why the U.S. National Institute of Justice has regularly resisted comprehensive evaluations of the science underlying forensic techniques. A possible answer can be found in the poor quality of the forensic human mitochondrial DNA

Published by AAAS

(mtDNA) database used by the Federal Bureau of Investigation (FBI), which is included in the Scientific Working Group on DNA Analysis Methods (SWGDAM) database (*1*).

A thorough inspection of the original "African-American" database, which has been contributed by the FBI laboratory, reveals a number of major deficiencies. Among 1148 entries, each comprising two separately sequenced segments from the mtDNA control region, we detected as many as five artificial combinations of totally unrelated mtDNA segments stemming from different samples, which suggest fatal sample mix-up in the lab or during data transcription (*2*). The most striking hybrid (USA.AFR.000942) we found combined segment I from an African haplogroup (referred to as L1b) (*3*) with segment II from a Native American haplogroup (called C1) (*4*).

Recently, the FBI attempted to correct this database by searching for clerical errors: only nine were spotted (*1*), three of which (in the "Hispanic" database) we actually communicated to Bruce Budowle (FBI laboratory) by way of example. Since only three of six clear recombinants (*2*) have been discovered by the FBI, one cannot exclude the possibility of mixups during sample-handling in the remaining instances, which could only be corrected through thorough resequencing of the original samples.

Several obvious clerical errors still remain in the revised database, such as the 100 base-pair shift that hit position 16126 in USA.CAU.000272. Moreover, biochemical problems are manifest, for example, in the "Greek Caucasian" series, where a large amount of undetermined nucleotides are recorded—up to six in one sequence (GRC.CAU.000056). These findings suggest that several parts of the SWGDAM database have not been subjected to the necessary scrutiny.

Since as early as 2001, the field of forensics has known (*5*–*7*) that many published mtDNA databases are of poor quality, obviously affected by contamination or sample mix-up, sequencing artifacts due to biochemical problems (yielding sporadic phantom mutations), misreading of automated sequencer outputs, and inadvertent documentation in print or in silico (*6*). These adverse

TECHNICAL COMMENT ABSTRACTS

COMMENT ON "Inhibition of Hepatitis B Virus Replication by APOBEC3G"

Christine Rösler, Josef Köck, Michael H. Malim, Hubert E. Blum, Fritz von Weizsäcker

Turelli *et al*. (Brevia, 19 March 2004, p. 1829) showed that APOBEC3G targets hepatitis B virus (HBV) pregenomic RNA packaging, yet significant nucleotide changes in newly synthesized HBV DNA were not detected. We found that this phenotype is cell line–dependent. APOBEC3G can edit a minority of HBV genomes and may contribute to the emergence of variants.

Full text at www.sciencemag.org/cgi/content/full/305/5689/1403a

RESPONSE TO COMMENT ON "Inhibition of Hepatitis B Virus Replication by APOBEC3G"

Priscilla Turelli, Stéphanie Jost, Bastien Mangeat, Didier Trono

The finding that APOBEC3G can occasionally mutate the HBV genome supports a role for editing in the genetic variability of this pathogen. We additionally show that HBV can be blocked by the related cytidine deaminase APOBEC3F. Both enzymes, and perhaps other APOBEC family members, may thus influence HBV-induced disease.

Full text at www.sciencemag.org/cgi/content/full/305/5689/1403b

effects could be directly observed in the most recent ring tests among European forensic laboratories (*8*).

A recent European initiative (European DNA Profiling Group, EDNAP) has fully addressed the notorious problems in forensic mtDNA analysis (*8*) by promoting the EDNAP mtDNA population database (EMPOP) project. EMPOP, currently based on cooperation between 33 forensic DNA laboratories worldwide, features fully automated error-free transcription processes and other technical improvements. Moreover, the DNA samples will be permanently linked to the corresponding raw data and database entries, so that present data are open to critical reexamination and future refinement.

In resisting comprehensive evaluations, the U.S. National Institute of Justice has certainly backed up the FBI in their advertising of the forensic utility of the SWGDAM database and thus inhibited the generation of a new reliable mtDNA database in the United States.

HANS-JÜRGEN BANDELT,[1] ANTONIO SALAS,[2] CLAUDIO BRAVI[3]

[1]Department of Mathematics, University of Hamburg, 20146 Hamburg, Germany. E-mail: bandelt@math.uni-hamburg.de [2]Unidad de Genética, Instituto de Medicina Legal, Facultad de Medicina, 15705 Santiago de Compostela, A Coruña, Galicia, Spain. [3]IMBICE, Calle 526 esq. 11, 1901 Tolosa, Argentina.

References

1. See www.fbi.gov/hq/lab/fsc/backissu/april2002/miller1.htm.
2. H.-J. Bandelt, A. Salas, S. Lutz-Bonengel, *Int. J. Legal Med.*, in press.
3. A. Salas *et al.*, *Am. J. Hum. Genet.* **71**, 1082 (2002).
4. H.-J. Bandelt *et al.*, *Ann. Hum. Genet.* **67**, 512 (2003).
5. H.-J. Bandelt, P. Lahermo, M. Richards, V. Macaulay, *Int. J. Legal Med.* **115**, 64 (2001).
6. A. Röhl, B. Brinkmann, L. Forster, P. Forster, *Int. J. Legal Med.* **115**, 29 (2001).
7. C. Dennis, *Nature* **421**, 773 (2003).
8. W. Parson *et al.*, *Forensic Sci. Int.* **139**, 215 (2004).

CORRECTIONS AND CLARICATIONS

News Focus: "New dead zone off Oregon coast hints at sea change in currents" by R. F. Service (20 Aug., p. 1099). The location given for the Hatfield Marine Science Center was incorrect. The center is in Newport, Oregon, not Newport, Rhode Island.

NetWatch: "DNA surfing" (6 Aug., p. 759). Exons should have been identified as coding DNA and introns as noncoding DNA.

Policy Forum: "Genomic research and human subject privacy" by Z. Lin *et al.* (9 July, p. 183). In the figure, the word on the colored arrow should be "relationships."

Editors' Choice: "Tsunami and its shadow" (11 June, p. 1569). This item indicated that tsunamis travel slowly in the open ocean. This is incorrect; tsunamis travel fast in open water and slow down as they approach the shore.

Comment on "Inhibition of Hepatitis B Virus Replication by APOBEC3G"

The cytidine deaminase APOBEC3G (A3G) was recently identified as a natural resistance gene that restricts efficient propagation of human immunodeficiency virus and other retroviruses. The enzyme induces massive cytidine to uridine (C→U) deamination of single-stranded retroviral DNA, resulting in DNA degradation or lethal guanine to adenine (G→A) hypermutation (*1*). Hepadnaviruses, including hepatitis B virus (HBV), replicate by reverse transcription of a pregenomic RNA intermediate inside nucleocapsids, placing them into the family of retroelements (*2*). These observations, along with an earlier report describing G→A hypermutations in natural HBV variants (*3*), raise the question of whether HBV represents another potential target for A3G. Turelli *et al*. showed that this is indeed the case (*4*). Surprisingly, however, inhibition of viral pregenome packaging rather than induction of G→A hypermutations was identified as the main antiviral mechanism. No significant nucleotide changes were detected in a total of 40 polymerase chain reaction (PCR)–amplified HBV clones derived from cotransfected Huh7 hepatoma cells. Turelli *et al*. discussed the possibility that A3G-mediated HBV editing may occur in a different cellular context.

We investigated the potential antiviral effect of A3G in cotransfected Huh7 cells and another human hepatoma cell line, HepG2 (*5*). Our results confirm that A3G interferes with proper packaging of viral pregenomic RNA, resulting in a marked suppression of viral DNA synthesis (data not shown). To search for potential A3G-mediated editing of HBV DNA in nucleocapsids that may have escaped the block in RNA packaging, we PCR-amplified newly synthesized HBV DNA from supernatants or cell lysates of cotransfected cells and sequenced individual clones (*6*). Figure 1 summarizes the results obtained from three experiments in HepG2 cells and two experiments in Huh7 cells. In total, 430 individual clones were sequenced. In Huh7 cells, G→A mutations were rare, irrespective of the presence or absence of A3G, thus confirming the finding of Turelli *et al*. (*4*). In A3G-expressing HepG2 cells, the majority of recovered sequences were wild-type as well. However, the number of clones bearing G→A mutations and the overall number of G→A mutations increased significantly (Fisher's exact test, $P = 0.034$), whereas other nucleotide substitutions were rare (Fig. 1). Further experiments revealed additional G→A mutations in other regions of HBV DNA (Fig. 2), which suggests that they were caused by processive enzymatic activity rather than by global imbalances in the cellular nucleotide pool. Targeted sequence motifs matched well with the hallmarks of A3G action [(*7*), Fig. 2].

In conclusion, A3G displays a dual antiviral effect: (i) interference with pregenomic RNA packaging and (ii) induction of extensive G→A mutations in a subset of HBV genomes. Interestingly, A3G-mediated editing of HBV DNA appears to be cell line–dependent. The cellular factor(s) accounting for differences in A3G deaminase activity remain to be defined. Conceivably, Huh7 cells either lack a cofactor that is important for deaminase activity or produce a suppressing factor. It is of note that HepG2 cells occasionally yielded some G→A mutations even in the absence of transfected A3G. Because endogenous A3G expression in HepG2 cells was minute (*8*), this might reflect the activity of another deaminase. Nevertheless,

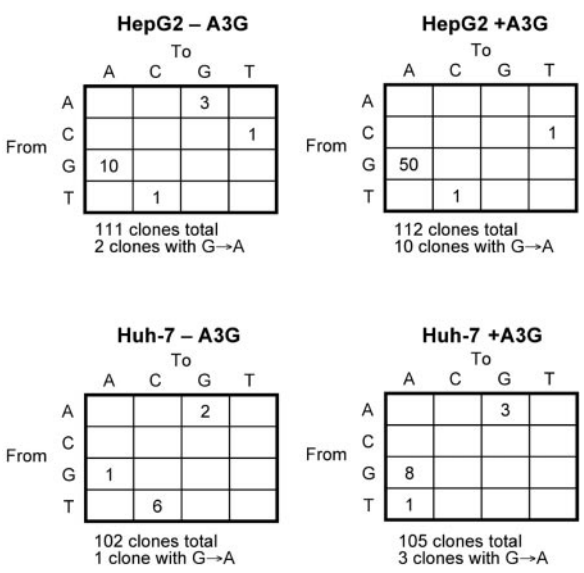

Fig. 1. G→A mutations in newly synthesized HBV DNA produced in HepG2 or Huh7 hepatoma cells in the presence (+) or absence (–) of A3G. Nucleocapsid-associated HBV DNA was PCR-amplified, cloned, and sequenced with primer 5′-ACAGTAGCTCCAAATTCTTTA-3′ (about 300 nucleotides per clone). Footnotes indicate the total number of sequenced clones and the number of clones displaying G→A mutations. Boxes display the total number of the respective mutations.

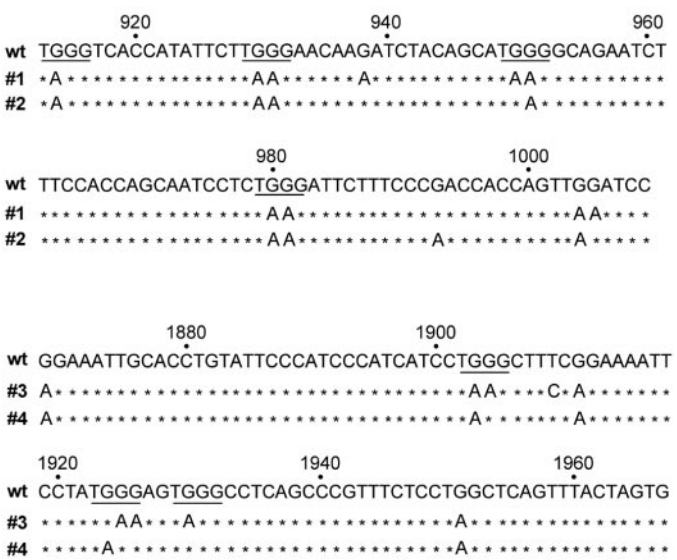

Fig. 2. Partial nucleotide sequence of four individual HBV genomes produced in HepG2 cells after transfection with a replication-competent HBV construct and an A3G expression vector. Nucleocapsid-associated HBV DNA was PCR-amplified, cloned, and sequenced with primer 5′-TTGCGGTGTTTGCTCTGAAGG-3′ (clones nos. 1 and 2) or primer 5′-GATTTTTTGTATGATGTG-3′ (clones nos. 3 and 4). Mutations are depicted with respect to the wild-type sequence above (wt). Asterisks represent nucleotide identity. Numbers indicate nucleotide positions relative to the start codon of the core protein. Underlined sequences represent preferred A3G targets (*7*).

the statistically significant overall increase in G→A mutations and their distinctive distribution in individual clones clearly demonstrates that A3G can edit HBV DNA in cotransfected HepG2 cells.

Whether A3G plays a role in down-regulating HBV replication during natural infection remains an intriguing question. Although detectable by reverse transcription PCR, baseline expression levels of A3G are low in primary human hepatocytes (*8*). Furthermore, A3G mRNA is not induced by HBV infection or cytokines in livers of infected chimpanzees (*9*). On the other hand, hepadnaviruses have been detected in extrahepatic cells that express high levels of A3G, such as white blood cells (*10*). Thus, it is tempting to speculate that A3G-driven editing of HBV DNA may occur in extrahepatic cells and may contribute to the emergence of variants (*3*, *11*). Clearly, further experiments are warranted to establish whether and how A3G can edit HBV DNA in nontransformed natural target cells.

Christine Rösler
Josef Köck
Department of Medicine II
University of Freiburg
Hugstetter Strasse 55
D-79106 Freiburg, Germany

Michael H. Malim
Department of Infectious Diseases
Guy's, King's, and St. Thomas' School of Medicine
King's College London
2nd Floor New Guy's House
GKT Guy's Hospital
London, SE1 9RT, UK

Hubert E. Blum
Fritz von Weizsäcker*
Department of Medicine II
University of Freiburg
**To whom correspondence should be addressed. E-mail: fritz.weizsaecker@uniklinik-freiburg.de*

References and Notes

1. V. N. KewalRamani, J. M. Coffin, *Science* **301**, 923 (2003).
2. C. Seeger, W. S. Mason, *Microbiol. Mol. Biol. Rev.* **64**, 51. (2000).
3. S. Gunther *et al.*, *Virology* **235**, 104 (1997).
4. P. Turelli, B. Mangeat, S. Jost, S. Vianin, D. Trono, *Science* **303**, 1829 (2004).
5. American Type Culture Collection (ATCC), catalog no. HB-8065
6. Cells were transfected with a replication-competent HBV construct (*12*) and an expression vector encoding A3G (*13*). Nucleocapsid-associated viral DNA from culture supernatants was PCR-amplified with forward primer 2908 (5′-GCCCACCAAAGCTTGCCCAAGGTC-3′) and reverse primer 1335 (5′-AATACAGGCCTCTCACTCTGG-3′). Purified PCR products were cloned into the EcoRI/ Hind III sites of pUC19 (Invitrogen). Nucleocapsid-associated viral DNA from cytoplasmic lysate was amplified with forward wobble primer 2896 (5′-ACCACCRTRAACRCCCACC-3′) and reverse primer 1305 (5′-GAGTTTGGTGGAAGGTTGTGG-3′). These PCR products were directly cloned with a TA Cloning Kit (Invitrogen). In additional experiments (Fig. 2, clones 3 and 4), nucleocapsid-associated viral DNA from cytoplasmic lysate was amplified with primers 2855 (5′-CCGGCAGATGAGAAGGCACAGACGG-3′) and 556 (5′-TCCTTGGACTCATAAGGTGGG-3′) and cloned into the EcoRI/SphI sites of pUC19 (Invitrogen). For sequencing of individual clones, primers 38 (5′-ACAGTAGCTCCAAATTCTTTA-3′, Fig. 1), 1032 (5′-TTGCGGTGTTTGCTCTGAAGG-3′; Fig. 2, clones nos. 1 and 2) or 2218 (5′-GATTTTTTGTATGATGTG-3′; Fig. 2, clones nos. 3 and 4) were used.
7. Q. Yu *et al.*, *Nature Struct. Mol. Biol.* **11**, 435 (2004)
8. J. Köck, F. von Weizsäcker, unpublished data
9. S. Wieland, R. Thimme, R. H. Purcell, F. V. Chisari, *Proc. Natl. Acad. Sci. U.S.A.* **101**, 6669 (2004).
10. T. I. Michalak, *Immunol. Rev.* **174**, 98 (2000).
11. D. Milich, T. J. Liang, *Hepatology* **38**, 1075 (2003).
12. K. Reifenberg *et al.*, *J. Gen. Virol.* **83**, 991, 2002.
13. A. M. Sheehy, *Nature* **418**, 646, 2002.
14. Supported by grants from the Deutsche Forschungsgemeinschaft (We 1365/5-1), the Bundesministerium für Bildung und Forschung (01K19951; HepNet), and Gilead Sciences (DE-103-509).

18 May 2004; accepted 6 August 2004

Response to Comment on "Inhibition of Hepatitis B Virus Replication by APOBEC3G"

Rösler *et al*. (*1*) nicely confirm that APOBEC3G blocks hepatitis B virus (HBV) replication by suppressing viral DNA synthesis and further reveal that this enzyme can occasionally edit the viral genome in the particular context of HepG2 cells. Even in this case, when APOBEC3G was overexpressed, fewer than one out of ten HBV genomes became hypermutated. Although these results demonstrate that HBV is not immune to APOBEC3G-mediated editing, we do not favor the hypothesis of Rösler *et al*. that cells in which blockage of HBV DNA synthesis occurs without noticeable editing lack a cofactor important for cytidine deamination or produce a suppressor of this activity. Indeed, we verified that APOBEC3G can efficiently hypermutate *vif*-defective human immunodeficiency virus–1 released from such cells, including Huh7 [(*2*) and data not shown]. Therefore, we think that the Rösler *et al*. data are more consistent with a model in which, in HepG2 cells, APOBEC3G is slightly less efficient at blocking HBV pregenomic RNA packaging or at destabilizing the HBV reverse transcription complex, so that minus-strand viral DNA is occasionally made. This DNA can then serve as a target for APOBEC3G-mediated editing. In Huh7 cells, the cytidine deaminase blocks DNA synthesis completely, thus depriving itself of its editing substrate.

Still, these new data lend credence to the suggestion that HBV editing might occur in certain tissues and, as such, contribute to HBV pathogenesis. HBeAg-negative HBV strains often result from a G-to-A change at the first position of a 5′-GGGG stretch in the precore coding sequence (*3*), a possible consequence of APOBEC3G-mediated editing because this enzyme acts preferentially on the 5′-C<u>C</u> dinucleotide (in the minus-strand DNA) (*4*). However, other naturally occurring HBV genomes exhibit a pattern of hypermutation that departs from this consensus, with a strong predominance of G-to-A changes in the 5′-<u>G</u>A motif (*5*). This suggests that, in these cases, another cytidine deaminase may be at play. APOBEC3F is a particularly attractive candidate, because it is also endowed with antiretroviral activity but markedly favors 5′-T<u>C</u> as its target (*6*–*8*).

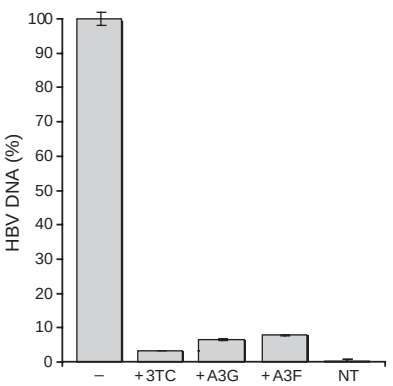

Fig. 1. Real-time PCR quantification of cytoplasmic core–associated HBV DNA purified from HBV-transfected Huh7 cells in the absence (–) or presence (+) of the reverse transcription inhibitor 3TC, of APOBEC3G, or of APOBEC3F, as previously described (*1*). NT, nontransfected.

Consistent with this model, we found that APOBEC3F can efficiently block HBV DNA synthesis (Fig. 1). We do not yet know whether it can also hypermutate the HBV genome in HepG2 or other cells, but our result already suggests that this cytidine deaminase might participate in the noncytopathic virus clearance that is observed during an acute HBV infection (*9*). A recent transcriptome analysis of the liver of chimpanzees acutely infected with HBV failed to document an induction of the expression of several APOBEC3 family members, including APOBEC3G, but the array used in these experiments did not seem to carry an APOBEC3F-specific probe (*10*). We agree that additional studies are warranted to investigate the full impact of APOBEC proteins on HBV infection.

Priscilla Turelli*
Stéphanie Jost*
Bastien Mangeat
Didier Trono†
Department of Microbiology and Molecular Medicine, Faculty of Medicine, and *"Frontiers in Genetics" Research Program*
University of Geneva
Geneva, Switzerland
**These authors equally contributed to this work.*
†E-mail: Didier.trono@medecine.unige.ch

References and Notes

1. C. Rösler, J. Köck, M. H. Malim, H. E. Blum, F. von Weizsäcker, *Science* **305**, 1403 (2004); www.sciencemag.org/cgi/content/full/305/5689/1403a.
2. P. Turelli, B. Mangeat, S. Jost, S. Vianin, D. Trono, *Science* **303**, 1829 (2004).
3. S. L. Ngui, R. Hallet, C. G. Teo, *Rev. Med. Virol.* **9**, 183 (1999).
4. R. C. Beale *et al.*, *J. Mol. Biol.* **337**, 585 (2004).
5. S. Gunther *et al.*, *Virology* **235**, 104 (1997).
6. H. L. Wiegand, B. P. Doehle, H. P. Bogerd, B. R. Cullen, *EMBO J.* **23**, 2451 (2004).
7. M. T. Liddament, W. L. Brown, A. J. Schumacher, R. S. Harris, *Curr. Biol.* **14**, 1385 (2004).
8. K. N. Bishop *et al.*, *Curr. Biol.* **14**, 1392 (2004).
9. S. F. Wieland, H. C. Spangenberg, R. Thimme, R. H. Purcell, F. V. Chisari, *Proc. Natl. Acad. Sci. U.S.A.* **101**, 2129 (2004).
10. S. Wieland, R. Thimme, R. H. Purcell, F. V. Chisari, *Proc. Natl. Acad. Sci. U.S.A.* **101**, 6669 (2004).
11. Supported by the Swiss National Science Foundation and the Roche Research Foundation.

25 June 2004; accepted 9 August 2004

PHILOSOPHY OF SCIENCE

The Embryo of a Dialogue

Günter P. Wagner

Embryology, Epigenesis, and Evolution
Taking Development Seriously
by Jason Scott Robert

Cambridge University Press, Cambridge, 2004. 174 pp. $60, £40. ISBN 0-521-82467-2. Studies in Philosophy and Biology.

Embryology, Epigenesis, and Evolution is a book on a scientific topic written by a philosopher. The author addresses the explanation of organismal development and the role of development in evolution. At this point, I suspect, at least those scientists who have contributed to the enormous success of developmental biology in the last twenty or so years will get nervous. Isn't it enough that, finally, development has yielded to the prying of experimental biology to prove that we are beyond the stage of mere speculation on the nature of development? So what can one expect from a philosopher that is worth knowing or even worth contemplating?

Before we go on, it might be worth remembering that the relationship between philosophy and the sciences is, historically and conceptually, that of parent and child—albeit a very much grown and independent child. Whether we like it or not, the scientific tradition descends from ancient philosophers, who were the first to provide alternatives to religious explanations of the world. This critical spirit lives on in the scientific enterprise, regardless of whether individual researchers receive philosophical training. The psychological script of a parent-child relationship provides a handle on the subject of Robert's book. As with most parent-offspring conflicts, the relation between philosophy and science is rooted in a deep mutual misunderstanding of each other's priorities and values. Philosophers are concerned with the question, What does it mean to properly understand a phenomenon? In developmental biology, is it sufficient to know the molecular events of gene expression and its regulation during development? Some of my colleagues certainly would answer yes. After all, genes determine whether a crocodile or a duckling crawls out of an egg, even though both types of eggs exist in roughly similar environments; there are environmental effects, but these are at most modulations on a theme written in the letters of DNA.

Robert, a philosopher at Dalhousie University, is not happy with this answer, and he devotes much of the book to explaining why. Where some see in the success of developmental biology a triumph of the scientific method, Robert perceives a massive self-deception, one that results from the method's very core. How is that? We all know that the lifeblood of experimental science is the standardization of those factors that one chose not to study—the elimination of their influence on the outcome of the experiment. Most contemporary developmental biologists study the role of genes, and in many instances they standardize the environment to remove its effects. The wrong inference, according to Robert, is to then conclude that such factors do not play a causal role in the process we are studying. I agree with Robert that this is a flawed conclusion, because the experimental approach was set up to screen off their influence. Although this conclusion is an easy trap to fall into, any developmental biologist will agree that the external environment and the cellular context of genes form parts of the overall causal process of development.

Drawing attention. The eyespots of butterflies such as the buckeye, *Junonia (Precis) coenia*, illustrate the complex interplay between development and evolution.

Where then is the mutual misunderstanding? Robert and his colleagues who argue for a similar interpretation are correct in that the genes alone cannot make an organism and instead are embedded in a large network of causal interactions. But scientists are usually not interested in general statements about what in principle is required to understand a phenomenon. What distinguishes them is their obsession with the questions of how ideas can be tested and whether we know that they are correct. I believe that this mismatch in priorities and values forms the core of the difficulty philosophers and scientists have in really understanding each other.

The author knows about that discrepancy and tries hard to argue his way out of the philosopher's corner. In my estimation, he has limited success. However, the best way to fight misunderstandings is an open dialog, and in that spirit, let me respond to the criticisms Robert raises: Yes, he is correct that the environment and the cell play causal roles in explaining development. And yes, the genetic explanation of development has its limits; however, we have not yet reached these limits. And no, genes and environment do not stand on the same footing in explanations of development. Yes, scientists make pragmatic decisions about what to study, but I think that these decisions are anything but arbitrary. The power of molecular genetic approaches did not come easily, rather it is the result of a long history of strenuous research based on a vision that derived from the work of Richard Goldschmidt, Alfred Kühn, and Thomas Hunt Morgan early in the 20th century. It is thus not intellectual laziness that drives the genetic research program; instead we are raking in the spoils of a hard-won victory over biological complexity.

But more important than these somewhat pedantic points is the possibility that the problems confronting our efforts to comprehend development and its role in evolution run deeper than the polarities between genes and environment and between genetic and epigenetic effects. The real difficulty we face in understanding organisms is that they are not simply formed by a combination of well-defined factors and effects—unlike a cannonball's trajectory, which can be understood as resulting from the combined effects of gravity, air friction, propulsive forces, and inertia. The only proper word we have for what is going on in biology is interaction. Interaction means that the effect of a factor depends on many other so-called factors, and this dependency on context ensures that the explanatory currency drawn from measuring the effects of causal factors is very limited. The intellectual and methodological problem does not cut cleanly between nucleus and cytoplasm or between genome and environment but applies across all of biology. It was after all a geneticist, Diethart Tautz, who pointed out the problem's theoretical implications [*BioEssays*

The reviewer is in the Department of Ecology and Evolution, Yale University, Osborn Memorial Laboratories, 165 Prospect Street, New Haven, CT 06520, USA. E-mail: gunter.wagner@yale.edu

14, 263 (1992)]. How can we assign a causal role to a gene if its effect is entirely context-dependent? What does it really mean to call a gene an eye gene if we can have eyes without it? It is very difficult to form a research program around this insight. Much of the scientific culture is based on the cause-effect schema, but in biology we often experience the limits of this way of thinking.

Worse than misunderstandings, which are in any case often unavoidable, is the cessation of dialogue. The dust jacket of *Embryology, Epigenesis, and Evolution* suggests a target audience of philosophers of science and of biology, but I hope the book will be more widely read. It might start a productive exchange between biologists and philosophers on how to overcome the limitations of our knowledge.

HISTORY OF SCIENCE

The First Lord from Science

John S. Rigden

Degrees Kelvin is a lovely book, and also a most welcome one. Its subject, William Thomson, is surprisingly unknown, even among physicists, perhaps in part because he worked during the 19th century, whose physics does not receive the attention it richly deserves. Any list of all-time great physicists will include a large number of his contemporaries, and Thomson stands shoulder-to-shoulder with the best of them. Physicist and writer David Lindley offers nonspecialists an engaging and informative account of Thomson's personal life and scientific career.

Degrees Kelvin: A Tale of Genius, Invention, and Tragedy
by David Lindley

Joseph Henry Press, Washington, DC, 2004. 374 pp. $27.95, C$37.95. ISBN 0-309-09073-3.

The Thomsons were a family of keen minds, but William was superior to them all. When he was approaching age 16, he read and mastered Fourier's *Théorie Analytique de la Chaleur*, and the mathematical methods he learned had an enormous influence on his professional career. He entered Cambridge University at age 17 and published a dozen papers as an undergraduate. However, like another famous physicist trained at Cambridge, J. J. Thomson (no relation), William failed to win the coveted top spot of senior wrangler in the university's mathematics competition.

Most of the content of current introductory physics textbooks was essentially created and brought to completion by 19th-century physicists. This organization of subject matter, called classical physics, comprises the physics of electricity and magnetism, heat and thermodynamics, the energy principle, optics, acoustics, kinetic theory of gases, and statistical mechanics. William Thomson made significant contributions to our understanding of electricity, magnetism, and thermodynamics. In 1852, he established the existence of an absolute zero of temperature. When, 40 years later, he became the first British scientist to be raised to the peerage and took the title Lord Kelvin (from the name of a small river that runs beside Glasgow University), the absolute temperature scale was destined to become the Kelvin scale.

Thomson was a man of many interests. Most of his contributions to basic physics came in his early life, before he discovered that patents of practical devices could generate money. He was fascinated by technology and he "existed in both spheres, as scientist and technologist, academic and entrepreneur, a philosopher and a practical man rolled into one." He played an important role in getting the first transatlantic cable in place and functioning. He designed a compass that became the sole official compass of the Royal Navy. He was interested in power production and chaired an international commission to study the possibility of generating electricity at Niagara Falls.

An enjoyable aspect of Lindley's account is that in the course of placing Thomson's life and work in context, he introduces readers to several of his subject's illustrious contemporaries and their work. Among the notable physicists who make brief appearances in the book's pages are Sadi Carnot, James Prescott Joule, Michael Faraday, Rudolf Clausius, James Clerk Maxwell, Hermann von Helmholtz, and Lord Rayleigh.

Lindley also discusses Thomson's better-known role in the controversy over Earth's age (*1*). Thomson first became embroiled in this dispute during the early 1860s. He was at odds with geologists who embraced uniformitarianism as well as with Darwin and the evolutionists who required an old Earth to enable the slow evolutionary process to produce the observed living world. Based on assumptions about the planet's structure and cooling rates, Thomson's Earth was much too young. Thomson, despite all his quantitative might, did not win this battle because the radioactive elements in the crust made his assumption—that Earth, once formed, cooled steadily—simply wrong.

The engineer and mathematician Oliver Heaviside noted that Thomson was "intensely mechanical, and could not accept any ether unless he could make a model of it. Without the model he did not consider electromagnetics to be dynamical." In this and other ways, Thomson was a creature of his era. Like some other prominent scientists, he was skeptical about atomism and he rejected absolutely the idea of atoms as little round balls because atoms in this form could not be the origin of spectral light. So Thomson adopted the purely dynamical vortex atoms of Helmholtz.

Kelvin lived a long and event-filled life. He authored scientific papers until a few months before his death at age 83. He was buried in Westminster Abbey, next to Isaac Newton, under the simple marker, "William Thomson, Lord Kelvin, 1824–1907." During the final years of his life, physicists were confronted by unexpected discoveries (e.g., x-rays, radioactivity, the electron) and the unsettling quantum idea. Kelvin often did not accept his colleagues' explanations of these new phenomena. For example, he rejected the idea that radioactivity represented the transmutation of one element into another. He also proposed that the heat associated with decaying atoms came not from the atoms, but from the surrounding ether.

This brings me to my only quibble with Lindley's fine book: the word tragedy in the subtitle. The word appears because, as an old man, Thomson became more stubborn—he was always stubborn—and did not quickly and easily adapt his thinking to new discoveries in physics. If this criterion were applied generally, many, if not most, physicists' lives would end in tragedy.

The reviewer is in the Department of Physics, Washington University, St. Louis, MO 63130. E-mail: jrigden@aip.org

Reference

1. J. D. Burchfield, *Lord Kelvin and the Age of the Earth* (Science History Publications, New York, 1975).

CREDIT: FROM *TORONTO GLOBE*, 21 AUGUST 1897/COURTESY JOSEPH HENRY PRESS

Published by AAAS

A World of Glass

Alan Macfarlane and Gerry Martin

This year's essay series highlights the benefits that scientists, science, and technology have brought to society throughout history.

Anyone who has looked at the long-term history of human civilizations over the last 50,000 years will notice that one of the most significant transformations took place during the period 1200 to 1850. This transformation affected two of the most important human capacities: the way in which we think and our sense of sight. Compare the nature of painting in Europe in 1200 with that in 1850, or the amount of chemical, physical, and biological knowledge in Europe in 1200 to that in 1850, and one would not hesitate to pronounce that a revolution took place within this 650-year period. This revolution manifested itself not only in the world of art and architecture, but also in transport, housing, energy sources, agriculture, and manufacturing.

Improvements in glass production contributed to the sweeping changes that engulfed Europe from 1200 to 1850.

We know that all this happened, but after that there is little agreement. We are still uncertain as to why the Renaissance of the 14th, 15th, and 16th centuries, and the scientific and industrial revolutions of the 17th and 18th centuries took place. Nor do we understand why these sweeping changes happened in western Europe, and not in the great Islamic or Chinese civilizations.

The interplay between the availability of more reliable information and the improved manufacture of tools, instruments, and artifacts contributed to the remarkable changes that swept through western Europe. Often in history, we witness the generation of new knowledge through experimentation, which then leads to significant innovations and a richer appreciation of new or improved physical artifacts. These artifacts, if they are useful, in demand, and relatively easy to produce, are often disseminated in large quantities. These objects then change the conditions of everyday life and may fund further theoretical explorations. Such artifacts can do this in two ways: by generating wealth that funds increased efforts to acquire fresh knowledge and by providing better tools for scientific enquiry.

Historically, this triangle of knowledge–innovation–quantification emerged in many spheres of life, most notably in agriculture. The loop is enduring when artifacts are widely disseminated and is a cumulative process. The speed of movement around the triangle and the frequency of its repetition provide a measure of the development of human civilizations. Our analysis of this triangle in the history of glass production and application reveals that glass contributed to the rampant changes that swept through western Europe between 1200 and 1850.*

A Brief History of Glass

No one is certain where, when, or how glass originated. It may have appeared first in the Middle East in regions such as Egypt and Mesopotamia around 3000 to 2000 B.C. although there are hints of glazing on pottery as early as 8000 B.C. Glass was almost certainly discovered by accident—so the Roman historian Pliny (A.D. 23–79) tells us—by Phoenician traders, who apparently noticed that a clear liquid formed when the nitrate blocks on which they placed their cooking pots melted and mixed with sand from the beach. Egyptian craftsmen developed a method for producing glass vessels around 1500 B.C., and the first manual of glassmaking appeared on Assyrian stone tablets about 650 B.C. About 2000 years ago, Syrian craftsmen invented glassblowing, a skill adopted by the Romans, who carried it with them as they swept through western Europe on their conquests. The rise of Venice to prominence in the 13th century enabled this city to become the center of glassmaking in the western world. As the industrial revolution gathered momentum, new manufacturing technologies enabled the mass production of glass scientific instruments, bottles, window panes, and many other items.

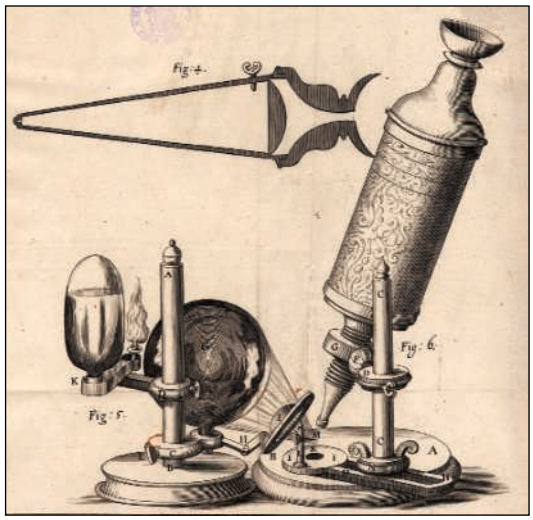

Through a glass brightly. The compound microscope used by Robert Hooke enabled him to produce one of the first illustrated books of microscopic objects. The book, *Micrographia*, published in London in 1665, helped to launch discoveries that led to the development of germ theory and the founding of infectious disease research. Hooke's compound microscope revealed a world invisible to the naked eye, which only scientists—with the help of glass—could probe. [Reproduced from the first edition of *Micrographia*, 1665]

The Many Uses of Glass

Historically, glass has been used in five different ways, which varied depending on the locality. Glass beads, counters, toys, and jewelry were produced almost universally throughout Eurasia before 1850, with glass becoming a substitute for precious stones. The great developers of glass vessels, vases, and containers were the Italians, first the Romans and later the Venetians. The use of glass vessels was largely restricted to the western part of Eurasia until the 1850s, with little evidence of use in India, China, and Japan. In the Islamic territories and Russia, the use of glass declined dramatically from about the 14th century until modern times due to the Mongol incursions.

Another crucial use of glass was for making windows. Until the 20th century, window glass was found mainly in the western regions of Eurasia (principally north of the Alps), appearing rarely in China, Japan, and India. Another application of glass depended on its reflective capacity when silvered. Produced by the Venetians in

A. Macfarlane is in the Department of Social Anthropology, University of Cambridge, Cambridge, CB2 3RF, UK. E-mail: am12@cam.ac.uk. The late Gerry Martin was an industrialist, cofounder of Eurotherm Ltd., and a collector of scientific instruments. *Alan Macfarlane and Gerry Martin, *Glass: A World History* (Chicago Univ. Press, Chicago, 2002). Further material is provided at www.alanmacfarlane.com. Among the best illustrated histories and encyclopedias about glass are: Chloe Zerwick, *A Short History of Glass* (Corning Museum, New York, 1990); Hugh Tait, Ed., *Five Thousand Years of Glass* (British Museum, London, 1995); Reino Liefkes Ed., *Glass* (Victoria and Albert Museum, London, 1997); Dan Klein and Ward Lloyd, Eds., *The History of Glass* (Orbis, London, 1984). An inspiring brief introduction to the contributions of glass to society is Lewis Mumford's *Technics and Civilization* (Harcourt Brace, New York, 1934).

CREDIT: HOWARD DAWES

Published by AAAS

the 16th century, the use of glass mirrors spread throughout the whole of western Europe, but appeared rarely if at all in Islamic civilizations or in India, China, or Japan. A final critical application of glass was in the production of lenses and prisms. This led to the manufacture of spectacles to improve human sight; eyeglasses first appeared in Europe during the 13th and 14th centuries. The concept of the light-bending and magnifying properties of glass, discovered by the Chinese in the 12th century, was probably known to all Eurasian civilizations. Yet only in western Europe did the practice of making lenses really develop. This coincides precisely with the surge in interest in optics and mathematics during medieval times, which fed into other branches of learning, including architecture and painting.

The reasons for the different uses of glass in different parts of the world may be largely accidental, reflecting variations in climate, drinking habits, availability of pottery, political events, and many other characteristics. Intention, planning, individual psychology, superior intellect, or better resources seem to have little to do with it. Yet these accidents instigated the move of western European societies around the knowledge–innovation–quantification triangle. Improvements in glassmaking and the production of more sophisticated glass instruments yielded more accurate information about the natural and physical worlds, which fed back into refinements in glass manufacture and, hence, in glass quality.

Glass and Scientific Knowledge

Glass helped to accelerate the amazing acquisition of knowledge about the natural and physical worlds by providing new scientific instruments: microscopes, telescopes, barometers, thermometers, vacuum flasks, retort flasks, and many others. Glass literally opened people's eyes and minds to new possibilities and turned western civilization from an aural to a visual mode of interpreting experience. We randomly picked 20 famous experiments that changed our world—Thomson's discovery of electrons, Faraday's work on electricity, and Newton's splitting of white light into its component colors with a prism, for example—and found that 15 of them could not have been performed without glass tools. That the knowledge revolution of the last 500 years took place in western Europe and not elsewhere, can be attributed in part to the collapse of glass manufacturing in Islamic civilizations and its diminished importance in India, Japan, and China.

The list of scientific fields of enquiry that could not have existed without glass instrumentation are legion: histology, pathology, protozoology, bacteriology, and molecular biology to name but a few. Astronomy, the more general biological sciences, physics, mineralogy, engineering, paleontology, vulcanology, and geology would have emerged much more slowly and in a very different form without the help of glass instruments. For example, without clear glass, the gas laws would not have been discovered and so there would have been no steam engine, no internal combustion engine, no electricity, no light bulbs, no cameras, and no television. Without clear glass, Hooke, van Leeuwenhoek, Pasteur, and Koch would not have been able to visualize microorganisms under the microscope, an achievement that led to the birth of germ theory and a new understanding of infectious disease, which launched the medical revolution (see the photograph on page 1407).

Chemistry depends heavily on glass instrumentation. Thanks to glass, European scientists elucidated the chemistry of nitrogen and learned to fix this gas in the form of ammonia to produce artificial nitrogenous fertilizers, a huge step forward in 19th- and 20th-century agriculture. Without glass, there would have been no means of demonstrating the structure of the solar system, no measurement of stellar parallax, no way of substantiating the conjectures of Copernicus and Galileo. The application of glass instruments revolutionized our understanding of the universe and deep space, completely altering our whole concept of cosmology. Furthermore, without glass, we would have no understanding of cell division (or of cells), no detailed understanding of genetics, and certainly no discovery of DNA. Without spectacles, most individuals over the age of 50 would not have been able to read this article. Glass may be an unforeseen accident, but it follows a predictable pattern of movement around the triangle: deeper reliable knowledge enabling the manufacture of innovative artifacts followed by their mass production.

Glass in Everyday Life

We have discussed the contributions of glass from the scientific perspective. But from 1200 onwards, all knowledge was interconnected. Without mirrors, lenses, and panes of glass, the startling changes that marked the Renaissance would not have taken place. A new understanding of the laws of optics, and the accuracy and precision of paintings by Da Vinci, Durer, and their contemporaries largely depended on glass instruments of various kinds. The divergence of world art systems between 1350 and 1500 is impossible to imagine without the development of very high quality glass by the Venetians. Glass in the form of church stained-glass windows affected what we believed; in the form of mirrors, it affected how we perceived ourselves.

Glass, however, is not just a tool to think and perceive with, but also a tool to improve everyday life. The period between the 13th and mid-19th centuries in Europe saw many changes made possible by glass that contributed not only to the intellectual flowering of this era but also to an improved standard of living for many people. For example, glass in the form of windows lengthened the working day and improved conditions for workers. Glass let light into interiors allowing house dirt to become more apparent leading to improvements in hygiene and health. Also, glass is a tough, protective surface that is easy to clean. Glass windows wrought changes not only in private homes, but also in shops with shopkeepers eventually placing much of their produce and merchandise behind glass windows and under glass cabinets.

This clear molten liquid began to transform agriculture and horticulture. The use of glass houses to promote the precocious growth of plants was not an invention of early modern Europe. Indeed, the Romans used forcing houses to promote plant growth and protected their grapes with glass. The Roman idea was revived in the later Middle Ages, when glass pavilions for growing flowers and later fruit and vegetables began to appear. As glass became cheaper and, particularly, flat window glass improved in quality, many more applications appeared. Glass cloches and greenhouses improved the cultivation of fruit and vegetables, bringing a healthier diet to the population. In the 19th century, glass made it possible to bring plants from all over the world to enrich European farms and gardens.

There are many other useful applications of glass that altered everyday life from the 15th century onward. Among them were storm-proof lanterns, enclosed coaches, watch-glasses, lighthouses, and street lighting. The sextant required glass, and the precision chronometer invented by Harrison in 1714, which provided a solution to calculating longitude at sea, would not have been possible without glass. Thus, glass directly contributed to navigation and travel. Then, there was the contribution of glass bottles, which increasingly revolutionized the distribution and storage of drinks, foods, and medicines. Indeed, glass bottles created a revolution in drinking habits by allowing wine and beer to be more easily stored and transported. First through drinking vessels and windows, then through lanterns, lighthouses, and greenhouses, and finally through cameras, television, and many other glass artifacts, our modern world has emerged from a sea of glass.

The different applications of glass are all interconnected—windows improved working conditions, spectacles lengthened working life, stained glass added to the fascination and mystery of light and, hence, a desire to study optics. The rich set of interconnections of this largely invisible substance have made glass both fascinating and powerful, a molten liquid that has shaped our world.

MOLECULAR BIOLOGY

Argonaute Journeys into the Heart of RISC

Erik J. Sontheimer and Richard W. Carthew

In Sophocles' *Oedipus the King*, the citizens of Thebes are cursed by a plague that will end only when the murderer of Laius, their former ruler, is identified and banished. The culprit is eventually revealed to be none other than the current king (and Laius' son), Oedipus. Although there are many things to be learned from this drama, one conclusion relates directly to the process of discovery: The object of an intensive search sometimes turns out to be hiding in plain view. So it is with the study of RNA interference (RNAi), as illustrated by two papers in this issue by Liu *et al*. on page 1437 (*1*) and by Song *et al*. on page 1434 (*2*). These authors now identify the long-sought catalytic subunit that executes RNAi, and show that it has been staring us in the face for years.

In most eukaryotes, RNAi is one of several mechanisms that silence the expression of specific genes in response to double-stranded RNA (dsRNA) (*3*). Within cells, the dsRNA silencing triggers are cleaved into 21- to 23-nucleotide short interfering RNA (siRNA) fragments. These fragments then associate with a large protein assembly called the RNA-induced silencing complex (RISC) (see the figure). An siRNA within RISC recognizes specific messenger RNAs (mRNAs) through base pairing, and in this way guides RISC to the appropriate targets. The complex harbors a catalytic activity that specifically cleaves the bound mRNA without affecting the guide siRNA. RISC was first discovered 4 years ago (*4*), and the race to identify its resident proteins—especially the catalytic subunit "Slicer"—has been raging ever since.

The first protein subunit discovered in RISC was Argonaute2 (*5*), one of a family of Argonaute proteins. Members of the Argonaute family are defined by the presence of PAZ and PIWI domains (*6*). The PAZ domain was recently shown to be important for binding to RNA (probably siRNA) (*7*), but beyond that the biochemical functions of Argonaute proteins within RISC remained elusive. The Hannon and Joshua-Tor laboratories have now used a battery of biophysical, biochemical, and genetic approaches to examine Argonaute structure and function (*1*, *2*). In doing so, they have lifted our understanding of RNAi to a new level. Most notably, they provide compelling evidence that human Argonaute2 (and, by extension, other Argonaute proteins in different species) is the elusive Slicer subunit.

Song *et al*. (*2*) have solved the crystal structure of a complete Argonaute ortholog from the archaebacterium *Pyrococcus furiosis*. The PAZ domain sits atop a crescent composed of three other domains (including PIWI) and matches the structures of other well-characterized PAZ domains. Most tellingly, the tertiary structure of the PIWI domain clearly resembles that of ribonuclease H (RNase H) enzymes, which cleave the RNA strand of RNA/DNA hybrid duplexes. The structural similarity includes three carboxylate residues that are thought to bind and position a catalytically important divalent metal ion. The proposed catalytic site lies at the edge of a positively charged groove that extends into the PAZ domain, providing a plausible binding site for the siRNA/mRNA substrate duplex. Because RISC and RNase H are both metal-dependent enzymes that cleave one specific strand of a nucleic acid duplex and leave chemically similar termini in the products, the structural similarity immediately suggests that the PIWI domain may harbor RISC's target mRNA cleavage activity.

Of course, functional conclusions require functional data, and to this end Liu *et al*. (*1*) generated mammalian cells that express epitope-tagged versions of four human Argonaute proteins. Although siRNAs and miRNAs (microRNAs; endogenous RNAs that silence gene expression via translational control) bind to all four tagged proteins, only Argonaute2 was associated with cleavage of target mRNAs. This suggests that the other Argonautes might operate in different forms of RNA silencing. The cleavage activity remained even when the immunoprecipitates were washed under harsh conditions, indicating that it associates tightly with Argonaute2 and may reside within Argonaute2 itself. Similar conclusions have also been reported recently by Meister *et al*. (*8*). Liu *et al*. further demonstrate that Argonaute2 is essential for mouse embryonic development. Mice deficient in Argonaute2 display multiple abnormalities including defects in neural tube closure and heart development. Furthermore, cells cultured from Argonaute2-deficient mice fail to mount an RNAi response upon siRNA transfection, consistent with a role for Argonaute2 in RISC.

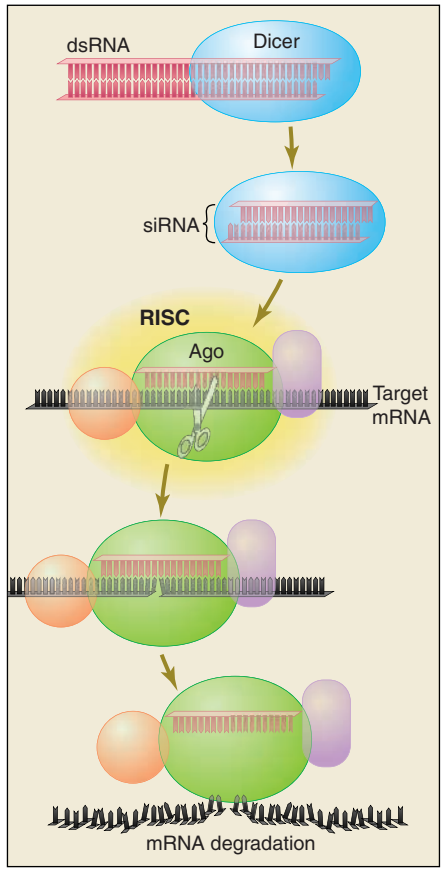

An endonuclease in plain sight. The RNA interference pathway of gene silencing culminates in target mRNA cleavage by the PIWI domain of Argonaute. Within most eukaryotic cells, dsRNA molecules (red) can be cleaved by the ribonuclease Dicer (blue) into 21- to 23-nucleotide fragments called siRNAs. The siRNAs assemble into the RNA-induced silencing complex (RISC), which includes a member of the Argonaute (Ago) protein family (green). RISC assembly is accompanied by siRNA unwinding, which enables the siRNA within RISC to recognize the mRNA target (black). The PIWI domain of human Argonaute2 appears to act as an endonuclease (scissors) that cleaves the mRNA strand within the siRNA/mRNA duplex. Other nucleases then complete the mRNA degradation process.

CREDIT: KATHARINE SUTLIFF/*SCIENCE*

The authors are in the Department of Biochemistry, Molecular Biology, and Cell Biology, Northwestern University, Evanston, IL 60208, USA. E-mail: erik@northwestern.edu; r-carthew@northwestern.edu

The crystal structure of Argonaute suggests that these proteins are nucleases, and functional data indicate that mRNA target cleavage activity is associated specifically with Argonaute2. Thus, Liu *et al*. proceeded to map some of the determinants of cleavage activity in Argonaute2. Several point mutations within the PIWI domain specifically blocked cleavage of target mRNAs without affecting Argonaute2 protein expression or siRNA binding. Notable among these are two of the three carboxylate residues proposed to bind to a catalytic metal ion. As the authors themselves note, these results do not formally prove that those residues constitute part of an active site; the mutations could block activity by disrupting an interaction with a separate enzymatic subunit. Nonetheless, when the mutagenesis results are combined with other functional data as well as with the structural similarity of RNase H to the PIWI domain, it makes for a compelling argument that human Argonaute2 is, in fact, the long-sought Slicer subunit of RISC. Thus, the answer to one of the RNAi field's most important questions appears to be in hand.

Naturally, many questions remain. What parts (if any) do Argonaute proteins play in earlier stages of the RNAi pathway, such as dsRNA cleavage and RISC assembly? Given that specific Argonautes are essential for distinct silencing pathways—including those that affect protein synthesis (*9*) and heterochromatin assembly (*10*)—how is functional specificity established for the different Argonaute family members? Do all Argonautes require or contain nuclease activity as part of their normal duties? A new entry into the nuclease lexicon is a reminder that a search for the familiar can lead to surprising discoveries.

References

1. J. Liu *et al*., *Science* **305**, 1437 (2004); published online 29 July 2004 (10.1126/science.1102513).
2. J.-J. Song, S. K. Smith, G. J. Hannon, L. Joshua-Tor, *Science* **305**, 1434 (2004); published online 29 July 2004 (10.1126/science.1102514).
3. G. J. Hannon, Ed., *RNAi: A Guide to Gene Silencing* (Cold Spring Harbor Laboratory, Cold Spring Harbor, NY, 2003).
4. S. M. Hammond, E. Bernstein, D. Beach, G. J. Hannon, *Nature* **404**, 293 (2000).
5. S. M. Hammond, S. Boettcher, A. A. Caudy, R. Kobayashi, G. J. Hannon, *Science* **293**, 1146 (2001).
6. M. A. Carmell, Z. Xuan, M. Q. Zhang, G. J. Hannon, *Genes Dev.* **16**, 2733 (2002).
7. L. Joshua-Tor, *Structure* **12**, 1120 (2004).
8. G. Meister *et al*., *Mol. Cell* **15**, 185 (2004).
9. D. P. Bartel, *Cell* **116**, 281 (2004).
10. S. I. S. Grewal, J. C. Rice, *Curr. Opin. Cell Biol.* **16**, 230 (2004).

PHYSICS

Crystalline Electron Pairs

Marcel Franz

At low temperatures, many compounds exhibit superconductivity, a state of vanishing electrical resistance. In high-temperature cuprate superconductors, the superconducting transition temperature T_c can be as high as 160 K. The mechanism through which this happens remains shrouded in mystery. The nature of the electronic state outside of the "superconducting dome" may hold some clues (see the figure). Much attention has been focused on the region intermediate between the antiferromagnetic Mott insulator (a state where spins are alternating) and the superconductor. Theoretical considerations predict two basic scenarios for the electron behavior in this region: Electrons either can form exotic liquid phases with "fractionalized" elementary excitations and no broken symmetries (*1*), or can organize into more conventional ordered states. The former possibility created a great deal of excitement among the researchers, but no convincing evidence for such exotic forms of electronic matter has been found.

Recent high-resolution scanning tunneling microscopy (STM) measurements of Hanaguri *et al*. (*2*) performed on the cuprate $Ca_{2-x}Na_xCuO_2Cl_2$ (known as Na-CCOC) offer an exciting glimpse of what lies to the left of the superconducting dome. They observe a periodic pattern in the local electron density of states (LDOS) whose period is independent of the energy of the tunneling electron (see the figure, inset). This observation is strongly suggestive of underlying crystalline electronic order. It comes on the heels of earlier experimental hints (*3*, *4*) of such static order in another cuprate, $Bi_2Sr_2CaCu_2O_{8+\delta}$ (known as BiSCCO).

There are essentially three ways to suppress superconductivity in a material (see arrows in the figure): raise the temperature above T_c, apply a magnetic field B, or change the doping level x by altering the chemical composition. One would expect to reach the same state of electronic matter via any of the three routes, unless another phase boundary is encountered in the process. By moving along the doping axis, Hanaguri *et al*. (*2*) complete the triad of tests that convincingly demonstrate the existence of crystalline electronic order inside and outside of the superconducting dome.

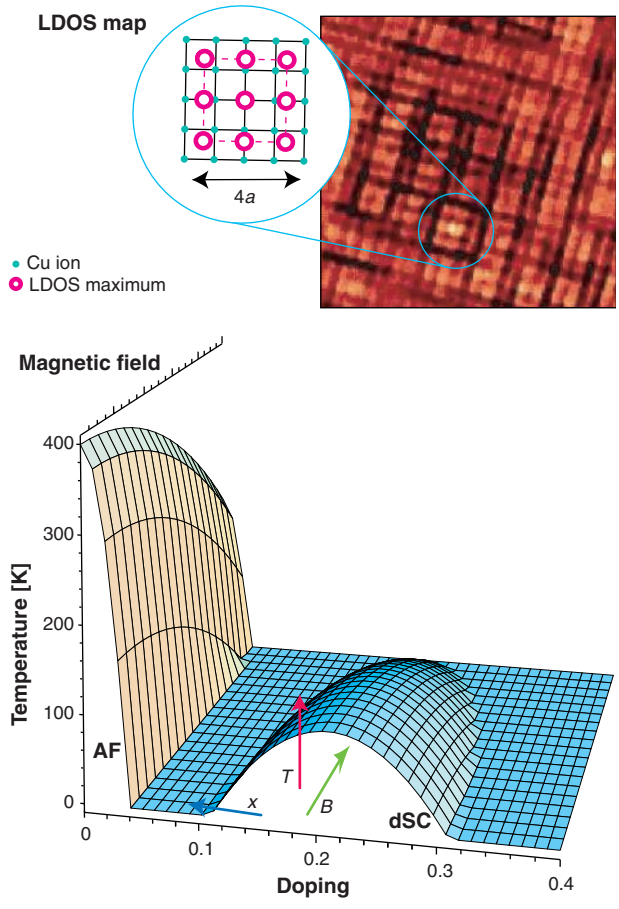

Phase diagram of cuprates. AF, antiferromagnetic state; dSC, *d*-wave superconducting state. Arrows indicate different ways to exit from the superconducting state (*2*–*5*). (**Inset**) Experimental LDOS pattern of Hanaguri *et al*. for a single crystal with doping level $x \cong 1/8$ (*2*). The LDOS exhibits a 4*a* × 4*a* unit cell, where *a* is the lattice constant. Each unit cell contains nine maxima, which (with the exception of the central one) are not registered to the Cu sites. The pattern is, however, commensurate with the underlying Cu lattice, with periodicity 4*a*. In contrast, the checkerboard for BiSCCO is incommensurate, with periodicity 4.3*a* to 4.7*a* (*3*, *4*).

The author is in the Department of Physics and Astronomy, University of British Columbia, Vancouver, British Columbia V6T 1Z1, Canada. E-mail: franz@physics.ubc.ca

In the first experiment in this triad, Hoffman *et al.* moved along the *B* axis and discovered checkerboard patterns in the LDOS in the vicinity of magnetic vortices (*5*). Next, Howald *et al.* explored the *T* direction and observed weak modulations deep inside the superconducting state (*3*). Soon afterward, Vershinin *et al.* reported an even more convincing observation of similar patterns above T_c (*4*, *6*).

The new results of Hanaguri *et al*. (*2*) are perhaps the most spectacular in this group, in that the checkerboards completely dominate the STM signal and can be seen clearly even in the raw data. This clarity, combined with atomic resolution, enables detailed examination of the phenomenon. Apparently, the same phenomenon occurs in the insulating state ($x = 0.08$) and in the superconducting state ($x = 0.10$ and 0.12, with $T_c = 15$ K and 20 K, respectively). This observation implies that superconductivity coexists with charge ordering in this material.

What do we learn from these beautiful data? First, the exotic fractionalized liquid states envisioned in early theoretical studies do not appear to materialize in cuprates. Instead, more conventional ordered states of electronic matter are observed. This conclusion has been anticipated for some time (*7*), but it was not clear which alternative ground state would be realized in cuprates. The new insights provided by STM clarify the situation considerably. Questions, however, abound concerning the precise nature of the ordered state and its relationship (if any) to the nearby superconducting state.

The observed order cannot be a simple charge density wave (CDW). In the electron excitation spectra, also measured in STM, the LDOS is always reduced near the Fermi level (the so-called "pseudogap" behavior), with the minimum pinned to the Fermi energy ε_F. An ordinary CDW produces a gap that is not pinned to ε_F over all of the Fermi surface. In fact, the shapes of the excitation spectra in the superconducting and insulating phases are essentially identical in Na-CCOC, suggesting that the two states are intimately related.

A possible link is furnished by the idea (*8*) that the pseudogap state may be understood as a phase-disordered superconductor. The superconducting order parameter Δ can be driven to zero by thermal or quantum fluctuations in its phase, while retaining nonzero amplitude. This scenario automatically ensures that the pseudogap, being a direct descendant of the superconducting gap, remains pinned to the Fermi energy. Moreover, the spectral line shapes are naturally similar to those in the superconducting state, with sharp features washed out by fluctuations (*9*).

Where do the observed checkerboard patterns (*2*–*5*) fit into this picture? According to the number-phase uncertainty principle (*10*), phase fluctuations in a superconductor tend to suppress fluctuations in the local charge density. One way to accommodate such a reduction in charge fluctuations is to set up a periodic charge modulation, consisting of a wave in the density of the Cooper pairs. An extreme form of such a pair density wave (PDW) is known as the Wigner crystal. In a Wigner crystal, Cooper pairs are localized in a lattice, much like ions in a solid. Recent theoretical studies of these interesting new forms of electronic matter indeed capture some qualitative features of the experimental data (*11*–*14*).

Another theoretical proposal starts from the Mott insulator and envisions a crystal of holes (*15*). Both scenarios predict periodic checkerboard patterns, as observed in (*2*–*5*), but there are qualitative differences that will, in due course, allow for experimental validation of the correct picture.

References and Notes

1. P. W. Anderson, *The Theory of Superconductivity in the High-T_c Cuprates* (Princeton Univ. Press, Princeton, NJ, 1997).
2. T. Hanaguri *et al*., *Nature* **430**, 1001 (2004); 26 August 2004 (10.1038/nature02861).
3. C. Howald, H. Eisaki, N. Kaneko, M. Greven, A. Kapitulnik, *Phys. Rev. B* **67**, 014533 (2003).
4. M. Vershinin *et al*., *Science* **303**, 1995 (2004); published online 12 February 2004 (10.1126/science.1093384).
5. J. E. Hoffman *et al*., *Science* **295**, 466 (2002).
6. M. Norman, *Science* **303**, 1985 (2004).
7. D. A. Bonn *et al*., *Nature* **414**, 887 (2001).
8. V. J. Emery, S. A. Kivelson, *Nature* **374**, 434 (1995).
9. M. Franz, A. J. Millis, *Phys. Rev. B* **58**, 14572 (1998).
10. This principle states that $\Delta N \Delta f \geq 1$, where ΔN and Δf are the uncertainty in particle number and phase, respectively.
11. H.-D. Chen, O. Vafek, A. Yazdani, S.-C. Zhang, www.arxiv.org/abs/cond-mat/0402323.
12. Z. Tesanovic, www.arxiv.org/abs/cond-mat/0405235.
13. P. W. Anderson, www.arxiv.org/abs/cond-mat/0406038.
14. One consequence of the PDW hypothesis is a possibility of formation of a "supersolid" phase, previously conjectured to occur in solid ^{4}He. The supersolid retains the crystalline order of the pair Wigner crystal but also exhibits superconductivity, presumably as a result of excess Cooper pairs that cannot be accommodated in the crystal. This picture would explain another enduring mystery in cuprates: that the superfluid density is proportional to doping x and not to the total electron density $1 - x$.
15. H. C. Fu, J. C. Davis, D.-H. Lee, www.arxiv.org/abs/cond-mat/0403001.

16. I thank J. C. Davis, A. P. Iyengar, T. Pereg-Barnea, Z. Tesanovic, and A. Yazdani for helpful discussions.

MEDICINE

Targeting Apoptotic Pathways in Cancer Cells

Catherine Denicourt and Steven F. Dowdy

From cell division to programmed cell death, protein-protein interactions are a central regulatory feature of nearly all biological processes in a living organism. Hence, modulating or mimicking protein-protein interactions with biologically active peptides or chemical compounds offers an attractive strategy for therapeutic intervention in specific disease pathways.

The authors are in the Howard Hughes Medical Institute and Department of Cellular and Molecular Medicine, University of California San Diego School of Medicine, La Jolla, CA 92093–0686, USA. E-mail: sdowdy@ucsd.edu

The ability to escape suicide (apoptosis) is a hallmark of most cancer cells and often correlates with tumor aggressiveness and resistance to traditional anticancer drug treatments (*1*). Consequently, academic and industrial laboratories are engaged in a Herculean effort to develop new molecules that reactivate the apoptotic program in tumor cells by specifically targeting protein-protein interactions (*2*). On pages 1466 and 1471 of this issue, Walensky *et al.* (*3*) and Li *et al.* (*4*) present two provocative approaches to inducing tumor-selective apoptosis. In each case, they have engineered an experimental therapeutic that mimics key interactions between proteins that belong to either the receptor-dependent (extrinsic) or mitochondrial-dependent (intrinsic) apoptotic pathways of normal cells.

There is much interest in exploiting biologically active peptides as pharmaceutical lead compounds. The use of peptides as therapeutics is, however, limited by their low bioavailability, their inefficiency in crossing cell membranes (due primarily to their size), and their poor metabolic stability in vivo. Efforts to overcome these limitations have led to the generation of synthetic peptides that contain nonnatural amino acids. These so-called "peptidomimetics" mimic the structural and functional properties of their native parental peptides and often have certain advantages. For example, they may be conformationally stable, resistant to degradation by enzymes, have an increased ability to penetrate cell membranes and, most important, can be engineered to specifically bind to the interaction surfaces of target proteins (*5*).

In their study, Walensky *et al.* (*3*) generated a peptidomimetic of a critical BH3 (BCL-2 homology 3) protein-protein interaction domain to induce mitochondrial-dependent apoptosis (see the figure). Members of the BCL2 family of proteins are central regulators of mitochondrial integrity and apoptotic cell death (*6*). However, BCL2 family members exist in two distinct flavors: inhibitors of apoptosis (BCL2 and BCL-X_L) and inducers of apoptosis (BAX, BAK, and BID). Proapoptotic members such as BID harbor a BH3 protein-protein interaction domain in the form of an amphipathic α helix that performs several essential functions. First, it interacts with a hydrophobic groove on antiapoptotic BCL2 family members and effectively blocks their function. Second, it induces oligomerization of proapoptotic members (BAX and BAK), resulting in release of cytochrome c from mitochondria, activation of the apoptosome, and subsequent induction of apoptosis (see the figure).

Walensky *et al.* (*3*) started with the parental BH3 peptide. Then, by substituting nonnatural amino acids on the surface opposite the protein-protein interaction surface using a chemical technique called hydrocarbon stapling, they were able to generate a covalent "staple" that stabilized the α-helical structure. The resulting BH3 peptidomimetic, called SAHB (stabilized α helix of BCL2 domains), has improved pharmacological properties relative to the native parental BH3 peptide. These properties include greater resistance to proteolytic degradation, and the ability to boost cytochrome c release and to induce apoptosis in a variety of leukemic cell lines. In vivo, SAHB (BH3) peptidomimetic treatment of mice bearing human leukemia xenografts substantially reduced the expansion and organ infiltration of leukemic cells without any detectable toxicity to normal organs.

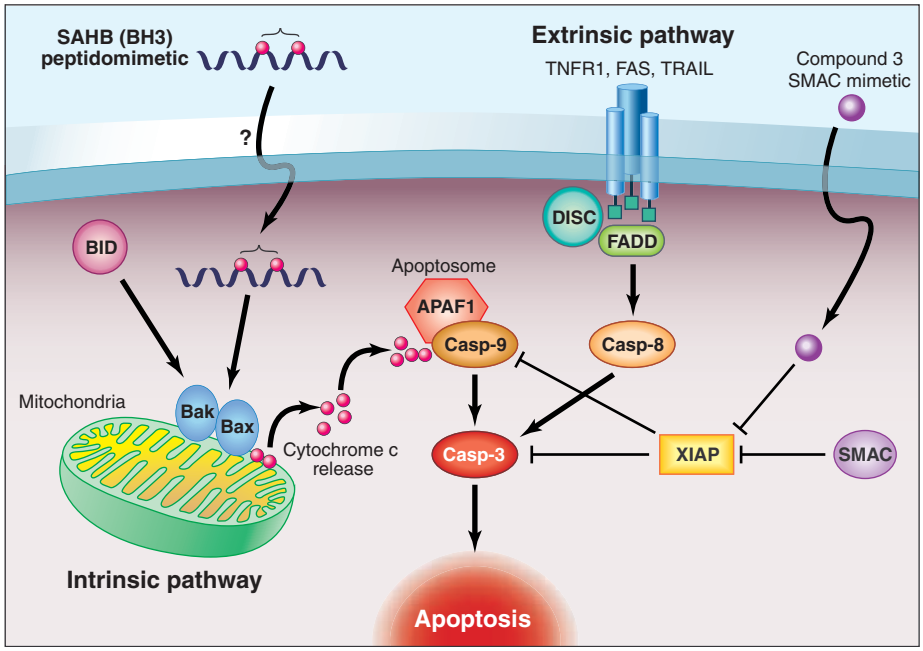

Death and the cancer cell. Macromolecular peptidomimetic manipulation of apoptosis. Cells of higher eukaryotes contain extrinsic receptor pathways and intrinsic pathways that activate effector caspases and induce apoptosis. **(Right)** The extrinsic cell death pathway is mediated by a subgroup of the TNF receptor superfamily called the death receptors (TNFR1, FAS, and TRAIL). Receptor-mediated cell death is initiated by the recruitment of adaptor proteins, like FADD, which then bind to DED-containing procaspases to generate a death-inducing signaling complex (DISC) that leads to activation of caspase-8. Caspase-8 directly cleaves and activates caspase-3, the executioner enzyme of apoptosis. **(Left)** In the mitochondrial or intrinsic pathway, proapoptotic BCL2 family members BAX and BAK translocate to the mitochondria. The BH3-only protein BID activates BAX and BAK to mediate the release of cytochrome c in the cytosol. This triggers the assembly of the apoptosome (APAF1 and caspase-9) and subsequent activation of caspase-3 and cell death. The SAHB BH3 peptidomimetic designed by Walensky *et al.* (*3*) mimics the BH3 helix of BID and hence is able to activate BAX and BAK, resulting in cytochrome c release from mitochondria. Inhibitor of apoptosis (IAP) proteins bind directly to caspases and inhibit their enzymatic activity. The inhibitory function of IAPs is countered by the second mitochondria-derived activator of caspases (SMAC). Four amino acid residues in the amino terminus of SMAC interact with the Bir domain of IAPs. Compound 3 designed by Li *et al.* (*4*) mimics the four amino-terminal residues of SMAC that interact with IAPs. This new molecule acts synergistically with TRAIL or TNF-α to induce apoptosis of glioblastoma cells.

The cell membrane is a formidable barrier that generally prevents passage of molecules greater than 500 daltons (roughly equivalent to the mass of five amino acids) (*7*). However, peptides encountered by the cell membrane are often larger than several thousand daltons. Walensky and co-workers showed that the SAHB (BH3) peptidomimetic (>2000 daltons) is taken up by a fluid-phase endocytic mechanism. Recent work on the transduction domain of the HIV-1 Tat protein has shown that poly(Arg)-containing peptides enter cells by fluid-phase macropinocytosis, a specialized form of endocytosis (*8*). However, the SAHB (BH3) peptidomimetic contains only three arginine residues, an insufficient number to induce macropinocytosis, suggesting that covalent stabilization of the α-helical structure by hydrocarbon stapling may confer the SAHB peptide with lipophilic properties that enable it to cross cellular membranes. The Walensky *et al.* results begin to open the experimental therapeutic door to entirely new types of therapies aimed at modulating specific protein-protein interactions.

In a complementary study, Li and coworkers (*4*) used a similar strategy of mimicking protein-protein interactions to induce tumor-selective apoptosis. However, they generated a synthetic compound that mimics the protein-protein interaction domain of an activator of apoptosis, SMAC. The key effectors of apoptosis are the caspase proteases that, when activated, result in the destruction of the cell's interior. Caspases are held in check, in part, by protein-protein interactions with IAPs, proteins that block apoptosis. Not surprisingly, IAPs undergo gene amplification and overexpression in human tumors (*9*). IAPs, in turn, are inhibited by protein-protein interactions with the amino-terminal four residues of proapoptotic SMAC. Following release from mitochondria after BAX/BAK activation, SMAC interacts with a groove in the Bir domain on the IAP surface (see the figure). Thus, inhibition of IAPs with SMAC molecular mimetics would be predicted to have valuable therapeutic potential for treating both cancer and inflammatory diseases. Indeed, Fulda *et al.* have previously shown that linkage of the native SMAC amino-terminal peptide to a protein transduction domain resulted in caspase activation and the killing of tumor cells in a mouse model of glioblastoma (*10*).

To enhance the pharmacological properties of the quadrimeric amino-terminal SMAC peptide, Li *et al.* started with the crystal structure of the SMAC-IAP interaction, then designed a 180-member peptidomimetic library harboring nonnatural amino acid replacements (*4*). The pep-

CREDIT: KATHARINE SUTLIFF/*SCIENCE*

tidomimetic library was screened to find molecules that could compete with the binding of the SMAC peptide to the Bir domain of different forms of IAP. After further chemical modification of a candidate molecule, Li *et al.* generated compound 3 that, like SMAC, has a high avidity for different forms of IAP including X-chromosome encoded IAP (XIAP), cellular IAP-1, and cellular IAP-2. Compound 3 blocked the interaction of XIAP with active caspase 9. In previous work, SMAC was shown to act synergistically with a death receptor called TRAIL to induce tumor-selective apoptosis (*10*). Impressively, treatment of glioblastoma cells with a combination of the ligand for the TRAIL receptor and compound 3 resulted in apoptosis of the tumor cells, whereas normal cells were not harmed. Li *et al.* (*4*) also demonstrated that compound 3 could potentiate apoptosis in cells treated with TNF-α (tumor necrosis factor–α) without activation of the nuclear transcription factor NF-κB. Because TNF-α mediates host responses in acute and chronic inflammatory conditions, these results suggest that compound 3 may have potential for treating inflammatory diseases (*11*). Although the efficacy of compound 3 was not evaluated in vivo, the authors are using compound 3 as a lead structure for the refinement of future therapeutic compounds with better pharmacological properties.

Peptidomimetics are only now emerging as a powerful solution for overcoming the limitations imposed by the physical properties of native peptides. Walensky *et al.* (*3*) and Li *et al.* (*4*) demonstrate provocative proof-of-concept approaches to the design of peptidomimetics that may have a decided impact on future therapeutics that target disease by modulating specific protein-protein interactions.

References

1. C. A. Schmitt, *Nature Rev. Cancer* **3**, 286 (2003).
2. J. C. Reed, *Cancer Cell* **3**, 17 (2003).
3. L. D. Walensky *et al.*, *Science* **305**, 1466 (2004).
4. L. Li *et al.*, *Science* **305**, 1471 (2004).
5. J. A. Patch, A. E. Barron, *Curr. Opin. Chem. Biol.* **6**, 872 (2002).
6. N. N. Danial, S. J. Korsmeyer, *Cell* **116**, 205 (2004).
7. V. A. Levin, *J. Med. Chem.* **23**, 682 (1980).
8. J. S. Wadia, R. V. Stan, S. F. Dowdy, *Nature Med.* **10**, 310 (2004).
9. G. S. Salvesen, C. S. Duckett, *Nature Rev. Mol. Cell Biol.* **3**, 401 (2002).
10. S. Fulda *et al.*, *Nature Med.* **8**, 808 (2002).
11. R. M. Pope, *Nature Rev. Immunol.* **2**, 527 (2002).

ECOLOGY

Spite Among Siblings

Andy Gardner and Stuart A. West

"Sometimes I work my brother over…I make him squirm, I've made him cry. He doesn't know how I do it. I'm smarter than he is. I don't want to do it. It makes me sick."

—John Steinbeck, *East of Eden*

Although sibling conflict abounds in the literary world—from the Bible to Steinbeck—it also features prominently in the real world. Recent research from the laboratories of Strand and Hardy (*1*–*3*) on sibling conflict among parasitic wasps sheds light on that most puzzling of social behaviors—spite.

Social behaviors are those that affect the fitness of multiple individuals (*4*). The social behavior that has provoked the most interest is altruism, in which an action incurs a direct fitness cost for the actor and provides a benefit for the actor's social partners. Hamilton showed that altruism is favored when individuals are helping their close relatives, and hence still passing on their genes to the next generation, albeit indirectly. A pleasingly simple and elegant method for quantifying this idea of kin selection is Hamilton's rule, which states that an altruistic behavior will be favored if the cost to the actor (C) is outweighed by the product of the benefit (B) and the genetic relatedness (R) to the social partners, resulting in $RB > C$ (*5*). Hamilton, however, also pointed out that his rule has a more sinister interpretation (*6*). His rule can be twisted to predict that spiteful behavior—which hurts both the actor and the recipient—may be favored when there is sufficient negative relatedness between the social partners.

Negative relatedness may seem like a bizarre concept, but it simply means that the recipient of a particular behavior is less related than other competitors to the actor (*6*–*8*). It has generally been assumed that spite is unlikely to be an important evolutionary force because the conditions required to obtain significant negative relatedness are too restrictive. Nonetheless, theoretical interest in spiteful behavior rumbles on. It is clear that spite can evolve given the right conditions: (i) when there is strong competition for local resources among social partners and (ii) when individuals have the capacity to recognize (and refrain from being spiteful to) their close kin (*6*, *7*). In recent work, Strand, Hardy, and their colleagues (*1*–*3*) investigated a biological system that appears to satisfy both conditions—the sterile soldier caste of polyembryonic parasitic wasps.

These small wasps deposit their eggs into the eggs of moths, and the wasp larvae develop within the moth caterpillars (see the figure). A single wasp egg proliferates asexually (clonally) to produce multiple larvae such that, when the host contains larvae from several eggs, the limited food resources within the caterpillar will permit only a fraction of those larvae to complete development and emerge as adults. Thus, there is intense competition for resources among the larvae within the host, satisfying the first condition for spite.

The majority of the wasp larvae develop normally, whereas others develop precociously to form a soldier caste that differs morphologically and behaviorally from normal wasp siblings (see the figure). Donnell *et al.* (*1*) demonstrate that the mechanism underlying caste formation in the clonally developing wasp population involves asymmetric inheritance of germ cells. Embryos that develop into normal larvae inherit the germ line, whereas embryos that develop into soldiers do not, making them obligately sterile—the cost of developing as a soldier. Upon hatching, soldiers distribute themselves throughout the host and launch aggressive attacks on other larvae, murdering their unfortunate victims. This has the potential to be spite and not altruism because the benefits of reduced competition accrue to all larvae in the host and not preferentially to closer relatives (*7*).

This would be an adaptive spiteful behavior if soldiers preferentially attacked the larvae they are least related to in the caterpillar, which requires kin recognition, the second condition for spite (*7*). In a new study, Giron and colleagues (*2*, *3*) demonstrate that soldiers are indeed capable of recognizing their kin, and the investigators then elucidate the mechanism. First, they varied kinship by introducing either full (but not genetically identical) sisters and brothers or unrelated larvae into a host caterpillar containing a developing female brood of wasp larvae (*2*). The introduced larvae were labeled with a fluorescent tracer, and attack rates were assessed by measuring how many of the resident soldiers ingested labeled larval tissue (see the figure). As predicted, the researchers found a strong negative correlation between attack rates and kinship.

The authors are in the School of Biological Sciences, University of Edinburgh, Edinburgh EH9 3JT, UK. E-mail: andy.gardner@ed.ac.uk

In a companion study (*3*), the investigators shed light on the mechanism of this kin recognition faculty. They reveal that the key element is the extraembryonic membrane surrounding each larva during its development in the caterpillar host. They show that attack rates correlated negatively with kinship when the membrane was present, but not when the membrane was removed. In addition, by transplanting membranes between larvae they were able to fool the soldiers, whose attack rates correlated negatively with the kinship of the membrane donor but not with the larva encased inside. Mechanisms of kin recognition are unstable because deceptive variants arise that signal strong kinship to everyone; such variants can become common. However, the importance of the membrane in protecting larvae from host immune attack means that rare variants are intrinsically favored and that common variants are disadvantageous, providing a robust, honest signal of kinship. This may be true for many endoparasites, rendering such species masters of kin recognition.

One potentially puzzling result is that manipulation of resource availability by starving the host caterpillars did not influence the level of aggression exhibited by the wasp soldier caste (*2*). Possibly because competition is always local, resource availability does not influence how soldiers vary their relatedness-dependent behavior. Alternatively, soldier larvae may not be able to assess the intensity of competition for resources, either because doing so is difficult or because natural variation in competition is negligible and there has been no need for this faculty to evolve. Future work on how local competition for resources relates to soldier aggression could benefit from explicit theoretical modeling, as well as alternative methods for varying the scale of competition such as selection experiments (*9*) or comparative studies across species and populations. Nonetheless, the existence of an aggressive soldier caste among parasitic wasps provides evidence that spite does exist in the real world, as Hamilton predicted it would.

A Life cycle of a polyembryonic wasp

A female wasp deposits her eggs into a caterpillar host egg.

The wasp larvae undergo clonal proliferation within the caterpillar host.

Larvae develop either precociously into soldiers (left) or normally (right).

B Caught in the spiteful act

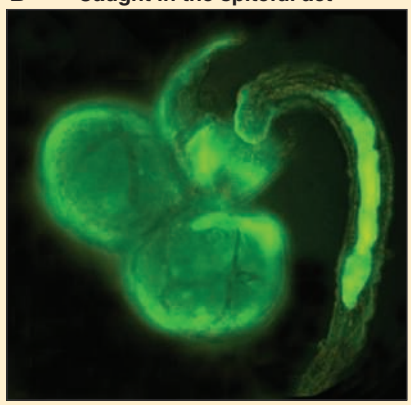

A soldier wasp larva ingests its fluorescently labeled victim.

References

1. D. Donnell, L. S. Corley, G. Chen, M. R. Strand. *Proc. Natl. Acad. Sci. U.S.A.* **101**, 10095 (2004).
2. D. Giron, D. W. Dunn, I. C. W. Hardy, M. R. Strand, *Nature* **430**, 676 (2004).
3. D. Giron, M. R. Strand, *Proc. R. Soc. B (Suppl.) Biol. Lett.*, 17 June 2004 (10.1098/rsb1.2004.0205).
4. S. A. Frank, *Foundations of Social Evolution* (Princeton Univ. Press, Princeton, NJ, 1998).
5. W. D. Hamilton, *Am. Nat.* **97**, 354 (1963).
6. W. D. Hamilton, *Nature* **228**, 1218 (1970).
7. A. Gardner, S. A. West, *J. Evol. Biol.*, 22 July 2004 (10.1111/j.1420-9101.2004.00775).
8. A. Grafen, *Oxford Surv. Evol. Biol.* **2**, 28 (1985).
9. A. S. Griffin, S. A. West, A. Buckling, *Nature* **430**, 1024 (2004).

PLANETARY SCIENCE

Looking into the Giant Planets

Jonathan J. Fortney

Images of Jupiter and Saturn from telescopes and space probes only show the outermost layers of these giant planets. Learning about their interiors, which consist mostly of hydrogen (H) and helium (He) and make up over 90% of the planetary mass in the solar system, is more challenging. Recent model studies (*1*–*3*) show how new measurements from the Cassini spacecraft—now in orbit around Saturn—could lead to a better understanding of the interior of Saturn and, by extension, all giant planets.

Enhanced online at www.sciencemag.org/cgi/content/full/305/5689/1414

The most important input into giant planet models is the equation of state—that is, the relation between pressure and density—of hydrogen. Uncertainties in the equation of state translate directly into uncertainties in the estimated size of the "heavy element" (elements more massive than He) cores of the giant planets and the abundances of elements in their hydrogen-rich envelopes (*1*). Two groups have measured the shock-induced compressibility of deuterium, a heavy isotope of H, but there is a 50% discrepancy between their data sets (*4*, *5*). As Saumon and Guillot (*1*) show in a recent paper in *The Astrophysical Journal*, this uncertainty profoundly affects inferences about the composition of the planets and the sizes of their cores. These quantities must be known before we can understand the process of giant planet formation and properties of the early solar system.

The authors created static models of Jupiter and Saturn that match all available constraints, including mass, radius, oblateness, rotation period, atmospheric temperature, and gravitational moments for each planet. They also used a wide range of possible equations of state for H to allow for the disparate experimental data sets. According to their model, Jupiter's core is 0 to 11 Earth masses. Saturn's core is likely larger, between 9 and 22 Earth masses. (For comparison, Jupiter is 317.8 Earth masses and Saturn 95.2 Earth masses.) Overall, Jupiter is enriched in heavy elements by a factor of 1.5 to 6 relative to the Sun, and Saturn by a factor of 6 to 14. The most striking of these results is that we cannot be sure whether Jupiter has a core.

The greatest uncertainty in the structure of Jupiter comes from unsatisfactory understanding of liquid metallic H at Mbar pressures. In contrast, for Saturn, poor knowledge of its gravitational moments, which describe how the planet's mass responds to its rotation, is the main obstacle. Gravitational moments are determined by measuring small accelerations of a spacecraft as it passes near a planet. During Cassini's 4-year mission, error bars on the low-degree gravitational mo-

The author is with the Planetary Systems Branch, NASA Ames Research Center, Moffett Field, CA 94035, USA. E-mail: jfortney@arc.nasa.gov

PHOTOS: M. STRAND, D. GIRON, J. JOHNSON

ments J_4 and J_6 should be reduced by factors of at least 50 and 20, respectively. These measurements will lead to much tighter constraints on Saturn's core mass and heavy-element enrichment. In a possible extended mission, additional moments could be determined for the first time (*6*).

Jupiter and Saturn both emit nearly twice as much energy as they receive from the Sun. This intrinsic flux is carried through each planet by convection in their fluid interiors. Both planets are thus likely to be adiabatic and well mixed in most of their interiors. A simple cooling model for a fully convective homogeneous Jupiter, radiating energy left over from its formation 4.55 billion years ago, gives a current luminosity that closely matches the measured value. In contrast, Saturn is over 50% more luminous than this model predicts (*7*). Saturn must possess a substantial additional internal energy source that is much smaller, or nonexistent, in Jupiter.

The gradual sinking of He could be such an additional energy source (*8*–*10*). If He phase-separates deep within a giant planet from the previously homogeneous mixture, this He could form stable droplets. The droplets, being denser than their surroundings, could fall to deeper layers of the planet and exchange their gravitational potential energy for thermal energy through viscous dissipation (*9*). The visible atmosphere would also be depleted in He, because it is connected with deeper layers through convection.

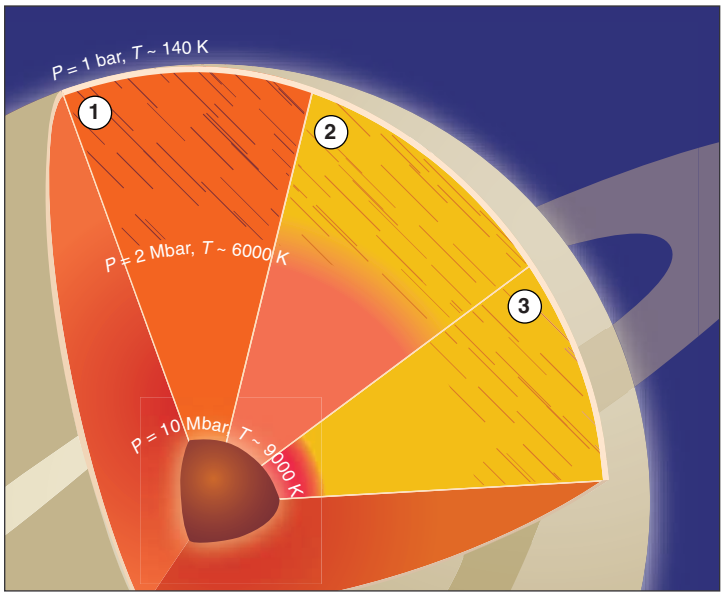

Three views of the interior of Saturn. Orange represents the protosolar He/H ratio. A yellower orange indicates less He, and a redder orange more He. Brown is the ice/rock core. The hashed regions indicate that H is liquid molecular, whereas in the unhashed regions it is liquid metallic. (**1**) Saturn at an age of ~1.5 billion years, before the onset of He phase separation. (**2**) The current Saturn according to a previously proposed H-He phase diagram (*11*). (**3**) The current Saturn according to a phase diagram derived from new evolutionary models (*2*).

Quantum mechanical calculations (*11*) put the onset of this phase separation at pressures above 2 Mbar and temperatures below 8000 K—conditions found in the interiors of gas giant planets. Consequently, the picture has emerged that Saturn has been differentiating for the past 2 to 3 billion years, whereas Jupiter, whose interior is warmer than Saturn's, has either not begun to differentiate, or has begun to do so only relatively recently. However, many details are still unclear.

Measurements of the atmospheric He abundance of Jupiter and Saturn support the view that differentiation is currently under way in both planets. The envelopes of Jupiter and Saturn are thought to have the protosolar He/H ratio of 0.096 ± 0.004 (by number). However, the Galileo entry probe gave a lower ratio of 0.079 ± 0.002 in Jupiter's atmosphere (*12*). Indirect measurements from Voyager, which used an inversion technique on infrared spectra of Saturn, put the ratio in Saturn's atmosphere at 0.055 to 0.080 (*13*). These data support the idea that He is "raining down" in both planets, but likely to a greater extent in Saturn. The deeper layers of the planets must contain the He missing from the visible atmosphere.

To test calculated H-He phase diagrams and place constraints on the temperature/pressure range of the He immiscibility region, for which there are no experimental data, Bill Hubbard and I recently coupled detailed evolutionary models of Saturn to high-pressure phase diagrams of He-H mixtures (*2*). We found that the original H-He phase diagram calculation (*11*) is likely incorrect. Evolutionary models of Saturn that use this phase diagram are 30% less luminous than the actual planet. We propose a new ad hoc phase diagram, guided by more recent molecular dynamics calculations (*14*).

The proposed phase diagram allows immiscible He to rain down further in Saturn's interior (to the core), liberating more gravitational potential energy. With this phase diagram, the current Saturn model agrees with all available constraints: At an age of 4.55 billion years, it matches the planet's known luminosity and has an atmospheric He abundance that matches the Voyager-derived value. The predicted shape of the H-He phase diagram can be tested by computer simulations and perhaps by future high-pressure shock experiments. The model indicates that He phase separation cannot be Saturn's only additional energy source if the planet's current atmospheric He/H ratio is greater than 0.063.

He phase separation can be accommodated into the evolution of Saturn, but Jupiter's smaller atmospheric He depletion remains unexplained. Can a H-He phase diagram be devised that allows both Jupiter and Saturn to reach their measured luminosities and atmospheric He abundances? This problem will continue to be addressed by planetary scientists during the Cassini mission. A more accurate determination of Saturn's He abundance would shed considerable light on the evolution of Saturn, Jupiter, and extrasolar giant planets like them (*3*). Cassini does not have a Saturn entry probe, but it could provide a better indirect measurement. The spacecraft will obtain many atmospheric pressure-temperature profiles over a range of latitudes and infrared spectra to wavelengths of 1 mm (*15*).

Saturn and Jupiter serve as calibrators for theories of the formation and evolution of all giant planets. In addition, both planets are vast natural laboratories with which to study He and H under high pressure. Further progress will require advanced computational modeling of the behavior of H/He mixtures, continued experiments on these elements under intense pressure, and accurate and precise determinations by the Cassini spacecraft of Saturn's gravitational moments and atmospheric He abundance.

CREDIT: PRESTON HUEY/*SCIENCE*

References

1. D. Saumon, T. Guillot, *Astrophys. J.* **609**, 1170 (2004).
2. J. J. Fortney, W. B. Hubbard, *Icarus* **164**, 228 (2003).
3. J. J. Fortney, W. B. Hubbard, *Astrophys. J.* **608**, 1039 (2004).
4. G. W. Collins *et al.*, *Science* **281**, 1178 (1998).
5. M. D. Knudson *et al.*, *J. Phys. A* **36**, 6149 (2003).
6. J. Castillo, personal communication.
7. W. B. Hubbard *et al.*, *Planet. Space Sci.* **47**, 1175 (1999).
8. R. Smoluchowski, *Nature* **215**, 691 (1967).
9. E. E. Salpeter, *Astrophys. J.* **181**, L83 (1973).
10. D. Stevenson, E. E. Salpeter, *Astrophys. J. Suppl.* **35**, 239 (1977).
11. D. Stevenson, *Phys. Rev. B* **12**, 3999 (1975).
12. U. von Zahn, D. M. Hunten, G. Lehmacher, *J. Geophys. Res.* **103**, 22815 (1998).
13. B. J. Conrath, D. Gautier, *Icarus* **144**, 124 (2000).
14. O. Pfaffenzeller, D. Hohl, P. Ballone, *Phys. Rev. Lett.* **74**, 2599 (1995).
15. F. M. Flasar, personal communication.

INTRODUCTION

Deconstructing Aging

Experts argue about what drives our decline over time, but most would agree about one hallmark feature of aging: It predisposes our bodies to fall apart. Organs, tissues, and even individual cells start misbehaving, rendering us susceptible to the familiar conditions that, for example, weaken our bones, scramble our neural messages, and condemn us to pain. This special joint issue of *Science* and two of its online sites, Science of Aging Knowledge Environment (SAGE KE) and Signal Transduction Knowledge Environment (STKE), explores how we age piece by piece.

Two articles focus on osteoporosis, a disease that undermines our skeletons. In a News story (p. 1420), Marx looks at some of the recent trends in research on this debilitating illness, with particular emphasis on the therapies that drug designers are developing to combat it. In an STKE Review (www.sciencemag.org/sciext/aging2004), Hughes-Fulford examines signaling pathways involved in the proliferation of bone-building cells—osteoblasts—in response to mechanical stress, such as weight-bearing exercise. Mechanical stress can even counteract some of the bone-weakening effects of estrogen loss after menopause.

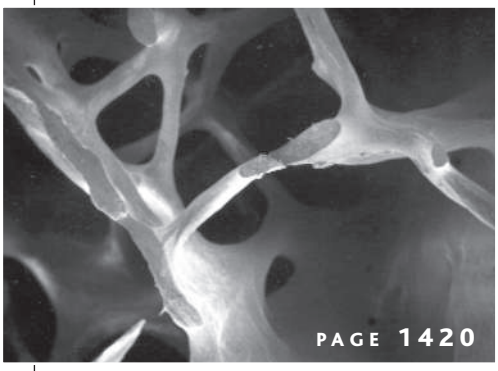

Like our bones, the cartilage that promotes smooth joint movement can break down with age. In SAGE KE (www.sciencemag.org/sciext/aging2004), a Case Study by Shakoor and Loeser describes the ravages of osteoarthritis, a major cause of disability and chronic pain in the elderly.

People with Werner syndrome display the premature onset of not only osteoporosis and osteoarthritis but many other age-related conditions. In their Review (p. 1426), Kipling *et al*. present evidence from investigations of this disease that suggests that somatic cell senescence promotes normal aging. A Viewpoint by Roth *et al*. (p. 1423) discusses another model for studying aging: nonhuman primates. Many similar age-related perturbations occur in rhesus monkeys and humans. In both creatures, for instance, concentrations of dehydroepiandrosterone sulfate (DHEAS) wane with increasing age. Blood-borne quantities of this compound are higher than normal in monkeys subjected to the life-extending regime of calorie restriction and in long-lived men. A SAGE KE Review by Hornsby explores the mechanisms by which the DHEAS-secreting adrenal cortex might change as we grow older.

Although the lethargy of many physiological activities seems to encourage aging, the exuberance of others might also contribute to our downfall. A SAGE KE Perspective by Mobbs probes the idea that neuroendocrine activity involving the pituitary, reproductive, or adrenal systems fosters age-related decay.

As researchers gain insight into how we disintegrate, they also are striving to renew our tired bodies. Kennedy points out in his Editorial (p. 1369) that stretching longevity without such bolstering of our ailing systems would be an unwelcome tradeoff. In a SAGE KE News story, Davenport surveys regeneration biology—an ancient field that is feeling new life from the application of modern genetic techniques. Using historical records as well as current interview material, a SAGE KE News story by Chen delves into the parallels between the public's responses to in vitro fertilization in the 1970s and to stem cell technology today. Time will tell whether emerging stem cell–based technology will evolve into a routine fixture of medical practice, as test tube baby–making has.

These articles detail attempts to understand the body's unraveling and to counteract it. Through such a piece-by-piece approach, answers to the mystery of aging are bound to come together.

–LISA CHONG, HEATHER MCDONALD, AND EVELYN STRAUSS

CONTENTS

See also related STKE and SAGE KE material on p. 1363 and Editorial on p. 1369.

Science

CREDIT: D. W. DEMPSTER *ET AL.*, *J. BONE AND MINERAL RES.* 1,15–21 (1986)

Published by AAAS

NEWS

Coming to Grips With Bone Loss

A better understanding of osteoporosis is leading to new therapies for preventing and treating the bone-weakening disease

Slowly and insidiously, the bones deteriorate, losing minerals and structure. A surprise fracture, usually of the hip, wrist, or one of the vertebra of the spinal column, is often the first indication that osteoporosis has been weakening a patient's bones for years. The consequences can be dire. One-fifth of people older than 50 die within a year of a hip fracture, and many others end up in nursing homes—a fate some consider even worse than death.

Researchers have long known that estrogen deficiency, such as that occurring at menopause, leads to fragile bones. That's why women account for about 80% of the estimated 10 million osteoporosis patients in the United States. Yet the most obvious preventive strategy, hormone replacement therapy (HRT), has fallen out of favor since the Women's Health Initiative found that extended HRT increases the risk of both breast cancer and cardiovascular disease (*Science*, 14 November 2003, p. 1136).

Fortunately, other drugs have come on the market in the last decade to take up the slack. Most of these, such as the bisphosphonates, which include alendronate (Fosamax) and risedronate (Actonel), primarily act to prevent bone loss. "They are working extremely well," says osteoporosis researcher B. Lawrence Riggs of the Mayo Clinic in Rochester, Minnesota. "They decrease the fracture rate by about 50%."

Such developments are bringing new patients into the clinic. Randall Stafford and his colleagues at Stanford University in Palo Alto, California, reported in the 26 July issue of the *Archives of Internal Medicine* that the number of physician visits for osteoporosis increased from 1.3 million in 1994, which was just before alendronate came on the market, to 6.3 million in 2003.

Even so, Stafford notes, osteoporosis still goes undiagnosed in millions of people. And current treatments aren't perfect. "The problem is 50% [of patients taking the drugs] still have fractures," Riggs says. "What you would really like to do is put the bone back to the point where fractures won't occur at all." So an intense hunt is on for drugs that can reverse the dangerous handiwork of osteoporosis.

A new drug that came on the market about 2 years ago is a step in that direction. Called teriparatide (Fortéo), it's a 34-amino-acid fragment of parathyroid hormone (PTH) that has been shown to increase bone mass. Teriparatide has its drawbacks, however: It has to be injected daily, much like insulin for diabetes, and there are other limitations on its use. Additional bone-building treatments, however, are showing promise in early stages of testing.

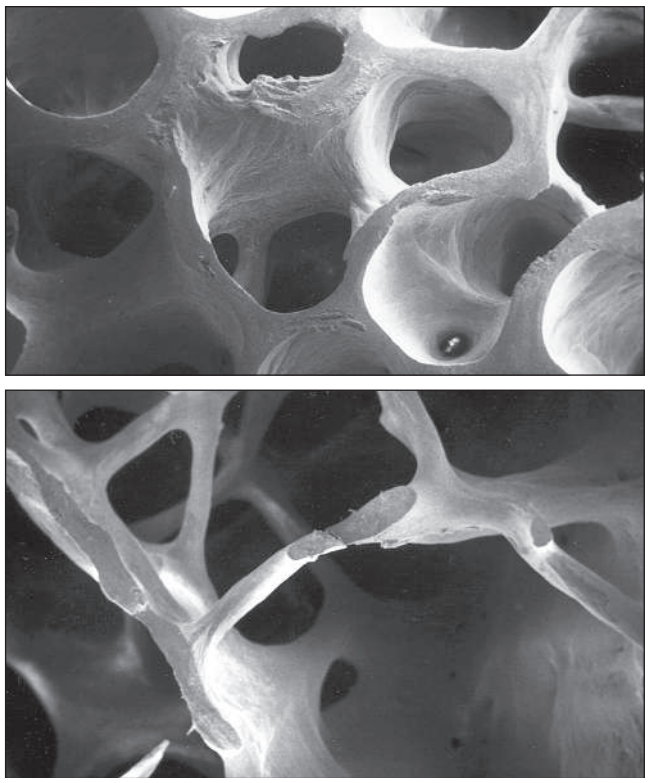

Fading away. These scanning electron micrographs show that, compared with normal bone (*top*), osteoporotic bone loses much of its internal structure, thus raising its risk of fracturing.

Researchers are also making headway in the search for new ways to prevent bone loss from occurring in the first place, a hunt that is fueled by new insights into both normal and osteoporotic bone. In particular, they've gotten a much better picture of how estrogen acts to preserve bone, information that may lead to new compounds that share the hormone's protective skills but not its dangers.

Dynamic bone

People tend to think of bone as a rigid, inert material that holds up their bodies. But bone is far more dynamic. It continuously dissolves and re-forms. Indeed, adults replace their entire skeletons roughly every 10 years. "Bone is like skin. You're constantly remodeling it," says Susan Greenspan of the University of Pittsburgh School of Medicine in Pennsylvania.

This remodeling is carried out by two types of bone cells: the bone-building osteoblasts and the bone-dissolving osteoclasts. The two cooperate like "teams of workers repairing potholes," says Stavros Manolagas of the University of Arkansas for Medical Sciences in Little Rock. "The osteoclasts dig a hole, and the osteoblasts fill it in and repair it." The bisphosphonates help preserve bone by binding to its surface and inhibiting osteoclast activity.

To maintain strong bones, both types of cells have to work equally hard. But with age, and the resulting loss of the sex hormones, particularly estrogen, osteoclasts gain the upper hand. The cells gradually rob bones of their minerals, weakening the skeleton over time. Recent findings indicate that estrogen is key in men as well as in women. Riggs notes that the critical estrogen concentration is about 30 nanograms per milliliter of blood. "Below that," he says, "men begin to lose bone." By age 70, he adds, about 50% of men and 100% of women have such estrogen deficiencies.

Although osteoporosis diagnosis currently depends on scans showing diminished bone density, other less readily detectable changes in bone structure also contribute to bone-fracture risk. "Osteoporosis is not just a reduction in bone density. There are also dramatic changes in bone microarchitecture," says David Dempster of Helen Hayes Hospital in West Haverstraw, New York.

For one, the pits left when the bone's potholes go unrepaired are points of weakness—stress risers in mechanical engineering terms—that make bones more prone to fracture. In addition, certain areas inside

CREDIT: D. W. DEMPSTER *ET AL.*, *J. BONE AND MINERAL RES.* 1,15–21 (1986)

bone have a lacelike structure of interconnected plates and rods with the bone marrow in between. In the early stages of osteoporosis, Dempster says, the rods deteriorate, destroying the connectivity in the internal bone superstructure. A few years ago, Erick Legrand, Maurice Audran, and their colleagues at the Centre Hospitalier Universitaire d'Angers, France, reported that this loss of connectivity is a risk factor, independent of bone density, for fractures in men with osteoporosis.

Such findings indicate that there is room for improvement in identifying persons at risk of developing osteoporosis. "We don't have a good test to use in the clinic to assess other aspects of bone strength" besides density, says Nelson Watts of the University of Cincinnati Bone Health and Osteoporosis Center. Researchers are investigating a number of molecular markers of bone turnover, such as breakdown products of the bone protein collagen that can be detected in the blood or urine.

There is a problem, though, with using such markers for diagnosing osteoporosis or assessing the effects of therapy: Bone turnover fluctuates from day to day. This "variability is a big issue," says Markus Seibel of the University of Sydney at Concord Repatriation General Hospital in Australia.

The parathyroid connection

When a physician does identify a person with osteoporosis, or one who is at risk of the condition, prescribing bisphosphonates to stop further bone loss is a relatively easy call. But building new bone remains a challenge, which is why there's a lot of excitement about the recent approval of the PTH derivative teriparatide. In clinical trials, it decreased fractures by as much as 75% and also increased bone mineral density by roughly 10%.

At first glance, PTH would seem to be a poor choice for a bone-building drug. People whose parathyroid glands are overactive suffer bone loss, not gain. But several decades ago, researchers found that intermittent PTH administration, as opposed to the continuous overexposure to the hormone that occurs in hyperparathyroidism, fosters bone formation. "The same agent can produce either bone gain or bone loss, depending on how long it's present," says Robert Neer of Harvard's Massachusetts General Hospital in Boston, an early pioneer of PTH research.

Why that happens remains unclear, but researchers have some clues. Riggs, Sundeep Khosla, also of Mayo, and their colleagues have evidence that intermittent PTH treatment increases osteoblast formation by stimulating production of insulin growth factor 1, whereas continuous PTH increases osteoclast formation.

Intermittent PTH administration may also help osteoblasts live longer. Manolagas and his colleagues found that in osteoblasts, PTH suppresses a form of cell death called apoptosis by increasing production of proteins needed for cell survival, such as Bcl2, while triggering other changes that inactivate proteins needed for apoptosis. But if the cells are exposed to the hormone for long periods, changes are set off that lead to the degradation of the survival factors and trigger apoptosis. Thus, repeated brief exposures to PTH promote osteoblast accumulation, but continued exposure tips the balance the other way and osteoclasts gain the upper hand.

Although there's no doubt that teriparatide works well, a glitch turned up during its testing that has resulted in its use being limited to a maximum of 24 months. The drug caused osteogenic sarcomas, a form of cancer, in rodents. No cancers have been detected in other species, including nonhuman primates, nor has hyperparathyroidism been linked to increased cancer incidence. But because teriparatide can't be taken indefinitely, researchers have begun testing whether following it with other drugs preserves the hormone's benefits.

In June, John Bilezikian and his colleagues at Columbia University College of Physicians and Surgeons in New York City reported that osteoporotic men who took a bisphosphonate after teriparatide not only maintained their bone density but showed an additional 5% gain by 1 year after they ceased taking the hormone. In contrast, men who opted not to take the second drug showed a bone density decline of nearly 4%.

A PTH relative that has not yet reached the market is also showing promise in early testing. Andrew Stewart, Mara Horwitz, and their colleagues at the University of Pittsburgh have been studying a protein called PTHrP, originally identified as a product of cancer cells, which causes extreme increases in blood calcium concentrations in some patients. Further work showed that all cells make the protein, although in much smaller quantities, and that its structure resembles that of PTH.

Follow-up experiments established that the protein stimulates bone formation in ways that are not yet understood. In a pilot study published last year, Stewart's team found that PTHrP boosted bone density in postmenopausal women by 4% to 5% in 3 months, apparently without stimulating bone resorption. As important, PTHrP didn't increase blood calcium levels or cause other side effects. "It sounds like the Holy Grail that people have been looking for," says Neer. PTHrP, like PTH, has to be injected, however.

How estrogen helps bones

Although estrogen can't build bone the way PTH can, it can protect against bone loss. Scientists have known for some time that estrogen safeguards bones by keeping osteoclasts in check. Now they are learning just how the hormone does that—information that is pointing to potential new ways to prevent and treat osteoporosis.

The development of osteoclasts is triggered by a signal sent by their partners in bone remodeling, the osteoblasts. About 6 years ago, William Boyle, David Lacey, and their colleagues at Amgen Inc., a biotech firm in Thousand Oaks, California, identified that signal. It's a protein called RANK ligand (RANKL), which osteoblasts and their immature precursors secrete. As its name implies, RANKL binds to a protein called

SOME CURRENT AND POTENTIAL OSTEOPOROSIS DRUGS

Drug	Manufacturer	Chemical Class	Action	Status
Alendronate (Fosamax)	Merck	Bisphosphonate	Inhibits osteoclasts	In clinical use
Risedronate (Actonel)	Procter & Gamble/ Aventis	"	"	"
Estrogen	Several	Sex steroid	Inhibits osteoclast development	"
Raloxifene (Evista)	Eli Lilly	Selective estrogen mimic	"	"
AMG 162	Amgen Inc.	RANKL antibody	"	Advanced clinical testing
Estren	Anabonix Inc.	Estrogen derivative	Inhibits osteoblast apoptosis	Preclinical testing
Calcitonin	Novartis	Peptide hormone	Inhibits osteoclasts	In clinical use
Teriparatide (Fortéo)	Eli Lilly	PTH fragment (peptide)	Unclear, but fosters bone formation	In clinical use
PTHrP	Osteotrophin	PTH relative (peptide)	"	Early clinical testing

Published by AAAS

RANK (receptor activator of NF-κB), which sits on the cell surface of immature osteoclasts. This binding both promotes the cells' differentiation and prolongs their survival by suppressing apoptosis. RANKL triggers "the final pathway by which osteoclasts are formed and leads to bone resorption," says Khosla, whose team at Mayo studies this pathway.

A variety of evidence points to estrogen as a key regulator of osteoblast signaling. For example, animal studies have shown that estrogen deprivation leads to increased production of a variety of regulatory cytokines, such as interleukin-1β, interleukin-6, and macrophage colony-stimulating factor, which boost RANKL production and thus osteoclast formation. And last year, the Mayo group, working in collaboration with Boyle and Lacey, implicated RANKL changes in postmenopausal osteoporosis.

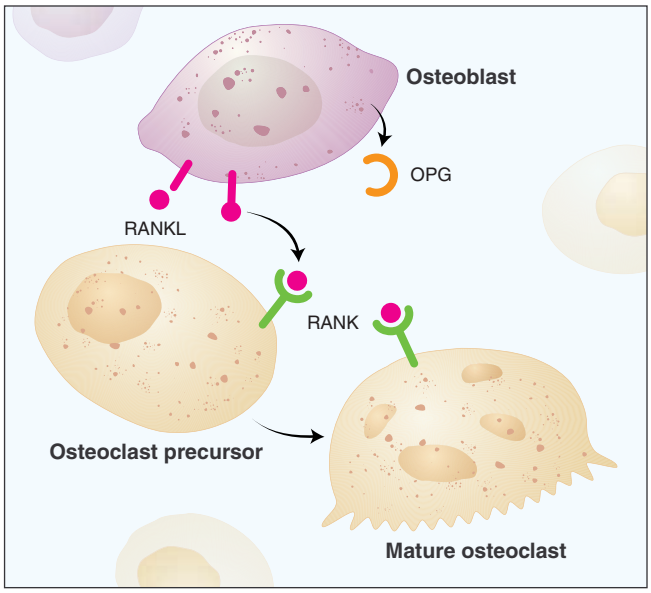

Remodeling partners. The bone-building osteoblasts release RANKL, which binds to its receptor RANK on osteoclasts and osteoclast precursors. This promotes osteoclast maturation and activity, thus fostering bone dissolution. Estrogen keeps osteoclast activity in check by inhibiting RANKL production and increasing production of the protein OPG, which binds RANKL, taking it out of commission.

The researchers used fluorescent-activated cell sorting to isolate osteoblast precursor cells from 12 premenopausal women, 12 women in early menopause, and another 12 menopausal women who were taking HRT. They found that the cells from the untreated menopausal women carried much higher levels of RANKL than did those from the women in the other two groups. The RANKL concentrations also correlated with the concentrations of certain collagen breakdown products in the women's blood and urine, an indication that the high RANKL levels contribute to bone loss.

Given such data, blocking the function of RANKL is an obvious strategy for preventing and treating osteoporosis. Osteoblasts make their own RANKL inhibitor, a protein called osteoprotegerin (OPG) that was previously identified by the Amgen team. It's a truncated form of RANK that is not bound to a cell membrane. When present, OPG effectively vacuums up RANKL molecules, taking them out of action before they can bind to the functional receptor on osteoclast precursors and stimulate their development. The estrogen β-estradiol turns up OPG production, providing another way in which the hormone can counter osteoclast action.

Although Amgen has done some early testing of OPG itself as a way to block RANKL action, the company is now concentrating on an antibody called AMG 162 that also takes RANKL out of commission. In the July *Journal of Bone and Mineral Research*, the company reported that a single dose of AMG 162 given to postmenopausal women produced a sustained decrease—lasting up to 6 months—in bone resorption, as indicated by a marked drop in the production of a collagen degradation product called NTx. Advanced clinical trials to more fully assess the effectiveness of the antibody are getting under way.

An antibody such as the Amgen product may be one way to replicate estrogen's effects on bone without affecting other tissues, but researchers are investigating others as well. Take the selective estrogen-receptor modulators (SERMs), which are designed to mimic the hormone's actions on some of its receptors, say those on bone, but not those on other tissues such as the breast or uterus. One SERM, the drug raloxifene (Evista), is already on the market as an osteoporosis therapy.

Raloxifene, like the bisphosphonates, is generally thought to block bone dissolution without actually building new bone. One new type of estrogen mimic may have bone-restoring potential, however. Many of estrogen's effects on reproductive tissues are initiated when the hormone binds to its receptor, which then migrates to the cell nucleus, where the duo triggers various changes in gene expression.

Calling on ANGELS

But about 3 years ago, Manolagas and his Arkansas colleagues found that the estrogen receptors on bone cells have a second mode of action that does not require their transport to the nucleus. It works instead through a cytoplasmic signaling path. The researchers also showed that estrogen uses this alternate path to block osteoblast apoptosis. This suggested that a drug that mimics this action could boost osteoblast activity without having the harmful side effects associated with estrogen itself.

Since then, the Manolagas group has identified a compound that they call estren (4-estren-3α,17β-diol) that triggers this same receptor action. It inhibits osteoblast apoptosis and also promotes the death of osteoclasts, thus increasing bone formation—all without apparent effects on the animals' reproductive organs. Manolagas has dubbed estren and similar drugs ANGELS—for activation of nongenotropic estrogen-like signaling—to indicate that their specificity is based on their mechanism of action rather than on receptor selectivity, as is the case with the SERMs.

Although new drug therapies for osteoporosis are on the horizon, some note that it would be unwise to forget the tried and true. In his survey, Stanford University's Stafford found that while prescriptions for the new drugs were increasing, recommendations for taking calcium and vitamin D supplements and performing weight-bearing exercise—all known to help build stronger bones—were decreasing. "With the reliance on these new medications, physicians may be neglecting some of the simpler interventions," he says. Not to mention cheaper: A year's treatment with teriparatide costs about $7000, compared with a few dollars a month for the supplements.

The role of vitamin D in particular may be underrated, says Michael McClung of the Oregon Osteoporosis Center in Portland. A meta-analysis published in the 28 April *Journal of the American Medical Association* by Heike Bischoff-Ferrari and her colleagues at Harvard Medical School in Boston reveals that supplementation with the vitamin decreases fall rates—and therefore a number of the fractures—apparently because it helps improve muscle strength in addition to boosting bone mineralization. "From a clinical viewpoint, that's as important as new drugs," McClung says.

All in all, osteoporosis researchers are highly encouraged by the progress they are making. "Ten to 15 years ago, there were no decent treatments for osteoporosis and not much on the horizon," Stewart says. "We've gone from nothing to a set of very effective drugs."

—JEAN MARX

CREDIT: PRESTON HUEY/*SCIENCE*

Aging in Rhesus Monkeys: Relevance to Human Health Interventions

George S. Roth,[1] Julie A. Mattison,[1] Mary Ann Ottinger,[2] Mark E. Chachich,[1] Mark A. Lane,[1] Donald K. Ingram[1]*

Progress in gerontological research has been promoted through the use of numerous animal models, which have helped identify possible mechanisms of aging and age-related chronic diseases and evaluate possible interventions with potential relevance to human aging and disease. Further development of nonhuman primate models, particularly rhesus monkeys, could accelerate this progress, because their closer genetic relationship to humans produces a highly similar aging phenotype. Because the relatively long lives of primates increase the administrative and economic demands on research involving them, new emphasis has emerged on increasing the efficient use of these valuable resources through cooperative, interdisciplinary research.

As gerontological research continues to gain both visibility and interest within the broader scientific community, the relevance of various model systems for eventual application of findings to humans has become a critical issue. Although rodents remain the most widely used animal model for gerontology, an increasing use of invertebrates has provided many new insights into aging processes, especially regarding possible longevity genes (*1*). Given the complexity of human physiology, however, models more phylogenetically similar to humans are needed.

Advantages and Disadvantages of Nonhuman Primate Models

Research using nonhuman primates can provide a valuable approach for elucidating the nature and causes of aging processes observed in humans as well as evaluating potential interventions. An ongoing longitudinal study of aging and nutrition in rhesus monkeys (*Macaca mulatta*) conducted since 1987 by the National Institute on Aging (NIA), as well as studies conducted at other sites, has revealed much about aging and age-related disease in these monkeys and has shed light on the advantages and disadvantages of their use in gerontological research. Because of their genetic homology to humans (92.5 to 95%), many biological similarities are observed in the profile of aging. Another advantage is that rhesus monkeys are well adapted for laboratory research, including established husbandry, nutrition, breeding practices, and veterinary medicine. Disadvantages of rhesus monkeys include their current limited availability, costs of procurement and maintenance, and genetic heterogeneity. In addition, cross-species risks of disease transmission exist, and issues of animal welfare require constant vigilance. Research in monkeys is only as good as their physical and emotional health.

The major scientific disadvantage is that rhesus monkeys are long-lived. Sexual maturity occurs at 3 to 5 years of age, median life-span is 25 years, and maximum life-span is 40 years (*2*, *3*). With an estimated maximum life-span of 122 years in humans (*4*), the rate of aging in rhesus monkeys is roughly three times as fast. Thus, rhesus monkeys offer a distinct advantage over long-term human aging research, but longitudinal studies in these primates require a major investment of time, resources, and effort.

Scope of Rhesus Monkey Research

The NIA supports colonies of aging rhesus monkeys at five primate research centers in the United States (*5*); however, most studies conducted in these monkeys are cross-sectional in design. Ongoing longitudinal studies of aging and age-related disease in rhesus monkeys are being conducted at three sites: the NIA, the Wisconsin National Primate Research Center (WNPRC), and the University of Maryland, Baltimore (UMB). Research at UMB has focused on obesity and diabetes (*6*). With the assistance of numerous international laboratories, studies at the WNPRC and the NIA are evaluating the hypothesis that a nutritious low-calorie diet can retard the rate of aging (*7*, *8*). These studies use a regimen of calorie restriction (CR) 30% below control levels and represent the first experiments to evaluate effects of CR on aging processes in a primate species. As demonstrated in numerous studies of invertebrate and vertebrate models, CR is the most robust and reproducible method for slowing aging, as evidenced by reduced incidence and delayed onset of age-related diseases, extension of mean and maximum life-span, increased stress resistance, and improved physiological and behavioral function (*9*). Emerging from years of research at many sites, abundant information on aging processes in rhesus monkeys has been generated to document parallels and relevance to human aging at organismic, tissue, cellular, and molecular levels of analysis.

Aging Parallels

Regarding morphology, physiology, and behavior, the profile of aging in rhesus monkeys is remarkably similar to human aging (Fig. 1). Sensory systems decline in rhesus monkeys, including presbyopia (loss of near vision) and presbycusis (loss of high-frequency hearing) (*10*, *11*). With advancing age, they lose accommodation of the lens and develop cataracts and macular degeneration (*11*). Regarding behavioral function, their general level of motor activity declines with age (*12*) with gradual decrements in fine-motor skills (*13*). Advancing age does not generally affect simple discrimination learning abilities, but when demands are placed on working memory capacity, the clear age-related decline in learning and memory performance is notably similar to humans (*14*).

Age-related changes in physiological function include declines in metabolic rate and core body temperature (*15*). Age-related changes have not been reliably observed in cardiac function, including heart rate, blood pressure, or measures of arterial stiffness, but the possible contribution of dietary sodium to these age-related changes is currently being addressed. Regarding diet, another interesting parallel to humans is an apparent decline in appetite, manifested as a gradual decline in food intake (*16*).

Structural changes with aging are also evident in rhesus monkeys. Their stature becomes diminished, and bone mineral density in selected sites declines with age (*17*). Age-related changes in cartilage occur as reduced space between vertebrae, similar to osteoarthritis in humans (*18*).

Body composition in rhesus monkeys also parallels changes observed in humans. Their fat mass, particularly abdominal fat, increases with age, whereas lean body mass declines (*19*). Regarding skin quality, age-related deterioration in wound healing has been documented (*20*). At a biochemical level, glycation of rhesus skin proteins is similar to that in humans but occurs at a predictably faster rate (*21*).

Age-related changes in the rhesus brain have also been studied. Although overall brain

[1]Laboratory of Experimental Gerontology, Intramural Research Program, Gerontology Research Center, National Institute on Aging, National Institutes of Health, 5600 Nathan Shock Drive, Baltimore, MD 21224, USA. [2]Department of Animal and Avian Sciences, University of Maryland, College Park, MD 20742–2311, USA.

*To whom correspondence should be addressed. E-mail: ingramd@grc.nia.nih.gov

mass does not decline with age as measured by weight (*22*), reductions have been observed in specific regional volumes with magnetic resonance imaging, such as the basal ganglia (*23*). Similar to humans, no significant loss of hippocampal or neocortical neurons occurs (*24*, *25*). Behavioral deficits associated with hippocampal dysfunction appear to result from decrements in interneuronal signaling rather than cell death (*25*). Cerebral blood volume decreases with age in the hippocampal dentate gyrus (*26*), and the cerebral cortex loses dendrites and arbors with age (*25*). Neurotransmitter receptor and transporter binding in specific regions, including postsynaptic dopamine receptors (*27*) and presynaptic vesicular acetylcholine transporters (*28*), show age-related loss in the basal ganglia. Hippocampal cholinergic fibers are also lost with age (*29*), and there are notable alterations in the integrity of white matter (*30*).

Rhesus monkeys also develop pathological characteristics of Alzheimer's disease (AD), specifically the deposition of amyloid-β (Aβ) plaques with regional deposition similar to humans (*31*). Aβ plaques are associated with angiopathy (*32*). Although Aβ accumulates in older rhesus brains, neurofibrillary tangles, another hallmark of AD pathology, have not been observed (*33*). Driven by the success in mice, there is growing interest in producing transgenic monkeys in which AD and other neurodegenerative diseases can be accurately modeled (*34*).

Parallels also exist between rhesus monkeys and humans regarding age-related hormonal changes, including decreased plasma levels of melatonin (*35*) and dehydroepiandrosterone sulfate (DHEAs) (*36*). Hormonal changes are also observed in the reproductive system. The circulating concentration of testosterone and its pulsatile release decline with age in male rhesus monkeys (*37*). Rhesus females experience the perimenopausal transition similar to women at similar stages of the life-span, but the age of initiation of endocrine changes varies in both species (*38*, *39*). As the perimenopausal transition progresses in women, gonadotropin levels increase. A simultaneous decrease in ovarian response results in insufficient hypothalamic-mediated stimulation of preovulatory luteinizing hormone release. Ultimately, declining function of the hypothalamic-pituitary-gonadal axis culminates in menopause (*40*). The rhesus monkey is an appropriate model because of similarities in the perimenopausal transition as well as providing essential data on the consequences of perimenopausal hormonal changes on neural systems (*39*). These observations are especially relevant considering the controversy surrounding hormone replacement therapy, and ongoing studies will greatly elucidate clinical applications for women.

Aging in human immune function is believed to manifest itself, at least in part, as an increased susceptibility to infectious and autoimmune disease and cancer. This may be related to age-related changes in cytokine production. Studies in rhesus monkeys have demonstrated age-related increases in interleukin (IL)–6 and IL-10 production and decreased interferon γ (*41*, *42*), similar to reports in humans (*43*).

Pathology

Accompanying the biological changes that parallel aging in humans, these animals develop and die from similar chronic diseases. Although with normal diets rhesus monkeys do not develop severe atherosclerosis, other cardiac pathologies occur, including aortic valve calcification, interstitial fibrosis, hypertrophy of cardiac muscle, myocardial infarction, cardiac arrest, and congestive heart failure (*3*). On high-fat diets, however, rhesus monkeys do develop atherosclerotic plaques (*44*). They also develop cancer, including carcinomas and sarcomas with intestinal adenocarcinomas as the most common malignant neoplasm (*45*). Additionally, endometriosis occurs in females (*46*). Interestingly, although prostate gland hypertrophy occurs in males (*47*), prostate neoplasia is rarely observed (*48*). Rhesus monkeys that are fed normal laboratory diets also develop diabetes, with increased incidence observed on high-fat or high-calorie diets (*3*, *6*). Considered together with altered body composition, reduced bone mineral density, increased serum triglycerides, and increased insulin resistance, rhesus monkeys provide an important new model of the increasingly prevalent "metabolic syndrome" (*49*).

Interventions

Evaluation of treatments designed to retard aging, such as CR, requires a virtual "head-to-toe" approach. Aging processes should be analyzed from molecular to behavioral levels. Table 1 provides a current overview of selected parameters from the NIA and WNPRC rhesus monkey aging studies evaluating the effects of CR. Clearly, findings indicate better health and lower disease risk for CR monkeys compared to controls. However, both studies are still ongoing, and data are still being amassed on CR effects on aging processes, mortality, and morbidity.

The widest application of rhesus monkeys has been to evaluate interventions bearing on brain aging and disease. Rhesus monkeys have shown great utility in evaluating hormone replacement therapies on cognition (*50*). In addition, successful studies of neurotrophic factors, including nerve growth factor and glia-derived neurotrophic factor, to treat AD and Parkinson's disease, respectively, have provided a basis to evaluate these treatments in humans (*51*, *52*). Rhesus monkeys have also been used to investigate gene therapy for neurodegenerative disorders (*53*). As stem cell therapies emerge for age-related brain diseases, rhesus monkeys will serve as a valuable model for evaluating their success, especially in treatment of disorders involving loss of specific neural systems, such as Parkinson's disease. Effective gene transfer into rhesus hematopietic stem cells has already proven successful (*54*). In addition, monkeys have been successfully used in studies to induce breast cancer–specific antibodies (*55*) and prostate-specific antigen immune response (*56*) and to test ovarian cancer chemoprevention (*57*).

Because rhesus monkeys can develop diet-dependent obesity and diabetes, they will also

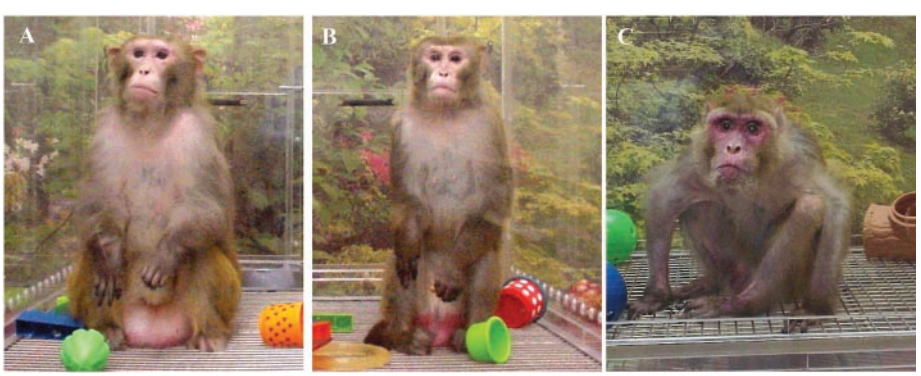

Fig. 1. (**A**) A 19-year-old male rhesus monkey weighing 13.6 kg on the control diet. (**B**) A 19-year-old male rhesus monkey weighing 7.9 kg on CR for 17 years. Notably, the CR monkey generally appears smaller. (**C**) A 38-year-old (estimated age) male rhesus monkey weighing 6.8 kg on CR for 17 years. This monkey is one of three in the NIA study for which the exact birth date was unknown, but he first arrived at NIH in July 1968 with an estimated age of 4 to 8 years on the basis of body size and dentition. He was placed on CR in 1987. He died 18 April 2004 at a minimal estimated age of 40 years, but he could have been as old as 44 years, making him one of the oldest recorded of this species. This monkey had stooped posture, loss of hair, and wrinkled and sagging skin with broken blood vessels, and he exhibited arthritis, osteoporosis, and cataracts.

serve as highly useful models for discovering anti-obesity and antidiabetic treatments. The amino acid sequence of the nuclear receptor, peroxisome proliferator-activated receptor alpha (PPARα), is highly homologous between humans and rhesus monkeys; thus, synthetic compounds, such as the fibrates, that can regulate lipid and lipoprotein metabolism through PPARα receptors have similar effects in both species (*58*). Studies have further shown the potential therapeutic value of antidiabetic and anti-obesity drugs in obese or insulin-resistant rhesus monkeys (*58–60*).

Mechanisms and Markers of Aging

Insight into basic mechanisms responsible for the age-related changes described above can also be obtained. Oxidative stress purported to be a major cause of aging and age-associated diseases is partially ameliorated by CR (*61*). Similarly, other forms of stress, glycation, and biological disordering in general are thought to contribute to aging and are attenuated by CR (*61*). As reviewed above, many age-related changes in humans occur in rhesus monkeys, boding well for the use of these nonhuman primates to devise interventions that delay or reduce dysfunction and pathology and possibly extend the quantity and quality of life.

In this regard, recent interest was focused on three "biomarkers of longevity" apparently common to both CR rhesus monkeys and longer lived human males not practicing CR (*62*). These are lower levels of plasma insulin and body temperature, and maintenance of higher plasma levels of DHEAs. The first two have been demonstrated in CR rodents (*9*) as well as in monkeys, although DHEA (the sulfated form is the major species) levels are too low to evaluate in rodents. Nevertheless, cross-species similarities in CR effects on two markers and changes during normal aging in all three markers further underscore their value for both mechanistic and intervention studies. Most recently, short-term (about 6 months) 25% CR in humans of both sexes has reduced both temperature and insulin levels (*63*).

A fundamental metabolic shift occurs in organisms on CR, from a growth and reproductive strategy to one of a life maintenance strategy. A drop in body temperature is evidence of this shift concomitant to increased protective mechanisms against various insults and pathologies, slower rate of tissue deterioration, and more reserve capacity observed in rodents on CR (*62*). Moreover, loss of insulin sensitivity during aging is probably tissue specific and secondary to changes in insulin signal transduction. Age-related decreases in circulating DHEAs may reflect a loss of adrenal parenchymal cells and/or reduced secretory function of surviving cells, which might affect important feedback mechanisms. This altered hormonal status is relevant for current discussion of the benefits of androgen replacement therapy. Because lower insulin levels and increased insulin sensitivity is protective against diabetes and DHEAs are purported to protect against both cancer and metabolic syndrome (*36*), the relevance of the rhesus model for age-related disease research and possible intervention strategies for eventual human application is obvious.

Table 1. Effects of CR on selected parameters of morphology, physiology, aging, and disease in rhesus monkeys. X indicates whether CR has been shown to decrease, increase, or produce no change in the these parameters.

Category/parameter	Decrease	Increase	No change
Body composition			
Body weight	X		
Fat and lean mass	X		
Trunk: Leg fat ratio	X		
Height	X		
Development			
Time to sexual maturity		X	
Time to skeletal maturity		X	
Metabolism			
Metabolic rate (short term)	X		
Metabolic rate (long term)			X
Metabolic rate (long term:nighttime)	X		
Body temperature	X		
Thriiodothyronine (T3)	X		
Thyroxin (T4)			X
Thyroid-stimulating hormone			X
Leptin	X		
Endocrinology			
Fasting glucose/insulin	X		
IGF-1/growth hormone	X		
Insulin sensitivity		X	
Age-related maintenance of melatonin and DHEAs		X	
Testosterone; estradiol			X
Cardiovascular parameters			
Systolic blood pressure	X		
Heart rate	X		
Serum triglycerides	X		
Serum HDL2B		X	
Low-density lipoprotein interaction with proteoglycans	X		
Lipoprotein (a)	X		
Immunological parameters			
IL-6	X		
IL-10	X		
Interferon-γ		X	
Oxidative stress			
Oxidative damage to skeletal muscle	X		
Cell biology			
Proliferative capacity of fibroblasts		X	
Glycation products	X		
Functional measures			
Locomotor activity			X
Acoustic responses		X	

Conclusions

Thus, we envision even more extensive use of the aging rhesus model in future research. Initial efforts to sequence the rhesus genome have also been initiated that will increase the value of this animal model. To aid in the further development of nonhuman primate models of aging, the NIA and the WNPRC are developing the Primate Aging Database (PAD), which involves a multisite cooperative effort to share and analyze data in multiple species. A preliminary report that uses the PAD has been published demonstrating the utility of cooperative efforts to increase information in this area of research and promote efficient use of nonhuman primate resources (*64*).

References and Notes

1. A list of genes and their aging phenotypes is available at http://sageke.sciencemag.org/cgi/genesdb.
2. R. J. Colman, J. W. Kemnitz, in *Methods in Aging Research*, B. P. Yu, Ed. (CRC Press, Boca Raton, FL, 1999), pp. 249–267.
3. N. L. Bodkin, T. M. Alexander, H. K. Ortmeyer, E. Johnson, B. C. Hansen, *J. Gerontol. Biol. Sci.* **58A**, 212 (2003).
4. More information about maximum human life-span is available at www.grg.org/calment.html.
5. U.S. NIA-supported primate research centers with colonies of aging rhesus monkeys include: Oregon Health Sciences University: http://onprc.ohsu.edu;

Tulane University: www.tpc.tulane.edu; University of California, Davis: www.crprc.ucdavis.edu; University of Washington: http://wanprc.org/WaNPRC; and University of Wisconsin: www.primate.wisc.edu.
6. N. L. Bodkin, *J. Gerontol.* **50A**, B142 (1995).
7. J. J. Ramsey *et al.*, *Exp. Gerontol.* **35**, 1131 (2000).
8. J. A. Mattison, M. A. Lane, G. S. Roth, D. K. Ingram, *Exp. Gerontol.* **38**, 35 (2003).
9. R. Weindruch, R. Walford, *The Retardation of Aging and Disease by Dietary Restriction* (Charles C. Thomas, Springfield, IL, 1988).
10. P. Torre, III, C. G. Fowler, *Hear. Res.* **142**, 131 (2000).
11. P. L. Kaufman, L. Z. Bito, *Exp. Eye Res.* **34**, 287 (1982).
12. T. D. Moscrip, D. K. Ingram, M. A. Lane, G. S. Roth, J. L. Weed, *J. Gerontol. Biol. Sci.* **55**, B373 (2000).
13. Z. Zhang *et al.*, *J. Gerontol.* **55A**, B473 (2000).
14. M. L. Voytko, *Neurobiol. Aging* **20**, 617 (1999).
15. M. A. Lane *et al.*, *Proc. Natl. Acad. Sci. U.S.A.* **93**, 4159 (1996).
16. J. A. Mattison *et al.*, *Neurobiol. Aging*, in press.
17. A. Black *et al.*, *Bone* **28**, 295 (2001).
18. P. A. Kramer, L. L. Newell-Morris, P. A. Simkin, *J. Orthop. Res.* **20**, 399 (2002).
19. S. M. Schwartz, J. W. Kemnitz, *Am. J. Phys. Anthropol.* **89**, 109 (1992).
20. G. S. Roth *et al.*, *J. Gerontol.* **52A**, B98 (1997).
21. D. R. Sell *et al.*, *Proc. Natl. Acad. Sci. U.S.A.* **93**, 485 (1996).
22. J. G. Herndon, J. Tigges, S. A. Klumpp, D. C. Anderson, *Neurobiol. Aging* **19**, 267 (1998).
23. J. A. Matochik *et al.*, *Neurobiol. Aging* **21**, 591 (2000).
24. J. I. Keuker, P. G. Luiten, E. Fuchs, *Neurobiol. Aging* **24**, 157 (2003).
25. H. Duan *et al.*, *Cereb. Cortex* **13**, 950 (2003).
26. S. A. Small, M. K. Chawla, M. Bunocore, P. R. Rapp, C. A. Barnes, *Proc. Natl. Acad. Sci. U.S.A.* **101**, 7181 (2004).
27. E. D. Morris *et al.*, *J. Cereb. Blood Flow Metab.* **19**, 218 (1999).
28. M. L. Voytko *et al.*, *Synapse* **39**, 95 (2001).
29. M. E. Calhoun, Y. Mao, J. A. Roberts, P. R. Rapp, *J. Comp. Neurol.* **475**, 238 (2004).
30. A. Peters, *Prog. Brain Res.* **136**, 455 (2002).
31. D. L. Price *et al.*, *Brain Pathol.* **1**, 287 (1991).
32. S. Sepehr *et al.*, *Acta Neuropathol.* **105**, 145 (2003).
33. H. Uno *et al.*, *Neurobiol. Aging* **17**, 275 (1995).
34. S. B. Dunnett, *Trends Pharmacol. Sci.* **22**, 211 (2001).
35. G. S. Roth, V. Lesnikov, M. Lesnikov, D. K. Ingram, M. A. Lane, *J. Clin. Endo. Metab.* **86**, 3292 (2001).
36. M. A. Lane, D. K. Ingram, S. S. Ball, G. S. Roth, *J. Clin. Endo. Metab.* **82**, 2093 (1997).
37. L. W. Kaler, P. Gleissman, D. L. Hess, J. Hill, *Endocrinology* **119**, 566 (1986).
38. K. V. Gilardi, S. E. Shideler, C. R. Valverde, J. A. Roberts, B. L. Lasley, *Biol. Reprod.* **57**, 335 (1997).
39. F. L. Bellino, P. M. Wise, *Biol. Reprod.* **68**, 10 (2003).
40. P. M. Wise, *Rec. Prog. Horm. Res.* **57**, 235 (2002).
41. P. Mascarucci *et al.*, *Aging Clin. Exp. Res.* **13**, 85 (2001).
42. M. J. Kim *et al.*, *J. Nutr.* **12**, 2293 (1997).
43. L. Rink, I. Cakman, H. Kirchner, *Mech. Ageing Dev.* **102**, 199 (1998).
44. T. B. Clarkson, R. W. Prichard, T. M. Morgan, G. S. Petrick, K. P. Klein, *JAMA* **271**, 317 (1994).
45. C. R. Valverde, R. P. Tarara, S. M. Griffey, J. A. Roberts, *Comp. Med.* **50**, 540 (2000).
46. J. W. Fanton, J. G. Golden, *Radiat. Res.* **126**, 141 (1991).
47. A. Baskerville, R. W. Cook, M. J. Dennis, M. P. Cranage, P. J. Greenaway, *J. Comp. Pathol.* **107**, 49 (1992).
48. G. B. Hubbard, R. L. Eason, D. H. Wood, *Vet. Pathol.* **22**, 88 (1985).
49. S. R. Steinbaum, *Prog. Cardiovasc. Dis.* **46**, 321 (2004).
50. P. R. Rapp, J. H. Morrison, J. A. Roberts, *J. Neurosci.* **23**, 5708 (2003).
51. R. Grondin *et al.*, *Brain* **125**, 2191 (2002).
52. D. E. Smith, J. Roberts, F. H. Gage, M. H. Tuszynski, *Proc. Natl. Acad. Sci. U.S.A.* **96**, 10893 (1999).
53. J. H. Kordower, *Ann. Neurol.* **53**, S120 (2003).
54. C. E. Dunbar, *J. Intern. Med.* **249**, 329 (2001).
55. M. Chakraborty *et al.*, *Cancer Res.* **55**, 1525 (1995).
56. J. J. Kim, J. S. Yang, K. Dang, K. H. Manson, D. B. Weiner, *Clin. Cancer Res.* **7**, 882s (2001).
57. M. Brewer *et al.*, *Comp. Med.* **51**, 424 (2001).
58. D. A. Winegar *et al.*, *J. Lipid Res.* **42**, 1453 (2001).
59. N. L. Bodkin, J. Pill, K. Meyer, B. C. Hansen, *Horm. Metab. Res.* **35**, 617 (2003).
60. W. R. Oliver, Jr. *et al.*, *Proc. Natl. Acad. Sci. U.S.A.* **98**, 5306 (2001).
61. G. S. Roth, D. K. Ingram, M. A. Lane, *Nature Med.* **1**, 414 (1995).
62. G. S. Roth *et al.*, *Science* **297**, 811 (2002).
63. L. Heilbronn, paper presented at the 33rd Annual Meeting of the American Aging Association, St. Petersburg, FL, 4 to 7 June 2004.
64. D. A. Smucny *et al.*, *J. Med. Primatol.* **33**, 48 (2004).
65. We thank the staff of the Primate Unit, Poolesville, MD, especially E. Tilmont, A. Hobbs, J. Young, T. Thompson, K. Reinsfelder, A. Cisar, M. Clark, B. White, as well as the veterinary staff of D. Powell and R. Herbert. We also acknowledge the contributions of our international collaborators too numerous to list here.

REVIEW

What Can Progeroid Syndromes Tell Us About Human Aging?

David Kipling,[1] Terence Davis,[1] Elizabeth L. Ostler,[2] Richard G. A. Faragher[2]*

Human genetic diseases that resemble accelerated aging provide useful models for gerontologists. They combine known single-gene mutations with deficits in selected tissues that are reminiscent of changes seen during normal aging. Here, we describe recent progress toward linking molecular and cellular changes with the phenotype seen in two of these disorders. One in particular, Werner syndrome, provides evidence to support the hypothesis that the senescence of somatic cells may be a causal agent of normal aging.

Aging is the universal, progressive, and intrinsic accumulation of deleterious changes. These compromise the physiological effectiveness of an organism, ultimately leading to death (*1*). Many have argued that the way to understand the aging process is to manipulate it (*2*). Today, our technological ability to take this approach is changing the study of the biology of aging from a field concerned primarily with description to one that is increasingly marked by intervention.

Strengths and Weaknesses of a Model System Approach to Human Aging

Various single-gene mutations increase the life-span of model species, including *Drosophila melanogaster*, *Caenorhabditis elegans*, and *Mus musculus* (*3*–*5*). These organisms offer obvious benefits as models for human aging, combining sequenced genomes with simple growth conditions and relatively short life-spans. Historically, this model system approach has met with great success in biology, partly because many of the processes under study (e.g., DNA replication) are highly conserved. The molecular machinery required to carry out such processes is also conserved, and thus meaningful cross-species insights are regularly obtained. However, an important philosophical question is to what extent this model system approach can be used to understand human aging. Aging may be a rather atypical biological process, because no genes appear to have evolved specifically to cause it (*6*, *7*). Indeed, because age-related changes are the unprogrammed results of stringent selection for early reproductive success, aging may be an example of a biological phenomenon in which there is a low level of mechanistic conservation between diverse metazoans.

One might reasonably expect closely related species to share some aging pathologies, reflecting similar solutions to the same evolutionary pressures; however, there is no a priori reason why the mechanisms that produce degenerative pathology should be uniform across all metazoan species. The lack of obvious selective pressure to evolve common aging mechanisms makes it all the more remarkable that common pathways controlling life-span may exist, as suggested by the re-

[1]Department of Pathology, School of Medicine, Cardiff University, Heath Park, Cardiff CF14 4XN, UK. [2]School of Pharmacy and Biomolecular Sciences, University of Brighton, Cockcroft Building, Brighton BN2 4GJ, UK.

*To whom correspondence should be addressed. E-mail: rgaf@brighton.ac.uk

cent identification of a series of mutations in genes that both affect the insulin and insulin-like growth factor (IGF) axis and lengthen life-span in a range of metazoan species (*3*–*5*). Work on this pathway in model systems as diverse as *C. elegans*, *D. melanogaster*, and mice could provide significant insights into human aging.

Despite these successes, an important caveat remains that the primary driver of aging can be quite diverse among metazoans. Thus, although the relevance of data obtained with the use of any particular nonhuman model systems to human aging could be immediate and profound, it could equally be very limited. An extreme example is seen in *D. melanogaster* females, where a major cause of aging and death is the toxic effect of compounds present in the seminal fluid products secreted from the male fruit fly accessory gland (*8*); seminal fluid toxicity is not considered a primary cause of mammalian aging. Similarly, human aging mechanisms do not necessarily have counterparts in every metazoan; replicative senescence (the loss of divisional capacity in the mitotic tissue compartments of the soma) is not a potential aging mechanism for organisms whose soma are completely postmitotic, such as *C. elegans* (*9*, *10*). In general, widespread aging mechanisms are not necessarily primary in every species, nor are mechanisms that are primary in one particular species necessarily widespread among others (Table 1).

Progeroid Syndromes as a Model System to Investigate Human Aging

The alternative to a model system is to study human aging directly. This would certainly ensure that any observations made are relevant to humans but brings with it many practical problems, including the highly polygenic nature of many of the pathologies of interest (*11*) and the confounding effect of outbred populations of individuals living in diverse environments. As with the analysis of polygenic diseases, a powerful approach to providing an experimentally tractable system is to study human genetic diseases whose phenotypes mimic at least some of the features of the aging process (*11*, *12*). The data obtained provide a complement to studies using nonhuman model systems.

Such progeroid (meaning premature aging–like) syndromes are usually monogenic and thus sufficiently simple to provide clear insights into the causes of their pathology. Their chief disadvantage is that they are, at best, phenocopies of normal aging rather than the genuine article. At worst, they may be misleading blind alleys, capable of informing only on themselves (*13*). Thus, any observations made with them must take place within the context of theories designed to explain how normal aging operates. As shown in Table 2, the progeroid features seen in several such syndromes may result from the acceleration of mechanisms postulated to play causal roles in normal aging. This suggests that the study of such disorders may shed light on the contribution that a given mechanism may make to the normal situation.

Although progeroid syndromes are often criticized for being only partial phenocopies of normal aging, this very selectivity, in which some tissues and not others are affected, provides for the experimental tractability that is the justification for use of a model system. Equally important, focused research on the diseases themselves can promote the formulation of extremely precise mechanistic hypotheses that are amenable to clear refutation and are thus extremely powerful in Popperian terms (*14*). This can best be illustrated by recent work on Werner syndrome.

Werner Syndrome

Werner syndrome (WS) is an autosomal recessive genetic disorder characterized by a shorter than normal stature (as a result of the failure of the teenage growth burst) together with the accelerated development of atherosclerosis, arteriosclerosis, graying of the hair, type II diabetes, cataracts, osteoporosis, and thymic atrophy (*15*, *16*). The clinical picture of WS is, however, more complex than a simple global acceleration of age-linked pathology. WS patients also show symptoms that are characteristic of aged individuals but manifest themselves much more severely. These include calcification of the cardiac valves and atrophy of the testicles and skin appendages. However, WS patients appear to have essentially normal immune function and lack notable pathology of the central nervous system. They also display a somewhat elevated cancer frequency, although this is largely restricted to mesenchymal neoplasms. Their limbs show poor muscular development, and ulcerative lesions often develop over pressure points. Death occurs at an average age of 47, usually as a result of cancer or arteriosclerosis.

WS is caused by a variety of loss-of-function mutations in a gene coding for a member of the RecQ helicase family (WRN) (*16*, *17*). The WRN helicase has been shown to interact with a wide variety of proteins, suggesting roles in DNA replication, recombination, and apoptosis (*18*, *19*). However, a major function appears to be the reinitiation of stalled replication forks (*20*). In the absence of WRN, such stalled forks either resolve by a complicated process of recombination and deletion events or cause the cell to arrest in the S phase of the cell cycle. This inability to reinitiate stalled replication forks produces sensitivity to a limited range of DNA-damaging agents coupled with a significantly elevated frequency of deletional mutations in vitro (mutator phenotype) (*19*, *21*). In human fibroblasts, loss of WRN also produces an extremely limited capacity to proliferate: 90% of WS fibroblast cultures have an in vitro life-span of less than 20 population doublings (compared to a normal range of 40 to 100 population doublings) (*22*, *23*). This limited replicative capacity correlates with a much faster rate of decline in the mitotic fraction per population doubling of WS fibroblasts as compared to normal controls (*24*, *25*).

Why Do WS Patients Look the Way They Do?

Although loss of WRN clearly produces profound physiological disturbance at both the cellular and organismal levels, what does this tell us about aging? Three possibilities suggest themselves. First, WS may tell us nothing about aging at all. Alternatively, because a relation has often been postulated between the maintenance of genomic integrity and organismal life-span, the key feature causing the pathology of WS may be the mutator phenotype. Thus, WS may be a demonstration that physiological effects reminiscent of aging can indeed result from poor genome maintenance and thus inform on the relationship between normal aging and aberrant DNA metabolism (*26*). Lastly, because a causal role for replicative senescence has also frequently been postulated in organismal aging, perhaps the premature replicative senescence seen in some WS cell types is the causal mechanism for much of the observed pathology. In this case, WS might provide evidence consistent with a causal role for senescent cells in the pathology of aging bodies, a concept often proposed but seldom shown (*27*, *28*). Such considerations make it possible to formulate tests that could exclude potential mech-

Table 1. Selected mechanisms that are proposed to operate across multiple species ("universal") compared to those that either show or are proposed to show genus- or species-specific action.

Universal aging mechanisms	Species-specific aging mechanisms
Oxidative damage	Toxic effect of male sperm (*D. melanogaster*)
Formation of advanced glycation end-products	Extreme cuticle thickness (*C. elegans*)
Alterations in the insulin-IGF axis	Extrachromosomal ribosomal DNA circles (*S. cerevisiae*)
Alterations in energy balance	Replicative senescence

anisms as contributing to the accelerated aging in WS and, by extension, normal aging.

The premature aging seen in WS shows a very pronounced tissue specificity, and this feature has allowed investigators to distinguish between these alternate hypotheses. Consider the observation that the dermal layer of the skin shows severe pathology in WS, whereas the immune system appears clinically unaffected (*29*, *30*). When studied in vitro, cultured WS fibroblasts display both the premature replicative senescence and mutator phenotypes. In contrast, T cells derived from WS patients display no life-span deficit compared with normal controls (*31*), whereas they show evidence of the mutator phenotype in vivo and display an elevated mutation (and deletion) rate at the hypoxanthine-guanine phosphoribosyltransferase locus when placed under 6-thioguanine selection in vitro (*32*). This observable mutator phenotype in cells from both clinically affected tissues (dermal fibroblasts) and those which are apparently normal (T cells) is not consistent with the hypothesis that simple genomic instability per se is the primary driver of mitotic tissue aging in WS. Such relatively simple experiments demonstrate the potential power of studying such progeroid syndromes.

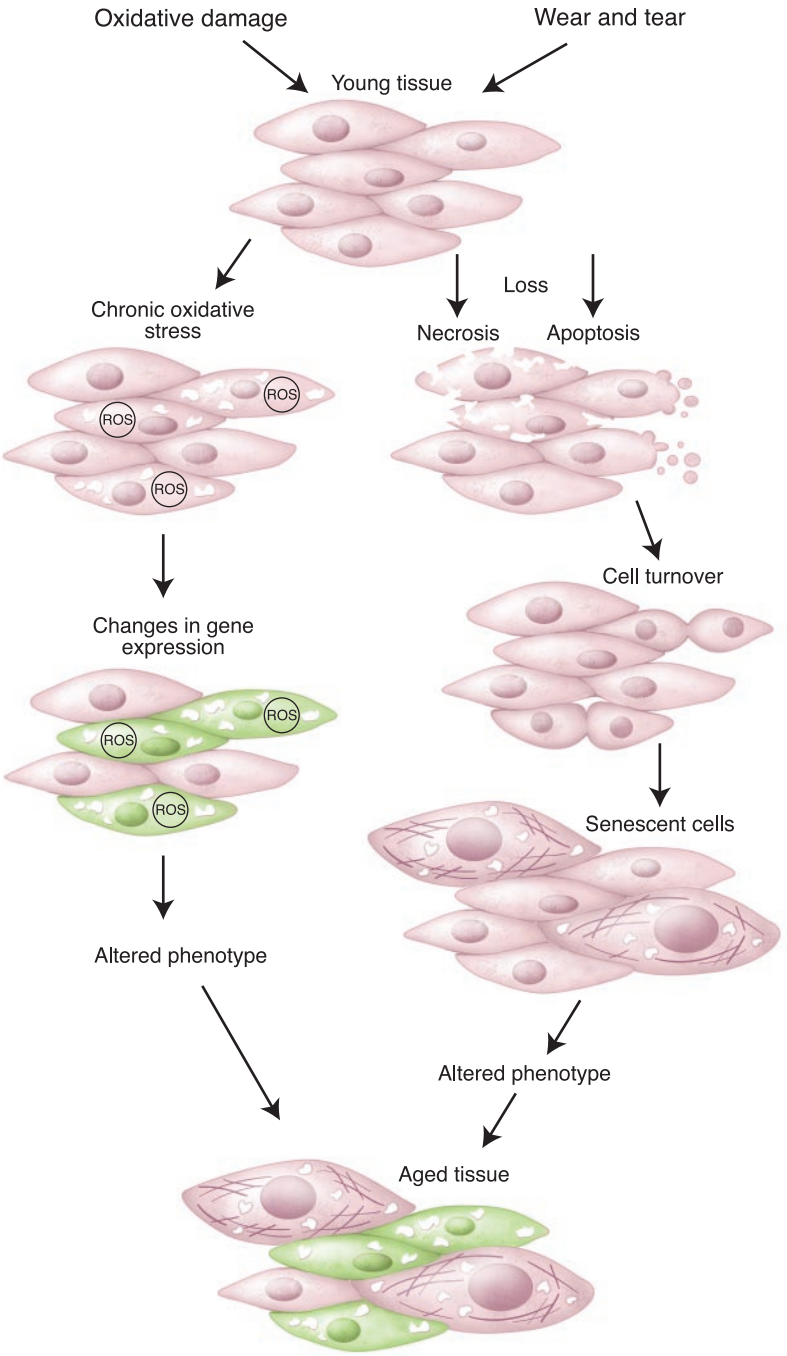

Fig. 1. Comparison of the replicative senescence hypothesis of aging (**right**) with the dysdifferentiation hypothesis of aging (**left**). The cell senescence hypothesis proposes that routine cell loss is balanced by cell division. One or more "replicometers" act to trigger senescence (see text), which is associated with a broad alteration in gene expression. This produces an altered phenotype that affects the microenvironment in which the cell resides and ultimately the entire tissue. In the dysdifferentiation model, chronic oxidative stress leads to a regearing of gene expression, generating an altered cellular phenotype, which contributes to tissue ageing. The two models have many essential similarities.

If the presence of senescent cells contributes to the premature aging seen in WS, a key question is how loss-of-function mutations in a RecQ helicase in all the cells in a body results in tissue-specific premature replicative senescence. One potential (and trivial) answer would be the tissue-specific expression of WRN itself. However, WRN is a ubiquitously expressed protein (*17*), and thus we must look elsewhere for a potential answer to the tissue-specific response to the *wrn* mutation. Answering this question requires some explanation of how senescent cells arise and how they are proposed to exert their "aging" effects.

Replicative senescence is a block to the further replication of mitotic cells, mediated by cyclin-dependent kinase inhibitors, that leads to a viable state of indefinite cell cycle arrest (*10*). A finite replicative capacity has been reported in many different cell types from many different species (*33*). In human cells, senescence can be triggered, at least in vitro, by several mechanisms. Classic experiments in the late 1990s demonstrated that the senescence of human fibroblasts (and many other human cell types) is telomere-driven. This involves progressive telomeric attrition by repeated rounds of cell cycle transit in the absence of sufficient quantities of the telomere maintenance enzyme telomerase (*34*, *35*). This telomere erosion in turn signals via a pathway involving p53 and $p21^{waf}$ that appears very similar to the pathway that senses and signals DNA damage, resulting in permanent arrest at the G_1-S phase transition (*36*, *37*). Several mechanisms can potentially cause telomeric erosion, including end replication losses, replication slippage, C-strand processing events, and terminal sequence loss as a consequence of oxidative damage (*38*, *39*). Whatever the cause of telomere shortening, forced expression of telomerase prevents senescence in multiple human cell types (*34*).

However, considerable evidence also exists that prevention of telomeric attrition does not always bypass senescence. In some human cell types, including thyroid

follicular epithelial cells, pancreatic islet β cells, and astrocytes, ectopic expression of telomerase alone is insufficient for immortalization (*40*–*44*). Although the pathways involved in triggering senescence in these examples are less well characterized, they often involve hypophosphorylation of the retinoblastoma protein (pRB), probably as a consequence of overexpression of $p16^{INK4A}$, a cyclin-dependent kinase (CDK) 4 and CDK 6 inhibitor. Because $p16^{INK4A}$ expression can be up-regulated by a wide variety of environmental stimuli, it is plausible (although as yet unproven) that at least some cell types become senescent in vivo as a result of the activation of this pathway (*45*). From an aging perspective, however, the most important issue is that, regardless of the nature of the signaling mechanism that causes a cell to enter the senescent state, senescent cells inevitably display broad alterations in their patterns of gene expression (*46*). This produces a wide range of phenotypic changes at the cellular level compared to their growing counterparts (Fig. 1), which, in turn, have been suggested to underpin age-related pathologies in tissues as diverse as skin and vasculature (*47*).

Several studies have shown that WS fibroblasts readily immortalize after the forced expression of telomerase (*48*). This is consistent with use of telomeric attrition to monitor divisional history. Follow-up studies have also shown that, like normal fibroblasts, establishment of the senescent state in WS cells requires the activity of p53 (*49*). Lastly, similar transcriptional changes after senescence have been observed in normal and WS fibroblasts (*50*, *51*). Indeed, the only significant difference that has emerged is the greatly accelerated rate of senescence in WS fibroblasts as compared to normal controls (Fig. 2).

Several possibilities exist for why *wrn* mutations produce a context-specific effect on replicative senescence. The amount of endogenous telomerase activity differs between cell types. In many cells, extremely low amounts of telomerase activity are present (*52*). In others, such as T cells, there are substantial amounts initially (*53*) that decline with sustained cell division, coincident with the onset of replicative senescence. Because *wrn* has been implicated in telomere metabolism, one could envision scenarios in which cells with very little telomerase activity would be more sensitive to the effects of loss of WRN. One might reasonably postulate that postmitotic and telomerase-positive cell types should be protected from WRN-induced pathology, whereas tissues with low amounts of telomerase that show a significant degree of cell turnover should show functional deficits (*54*). Somewhat more subtle variations on this idea also exist (*28*, *55*).

Alternatively, WRN may primarily affect processes that are unrelated to telomere metabolism but that can cooperate with short telomeres to drive cells into senescence. If a significant fraction of WS cells were to exit the mitotic pool in such a telomere-independent manner, this could accelerate telomere-dependent senescence because of the additional turnover required from the remaining cells still capable of division. A recent study concluded that the accelerated senescence of WS fibroblasts in culture was more consistent with such a synergy between standard telomere-driven senescence and a second, as-yet-unknown telomere-independent mechanism than with a simple acceleration of telomere shortening (*56*). Several telomere-independent routes to senescence have been shown to exist in normal human fibroblasts, most of which have the potential to cooperate with telomere shortening to produce additional

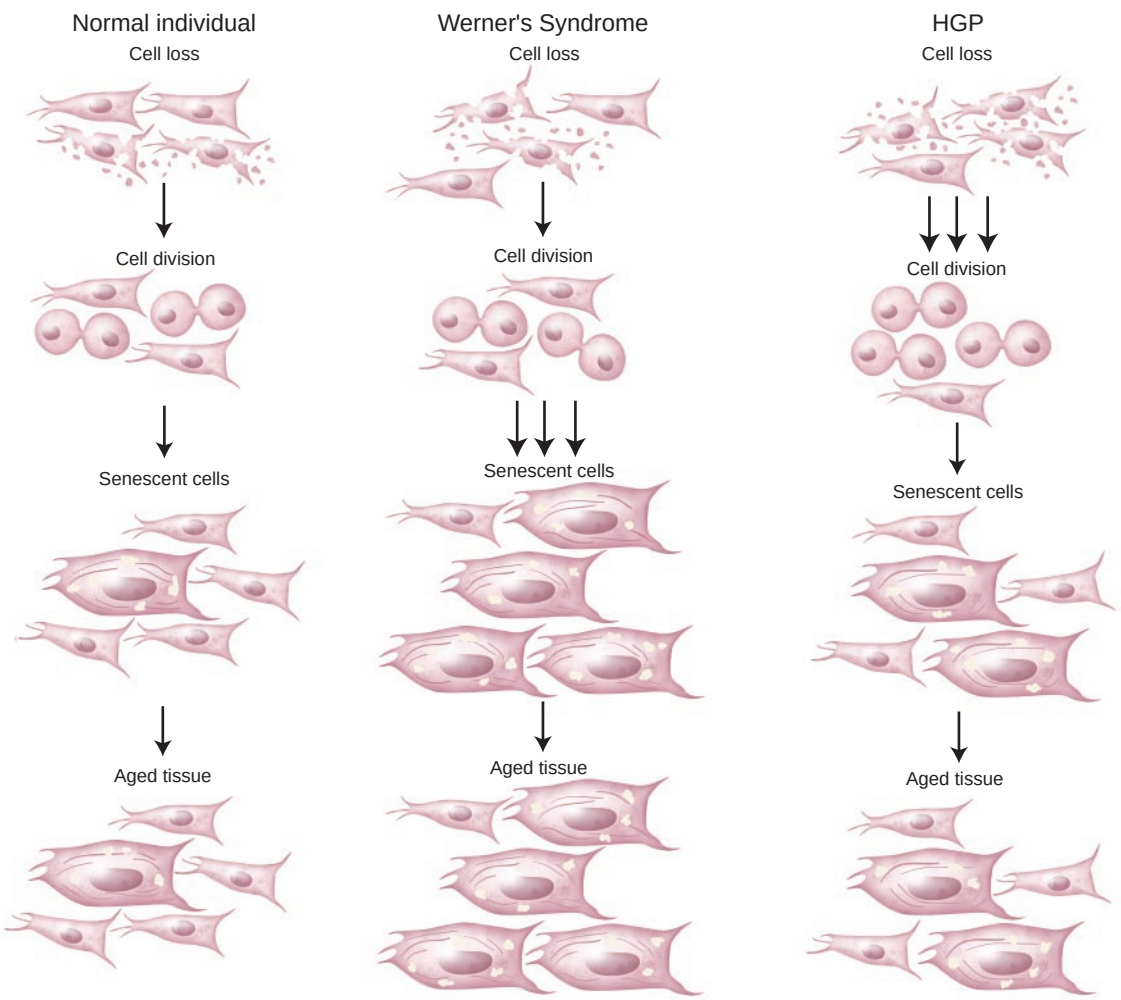

Fig. 2. Comparison of the causal pathology seen in normal, WS, and HGP individuals. Normally, cell loss within a tissue is balanced by cell division. This produces senescent cells that contribute to mitotic tissue aging through their altered phenotype. In individuals with WS, normal rates of cell loss produce an accelerated buildup of senescent cells and hence accelerated aging of some tissues. In contrast, in HGP, rates of cell loss by apoptosis are elevated, producing increased cell turnover (and hence elevated numbers of senescent cells).

Table 2. Genetic syndromes considered high ranking candidates for segmental progeroid syndromes (*67*). Ranking has its basis in (*12*). These disorders also show significant differences from normal aging.

Syndrome	Inheritance	Mean life-span (years)	Progeroid features	Causal mutation	Potential mechanistic relevance to normal aging
Down	De novo trisomy	~60	Cataracts, graying of hair, alopecia, diminished subcutaneous fat, thyroid dysfunction, neurodegeneration	Unknown	?
Werner	Autosomal recessive	~47	Cataracts, osteoporosis, arteriosclerosis, atherosclerosis, diabetes, malignancies	Loss of function mutations in WRN (RECQL2)	Acceleration of replicative senescence
Cockayne	Autosomal recessive	~20	Deafness, retinal degeneration, atherosclerosis, demyelination	Loss of function mutations in CS-A (ERCC8) and CS-B (ERCC6)	Decreased genome maintenance?
Hutchinson-Gilford	Dominant negative	~12	Atherosclerosis, sarcopenia, osteolysis, diminished adipose tissue	Dominant negative form of lamin A (LMNA)	Decreased ability to maintain cells?
Ataxia telangiectasia	Autosomal recessive	~20	Dermal sclerosis, immunodeficiency, malignancies, greying of hair, cerebellar ataxia	Loss of function mutation in ATM (phosphatidylinositol 3-kinase)	(i) Decreased genome maintenance (ii) Accelerated neurodegeneration? (iii) Reduced immune diversity?
Berardinelli-Seip syndrome (congenital generalized lipodystrophy type 1 and 2)	Autosomal recessive	~40	Absence of adipose tissue, severe insulin resistance, diabetes mellitus, cardiomyopathy, hypertension, vascular disease	Loss of function mutations in AGPAT2 (encoding 1-acylglycerol-3-phosphate O-acyltransferase) or BSCL2 (encoding seipin)	Altered insulin signalling? Decreased membrane integrity? Increased glycation damage?

senescent cells within a population (*57*). One likely candidate is a stress signal from the stalled replication forks (*58*) that occur as a consequence of the absence of WRN (*20*).

Why Don't *wrn*$^{-/-}$ Mice Always Look Like WS Humans?

The most striking example of how the response to the WRN mutation can be context-dependent comes from recent work on WRN-deficient mice. Analyses of the phenotypes of mice deficient for WRN showed little by way of any obvious premature aging phenotype (*59*). This was despite the fact that most of the cellular phenotypes of human WS were successfully recapitulated, including a mutator phenotype and increased sensitivity to the effects of selected DNA-damaging agents. This suggested that the genomic instability caused by loss of WRN was not, in itself, sufficient to produce premature aging in mice. However, differences in replicative life-span between wild-type and *wrn*$^{-/-}$ mouse fibroblasts were slight, suggesting that the premature replicative senescence seen in human WS was not successfully recapitulated. Obvious explanations for this difference between the two species are the differences between their telomere lengths, telomerase expression patterns, and mechanisms of replicative senescence (*60*). Normal rodent fibroblasts do not show telomere-driven senescence. However, something closely akin to it can be produced in fibroblasts from late-generation telomerase-null (*terc*$^{-/-}$) mice (*61*). To this end, Chang and colleagues recently crossed the *wrn*$^{-/-}$ mutation onto a *terc*$^{-/-}$ background and then bred the compound mutants for several generations in the telomerase-null state (*62*). Successive generations thus started life with progressively shorter telomeres, effectively humanizing telomere length in the mouse. Late-generation double-mutant mice developed age-dependent pathologies that appear to closely parallel those seen in WS humans. These included gray hair, osteoporosis, type II diabetes, cataracts, an elevated frequency of nonepithelial malignancies, and premature death. At a cellular level, mouse *wrn*$^{-/-}$ *terc*$^{-/-}$ fibroblasts showed accelerated replicative senescence in vitro and the presence of markers characteristic of telomere-driven senescence in human cells. It seems that loss of WRN can produce the same phenotype in mice and humans only if the mouse cells have first been humanized to an extent, with regard to telomere biology, to show something very close to telomere-dependent senescence.

Conclusion: Does WS Provide Unique Insights?

The evidence from WS humans and WRN$^{-/-}$ rodents is sufficiently coherent for us to propose a working model for why the clinical appearance of WS patients resembles that seen in normal human aging (Figs. 1 and 2). It is important to bear in mind that WS is a naturally occurring human genetic disease and not a form of designer aging. Thus, it is to be expected that some aspects of the disorder differ significantly from the normal process of aging. One of the challenges of work on WS has been to determine which (if any) aspects of the pathology are relevant to aging. At this time, the data argue for the premature replicative senescence of WS cells being causal in those aspects of the pathology that resemble premature aging. WS phenotypes that are not seen in normal aging, such as the elevated mesenchymal tumor frequency, probably do result from genomic instability.

Although the insights it has provided have been particularly clear, WS is not unique in its capacity to inform on human aging. Hutchinson-Gilford progeria (HGP) is another progeroid syndrome that shows distinct tissue-specific features. The cause of HGP proved elusive for many years but was recently shown to be dominant negative mutations in lamin A/C (*63*). HGP fibroblasts

show disruptions in the nuclear lamina that worsen with ongoing cell division. It is likely that this in turn disrupts the various processes that require an intact lamina, such as transcription, DNA replication, and the organization of higher order chromatin structure. Perhaps as a direct result, some HGP fibroblasts appear refractive to telomerase-mediated immortalization (*64*), and most cultures show elevated apoptosis (*65*). Although our understanding of the mechanistic basis of HGP is limited, one possibility is that some features of HGP result from deficits in cell turnover and accelerated senescence. It seems unlikely that the mechanism driving the tissue pathology is an enhanced rate of generation of senescent cells in the context of normal rates of cell loss (as seen in WS), although it cannot be excluded that the elevated rates of apoptosis in HGP cells drive an increased rate of production of senescent cells because of the resultant increased rate of cell turnover (Fig. 2). The availability of a transgenic mouse that recapitulates many of the features of human HGP (*66*) should allow this and other hypotheses to be tested and the causes of the tissue specificity seen in HGP to be understood in greater detail.

In summary, progeroid syndromes have the potential to be informative models of the normal human aging process. WS in particular provides evidence that supports a causal role for replicative senescence in normal human aging. It also gives an answer, albeit crude, to a problem that remains unsolved for replicative senescence and for all other mechanisms proposed to cause tissue aging: Currently, no clear idea exists of the precise number of senescent cells (or aberrant mitochondria or oxidized proteins) that are required to induce the subtle physiological deficits seen in aging tissue. Although we do not know yet how many "criminals" make a crime wave, the data are consistent with a reduction of the overall fibroblast divisional capacity within the dermal layer of a human to 20 population doublings or less being sufficient to yield the accelerated aging seen in the skin of a WS patient. Similar insights from the other progeroid syndromes are awaited.

References and Notes

1. B. L. Strehler, *Time, Cells and Aging* (Academic Press, New York, 1962).
2. I. Davis, *Ageing*, vol. 151 of *Studies in Biology* (Edward Arnold, London, 1983).
3. A. L. Hsu, C. T. Murphy, C. Kenyon, *Science* **300**, 1142 (2003).
4. D. J. Clancy, D. Gems, E. Jafen, S. J. Leevers, L. Partridge, *Science* **296**, 319 (2002).
5. C. S. Carter *et al.*, *J. Gerontol. A Biol. Sci. Med. Sci.* **57**, B177 (2002).
6. L. Partridge, D. Gems, *Curr. Biol.* **12**, R544 (2002).
7. T. B. L. Kirkwood, *Bioessays* **18**, 1009 (1996).
8. T. Chapman *et al.*, *Nature* **373**, 241 (1995).
9. L. A. Herndon, *Nature* **419**, 808 (2002).
10. R. G. A. Faragher, in *Aging of Organs and Systems* (Kluwer, Dordrecht, Netherlands, 2003), pp. 1–28.
11. G. M. Martin, *Adv. Exp. Med. Biol.* **190**, 161 (1985).
12. G. M. Martin, in *Birth Defects: Original Article Series* (National Foundation, New York, 1978), vol. 14, pp. 5–39.
13. R. A. Miller, *Aging Cell* **3**, 47 (2004).
14. K. Popper, *Conjectures and Refutations: The Growth of Scientific Knowledge* (Routledge Classics Series, London, 2002).
15. D. Kipling, R. G. A. Faragher, *Mol. Pathol.* **50**, 234 (1997).
16. C. J. Epstein *et al.*, *Medicine* **45**, 177 (1966).
17. C.-E. Yu *et al.*, *Science* **272**, 258 (1996).
18. H. Yan *et al.*, *Nat. Genet.* **19**, 375 (1998).
19. J. Shen, L. A. Loeb, *Mech. Ageing Dev.* **122**, 921 (2001).
20. A. M. Rodríguez-López *et al.*, *Aging Cell* **1**, 30 (2002).
21. K. Fukuchi *et al.*, *Proc. Natl. Acad. Sci. U.S.A.* **86**, 5893 (1989).
22. T. O. Tollefsbol, H. J. Cohen, *Age* (*Omaha*) **7**, 75 (1984).
23. D. Salk *et al.*, *Hum. Genet.* **58**, 310 (1981).
24. R. G. A. Faragher *et al.*, *Proc. Natl. Acad. Sci. U.S.A.* **90**, 12030 (1993).
25. I. R. Kill *et al.*, *J. Cell Sci.* **107**, 571 (1994).
26. P. Hasty, J. Campisi, J. Hoeijmakers, H. van Steeg, J. Vijg, *Science* **299**, 1355 (2003).
27. W. D. Funk *et al.*, *Exp. Cell Res.* **258**, 270 (2000).
28. J. Bird *et al.*, *Exp. Gerontol.* **38**, 1396 (2003).
29. M. Goto *et al.*, *Adv. Exp. Med. Biol.* **190**, 263 (1985).
30. R. A. Miller, *Biochem. Soc. Trans.* **28**, 241 (2000).
31. S. E. James *et al.*, *Mech. Ageing Dev.* **121**, 139 (2000).
32. K. Fukuchi *et al.*, *Hum. Genet.* **84**, 249 (1990).
33. D. Rohme, *Proc. Natl. Acad. Sci. U.S.A.* **78**, 5009 (1981).
34. A. G. Bodnar *et al.*, *Science* **279**, 349 (1998).
35. E. Chang, C. Harley, *Proc. Natl. Acad. Sci. U.S.A.* **92**, 11190 (1995).
36. F. d'Adda di Fagagna *et al.*, *Nature* **426**, 194 (2003).
37. V. Gire, D. Wynford-Thomas, *Mol. Cell. Biol.* **18**, 1611 (1998).
38. T. von Zglinicki, *Exp. Gerontol.* **38**, 1259 (2003).
39. K. E. Huffman *et al.*, *J. Biol. Chem.* **275**, 19719 (2000).
40. J. G. Rheinwald *et al.*, *Mol. Cell. Biol.* **22**, 5157 (2002).
41. T. Kiyono *et al.*, *Nature* **396**, 84 (1998).
42. C. J. Jones *et al.*, *Mol. Cell. Biol.* **20**, 5690 (2000).
43. R. J. Evans *et al.*, *Cancer Res.* **63**, 4854 (2003).
44. T. L. Halvorsen *et al.*, *J. Endocrinol.* **166**, 103 (2000).
45. J. Bond *et al.*, *Exp. Cell Res.* **292**, 151 (2004).
46. D. N. Shelton *et al.*, *Curr. Biol.* **9**, 939 (1999).
47. T. Minamino *et al.*, *J. Mol. Cell. Cardiol.* **36**, 175 (2004).
48. F. S. Wyllie *et al.*, *Nat. Genet.* **24**, 16 (2000).
49. T. Davis *et al.*, *J. Cell Sci.* **116**, 1349 (2003).
50. K. J. Kyng *et al.*, *Proc. Natl. Acad. Sci. U.S.A.* **100**, 12259 (2003).
51. B. Lecka-Czernik *et al.*, *Exp. Gerontol.* **31**, 159 (1996).
52. K. Masutomi *et al.*, *Cell* **114**, 241 (2003).
53. A. G. Bodnar *et al.*, *Exp. Cell Res.* **228**, 58 (1996).
54. F. B. Johnson, *EMBO J.* **20**, 905 (2001).
55. E. L. Ostler *et al.*, *Exp. Gerontol.* **37**, 285 (2002).
56. D. M. Baird *et al.*, *Hum. Mol. Genet.* **13**, 1515 (2004).
57. J. W. Shay, I. B. Roninson, *Oncogene* **23**, 2919 (2004).
58. P. Pichierri, A. Franchitto, *Bioessays* **26**, 306 (2004).
59. M. Lebel, P. Leder, *Proc. Natl. Acad. Sci. U.S.A.* **95**, 13097 (1998).
60. J. W. Shay, W. E. Wright, *Science* **291**, 839 (2001); published online 18 January 2001; 10.1126/science.1058546.
61. S. Espejel, M. A. Blasco, *Exp. Cell Res.* **276**, 242 (2002).
62. S. Chang *et al.*, *Nat. Genet.* **36**, 877 (2004).
63. R. D. Goldman *et al.*, *Proc. Natl. Acad. Sci. U.S.A.* **101**, 8963 (2004).
64. C. V. Wallis et al., *Exp. Gerontol.* **39**, 461 (2004).
65. J. M. Bridger, I. R. Kill, *Exp. Gerontol.* **39**, 717 (2004).
66. L. C. Mounkes *et al.*, *Nature* **423**, 298 (2003).
67. More detailed descriptions can be found at Online Mendelian Inheritance in Man, www.ncbi.nlm.nih.gov/entrez/query.fcgi?db=OMIM.

68. Supported by the UK Biotechnology and Biological Sciences Research Council (BBSRC) Science of Ageing (SAGE) and Experiment Research on Ageing (ERA) special initiatives.

Evolution of Coral Pigments Recreated

Juan A. Ugalde,[1,3] Belinda S. W. Chang,[4] Mikhail V. Matz[1,2]*

In proteins homologous to the green fluorescent protein from *Aequorea victoria* (GFP), green and cyan emission colors require two consecutive autocatalytic reactions to complete chromophore synthesis. Red fluorescent proteins and purple-blue chromoproteins require a third reaction, thereby manifesting a higher level of functional complexity (*1*). Multiple events of red/green color diversification within the GFP superfamily (*2*) may therefore reflect convergent evolution of molecular complexity.

To examine this issue, we studied one of these events, that which gave rise to the color diversity exhibited by the great star coral *Montastraea cavernosa.* This coral possesses several genes coding for fluorescent GFP-like proteins of cyan, shortwave green, longwave green, and red emission colors (*3*) (Fig. 1C). We statistically inferred and synthesized the ancestral genes corresponding to the common ancestor of all *M. cavernosa* colors ("ALL ancestor"), the common ancestor of red proteins ("Red ancestor"), and two intermediate nodes corresponding to the possible common ancestors of red and longwave green proteins ("Red/Green ancestor" and "pre-Red ancestor") (Fig. 1B). Bacteria were transformed with plasmids carrying the ancestral genes, and the color of the expressed proteins was evaluated spectroscopically (Fig. 1A). Green color at any of the ancestral nodes would indicate that red proteins from other parts of the phylogeny [such as dendRFP (Fig. 1B)] were the result of convergent evolution, whereas if red only arose once, then all ancestors would be red.

Statistical inference of the ancestral sequences was performed with the data set described elsewhere (*2*, *3*) under three models of evolution based on different types of sequence information: amino acids, codons, and nucleotides (*4*). The reconstructions of all four ancestral sequences were robust under these models, with average posterior probabilities at a site ranging from 0.96 to 0.99. Still, the models were in disagreement at several sites (between 4 and 8 out of a total of 217). When planning ancestral gene synthesis, we designed the codons corresponding to these sites to be degenerate in order to incorporate alternative predictions.

For each type of the ancestral gene, the protein products displayed identical fluorescent phenotypes, even though the gene sequences were different at the degenerate sites. The ALL ancestor turned out to be shortwave green. The two possible common ancestors of red and green proteins (Red/Green and pre-Red) showed an intermediate longwave green/red phenotype: Although the main bulk of the protein remained longwave green, a small fraction was able to complete the third chromophore synthesis reaction, resulting in a minor peak of red emission. Clones of the Red ancestor showed an "imperfect red" phenotype: Although the red emission peak dominated, the rate of green to red conversion was still less efficient than in extant reds, resulting in a prominent peak of green fluorescence (Fig. 1, A and C).

Our results indicate that because the ALL ancestor was green and not red, red color within the superfamily of GFP-like proteins has more than one origin, demonstrating the convergent evolution of a complex molecular system. The more complex red color evolved from green through small incremental transitions (a stepwise accumulation of improvements), each identified in our experiments by ancestral gene reconstruction (Fig 1D). This mode of evolution has been anticipated since Darwin, but has only recently been demonstrated in computer simulation experiments (*5*).

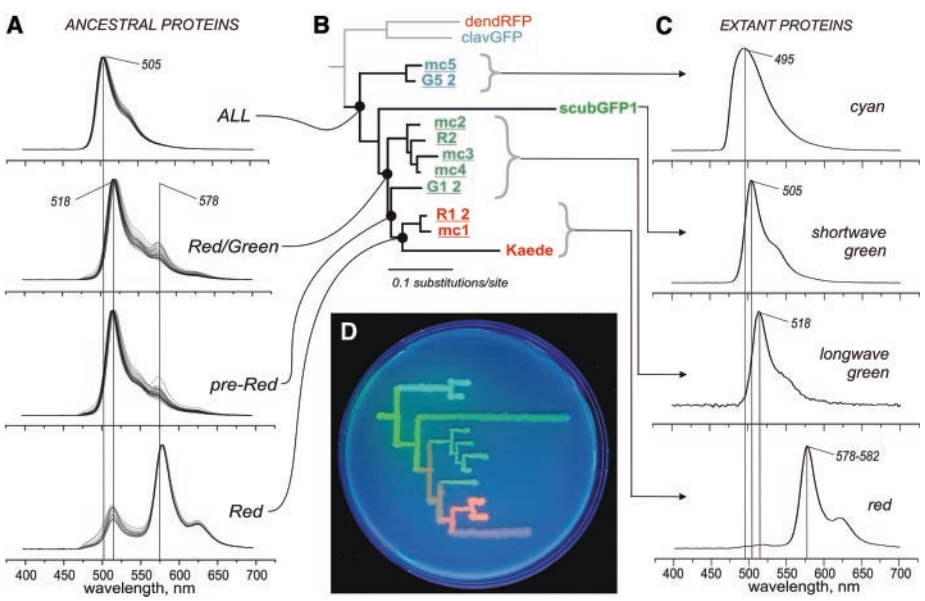

Fig. 1. (**A**) Fluorescence spectra of the reconstructed ancestral proteins. Multiple curves correspond to clones bearing variations at degenerate sites. (**B**) Phylogeny of GFP-like proteins from the great star coral *M. cavernosa* (sequence names are underlined) and closely related coral species. The red and cyan proteins from soft corals (dendRFP and clavGFP) represent an outgroup. (**C**) Fluorescence spectra of extant proteins. (**D**) Phylogenetic tree of colors from the great star coral, drawn on a petri dish with bacteria expressing extant and ancestral proteins, under ultraviolet light.

References and Notes

1. A. Miyawaki, T. Nagai, H. Mizuno, *Curr. Opin. Chem. Biol.* **7**, 557 (2003).
2. D. A. Shagin *et al.*, *Mol. Biol. Evol.* **21**, 841 (2004).
3. I. Kelmanson, M. Matz, *Mol. Biol. Evol.* **20**, 1125 (2003).
4. Z. Yang, *Comput. Appl. Biosci.* **13**, 555 (1997).
5. R. E. Lenski, C. Ofria, R. T. Pennock, C. Adami, *Nature* **423**, 139 (2003).
6. We thank N. V. Grishin for providing access to computer resources and D. Zacharias and K. Lukyanov for critical reading of the manuscript. Supported by grants from the Grass Foundation (J.A.U.), the U.S. Department of Defense and NIH (M.V.M.), and NSF and the Natural Sciences and Engineering Research Council of Canada (B.S.W.C.).

Supporting Online Material
www.sciencemag.org/cgi/content/full/305/5689/1433/DC1
Materials and Methods
Fig. S1
References and Notes

26 April 2004; accepted 7 July 2004

[1]Whitney Laboratory, [2]Department of Molecular Genetics and Microbiology, University of Florida, Gainesville, FL, USA. [3]Laboratory of Bioinformatics and Gene Expression, University of Chile, Santiago, Chile. [4]Department of Zoology, University of Toronto, Toronto, Canada.

*To whom correspondence should be addressed. E-mail: matz@whitney.ufl.edu

Crystal Structure of Argonaute and Its Implications for RISC Slicer Activity

Ji-Joon Song,[1,2] Stephanie K. Smith,[2] Gregory J. Hannon,[1] Leemor Joshua-Tor[1,2]*

Argonaute proteins and small interfering RNAs (siRNAs) are the known signature components of the RNA interference effector complex RNA-induced silencing complex (RISC). However, the identity of "Slicer," the enzyme that cleaves the messenger RNA (mRNA) as directed by the siRNA, has not been resolved. Here, we report the crystal structure of the Argonaute protein from *Pyrococcus furiosus* at 2.25 angstrom resolution. The structure reveals a crescent-shaped base made up of the amino-terminal, middle, and PIWI domains. The Piwi Argonaute Zwille (PAZ) domain is held above the base by a "stalk"-like region. The PIWI domain (named for the protein piwi) is similar to ribonuclease H, with a conserved active site aspartate-aspartate-glutamate motif, strongly implicating Argonaute as "Slicer." The architecture of the molecule and the placement of the PAZ and PIWI domains define a groove for substrate binding and suggest a mechanism for siRNA-guided mRNA cleavage.

RNA interference (RNAi) is triggered by the presence of double-stranded RNA (dsRNA) (*1*). A ribonuclease (RNase) III family enzyme, Dicer, initiates silencing by releasing ~20 base duplexes, with two-nucleotide 3′ overhangs called siRNAs (*2*, *3*). The RNAi pathway also mediates the function of endogenous, noncoding regulatory RNAs called microRNAs (miRNAs) [reviewed in (*4*)]. Both miRNAs and siRNAs guide substrate selection by similar if not identical effector complexes called RISC (*4*). These contain single-stranded versions of the small RNA and additional protein components (*5*–*7*). Of those, the signature element, which virtually defines a RISC, is a member of the Argonaute family of proteins (*8*).

Argonaute proteins are defined by the presence of PAZ and PIWI domains (*9*). Recent structural and biochemical analyses of the PAZ domain have begun to reveal Argonaute as the protein that interacts directly with the small RNA in RISC (*10*–*14*). The PAZ domain forms a deviant oligonucleotide/oligosaccharide-binding (OB) fold containing a central cleft lined with conserved aromatic residues that bind specifically to single-stranded 3′ ends (*10*, *12*). This was confirmed by subsequent structural studies of PAZ complexed with nucleic acids (*13*, *14*). On the basis of these studies, we first proposed a model in which the PAZ domain interacts with the 3′ ends of siRNAs in the two proteins containing this domain, Dicer and Argonaute (*10*). In RISC, the Argonaute PAZ domain would hold the 3′ end of the single-stranded siRNA, perhaps orienting recognition and cleavage of mRNA substrates. However, the nuclease responsible for cleavage, dubbed "Slicer," has so far escaped identification.

In an effort to deepen our understanding of the role of Argonaute proteins in RNAi, we have conducted structural studies of a full-length Argonaute protein from *P. furiosus*.

Overall architecture. The structure of the full-length Argonaute from the archaebacterium *P. furiosus* (PfAgo) was determined by x-ray crystallography to 2.25 Å resolution (table S1). The N-terminal, middle, and PIWI domains form a crescent-shaped base, with the PIWI domain at the center of the crescent. The region following the N-terminal domain forms a "stalk" that holds the PAZ domain above the crescent and an interdomain connector cradles the four domains of the molecule (Fig. 1). This architecture forms a groove at the center of the crescent and the PAZ domain closes off the top of this groove.

The N-terminal domain consists of a long strand at the bottom of the crescent, followed by a region of a small four-stranded β sheet, three α helices, and a β hairpin, which then extends to the three-stranded antiparallel β sheet stalk. The PAZ domain (residues 152 to 275) is a globular domain that adopts an OB-like β barrel fold with an attachment of two α helices on one side of the barrel and a cleft in between. This cleft is angled toward the crescent. The middle domain (residues 362 to 544) is an α/β open sheet domain composed of a central three-stranded parallel β sheet surrounded by α helices. This domain is similar to the glucose-galactose-arabinose-ribose–binding protein family and is most similar to Lac repressor (*15*). The middle domain also has a small three-stranded β sheet on the outer surface of the crescent, connecting it to the rest of the molecule.

The PIWI domain, which is at the C terminus of Argonaute (residues 545 to 770), is the most surprising portion of the structure, as we describe below. It sits in the middle of the

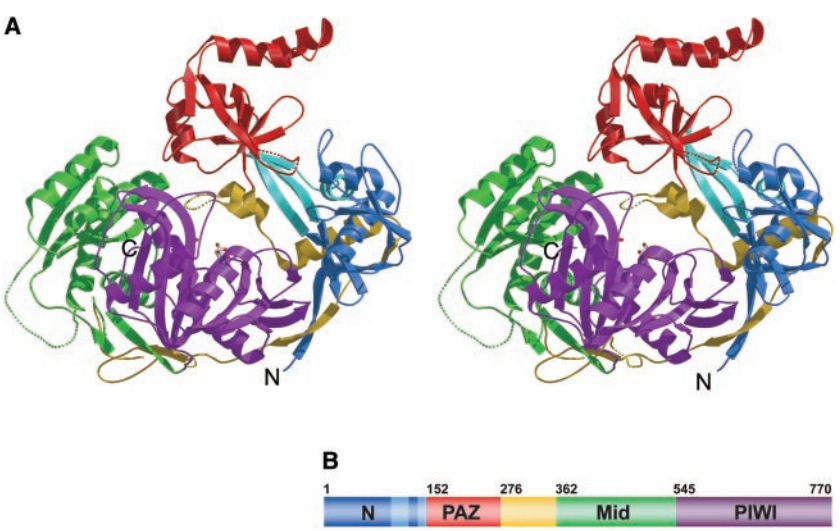

Fig. 1. Crystal structure of *P. furiosus* Argonaute. (**A**) Stereoview ribbon representation of Argonaute showing the N-terminal domain (blue), the "stalk" (light blue), the PAZ domain (red), the middle domain (green), the PIWI domain (purple), and the interdomain connector (yellow). Active site residues are drawn in stick representation. Disordered loops are drawn as dotted lines. (**B**) Schematic diagram of the domain borders.

[1]Watson School of Biological Sciences, [2]Keck Structural Biology Laboratory, Cold Spring Harbor Laboratory, 1 Bungtown Road, Cold Spring Harbor, NY 11724, USA.

*To whom correspondence should be addressed. E-mail: leemor@cshl.edu

crescent and below the PAZ domain. The crystal structure reveals the presence of a prominent central five-stranded β sheet flanked on both sides by α helices. A smaller β sheet extends from the central β sheet and attaches PIWI to the N-terminal domain and to portions of the interdomain connector.

The PAZ domain. The PAZ domain superimposes well with other PAZ domains that have known structures (*10*–*12*, *14*), although the attachment in the archael protein has two α helices rather than an α helix and a β hairpin (Fig. 2A). Other differences lie in loop regions. The root mean square deviation (RMSD) between human Argonaute-1 (hAgo1)–PAZ (*14*) and the PAZ domain in this structure is about 1.4 Å (for 53 Cα's). Despite close structural similarities, primary sequence comparisons failed to reveal a PAZ domain in PfAgo (fig. S1), whereas the presence and location of the PIWI domain was easily detected in Basic Local Alignment Search Tool (BLAST) searches.

Importantly, conserved aromatic residues that bind the two-nucleotide 3′ overhang of an siRNA (*10*, *13*, *14*) are all present in PfAgo (Fig. 2B). Curiously, in some cases, these side chains occupy similar positions in space, although they are anchored to positions on the peptide backbone differing from those in the eukaryotic proteins. Specifically, Y^{212}, Y^{216}, H^{217}, and Y^{190} of PfAgo are equivalent to Y^{309}, Y^{314}, H^{269}, and Y^{277}, respectively, of hAgo1 (*16*), which bind the oxygens of the phosphate that links the two bases in the overhang. Residue Y^{190} of PfAgo superimposes perfectly on hAgo1-Y^{277}, which binds the 2′ hydroxyl of the penultimate nucleotide. Residues L^{263} and I^{261} can assume the role of L^{337} and T^{335}, which anchor the sugar ring of the terminal residue through van der Waals interactions. An aromatic residue, F^{292} in hAgo1 stacks against the terminal nucleotide. This position is occupied by another aromatic, W^{213}, in PfAgo. Finally, R^{220} in our structure is positioned similarly to K^{313} that contacts the penultimate nucleotide. Residues that bind other regions of the RNA include K^{191} (R^{278} in hAgo1) and Y^{259} (K^{333} in hAgo1) to bind phosphates. Additional PAZ residues, such as K^{252}, K^{248}, Q^{276}, and N^{176} are probably also used to bind that siRNA strand. We therefore reason that the PAZ domain in PfAgo binds RNA 3′ ends, as do PAZ domains of fly and human Argonautes.

PIWI is an RNase H domain. The PIWI domain core has a tertiary structure belonging to the RNase H family of enzymes. This fold is also characteristic of other enzymes with nuclease or polynucleotidyl transferase activities, such as human immunodeficiency virus and avian sarcoma virus integrases (*17*, *18*), RuvC (a Holliday junction endonuclease) (*19*), and transposases such as Mu (*20*) and Tn5 (*21*). The closest matches, however, are

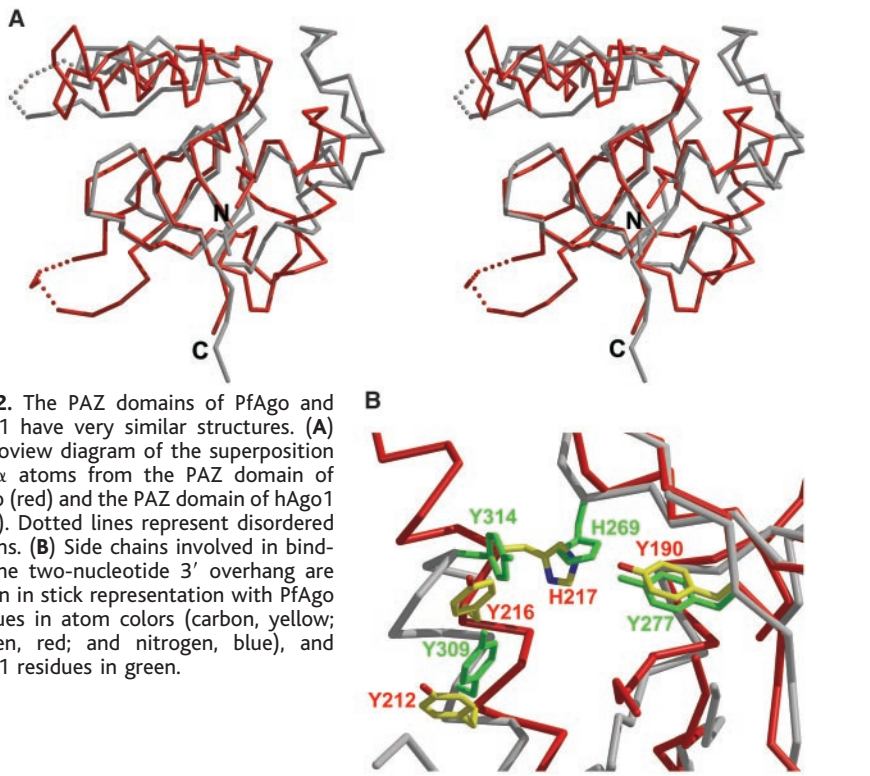

Fig. 2. The PAZ domains of PfAgo and hAgo1 have very similar structures. (**A**) Stereoview diagram of the superposition of Cα atoms from the PAZ domain of PfAgo (red) and the PAZ domain of hAgo1 (gray). Dotted lines represent disordered regions. (**B**) Side chains involved in binding the two-nucleotide 3′ overhang are shown in stick representation with PfAgo residues in atom colors (carbon, yellow; oxygen, red; and nitrogen, blue), and hAgo1 residues in green.

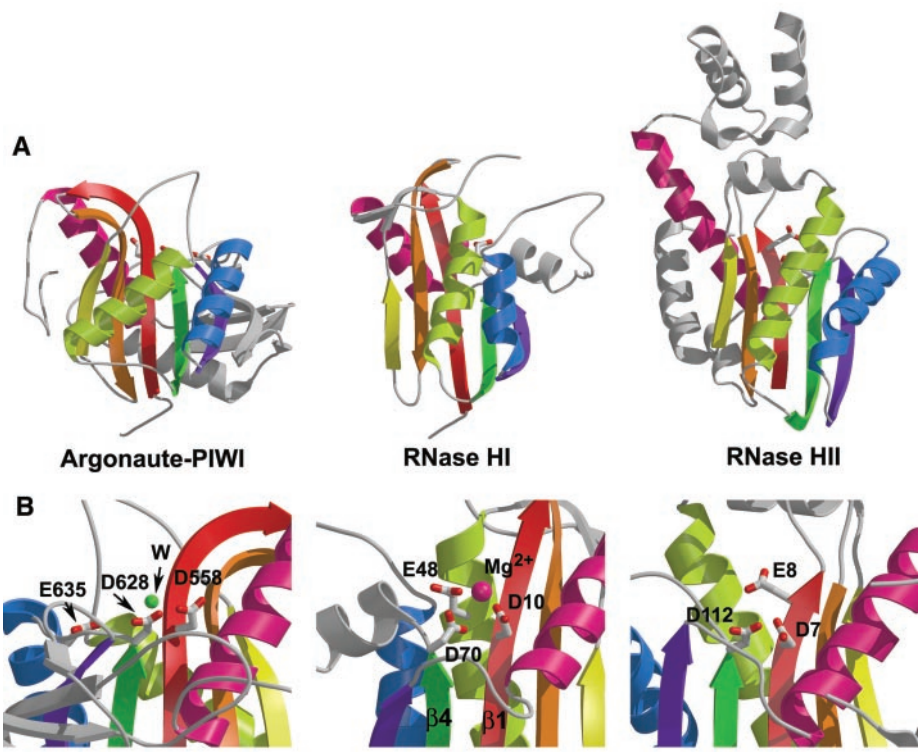

Fig. 3. PIWI is an RNase H domain. (**A**) Ribbon diagrams of the PIWI domain, *Escherichia coli* RNase HI and *Methanococcus jannaschii* RNase HII. The three structures are shown in a similar view with the secondary structure elements of the canonical RNase H fold in color. Active site residues are shown in stick representation. (**B**) This view of the active site residues is rotated ~180° about the *y* axis compared with the view in (A). The Mg^{2+} ion in RNase HI is shown as a pink sphere. A strong difference electron density (>4.5σ) found in the active site of PIWI that was assigned as a water molecule is shown as a green sphere. Secondary structural elements of the RNase H fold are colored from red to pink (red, orange, yellow, green, blue, purple, pink) as ordered in the protein sequence.

with RNase HII (*22*) and RNase H1 (*23*). The domains are topologically identical: The RMSDs between RNase HII and PfAgo (for 74 Cα's) and between RNase HI and PfAgo (for 66 Cα's) are both 1.9 Å (Fig. 3A). RNase H fold proteins all have a five-stranded mixed β sheet surrounded by helices. PIWI has an insertion between the last strand and the last helix of the RNase H fold that links it to the rest of the protein.

All of these enzymes contain three highly conserved catalytic carboxylates, which comprise the DDE motif (*24*). Two of these side chains are always located on the first strand, β1, which is the central strand of the β sheet, and at the C terminus of the fourth strand, β4, of the RNase H fold, which is adjacent to β1. The position of the third carboxylate varies. Notably, two aspartate residues in PIWI were located at the same positions as the invariant carboxylates of the RNase H fold (Fig. 3B). These are D^{558}, located on the first β strand, and D^{628}, located at the end of the fourth strand of the PIWI domain. The only requirement for the third variable carboxylate is a reasonable spatial position at the active site. E^{635} is in close proximity to the two aspartates and we suggest that this glutamate serves as the third active-site residue. This residue is positioned on the second helix of the RNase H fold of PIWI (the blue helix in Fig. 3). These three residues are almost completely invariant in the 136 Argonaute protein sequences examined (fig. S2). Interestingly, an arginine, R^{627}, is also positioned at the center of the active site, as in the case of the IS4 family of transposases such as Tn5, which appear to have a DDRE motif (*21*). The active site is thus positioned in a cleft in the middle of the crescent in the groove below the PAZ domain.

Ago as Slicer. The observation that the PIWI domain in Argonaute is an RNase H domain immediately implicated Argonaute as Slicer, the enzyme in RISC that cleaves the mRNA. RNase H enzymes cleave single-stranded RNA "guided" by the DNA strand in an RNA/DNA hybrid. Similarly, Argonautes might specialize in RNA cleavage, guided by the siRNA strand in a dsRNA substrate. Moreover, RNase H enzymes produce products with 3′-OH and 5′ phosphate groups (*25*), in agreement with the products of mRNA cleavage by RISC (*26*, *27*). A dependence on Mg^{2+} for activity is another hallmark of RNase H enzymes, a requirement that RISC shares (*27*). The PAZ domain, recognizing the 3′ ends of siRNAs, and the PIWI domain, now shown to be an RNase H domain, combine the necessary features of the slicing component of the RNAi machinery. Therefore, Argonaute, the signature component of RISC, appears to be Slicer itself.

A model for siRNA-guided mRNA cleavage. The overall structure of Argonaute defines a distinct groove through the protein, which has a claw shape and bends between the PAZ and N-terminal domains. A notable feature of the structure is evident when the electrostatic potential is mapped on the surface of the protein. As shown in Fig. 4A, the surface of this inner groove is lined with positive charges suitable for interaction with the negatively charged phosphate backbone and with the 2′ hydroxyl moieties of RNA, implicating the groove for substrate binding.

To examine possible substrate binding modes for Argonaute, we superimposed the PAZ domains from PfAgo and hAgo1 (*14*) and examined the position of the RNA in the hAgo1 complex with respect to PfAgo. The strand that interacts with the PAZ cleft is the siRNA guide (Fig. 4B). Leaving the cleft, the RNA tracks the top of the PAZ β barrel allowing similar, if not identical, interactions with the PfAgo PAZ, as observed in the hAgo1 PAZ-RNA complex. A long loop present in the PfAgo PAZ domain would probably move up slightly to accommodate the siRNA. The other strand would represent the mRNA substrate and would enter the binding groove with its 5′ end between the PAZ and N-terminal domains, with the latter acting as an "mRNA grip." Another extension of the groove lies between the N-terminal and the PIWI domains and could accommodate a single-stranded nucleic acid. However, the function of this feature is presently difficult to predict.

Extending the dsRNA further into the molecule along the binding groove by model building positions the mRNA above the active site located in the PIWI domain, nine nucleotides from the 5′ side end of the double-stranded region. On the basis of this model, the scissile bond falls between nucleotides 11 and 12, counting from the 3′ end of the guide. This precisely coincides with the demonstrated cleavage of mRNAs by RISC, 10 nucleotides from the 5′ end of a 21-nucleotide siRNA. The remainder of the RNA would continue along the binding groove (Fig. 4C). The length of the groove appears sufficient to accommodate the entire siRNA guide, with the 5′ end of the guide probably interacting with the other side of the groove to sense the siRNA 5′ phosphate. Additionally, from studies of other RNase H enzymes, we expect Argonaute to sense the minor groove width of the dsRNA, which differs from that of dsDNA and from an RNA/DNA hybrid. Such a hypothesis is in accord with the inability of RISC to cut DNA substrates (*26*). Although

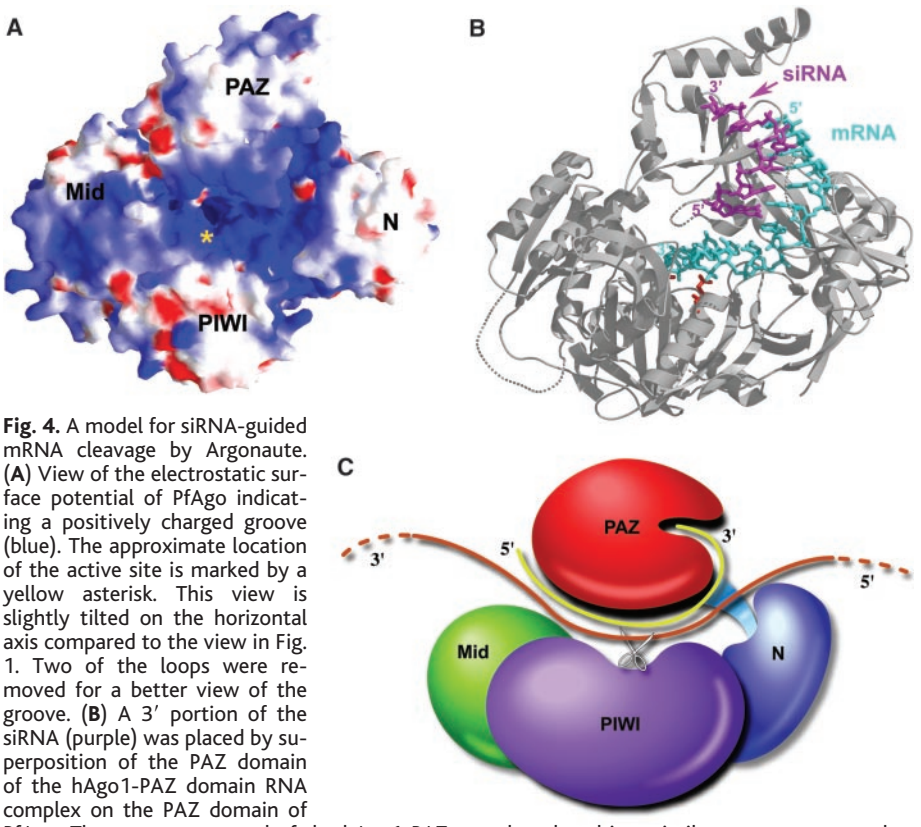

Fig. 4. A model for siRNA-guided mRNA cleavage by Argonaute. (**A**) View of the electrostatic surface potential of PfAgo indicating a positively charged groove (blue). The approximate location of the active site is marked by a yellow asterisk. This view is slightly tilted on the horizontal axis compared to the view in Fig. 1. Two of the loops were removed for a better view of the groove. (**B**) A 3′ portion of the siRNA (purple) was placed by superposition of the PAZ domain of the hAgo1-PAZ domain RNA complex on the PAZ domain of PfAgo. The passenger strand of the hAgo1-PAZ complex placed in a similar manner was used to model the mRNA strand (light blue) by extending the RNA two nucleotides at the 5′ end, and from the middle of that strand along the binding groove toward the active site in PIWI. The phosphate between nucleotides 11 and 12 from the 5′ end of the mRNA falls near the active site residues (red). The view is similar to the view in Fig. 1. (**C**) Schematic depiction of the model for siRNA-guided mRNA cleavage. The domains are colored as in Fig. 1. The siRNA (yellow) binds with its 3′ end in the PAZ cleft and the 5′ is predicted to bind near the other end of the cleft. The mRNA (brown) comes in between the N-terminal and PAZ domains and out between the PAZ and middle domain. The active site in the PIWI domain (shown as scissors) cleaves the mRNA opposite the middle of the siRNA guide.

a single-stranded RNA should bind fairly readily, opening the claw of the molecule might assist binding the mRNA, after which Argonaute might close on the double-stranded substrate. A possible hinge region exists in the interdomain connector at residues 317 to 320. This hinge could lift the PAZ away from the crescent base, perhaps allowing the RISC loading complex to assist in assembling an active complex (*28*, *29*).

The notion that RISC "Slicer" activity resides in Argonaute itself was tested in a mammalian system, by mutational analysis of hAgo2 (*30*). Conserved active site aspartates in hAgo2 were altered and the mutants lost nuclease activity but retained siRNA binding. This supports the model in which Argonaute itself functions as the Slicer enzyme in the RNAi pathway.

Many questions regarding the details of the mechanism for siRNA-guided mRNA cleavage remain. Several Argonaute protein family members appear to be inactive toward mRNA cleavage despite the presence of the catalytic residues. This situation might be analogous to the case of the Tn5 transposase and its inhibitor, which possess a catalytic domain with an RNase H–like fold. Tn5 inhibitor is a truncated version of the active Tn5 transposase and retains essential catalytic residues. However, there are major conformational differences between the two (*21*). Mutations have been introduced into a catalytically active Ago protein, hAgo2, in the vicinity of the active site, which change residues to corresponding residues in an inactive Ago, hAgo1. These inactivate Ago2 for cleavage, indicating that there are determinants for catalysis beyond simply the catalytic triad and that relatively minor alterations in the PIWI domain can have profound effects on its activity toward RNA substrates. In addition, interactions with other factors may be needed to create a fully active Slicer. The common fold in the catalytic domain of Argonaute family members and transposases and integrases is also intriguing given the relationship of RNAi with control of transposition. Notably, the identification of the catalytic center of RISC awaited a drive toward understanding RNAi at a structural level. Thus, it seems likely that, as in the present example, a full understanding of the underlying mechanism of RNAi will derive from a combination of detailed biochemical and structural studies of RISC.

References and Notes

1. A. Fire *et al.*, *Nature* **391**, 806 (1998).
2. S. M. Elbashir, J. Martinez, A. Patkaniowska, W. Lendeckel, T. Tuschl, *EMBO J.* **20**, 6877 (2001).
3. E. Bernstein, A. A. Caudy, S. M. Hammond, G. J. Hannon, *Nature* **409**, 363 (2001).
4. D. P. Bartel, *Cell* **116**, 281 (2004).
5. A. Nykanen, B. Haley, P. D. Zamore, *Cell* **107**, 309 (2001).
6. D. S. Schwarz, G. Hutvagner, B. Haley, P. D. Zamore, *Mol. Cell* **10**, 537 (2002).
7. J. Martinez, A. Patkaniowska, H. Urlaub, R. Luhrmann, T. Tuschl, *Cell* **110**, 563 (2002).
8. S. M. Hammond, E. Bernstein, D. Beach, G. J. Hannon, *Nature* **404**, 293 (2000).
9. L. Cerutti, N. Mian, A. Bateman, *Trends Biochem. Sci.* **25**, 481 (2000).
10. J. J. Song *et al.*, *Nature Struct. Biol.* **10**, 1026 (2003).
11. K. S. Yan *et al.*, *Nature* **426**, 468 (2003).
12. A. Lingel, B. Simon, E. Izaurralde, M. Sattler, *Nature* **426**, 465 (2003).
13. A. Lingel, B. Simon, E. Izaurralde, M. Sattler, *Nature Struct. Mol. Biol.* **11**, 576 (2004).
14. J. B. Ma, K. Ye, D. J. Patel, *Nature* **429**, 318 (2004).
15. A. M. Friedman, T. O. Fischmann, T. A. Steitz, *Science* **268**, 1721 (1995).
16. Single-letter abbreviations for the amino acid residues are as follows: A, Ala; C, Cys; D, Asp; E, Glu; F, Phe; G, Gly; H, His; I, Ile; K, Lys; L, Leu; M, Met; N, Asn; P, Pro; Q, Gln; R, Arg; S, Ser; T, Thr; V, Val; W, Trp; and Y, Tyr.
17. F. Dyda *et al.*, *Science* **266**, 1981 (1994).
18. J. Lubkowski *et al.*, *Biochemistry* **38**, 13512 (1999).
19. M. Ariyoshi *et al.*, *Cell* **78**, 1063 (1994).
20. P. Rice, K. Mizuuchi, *Cell* **82**, 209 (1995).
21. D. R. Davies, I. Y. Goryshin, W. S. Reznikoff, I. Rayment, *Science* **289**, 77 (2000).
22. L. Lai, H. Yokota, L. W. Hung, R. Kim, S. H. Kim, *Struct. Fold Des.* **8**, 897 (2000).
23. K. Katayanagi, M. Okumura, K. Morikawa, *Proteins* **17**, 337 (1993).
24. W. Yang, T. A. Steitz, *Structure* **3**, 131 (1995).
25. U. Wintersberger, *Pharmacol. Ther.* **48**, 259 (1990).
26. J. Martinez, T. Tuschl, *Genes Dev.* **18**, 975 (2004).
27. D. S. Schwarz, Y. Tomari, P. D. Zamore, *Curr. Biol.* **14**, 787 (2004).
28. Y. Tomari *et al.*, *Cell* **116**, 831 (2004).
29. J. W. Pham, J. L. Pellino, Y. S. Lee, R. W. Carthew, E. J. Sontheimer, *Cell* **117**, 83 (2004).
30. J. Liu *et al.*, *Science* **305**, 1437 (2004); published online 29 July 2004 (10.1126/science.1102513).
31. We thank E. Enemark for help with data collection, R. Martienssen and members of the Joshua-Tor laboratory for helpful discussions, and M. Becker (beamline X25) for support with data collection at the National Synchrotron Light Source (NSLS). The NSLS is supported by the U.S. Department of Energy, Division of Material Sciences and Division of Chemical Sciences. J.-J.S. is a Bristol-Myers Squibb Predoctoral Fellow. Coordinates have been deposited in the Protein Data Bank (accession code 1U04).

Supporting Online Material

www.sciencemag.org/cgi/content/full/1102514/DC1
Materials and Methods
Figs. S1 to S3
Table S1
References

8 July 2004; accepted 21 July 2004
Published online 29 July 2004;
10.1126/science.1102514
Include this information when citing this paper.

Argonaute2 Is the Catalytic Engine of Mammalian RNAi

Jidong Liu,[1]* Michelle A. Carmell,[1,2]* Fabiola V. Rivas,[1] Carolyn G. Marsden,[1] J. Michael Thomson,[3] Ji-Joon Song,[1] Scott M. Hammond,[3] Leemor Joshua-Tor,[1] Gregory J. Hannon[1]†

Gene silencing through RNA interference (RNAi) is carried out by RISC, the RNA-induced silencing complex. RISC contains two signature components, small interfering RNAs (siRNAs) and Argonaute family proteins. Here, we show that the multiple Argonaute proteins present in mammals are both biologically and biochemically distinct, with a single mammalian family member, Argonaute2, being responsible for messenger RNA cleavage activity. This protein is essential for mouse development, and cells lacking Argonaute2 are unable to mount an experimental response to siRNAs. Mutations within a cryptic ribonuclease H domain within Argonaute2, as identified by comparison with the structure of an archeal Argonaute protein, inactivate RISC. Thus, our evidence supports a model in which Argonaute contributes "Slicer" activity to RISC, providing the catalytic engine for RNAi.

The presence of double-stranded RNA (dsRNA) in most eukaryotic cells provokes a sequence-specific silencing response known as RNA interference (RNAi) (*1*, *2*). The dsRNA trigger of this process can be derived from exogenous sources or transcribed from endogenous noncoding RNA genes that produce microRNAs (miRNAs) (*1*, *3*).

RNAi begins with the conversion of dsRNA silencing triggers into small RNAs of ~21 to 26 nucleotides (nts) in length (*4*). This is accomplished by the processing of triggers by specialized ribonuclease III (RNase III)–family nucleases, Dicer and Drosha (*5*, *6*). Resulting small RNAs join an effector complex, known as RISC (RNA-induced silencing complex) (*7*). Silencing by RISC can occur through several mechanisms. In flies, plants, and fungi, dsRNAs can trigger chromatin remodeling and transcriptional gene silencing (*8–11*). RISC can also interfere with protein synthesis, and this is the predominant mechanism used by miRNAs in mammals (*12*, *13*). However, the best studied mode of

[1]Cold Spring Harbor Laboratory, Watson School of Biological Sciences, 1 Bungtown Road, Cold Spring Harbor, NY 11724, USA. [2]Program in Genetics, Stony Brook University, Stony Brook, NY 11794, USA. [3]Department of Cell and Developmental Biology, University of North Carolina, Chapel Hill, NC 27599, USA.

*These authors contributed equally to this work.
†To whom correspondence should be addressed. E-mail: hannon@cshl.edu

RISC action is mRNA cleavage (*14*, *15*). When programmed with a small RNA that is fully complementary to the substrate RNA, RISC cleaves that RNA at a discrete position, an activity that has been attributed to an unknown RISC component, "Slicer" (*16*, *17*). Whether or not RISC cleaves a substrate can be determined by the degree of complementarity between the siRNA and mRNA, as mismatched duplexes are often not processed (*16*). However, even for mammalian miRNAs, which normally repress at the level of protein synthesis, cleavage activity can be detected with a substrate that perfectly matches the miRNA sequence (*18*). This result prompted the hypothesis that all RISCs are equal, with the outcome of the RISC-substrate interaction being determined largely by the character of the interaction between the small RNA and its substrate.

RISC contains two signature components. The first is the small RNA, which cofractionated with RISC activity in *Drosophila* S2 cell extracts (*7*), and whose presence correlated with dsRNA-programmed mRNA cleavage in *Drosophila* embryo lysates (*14*, *15*). The second is an Argonaute (Ago) protein, which was identified as a component of purified RISC in *Drosophila* (*19*). Subsequent studies have suggested that Argonautes are also key components of RISC in mammals, fungi, worms, protozoans, and plants (*17*, *20*).

Argonautes are often present as multiprotein families and are identified by two characteristic domains, PAZ and PIWI (*21*). These proteins mainly segregate into two subfamilies, comprising those that are more similar to either *Arabidopsis* Argonaute1 or *Drosophila* Piwi. The Argonaute family was first linked to RNAi through genetic studies in *Caenorhabditis elegans*, which identified Rde-1 as a gene essential for silencing (*22*). Our subsequent placement of a *Drosophila* Argonaute protein in RISC (*19*) prompted us to explore the roles of this protein family. Toward this end, we have undertaken both biochemical and genetic studies of the Ago1 subfamily proteins in mammals.

Mammals contain four Argonaute1 subfamily members, Ago1 to Ago4 [nomenclature as in (*23*); see fig. S1]. We have previously shown that different Argonaute family members in *Drosophila* preferentially associate with different small RNAs, with Ago1 preferring miRNAs and Ago2 siRNAs (*24*). Recent studies of *Drosophila melanogaster* (dm) Ago1 and dmAgo2 mutants have strengthened these conclusions (*25*). To assess whether mammalian Ago proteins specialized in their interactions with small RNAs, we examined Ago-associated miRNA populations by microarray analysis. Ago1-, Ago2- and Ago3-associated RNAs were hybridized to microarrays that report the expression status of 152 human microRNAs. Patterns of associated RNAs were identical within experimental error in each case (Fig. 1A). Additionally, each of the tagged Ago proteins associated similarly with a cotransfected siRNA (Fig. 1C).

Previous studies have used tagged siRNAs to affinity purify Argonaute-containing RISC (*17*). These preparations, containing mixtures of at least two mammalian Argonautes, were capable of cleaving synthetic mRNAs that were complementary to the tagged siRNA. We examined the ability of purified complexes containing individual Argonaute proteins to catalyze similar cleavages. Unexpectedly, irrespective of the siRNA sequence, only Ago2-containing RISC was able to catalyze cleavage (Fig. 1B and fig. S2). All three Ago proteins were similarly expressed and bound similar amounts of transfected siRNA (Fig. 1, C and D).

These results demonstrated that mammalian Argonaute complexes are biochemically distinct, with only a single family member being competent for mRNA cleavage. To examine the possibility that Ago proteins might also be biologically specialized, we disrupted the mouse Ago2 gene by targeted insertional mutagenesis (fig. S3 and Fig. 2A) (*26*). Intercrosses of Ago2 heterozygotes produced only wild-type and heterozygous offspring, strongly suggesting that disruption of Ago2 produced an embryonic-lethal phenotype.

Ago2-deficient mice display several developmental abnormalities beginning approximately halfway through gestation. Both gene-trap and in situ hybridization data of day 9.5 embryos show broad expression of Ago2 in the embryo, with some hot spots of expression in the forebrain, heart, limb buds, and branchial arches (Fig. 2, F and G). The most prominent phenotype is a defect in neural tube closure (Fig. 2, D and E), often accompanied by apparent mispatterning of anterior structures, including the forebrain (Fig. 2, C and D). Roughly half of the embryos display complete failure of neural tube closure in the head region (Fig. 2E), while all embryos display a wavy neural tube in more caudal regions. Mutant embryos also suffer from apparent cardiac failure. The hearts are enlarged and often accompanied by pronounced swelling of the pericardial cavity (Fig. 2C). By day 10.5, mutant embryos are severely developmentally delayed compared with wild-type and heterozygous littermates (Fig. 2B). This large difference in size, like the apparent cardiac failure, may be accounted for by a general nutritional deficiency caused by yolk sac and placental defects (*27*), as histological analysis reveals abnormalities in these tissues.

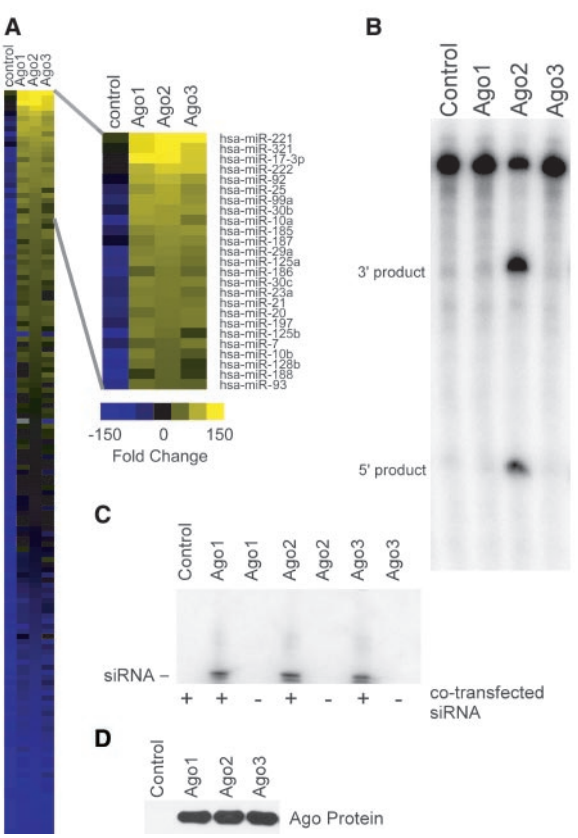

Fig. 1. Only mammalian Ago2 can form cleavage-competent RISC. (**A**) The miRNA populations associated with Ago1, Ago2, and Ago3 were measured by microarray analysis as described in (*44*). The heat map shows normalized log-ratio values for each data set, with yellow representing increased relative amounts and blue indicating decreased amounts relative to the median. The top 25 log ratios are shown in the expanded region. In each panel, "control" indicates parallel analysis of cells transfected with a vector control. (**B**) The 293T cells were transfected with a control vector or with vectors encoding myc-tagged Ago1, Ago2, or Ago3, along with an siRNA that targets firefly luciferase. Immunoprecipitates were tested for siRNA-directed mRNA cleavage as described in (*44*). Positions of 5′ and 3′ cleavage products are shown. (**C**) Immunoprecipitates as in (B) were tested for in vivo siRNA binding by Northern blotting of Ago immunoprecipitates (*44*). (**D**) Western blots of transfected cell lysates show similar levels of expression for each recombinant Argonaute protein.

Not all Argonaute proteins are required for successful mammalian development (*28*, *29*). Thus, it is unclear why Ago2 should be required for development, while other Ago proteins are dispensable. Ago subfamily members are expressed in overlapping patterns in humans (*30*). In situ hybridization demonstrates overlapping expression patterns for Ago2 and Ago3 in mouse embryos (Fig. 2F and fig. S4). Considered together with the essentially identical patterns of miRNA binding, our results suggest the possibility that the ability of Ago2 to assemble into catalytically active complexes might be critical for mouse development. Although most miRNAs regulate gene expression at the level of protein synthesis, recently miR196 has been demonstrated to cleave the mRNA encoding HoxB8, a developmental regulator (*31*). Evolutionary conservation of an essential cleavage-competent RISC in organisms in which miRNAs predominantly act by translational regulation raises the possibility that target cleavage by mammalian miRNAs might be more important and widespread than previously appreciated.

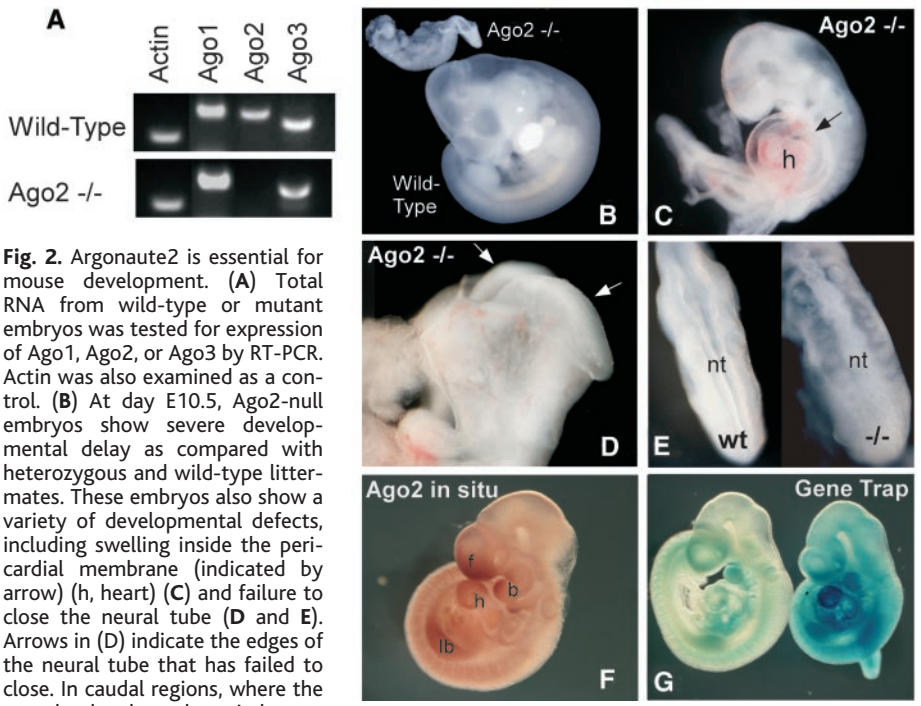

Fig. 2. Argonaute2 is essential for mouse development. (**A**) Total RNA from wild-type or mutant embryos was tested for expression of Ago1, Ago2, or Ago3 by RT-PCR. Actin was also examined as a control. (**B**) At day E10.5, Ago2-null embryos show severe developmental delay as compared with heterozygous and wild-type littermates. These embryos also show a variety of developmental defects, including swelling inside the pericardial membrane (indicated by arrow) (h, heart) (**C**) and failure to close the neural tube (**D** and **E**). Arrows in (D) indicate the edges of the neural tube that has failed to close. In caudal regions, where the neural tube does close, it has an abnormal appearance, being wavy as compared with wild-type embryos (E) (compare wild-type and Ago2 −/−). Ago2 is expressed in most tissues of the developing embryo as measured by in situ hybridization (**F**) or by analysis of an Ago2 gene-trap animal (**G**). In (F), f is forebrain, b is branchial arches, h is heart, and lb is limb bud, all of which are relative hot spots for Ago2 mRNA. In (G), the left embryo shows similar patterns when staining for the gene-trap marker, β-galactosidase, proceeds for only a short period. Longer incubation (G, right) gives uniform staining throughout the embryo.

Numerous studies have indicated that experimentally triggered RNAi in mammalian cells proceeds through siRNA-directed mRNA cleavage because in many, but not all, cases, reiterated binding sites are necessary for repression at the level of protein synthesis [see, for example (*13*, *32*, *33*)]. If Ago2 were uniquely capable of assembling into cleavage-competent complexes in mice, then embryos or cells lacking Ago2 might be resistant to experimental RNAi. To address this question, we prepared mouse embryo fibroblasts (MEFs) from E10.5 embryos from Ago2 heterozygous intercrosses. Reverse transcription polymerase chain reaction (RT-PCR) analysis and genotyping revealed that we were able to obtain wild-type, mutant, and heterozygous MEF populations. Importantly, MEFs also express other Ago proteins, including Ago1 and Ago3 (Fig. 3A). Ago2-null MEFs were unable to repress gene expression in response to an siRNA (Fig. 3B and fig. S5). This defect could be rescued by the addition of a third plasmid that encoded human Ago2 but not by a plasmid encoding human Ago1 (Fig. 3B). In contrast, responses were intact for a reporter of repression at the level of protein synthesis, mediated by an siRNA binding to multiple mismatched sites (*32*) (Fig. 3C).

Because Ago2 is exceptional in its ability to form cleavage-competent complexes, we set out to map the determinants of this capacity. Deletion analysis indicated that an intact Ago2 was required for RISC ac-

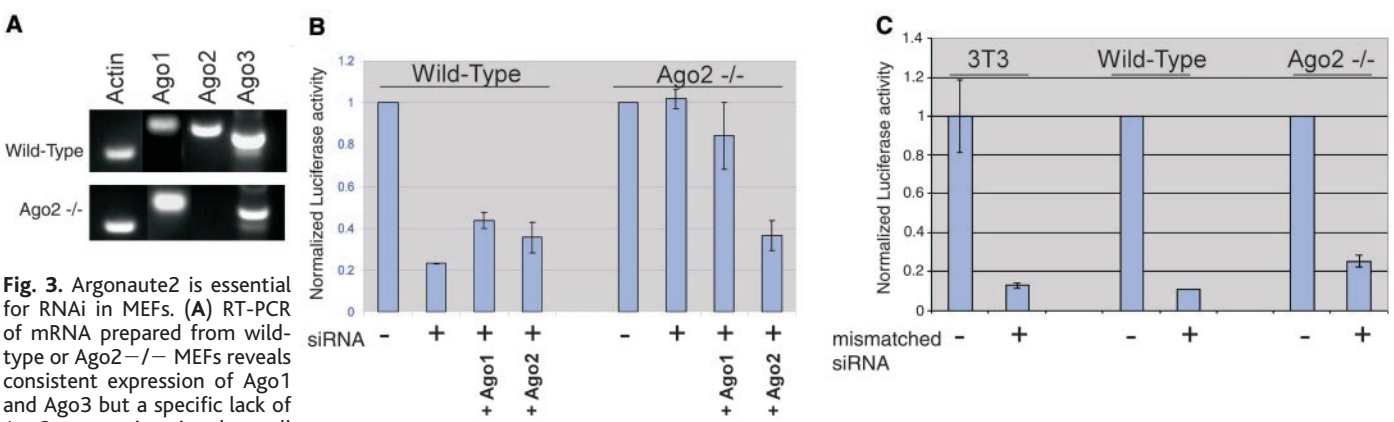

Fig. 3. Argonaute2 is essential for RNAi in MEFs. (**A**) RT-PCR of mRNA prepared from wild-type or Ago2−/− MEFs reveals consistent expression of Ago1 and Ago3 but a specific lack of Ago2 expression in the null MEF. Actin mRNA serves as a control. (**B**) Wild-type and mutant MEFs were cotransfected with plasmids encoding *Renilla* and firefly luciferases, either with or without firefly siRNA. Ratios of firefly to *Renilla* activity, normalized to 1 for the no-siRNA control, were plotted. For each genotype, the ability of Ago1 and Ago2 to rescue suppression was tested by cotransfection with expression vectors encoding each protein as indicated. (**C**) NIH-3T3 cells, wild-type MEFs, or Ago2 mutant MEFs were tested as described in (B) (except that *Renilla*/firefly ratios are plotted) for their ability to suppress a reporter of repression at the level of protein synthesis. In this case, the *Renilla* luciferase mRNA contains multiple imperfect binding sites for a CXCR4 siRNA. Cells were transfected with a mixture of firefly and *Renilla* luciferase plasmids with or without the siRNA.

tivity (fig. S6). We therefore used the sequence of highly conserved but cleavage-incompetent Ago proteins as a guide to the construction of Ago2 mutants. A series of point mutations included H634P, H634A, Q633R, Q633A, H682Y, L140W, F704Y, and T744Y. Whereas all of these mutations retain siRNA-binding activity and most retain cleavage activity, changes at Q633 and H634 have a profound effect on target cleavage (Fig. 4). Both the Q633R and H634P mutations, in which residues were changed to corresponding residues in Ago1 and Ago3, abolished catalysis. Changing H634 to A also inactivated Ago2, whereas a similar change, Q633A, was permissive for cleavage. Thus, even relatively conservative changes can negate the ability of Ago2 to form cleavage-competent RISC.

Several possibilities could explain a lack of cleavage activity for Ago2 mutants. Such mutations could interfere with the proper folding of Ago2. However, this seems unlikely because those same residues presumably permit proper folding in closely related Argonaute proteins, and mutant Ago2 proteins retained the ability to interact with siRNAs. Alternatively, cleavage-incompetent Ago2 mutants could lose the ability to interact with the putative Slicer. Finally, Ago2 itself might be Slicer, with our conservative substitutions altering the active center of the enzyme in a way that prevents cleavage.

The last possibility predicted that we might reconstitute an active enzyme with relatively pure Ago2 protein. We immunoaffinity purified Ago2 from 293T cells and attempted to reconstitute RISC in vitro. Incubation with the double-stranded siRNA produced no appreciable activity, whereas Ago2 could be successfully programmed with single-stranded siRNAs to cleave a complementary substrate (Fig. 5A). Formation of the active enzyme was unaffected by first washing the immunoprecipitates with up to 2.5 M NaCl or 1 M urea. A 21-nt single-stranded DNA was unable to direct cleavage (Fig. 5A). Programming could be accomplished with different siRNAs that direct activity against different substrates (fig. S7). RISC is formed though a concerted assembly process in which the RISC-loading complex (RLC) acts in an adenosine triphosphate (ATP)–dependent manner to place one strand of the small RNA into RISC (*34–36*). In vitro reconstitution occurs in the absence of ATP, which suggests that Ago2 could be programmed with siRNAs without a need for the normal assembly process (Fig. 5A). However, in vitro reconstitution of RISC still requires

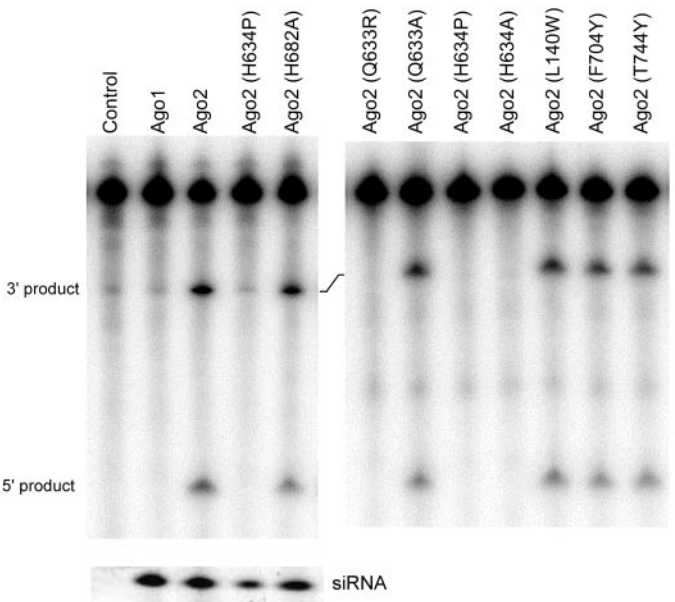

Fig. 4. Mapping the requirements for assembly of cleavage-competent RISC. Ago1, Ago2, or mutants of Ago2 were expressed as myc-tagged fusion proteins in 293T cells. In all cases, expression constructs were cotransfected with a luciferase siRNA. Western blotting indicated similar expression for each mutant. Immunoprecipitates containing individual proteins were tested for cleavage activity against a luciferase mRNA (*44*). Positions of 5′ and 3′ cleavage products are indicated. SiRNA binding was examined for each mutant by Northern blotting of immunoprecipitates or by staining of immunoprecipitates with Sybr Gold (Molecular Probes, Eugene, Oregon). Representatives for these assays are shown. In no case did we detect a defect in interaction of mutants with siRNAs.

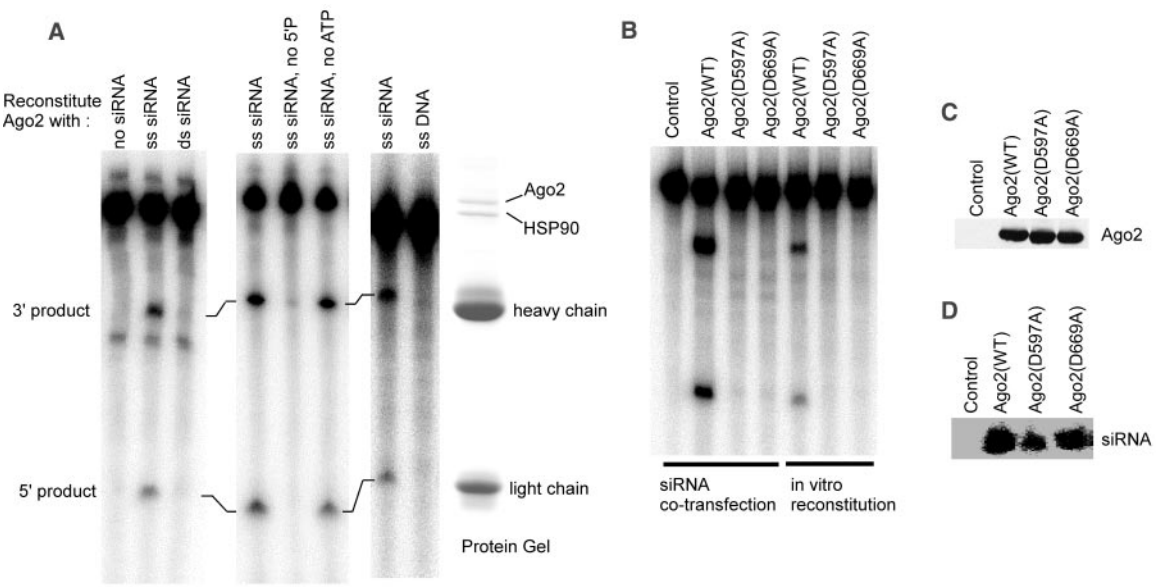

Fig. 5. Argonaute2 is a candidate for Slicer. (**A**) Ago2 protein was immunoaffinity purified from transiently transfected 293T cells. The preparation contained two major proteins (protein gel), in addition to heavy and light chains. These were identified by mass spectrometry as Ago2 and HSP90. Immunoprecipitates were mixed (*44*) in vitro with single- or double-stranded siRNAs or with a 21-nt DNA having the same sequence as the siRNA. Reconstituted RISC was tested for cleavage activity with a uniformly labeled synthetic mRNA. Positions of 5′ and 3′ cleavage products are noted. Where indicated, the siRNA was not 5′ phosphorylated and, in one case, ATP was not added to the reconstitution reaction. (**B**) Ago2 or Ago2 mutants were assembled into RISC in vivo by cotransfection with siRNAs, followed by immunoaffinity purification or by in vitro reconstitution, mixing affinity-purified proteins with single-stranded siRNAs. These mutants were tested for activity against a complementary mRNA substrate. 5′ and 3′ cleavage products are as in (A). (**C** and **D**) Both mutant proteins were expressed at levels similar to wild-type Ago2 and bound siRNAs as readily. Ago2 (H634P) and Ago2 (Q633R) behave similarly in this assay.

the essential characteristics of an siRNA. For example, single-stranded siRNAs that lack a 5′ phosphate group cannot reconstitute an active enzyme.

Although consistent with the possibility that the catalytic activity of RISC is carried within Ago2, these results do not rule out the possibility that a putative Slicer copurifies with Ago2. To demonstrate more conclusively that Ago2 is Slicer, we turned to the crystal structure of an Argonaute protein from an archebacterium, *Pyrococcus furiosus* (*37*). This structure revealed that the PIWI domain folds into a structure analogous to the catalytic domain of RNase H and avian sarcoma virus (ASV) integrase. The notion that such a domain would lie at the center of RISC cleavage is consistent with previous observations. RNase H and integrases cleave their substrates, leaving 5′ phosphate and 3′ hydroxyl groups through a metal-catalyzed cleavage reaction (*38*, *39*). Notably, previous studies have strongly indicated that the scissile phosphate in the targeted mRNA is cleaved via a metal ion in RISC to give the same phosphate polarity (*40*). Our in vitro data are consistent with the reconstituted RISC also requiring a divalent metal (fig. S8).

The active center of RNase H and its relatives consists of a catalytic triad of three carboxylate groups contributed by aspartic or glutamic acid (*38*, *39*). These amino acid residues coordinate the essential metal and activate water molecules for nucleolytic attack. Reference to the known structure of RNase H reveals two aspartate residues in the archeal Ago protein present at the precise spatial locations predicted for formation of an RNase H–like active site (*37*). These align with identical residues in the human Ago2 protein (fig. S9). Therefore, to test whether the PIWI domain of Ago2 provides catalytic activity to RISC, we changed the two conserved aspartates, D597 and D669, to alanine, with the prediction that either mutation would inactivate RISC cleavage. Consistent with our hypothesis, the mutant Ago2 proteins were incapable of assembling into a cleavage-competent RISC in vitro or in vivo, despite retaining the ability to bind siRNAs (Fig. 5, B to D).

Considered together, our data provide strong support for the notion that Argonaute proteins are the catalytic components of RISC. First, the ability to form an active enzyme is restricted to a single mammalian family member, Ago2. This conclusion is supported both by biochemical analysis and by genetic studies in mutant MEFs. Second, single amino acid substitutions within Ago2 that convert residues to those present in closely related proteins negate RISC cleavage. Third, the structure of the *P. furiosis* Argonaute protein reveals provocative structural similarities between the PIWI domain and the RNase H domains, providing a hypothesis for the method by which Argonaute cleaves its substrates. We tested this hypothesis by introducing mutations in the predicted Ago2 active site. It is extremely unlikely that such mutations could affect interactions with other proteins, because they are buried within a cleft of Ago.

Our studies indicate that the Argonaute proteins that are unable to form cleavage-competent RISC differ from Ago2 at key positions that do not include the putative metal-coordinating residues themselves. However, we cannot yet, based either on biochemical or structural studies, provide a precise explanation for the catalytic defects in these proteins. It is conceivable that Ago1 and Ago3 fail to coordinate the catalytic metal or that the structure of the active site is distorted sufficiently that a bound metal is unable to access the scissile phosphate. Alternatively, catalytic mechanisms with two metal ions have been proposed for RNase H (*38*, *39*), which leaves open the possibility that catalytically inert Ago family members might lack structures essential to bind the second metal ion.

The relationship between the nuclease domain in PIWI and conserved nuclease domains in viral reverse transcriptases, transposases, and viral integrases has potential evolutionary implications. In *Drosophila*, plants, and *C. elegans*, the RNAi pathway has a major role in controlling parasitic nucleic acids such as viruses and transposons (*41*–*43*). The fact that the RNAi machinery shares a core structural domain with viruses and transposons suggests that this nucleic acid immune system may have arisen in part by pirating components from the replication and movement machineries of the very elements that RNAi protects against. This hypothesis is made even more poignant by considering the role of RNA-dependent RNA polymerases in RNAi, their functional relationship to viral replicases, and the possibility that the siRNAs themselves might first have served as primers that enable such replicases to duplicate primordial genomes.

References and Notes

1. G. J. Hannon, *Nature* **418**, 244 (2002).
2. A. Fire *et al*., *Nature* **391**, 806 (1998).
3. G. Hutvagner, P. D. Zamore, *Curr. Opin. Genet. Dev.* **12**, 225 (2002).
4. A. Hamilton, O. Voinnet, L. Chappell, D. Baulcombe, *EMBO J.* **21**, 4671 (2002).
5. E. Bernstein, A. A. Caudy, S. M. Hammond, G. J. Hannon, *Nature* **409**, 363 (2001).
6. Y. Lee *et al*., *Nature* **425**, 415 (2003).
7. S. M. Hammond, E. Bernstein, D. Beach, G. J. Hannon, *Nature* **404**, 293 (2000).
8. M. F. Mette, W. Aufsatz, J. van der Winden, M. A. Matzke, A. J. Matzke, *EMBO J.* **19**, 5194 (2000).
9. I. M. Hall *et al*., *Science* **297**, 2232 (2002).
10. T. Volpe *et al*., *Science* **297**, 1833 (2002).
11. M. Pal-Bhadra, U. Bhadra, J. A. Birchler, *Mol. Cell* **9**, 315 (2002).
12. P. H. Olsen, V. Ambros, *Dev. Biol.* **216**, 671 (1999).
13. D. P. Bartel, *Cell* **116**, 281 (2004).
14. T. Tuschl, P. D. Zamore, R. Lehmann, D. P. Bartel, P. A. Sharp, *Genes Dev.* **13**, 3191 (1999).
15. P. D. Zamore, T. Tuschl, P. A. Sharp, D. P. Bartel, *Cell* **101**, 25 (2000).
16. S. M. Elbashir, J. Martinez, A. Patkaniowska, W. Lendeckel, T. Tuschl, *EMBO J.* **20**, 6877 (2001).
17. J. Martinez, A. Patkaniowska, H. Urlaub, R. Luhrmann, T. Tuschl, *Cell* **110**, 563 (2002).
18. G. Hutvagner, P. D. Zamore, *Science* **297**, 2056 (2002).
19. S. M. Hammond, S. Boettcher, A. A. Caudy, R. Kobayashi, G. J. Hannon, *Science* **293**, 1146 (2001).
20. M. A. Carmell, G. J. Hannon, *Nature Struct. Mol. Biol.* **11**, 214 (2004).
21. L. Cerutti, N. Mian, A. Bateman, *Trends Biochem. Sci.* **25**, 481 (2000).
22. H. Tabara *et al*., *Cell* **99**, 123 (1999).
23. M. A. Carmell, Z. Xuan, M. Q. Zhang, G. J. Hannon, *Genes Dev.* **16**, 2733 (2002).
24. A. A. Caudy, M. Myers, G. J. Hannon, S. M. Hammond, *Genes Dev.* **16**, 2491 (2002).
25. K. Okamura, A. Ishizuka, H. Siomi, M. C. Siomi, *Genes Dev.* **18**, 1655 (2004).
26. B. Zheng, A. A. Mills, A. Bradley, *Nucleic Acids Res.* **27**, 2354 (1999).
27. S. J. Conway, A. Kruzynska-Frejtag, P. L. Kneer, M. Machnicki, S. V. Koushik, *Genesis* **35**, 1 (2003).
28. W. Deng, H. Lin, *Dev. Cell* **2**, 819 (2002).
29. S. Kuramochi-Miyagawa *et al*., *Development* **131**, 839 (2004).
30. T. Sasaki, A. Shiohama, S. Minoshima, N. Shimizu, *Genomics* **82**, 323 (2003).
31. S. Yekta, I. H. Shih, D. P. Bartel, *Science* **304**, 594 (2004).
32. J. G. Doench, C. P. Petersen, P. A. Sharp, *Genes Dev.* **17**, 438 (2003).
33. M. Kiriakidou *et al*., *Genes Dev.* **18**, 1165 (2004).
34. A. Nykanen, B. Haley, P. D. Zamore, *Cell* **107**, 309 (2001).
35. J. W. Pham, J. L. Pellino, Y. S. Lee, R. W. Carthew, E. J. Sontheimer, *Cell* **117**, 83 (2004).
36. Y. Tomari *et al*., *Cell* **116**, 831 (2004).
37. J.-J. Song *et al*., *Science* **305**, 1434 (2004). Published online 29 July 2004; 10.1126/science.1102514.
38. B. R. Chapados *et al*., *J. Mol. Biol.* **307**, 541 (2001).
39. W. Yang, T. A. Steitz, *Structure* **3**, 131 (1995).
40. D. S. Schwarz, Y. Tomari, P. D. Zamore, *Curr. Biol.* **14**, 787 (2004).
41. R. F. Ketting, T. H. Haverkamp, H. G. van Luenen, R. H. Plasterk, *Cell* **99**, 133 (1999).
42. T. Sijen, R. H. Plasterk, *Nature* **426**, 310 (2003).
43. E. Sarot, G. Payen-Groschene, A. Bucheton, A. Pelisson, *Genetics* **166**, 1313 (2004).

44. Materials and methods are available as supporting material on *Science* Online.

45. The authors thank members of the Hannon lab for helpful discussions, Alea Mills for advice on ES cell work and for providing the library of targeting constructs, Sang Yong Kim for generating chimeras, Kathryn Anderson for insightful discussions and advice, and Phil Sharp for providing the CXCR4 constructs. M.C. is supported by the U.S. Army Breast Cancer Research Program, F.V.R. by the Jane Coffin Childs Memorial Fund, and J.S. by a Bristol Myers Squibb predoctoral fellowship. S.M.H. is a General Motors Cancer Research Foundation Scholar. This work was supported in part by grants from NIH (L.J. and G.J.H.).

Supporting Online Material

www.sciencemag.org/cgi/content/full/1102513/DC1
Materials and Methods
Figs. S1 to S9
References

8 July 2004; accepted 19 July 2004
Published online 29 July 2004;
10.1126/science.1102513
Include this information when citing this paper.

Substructure in the Circumstellar Disk Around the Young Star AU Microscopii

Michael C. Liu

Keck adaptive optics imaging with a physical resolution of 0.4 astronomical units (AU) resolves the inner (15 to 80 AU) disk of AU Microscopii (AU Mic, GJ 803, HD 197481), the nearest known scattered light disk to Earth. The inner disk is asymmetric and possesses a sharp change in structure at 35 AU. The disk also shows spatially localized enhancements and deficits at 25- to 40-AU separations. The overall morphology points to the influence of unseen larger bodies and resembles structures expected from recent planet formation. AU Mic is coeval with the archetypical debris disk system β Pictoris, and the similarities between their two disks point to synchronous disk evolution. Multiple indications of substructure appear to be common in circumstellar disks at an age of ≈12 million years.

After dissipation of their primordial disks of gas and dust, many stars develop debris disks, which are composed solely of collisionally regenerated dust. Debris disks have been identified by their thermal emission at infrared (IR) and submillimeter wavelengths (*1*, *2*). Their spectral energy distributions (SEDs) convey only limited information about the extant physical processes. In this regard, the large resolved disk around β Pictoris (β Pic) has been a gold mine for scrutinizing the structure, composition, and dynamics of a debris disk (*3*–*9*). However, a broader understanding has been hampered by the small number of systems that are spatially resolved.

The newly discovered disk around the young star AU Mic offers a promising opportunity to examine the debris disk phenomenon. This well-studied flare star is among the youngest known M dwarfs in the solar neighborhood, with an estimated age of 12^{+8}_{-4} million years (My) (*10*, *11*) and a distance of only 9.94 ± 0.13 pc from Earth (*12*). A recent search of nearby young (~10 to 50 My) stars identified AU Mic as a bright submillimeter source, possessing 0.01 Earth masses of cold (40 K) dust with a fractional luminosity of $L_{dust}/L_{star} = 6 \times 10^{-4}$ (*13*). Follow-up *R*-band (0.65 μm) coronagraphic imaging discovered that AU Mic has a large disk seen in scattered light (*14*), the closest such disk to Earth. The seeing-limited discovery images detected the disk as close to the star as the outer edge of the focal plane mask, which was 5″ (50 AU) in radius. Little is known about AU Mic's disk inside of 50 AU, a scale that corresponds to the edge of the classical Kuiper belt in our own solar system (*15*).

Institute for Astronomy, University of Hawaii, 2680 Woodlawn Drive, Honolulu, HI 96822, USA. E-mail: mliu@ifa.hawaii.edu

AU Mic was observed on 27 to 28 June 2004 UT using the adaptive optics (AO) system on the Keck II 10-m telescope (*16*) with the facility coronagraphic camera NIRC2 and the *H*-band (1.63 μm) filter. Conditions were clear, and the AO-corrected images have a full width at half maximum (FWHM) of 0.04″ (0.4 AU). Photometric calibrations were based on IR standard stars (*17*) and 2MASS photometry of the star 21″ to the southwest (SW) of AU Mic (2MASS J20450821-3120397). The edge-on disk of AU Mic is remarkably bright, noticeable in individual raw images. No similar features were seen in images of other stars obtained as a control sample.

A "roll subtraction" technique was developed to remove the point spread function (PSF) from the images, thereby enabling study of the inner disk against the bright glare of the central star (*18*). This technique is similar to that used for observing programs with the Hubble Space Telescope (*19*, *20*). The AU Mic disk is detected in the Keck AO imaging from 15 to 80 AU in projected separation (Fig. 1). The disk midplane is resolved, with an observed FWHM of 2.0 to 2.5 AU inside of 50 AU. The innermost (<15 AU) regions are dominated by PSF subtraction residuals and are inaccessible to study in this data set.

The AU Mic disk shows two large-scale asymmetries. (i) The midplanes are different sizes. The outer isophotes of the southeast (SE) side are ≈10% smaller than those of the northwest (NW) side. (ii) The disk midplanes are not aligned. From 2 to 5″ in radius, their position angles (PA) are 129.3 ± 0.8° and 311.4 ± 1.0°, as measured east of north. The relative tilt from the *H*-band data is 2.1 ± 1.3°, consistent with the 6 ± 3° tilt seen at *R*-band for the outer disk (*14*). Unlike the other asymmetries discussed in this report, this tilt asymmetry can be explained by the intrinsic dust-scattering properties (*21*), rather than by a structural asymmetry in the disk.

The disk midplanes do not follow a constant position angle. Both midplanes curve slightly to the north, with a ≈1° change in orientation seen in the *H*-band imaging. This bowing is suggestive of an interaction between the disk and the local interstellar medium (*22*). However, the direction of AU Mic's proper motion (*12*) is nearly aligned with the disk midplane, which is not consistent with this idea. The bowing may reflect the internal dynamics of the disk.

The radial surface brightness profile f_ν is well-described by a power law, $f_\nu \propto r^\alpha$, where r is the projected separation (Fig. 2). From 35- to 60-AU separation, $\alpha = -4.4 \pm 0.4$ and -4.4 ± 0.3 for the SE and NW sides, respectively. These are somewhat steeper than the *R*-band measurements from 50 to 210 AU, which have slopes of −3.6 to −3.9 (*14*), although the different angular resolution of the two data sets impedes direct comparison (0.04″ for *H*-band, 1.1″ for *R*-band). In the innermost disk, there is a change in slope at 35 AU, with $\alpha = -1.0 \pm 0.3$ and -1.4 ± 0.3 for the SE and NW sides, respectively, as measured from 20- to 35-AU separation. Also, there is an indication that the break occurs at slightly different radii for the two midplanes, ≈32 AU for the SE side and ≈38 AU for the NW side, pointing to a nonaxisymmetric structure.

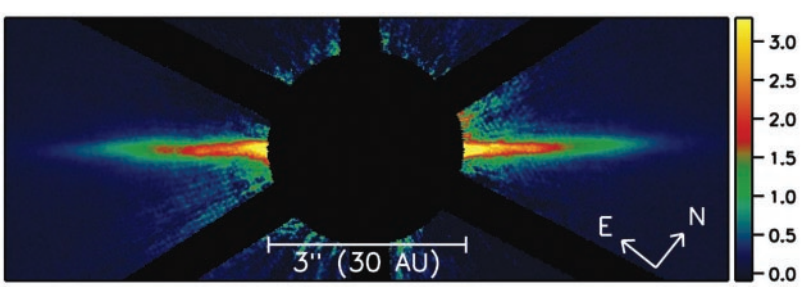

Fig. 1. *H*-band (1.63 μm) image of the AU Mic dust disk obtained with the Keck II Telescope. The image is 11″ (110 AU) wide and 4″ (40 AU) high. A software mask blocks the PSF subtraction residuals in the central 1.5″ (15 AU) in radius and around the six diffraction spikes. The color bar gives the observed flux in units of millijanskys per arc sec^2.

In addition to the large-scale asymmetries, the Keck AO imaging reveals smaller-scale asymmetries in the disk at 25 to 40 AU, both radially and vertically. These features are spatially resolved, being broader than the PSF; they lie outside the region of strong PSF subtraction residuals; and they are consistent in independent subsets of the data. Because the disk is seen nearly edge-on, the true physical prominence of the substructure is diminished by the smooth component of the disk along the line of sight.

The most obvious substructure resides in the SE midplane (Figs. 1 and 3). The SE side contains at least two radial enhancements, one at 25 AU and the other at 31 AU. There is also a relative deficit in the scattered light at 29 AU. The NW side shows an enhancement at 25 AU aligned with the SE feature at 25 AU, indicative of a limb-brightened ring of material. However, no other obvious counterparts for the SE features are seen in the NW side, indicating structures with nonzero eccentricity and/or incomplete aziumuthal extent (e.g., clumps). Such nonaxisymmetric structures are most naturally explained by the dynamical influence of unseen planets (*23*, *24*).

The disk also possesses vertical substructure (Fig. 4). The prominent SE lumps at 25 and 31 AU reside at different elevations. Furthermore, the NW side shows a local enhancement at 37 AU that is displaced from the inner midplane. The micrometer-sized dust grains responsible for the scattered light are removed by collisions and/or Poynting-Robertson drag on time scales shorter than the age of the star (*14*). Therefore, the observed vertical substructure may originate from the inclined (≳1°) orbits of larger unseen bodies, either the parent bodies that collisionally produce the dust or planets that gravitationally perturb the dust.

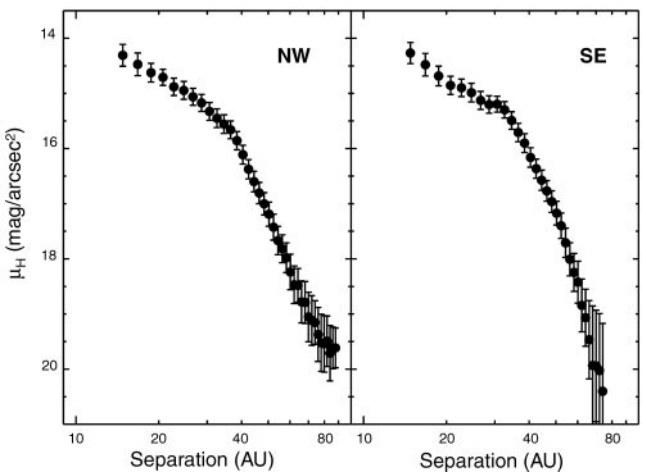

Fig. 2. *H*-band (1.63 μm) surface brightness profile of the AU Mic disk midplane derived from a photometry aperture 0.6″ wide in the direction perpendicular to the midplane. The NW side of the disk is larger than the SE side. A break in the surface brightness profile is seen at 35 AU.

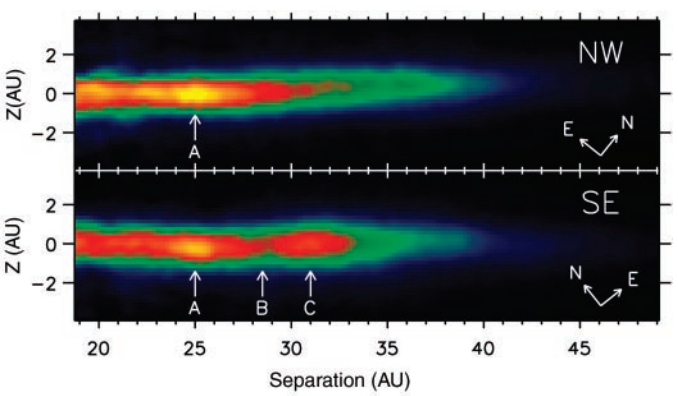

Fig. 3. Radial substructure in the AU Mic disk. The SE data have been mirrored about the axis perpendicular to the disk midplane. To highlight the substructure, each pixel has been multiplied by its distance from the star, in order to compensate for the overall decrease in disk flux with radius. The data have been Gaussian smoothed to the image resolution of 0.04″ (0.4 AU). The data are oriented with the SE midplane horizontal; the small relative tilt of the NW midplane can be seen.

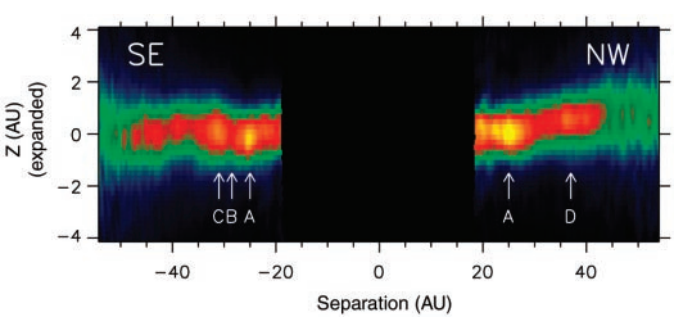

Fig. 4. Vertical substructure in the AU Mic disk. The plot's vertical axis has been expanded by a factor of 5. The NW concentration at 25 AU is aligned with its SE counterpart, but the strong features at 25 and 31 AU in the SE midplane reside at different heights. The elevated NW structure at 37 AU has no clear counterpart. To show the structure over a wide range of separations, the disk flux has been normalized by the radial surface brightness profile in Fig. 2 (different from the normalization used for Fig. 3). The data have been Gaussian smoothed to the image resolution of 0.04″ (0.4 AU). The image orientation is the same as in Fig. 1.

The debris disk archetype β Pic is the best-studied spatially resolved disk system. Many of the structural features present in the β Pic disk are also found in the AU Mic disk:

1) Both disks have unequal-sized midplanes. In the case of β Pic, the NE side is larger than the SW side (*21*, *25*), an effect that has been attributed to eccentricity perturbations driven by a substellar companion (*26*).

2) The surface brightness profiles for the β Pic and AU Mic disks are similar, with steep outer profiles ($\alpha \approx -4$ to -5) and a strong flattening ($\Delta\alpha \approx 2$ to 3) in the inner profile. For β Pic, the profile changes markedly inside of 100 AU compared with the outer disk (*19*, *21*, *25*). For AU Mic, the change occurs at 35 AU.

The steep slope of the β Pic outer disk has been modeled as dust originating from an inner collisional planetesimal disk and then radiatively driven outward [(*27*); compare with (*28*)]. The strong flattening at 100 AU demarcates the outer extent of the β Pic planetesimal disk. By analogy, the similar flattening of the AU Mic profile suggests a planetesimal disk of 35 AU extent. This value is consistent with the ≈17-AU inner radius inferred from the IR/submillimeter SED (*13*). And taken together, the data suggest that AU Mic's planetesimal disk is restricted to ≈17 to 35 AU in radius.

The factor of 3 difference in the inferred sizes of the underlying planetesimal disks can be understood in the context of different agglomeration rates. The time scale for planetesimal growth scales as $t \propto P/\Sigma$, where P is the orbital period and Σ is the surface density (*29*). For a disk profile of $\Sigma \propto \Sigma_0 a^{-3/2}$, the growth time scale is then $t \propto a^3/(\Sigma_0 M_*^{1/2})$, i.e., strongly dependent on the orbital radius a. The two stars are coeval, with a factor of 4 difference in stellar mass. Assuming that the difference in the total disk masses is reflected in the factor of 10 difference in the observed submillimeter emitting dust masses (*13*, *30*), planetesimal growth should have proceeded to ~2.7 times larger radii for β Pic compared with AU Mic, in accord with the observational estimates.

3) The β Pic disk exhibits small-scale structures in its inner disk that are radially confined and vertically displaced (*8*), similar to the AU Mic disk. These features are naturally explained by radially localized structures in the dust with nonzero eccentricities and inclinations (e.g., rings, clumps, and gaps), perhaps arising from resonant

interactions of multiple planets (*31*). The β Pic disk also displays a prominent inner warp (*5*, *19*), with a 3° to 4° tilt relative to the outer disk. Such a strong warp is not seen in the AU Mic disk, although its detectability would depend on its radial extent and orientation to the line of sight.

Since its discovery, the singular nature of the large scattered light disk around β Pic has raised the question of whether the system represents a typical phase in early disk evolution (*4*, *32*) or an anomalous occurrence, e.g., caused by the recent gravitational perturbation of a passing star (*6*). The discovery and characterization of the coeval AU Mic disk demonstrate that a common phase in disk evolution involves optically thin, asymmetric, bright scattered-light disks with multiple indications of substructure. Given that AU Mic and β Pic are members of the same moving group (*10*, *11*), the high degree of similarity between these two disks suggests that synchronous evolution has occurred.

Dust with sufficient optical depth to produce detectable scattered light spans a large range in radius around β Pic and AU Mic, from as close as ≈15 AU out to hundreds of AU. This is in contrast to older (≳200 My) debris disk systems, where the dust is confined to ringlike structures detected in submillimeter thermal emission (*33*, *34*) but not in scattered light (*35*, *36*). Recent simulations of evolving planetesimal disks are in accord with this observed morphological transformation from young dusty disks to old dusty rings (*37*). However, the young (~8 My) A star HR 4796A has its scattered light confined to a single bright ring (*38*), as opposed to a large disk, so stellar age cannot be the only factor governing disk morphology.

The spatially localized enhancements and deficits found in the AU Mic disk resemble the expected signposts of recent and/or ongoing planet formation in young disks. Simulations of planet formation by agglomeration find that bright rings of dust arise from gravitational stirring of planetesimals by recently formed planets of ≳1000-km radius (*37*, *39*). Dark gaps occur where the dust has been dynamically removed by planets or represent regions shadowed by interior rings that are optically thick. In this interpretation, the multiple structures present in the AU Mic disk suggest that planets massive enough to induce appreciable gravitational stirring form contemporaneously over a range of radii.

Finally, the stellar masses of β Pic (2 $M_\odot$) and AU Mic (0.5 $M_\odot$) straddle those of solar-mass stars. Hence, scrutiny of these two well-resolved disks may provide a window into the early solar system. The young Kuiper belt was about a factor of 100 more massive than its current state (*40*); its fractional dust luminosity would have been around 10^{-3} to 10^{-5} (*15*, *41*), comparable to that of the β Pic and AU Mic disks. This Keck AO study reveals that multiple dynamical substructures are common to optically thin disks at ages of ≈12 My. These structures may also reflect the dynamics that were active in the young Kuiper belt.

References and Notes

1. D. E. Backman, F. Paresce, in *Protostars and Planets III*, E. H. Levy, J. I. Lunine, Eds. (University of Arizona Press, Tucson, AZ, 1993), p. 1253.
2. A.-M. Lagrange, D. E. Backman, in *Protostars and Planets IV*, V. Mannings, A. P. Boss, S. S. Russell, Eds. (University of Arizona Press, Tucson, AZ, 2000), p. 639.
3. B. A. Smith, R. J. Terrile, *Science* **226**, 1421 (1984).
4. P. Artymowicz, *Annu. Rev. Earth Planet. Sci.* **25**, 175 (1997).
5. D. Mouillet *et al.*, *Mon. Not. R. Astron. Soc.* **292**, 896 (1997).
6. P. Kalas *et al.*, *Astrophys. J.* **530**, L133 (2000).
7. A. J. Weinberger *et al.*, *Astrophys. J.* **584**, L33 (2003).
8. Z. Wahhaj *et al.*, *Astrophys. J.* **584**, L27 (2003).
9. A. Brandeker *et al.*, *Astron. Astrophys.* **413**, 681 (2004).
10. D. Barrado y Navascués, *et al.*, *Astrophys. J.* **520**, L123 (1999).
11. B. Zuckerman *et al.*, *Astrophys. J.* **562**, L87 (2001).
12. M. A. C. Perryman *et al.*, *Astron. Astrophys.* **323**, L49 (1997).
13. M. C. Liu *et al.*, *Astrophys. J.* **608**, 526 (2004).
14. P. Kalas *et al.*, *Science* **303**, 1990 (2004).
15. D. C. Jewitt, J. X. Luu, in *Protostars and Planets IV*, V. Mannings, A. P. Boss, S. S. Russell, Eds. (University of Arizona Press, Tucson, AZ, 2000), p. 1201.
16. P. Wizinowich *et al.*, *Pub. Astron. Soc. Pac.* **112**, 315 (2000).
17. S. E. Persson *et al.*, *Astron. J.* **116**, 2475 (1998).
18. Materials and methods are available as supporting material on *Science* Online.
19. S. R. Heap *et al.*, *Astrophys. J.* **539**, 435 (2000).
20. G. Schneider, M. D. Silverstone, *Proc. SPIE* **4860**, 1 (2003).
21. P. Kalas, D. Jewitt, *Astron. J.* **110**, 794 (1995).
22. P. Artymowicz, M. Clampin, *Astrophys. J.* **490**, 863 (1997).
23. J. Liou, H. A. Zook, *Astron. J.* **118**, 580 (1999).
24. L. M. Ozernoy *et al.*, *Astrophys. J.* **537**, L147 (2000).
25. D. A. Golimowski *et al.*, *Astrophys. J.* **411**, L41 (1993).
26. D. P. Whitmire *et al.*, *Astron. Astrophys.* **203**, L13 (1988).
27. J. C. Augereau, R. P. Nelson, A. M. Lagrange, J. C. B. Papaloizou, D. Mouillet, *Astron. Astrophys.* **370**, 447 (2001).
28. A. Lecavelier Des Etangs, A. Vidal-Madjar, R. Ferlet, *Astron. Astrophys.* **307**, 542 (1996).
29. J. J. Lissauer, *Icarus* **69**, 249 (1987).
30. I. Sheret, W. R. F. Dent, M. C. Wyatt, *Mon. Not. R. Astron. Soc.* **348**, 1282 (2004).
31. E. W. Thommes, J. J. Lissauer, *Astrophys. J.* **597**, 566 (2003).
32. M. Jura *et al.*, *Astrophys. J.* **505**, 897 (1998).
33. J. S. Greaves *et al.*, *Astrophys. J.* **506**, L133 (1998).
34. W. S. Holland *et al.*, *Nature* **392**, 788 (1998).
35. B. A. Smith, J. W. Fountain, R. J. Terrile, *Astron. Astrophys.* **261**, 499 (1992).
36. P. Kalas, D. Jewitt, *Astron. J.* **111**, 1347 (1996).
37. S. J. Kenyon, B. C. Bromley, *Astron. J.* **127**, 513 (2004).
38. G. Schneider *et al.*, *Astrophys. J.* **513**, L127 (1999).
39. S. J. Kenyon, B. C. Bromley, *Astrophys. J.* **577**, L35 (2002).
40. S. A. Stern, J. E. Colwell, *Astron. J.* **114**, 841 (1997).
41. C. Dominik, G. Decin, *Astrophys. J.* **598**, 626 (2003).

42. I thank E. Chiang, G. Herczeg, M. Jura, P. Kalas, J. Krist, J. Linsky, and B. Macintosh for enlightening discussions. I am very grateful to A. Bouchez, D. LeMignant, R. Campbell, P. Wizinowich, and the staff of Keck Observatory for their assistance with the observations. This research has made use of the NASA/IPAC, 2MASS, and SIMBAD databases. I acknowledge support from NSF grant AST04-07441 and NASA grant HST-GO-09845.01-A.

Supporting Online Material
www.sciencemag.org/cgi/content/full/1102929/DC1
Materials and Methods

19 July 2004; accepted 4 August 2004
Published online 12 August 2004;
10.1126/science.1102929
Include this information when citing this paper.

Electrically Driven Single-Cell Photonic Crystal Laser

Hong-Gyu Park,[1] Se-Heon Kim,[1] Soon-Hong Kwon,[1] Young-Gu Ju,[2] Jin-Kyu Yang,[1] Jong-Hwa Baek,[1] Sung-Bock Kim,[2] Yong-Hee Lee[1]*

We report the experimental demonstration of an electrically driven, single-mode, low threshold current (~260 μA) photonic band gap laser operating at room temperature. The electrical current pulse is injected through a sub-micrometer-sized semiconductor wire at the center of the mode with minimal degradation of the quality factor. The actual mode of interest operates in a nondegenerate monopole mode, as evidenced through the comparison of the measurement with the computation based on the actual fabricated structural parameters. As a small step toward a thresholdless laser or a single photon source, this wavelength-size photonic crystal laser may be of interest to photonic crystals, cavity quantum electrodynamics, and quantum information communities.

The laser physics and quantum optics communities have been interested for some time in extremely small, low-loss, low-power lasers (*1*–*3*). The potential to localize photons into photonic band gap semiconductor microcavities having wavelength-scale volumes and high quality factors enables us to study the cavity quantum electrodynamics in solids and to construct quantum optical devices such as on-demand single photon sources. Several optically pumped, ultra-small, photonic crystal lasers (*4*–*8*) or electrically driven light-emitting structures using the concept of photonic crystals (*9*–*11*) have been recently reported. Two kinds of electrically driven photonic band edge lasers, large-volume lasers with high output power

[1]Department of Physics, Korea Advanced Institute of Science and Technology, Daejeon 305-701, Korea. [2]Telecommunication Basic Research Laboratory, Electronics and Telecommunications Research Institute, Daejeon 305-600, Korea.

*To whom correspondence should be addressed. E-mail: yhlee@kaist.ac.kr

(*12*) and quantum cascade lasers (*13*), especially draw our attention. However, the electronic activation of the wavelength-scale single-cell laser operating in a single mode, a crucial step toward a practical form of the thresholdless laser, has yet to be demonstrated.

One of the most daunting problems in trying to implement a single-cell, free-standing slab photonic crystal laser (*4*–*7*) is how to make electrical contact with the sub-micrometer-sized photonic crystal resonator structure (*14*). Locating the proper region inside the laser cavity to position an electrical contact requires an understanding of the resonant modes that are available in a single-cell triangular lattice photonic crystal cavity (*15*). Three potential candidates, each with a central node, were considered, because the introduction of a small central post as an electrical contact did not notably degrade the quality (*Q*) factor of the mode (*15*). The small central post functions as an electrical wire, a mode selector, and a heat sinker at the same time (*16*).

A sub-micrometer-sized semiconductor post is placed at the center of the single-cell photonic crystal resonator (Fig. 1A). The thickness of the semiconductor slab is 282.5 nm. Electrons are supplied laterally from the top electrode, whereas holes are injected directly through the bottom post. The carriers recombine in the six strain-compensated InGaAsP quantum wells that are designed to have an electroluminescence (EL) peak near communications wavelength of 1.5 μm. A doping structure that is inverted from that of a typical semiconductor laser is used to exploit the low mobility of the holes that are funneled through the sub-micrometer-sized post. The introduction of this heterojunction *n-i-p* structure also limits the occurrence of bimolecular recombination to the proximity of the central post and promotes an efficient overlap of the optical gain region with the mode profile. In addition, the modified single-cell photonic crystal cavity is surrounded by five heterogeneous photonic crystal lattices with the same lattice constant (*a*) but different air-hole sizes to improve the position and size of the central InP post (Fig. 2A). The peripheral dielectric material underneath the slab was added for mechanical support.

The fabrication procedure contains two main steps: the mesa formation and the definition of photonic crystal patterns (*17*). The scanning electron microscope (SEM), cross-sectional view in Fig. 1B shows a fabricated sub-micrometer-sized InP post. It was discovered that the speed of wet etching depends on the radii of the air holes and that the position and size of the post can be improved by systematically modifying the size distribution of the air holes. This chirped photonic crystal resonator structure improves the *Q* factor slightly; however, the resonant frequency and the modal volume of the relevant modes remain almost unchanged. This was confirmed by a three-dimensional (3D) finite-difference time-domain (FDTD) calculation.

The fabricated single-cell photonic crystal cavities are electrically pulse-pumped at room temperature. The width and the period of the injected electrical current pulse are ~6 ns and 2.5 μs, respectively (*18*). The emitted photons are collected by a 50× microscope objective lens with a numerical aperture of 0.42 and fed to a spectrometer. Single-mode lasing action was observed at a wavelength of 1519.7 nm (Fig. 3A). Above the threshold, a spectrometer-limited linewidth of 0.5 nm was measured from this nondegenerate lasing mode. The mode profile as captured by an infrared (IR) camera (Fig. 2B) exhibits a central intensity minimum and the characteristic features of a monopole mode (*5*, *15*). Monopole mode operation was confirmed by comparing the measured resonant frequencies with those obtained from the 3D FDTD calculation. Numerical structural input data directly from the SEM image were used in the FDTD computation to truthfully compensate for any fabrication imperfections. In addition, no preferred direction of polarization is observed from the top, as expected from the monopole mode (*5*).

The calculated field profiles associated with the monopole mode are shown in Fig. 2, C and D. The measured near-field profile (Fig. 2B) represents the intensity of the propagating field in the proximity of the slab within the depth of focus of the 50× objective and compares well with the vertical component of the Poynting vector computed at a plane 3.0 μm above the laser cavity that has a small post (Fig. 2C). Even the asymmetry originating from the imperfect fabrication is reasonably reproduced in the FDTD computation with the use of numerical structural input data. As a reference, the energy distribution confined in the slab is shown in Fig. 2D.

Among several theoretically identified resonant modes in the lattice parameters of Fig. 2A, only the monopole mode was experimentally observed with a gain spectrum and resonant frequency in agreement with theoretic predictions. This is attributed to the fact that the other potential central node modes, such as quadrupole or hexapole modes (*15*), are located outside the spectral gain region. No adjustable parameter was used in our computation.

The measured *Q* factor of a cold cavity for the monopole mode, as estimated from the spectral line width associated with a transparent current of ~225 μA (*8*), is ~>2500 and compares well with the computed *Q* factor of ~3480 obtained with a diamond-like post with 0.64*a* by 0.51*a* estimated from the SEM picture, where *a* is the lattice constant. The *Q* factor degrades rapidly when the post size becomes larger

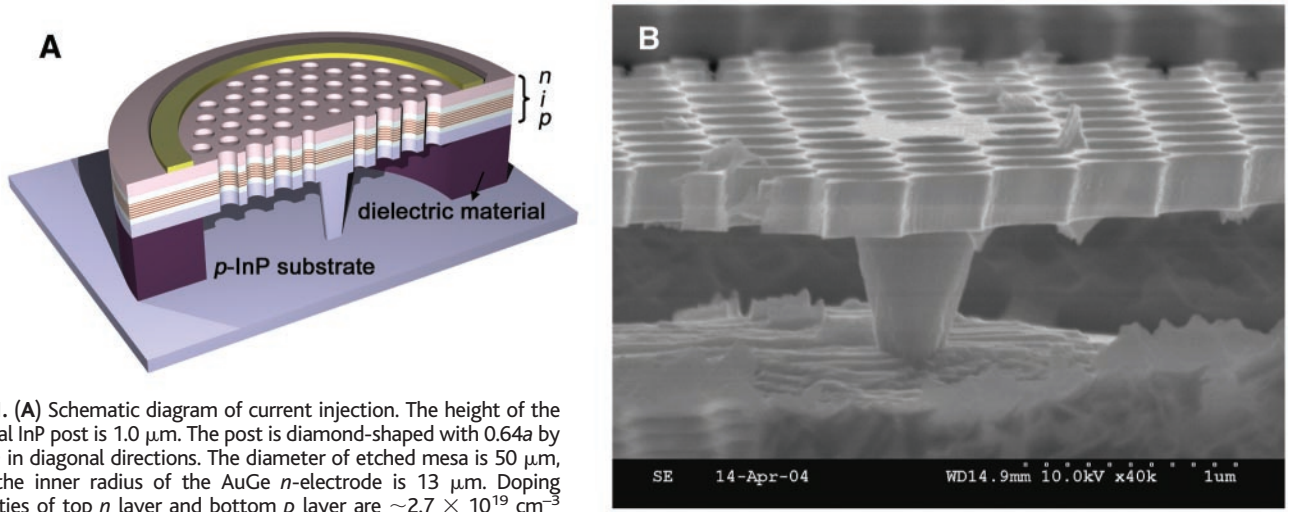

Fig. 1. (**A**) Schematic diagram of current injection. The height of the central InP post is 1.0 μm. The post is diamond-shaped with 0.64*a* by 0.51*a* in diagonal directions. The diameter of etched mesa is 50 μm, and the inner radius of the AuGe *n*-electrode is 13 μm. Doping densities of top *n* layer and bottom *p* layer are ~2.7×10^{19} cm^{-3} and ~2.5×10^{18} cm^{-3}, respectively. (**B**) Cross-sectional SEM image. From an intentionally broken sample, the region around the central post is clearly shown. Dusts around the post are remnants of the dielectric material, a photoresist, which are produced in the breaking process.

than the above value and improves slightly with smaller post size; however, the smaller post size leads to electrical resistance and thermal problems. Thus, it is important to optimize the post size considering both the optical and electrical characteristics.

The modal volume, V, of the monopole mode is found to be 5.87×10^{-2} μm^3. This value corresponds to 0.684 $(\lambda/n)^3$, where n is the refractive index of the slab material (3.4) and approaches the smallest theoretical value (*4*). The large estimated Purcell factor (389) of the current resonator implies the possibility of observing cavity quantum electrodynamic effects in an electrically driven, small, high Q cavity, photonic crystal laser (*1*).

A low threshold current of ~260 μA was observed from the peak output intensity (Fig. 3A) and compares favorably with those estimated in the optical pumping experiment (*5*–*8*). Considering that there are nonnegligible current leakage paths in the structure, the actual threshold current may be even smaller.

The soft turn-on shoulder near the threshold (Fig. 3A) implies a large spontaneous emission factor (β). The β value can be estimated from simple laser rate equations, given the experimental values and typical parameters of InGaAsP quantum wells (*15*, *19*). The critical parameter, such as the active surface area, is measured directly from the shape and size of the electroluminescent image obtained near the transparency. We found the β value is determined mostly by the shape of the light-current (L-*I*) curve below and near threshold, where slight variations of the parameters other than the surface recombination are tolerable. A β value of ~0.25 can be calculated by comparing measured spectrally integrated output intensities with L-*I* curves obtained from the rate equation (Fig. 3B). This β value is considerably higher than previously reported from the semiconductor nanolasers (*15*, *19*, *20*) and attributed to the effective carrier localization by electrical pumping together with the nondegeneracy and the small modal volume (*21*, *22*).

Typical electrical characteristics for a single-cell photonic crystal laser are shown (Fig. 3B, inset), where peak voltage and current values are used. The turn-on voltage is less than 1.0 V, and the electrical resistance is ~2.2 kΩ. Noticeable current leakage is identified from the (I dV/dI) curve. The relatively high resistance is mainly attributed to the sub-micrometer size of the p-InP post and partly attributed to the lateral distance between the n electrode and the center. The current leakage is attributed to the nonradiative recombination at the air-semiconductor air hole interfaces and at the edge of the mesa (*23*).

There are various issues still remain to be addressed before this electrically driven, ultrasmall cavity with a large Purcell factor becomes the practical on-demand single photon source. For example, one needs to find ways to place well-defined quantum dots or impurity atoms (*24*) at the antinode of the cavity and to inject

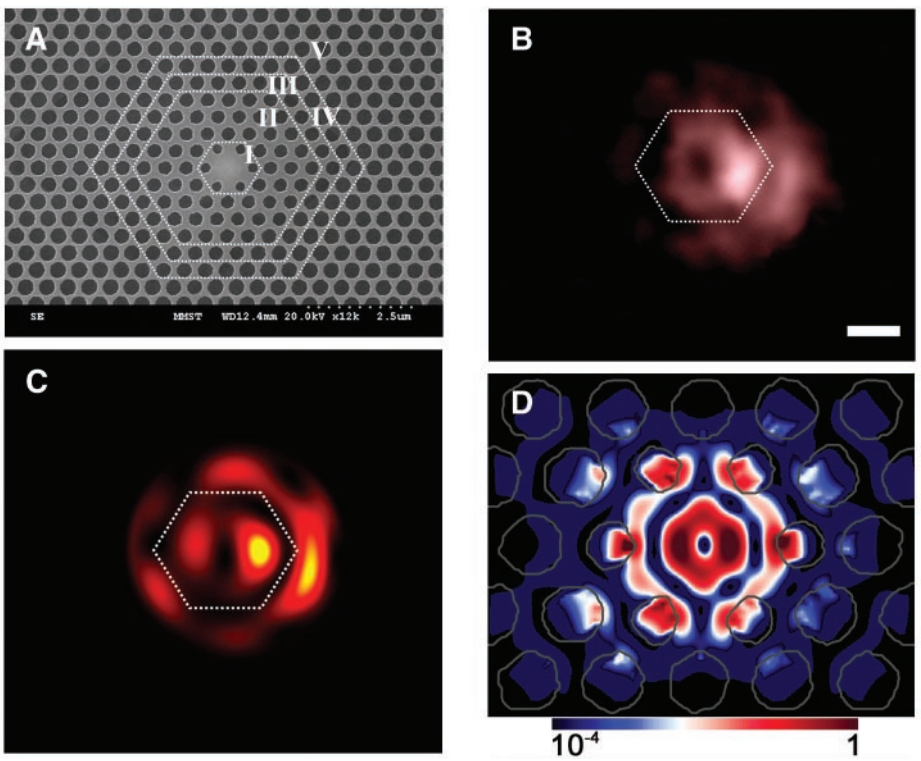

Fig. 2. (**A**) Top view of fabricated sample. The lattice constant, a, is ~510 nm, and the radii of the air holes in regions I, II, III, IV, and V are 0.28a, 0.35a, 0.385a, 0.4a, and 0.41a, respectively. (**B**) Monopole-mode image captured by an IR camera. The white bar represents 2-μm ruler. The white hexagon corresponds to region II-III interface in (A). (**C**) The vertical component of the Poynting vector obtained with the use of the structural data of (A) by 3D FDTD calculation. The calculation is performed at a vertical position of 3.0 μm above the slab, with consideration of a blurring effect by the objective lens. (**D**) The electric field intensity profile of the monopole mode calculated at the center of the slab (log scale).

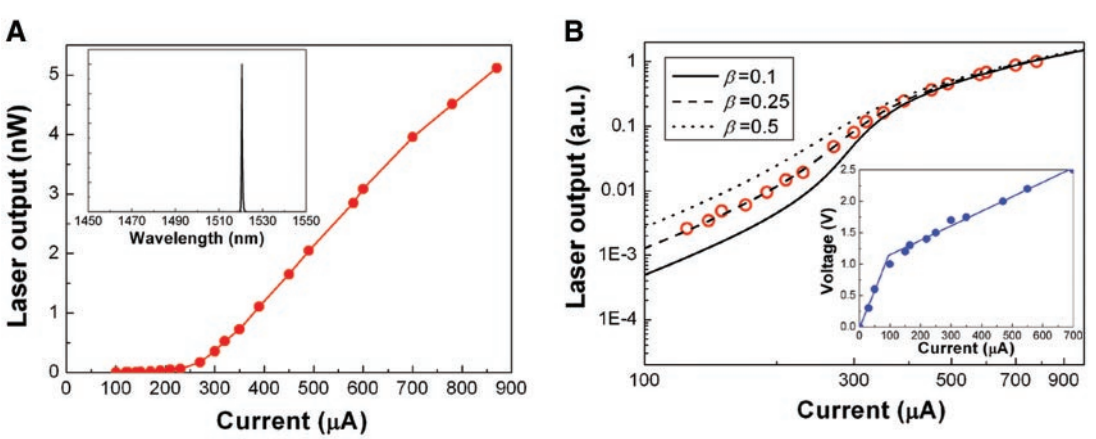

Fig. 3. (**A**) Typical L-I curve of the monopole-mode laser. Threshold current is ~260 μA, and output power indicates the peak value measured at the spectrometer. (Inset) The spectrum is taken at 700 μA. (**B**) Comparison of the measured L-I curves (red dots) with those obtained from the rate equations (black lines) for the monopole mode. Main parameters are as follows: internal efficiency η_i = 0.25, confinement factor Γ = 0.175, surface recombination velocity $v_s = 1.2 \times 10^4$ cm s^{-1}, bimolecular radiative coefficient $B = 1.6 \times 10^{-10}$ cm^3 s^{-1}, Auger coefficient $C = 5.0 \times 10^{-29}$ cm^6 s^{-1}, transparent carrier density $N_{tr} = 1.5 \times 10^{18}$ cm^{-3}, active volume $V_a = 1.72 \times 10^{-13}$ cm^3 and active surface area $A_a = 1.47 \times 10^{-8}$ cm^2. (Inset) Typical electrical characteristics are shown. a.u., arbitrary units.

single electron-hole pairs efficiently (*25*). The vertical coupling efficiency out of the cavity should be also improved by proper modifications of the cavity structure, e.g., the size of the air holes (*26*) and/or the reflectivity of the substrate. Alternatively, the photons localized in the cavity could be funneled horizontally into the neighboring low-loss photonic crystal waveguide (*27*) prepared by the quantum well intermixing (*28*). Together with all the challenging issues, the demonstration of electrically driven single-cell photonic crystal laser is believed to represent a small but meaningful step toward the ultimate photon source.

References and Notes

1. K. J. Vahala, *Nature* **424**, 839 (2003).
2. E. Yablonovitch, *Phys. Rev. Lett.* **58**, 2059 (1987).
3. T. F. Krauss, R. M. De La Rue, *Prog. Quantum Electron.* **23**, 51 (1999).
4. O. Painter *et al.*, *Science* **284**, 1819 (1999).
5. H. G. Park *et al.*, *Appl. Phys. Lett.* **79**, 3032 (2001).
6. H. Y. Ryu *et al.*, *Appl. Phys. Lett.* **80**, 3883 (2002).
7. M. Loncar, T. Yoshie, A. Scherer, P. Gogna, Y. Qiu, *Appl. Phys. Lett.* **81**, 2680 (2002).
8. K. Srinivasan *et al.*, *Appl. Phys. Lett.* **83**, 1915 (2003).
9. W. D. Zhou *et al.*, *IEEE J. Quantum Electron.* **37**, 1153 (2001).
10. D. S. Song, S. H. Kim, H. G. Park, C. K. Kim, Y. H. Lee, *Appl. Phys. Lett.* **80**, 3901 (2002).
11. T. D. Happ *et al.*, *Appl. Phys. Lett.* **82**, 4 (2003).
12. S. Noda, M. Yokoyama, M. Imada, A. Chutinan, M. Mochizuki, *Science* **293**, 1123 (2001).
13. R. Colombelli *et al.*, *Science* **302**, 1374 (2003); published online 30 October 2003; 10.1126/science.1090561.
14. A. F. J. Levi *et al.*, *Electron. Lett.* **28**, 1010 (1992).
15. H. G. Park *et al.*, *IEEE J. Quantum Electron.* **38**, 1353 (2002).
16. H. G. Park *et al.*, *IEEE Photonics Technol. Lett.* **15**, 1327 (2003).
17. Materials and methods are available as supporting material on *Science* Online.
18. The large thermal resistance (346 K mW^{-1}) of the post structure is responsible for this small duty cycle.
19. M. Fujita, R. Ushigome, T. Baba, *IEEE Photonics Technol. Lett.* **13**, 403 (2001).
20. R. E. Slusher *et al.*, *Appl. Phys. Lett.* **63**, 1310 (1993).
21. H. Yokoyama, *Science* **256**, 66 (1992).
22. J. Vuckovic *et al.*, *IEEE J. Quantum Electron.* **35**, 1168 (1999).
23. L. A. Coldren, S. W. Corzine, *Diode Lasers and Photonic Integrated Circuits* (Wiley, New York, 1995).
24. Z. Yuan *et al.*, *Science* **295**, 102 (2002); published online 13 December 2001; 10.1126/science.1066790.
25. J. Kim, O. Benson, H. Kan, Y. Yamamoto, *Nature* **397**, 500 (1999).
26. S. H. Kim, S. K. Kim, Y. H. Lee, unpublished data.
27. S. Noda, A. Chutinan, M. Imada, *Nature* **407**, 608 (2000).
28. D. G. Deppe, N. Holonyak Jr., *J. Appl. Phys.* **64**, R93 (1988)

29. This work was supported by the National Research Laboratory Project of Korea and the National Research and Development Project for Nano Science and Technology.

Supporting Online Material

www.sciencemag.org/cgi/content/full/305/5689/1444/DC1

Materials and Methods

Figs. S1 to S4

1 June 2004; accepted 29 July 2004

Macroscopic, Neat, Single-Walled Carbon Nanotube Fibers

Lars M. Ericson,[1,2] Hua Fan,[1,2] Haiqing Peng,[1,2] Virginia A. Davis,[1,3] Wei Zhou,[5] Joseph Sulpizio,[1,2] Yuhuang Wang,[1,2] Richard Booker,[1,2] Juraj Vavro,[5] Csaba Guthy,[5] A. Nicholas G. Parra-Vasquez,[1,3] Myung Jong Kim,[1,2] Sivarajan Ramesh,[1,2] Rajesh K. Saini,[1,4] Carter Kittrell,[1,2] Gerry Lavin,[6] Howard Schmidt,[1,2] W. Wade Adams,[1,2] W. E. Billups,[1,4] Matteo Pasquali,[1,3] Wen-Fang Hwang,[1,2]* Robert H. Hauge,[1,2] John E. Fischer,[5] Richard E. Smalley[1,2]*

Well-aligned macroscopic fibers composed solely of single-walled carbon nanotubes (SWNTs) were produced by conventional spinning. Fuming sulfuric acid charges SWNTs and promotes their ordering into an aligned phase of individual mobile SWNTs surrounded by acid anions. This ordered dispersion was extruded via solution spinning into continuous lengths of macroscopic neat SWNT fibers. Such fibers possess interesting structural composition and physical properties.

Individual single-walled carbon nanotubes (SWNTs) possess remarkable mechanical (*1–3*), electrical (*4–6*), and thermal (*7*, *8*) properties that equal, or even surpass, those of other benchmark materials (steel, copper, and diamond, respectively). Applications on the nanometer and micrometer scale, such as SWNT-based transistors (*9*) and chemical sensors (*10*), are progressing rapidly. To date, SWNT composite fibers have been produced that show notable mechanical reinforcement (*11–13*) or improvements in otherwise marginal transport properties (*14*). However, they still fall far short of the impressive properties of individual SWNTs. Neat SWNT fibers have only been produced in relatively short centimeter lengths through laboratory processes with limited industrial scalability (*15–17*), or have been produced in continuous lengths during the nanotube synthesis process, with high levels of impurities and marginal alignment (*18*). Starting with purified SWNTs, we have produced well-aligned continuous macroscopic fibers, without any supporting surfactant or polymer structure. Fibers were made from concentrated dispersions of SWNTs in 102% sulfuric acid via an industrially viable wet spinning technique.

Because of the high temperature stability of SWNTs, melt spinning is not an option. Wet spinning is the only viable approach, as is the case for conventional rodlike polymers such as poly(p-phenylene benzobisoxazole) (PBO), poly(p-phenylene terephthalamide) (PPTA), and poly(p-phenylene benzobisthiazole) (PBZT). The main challenge to the production of neat SWNT fibers is dispersing the SWNTs at high enough concentrations suitable for efficient alignment and effective coagulation. However, because of their chemical inertness and strong intertube van der Waals attractions, SWNTs aggregate into ropes with limited solubility in aqueous, organic, or acidic media. Even in stable organic (such as dimethyl formamide or dichlorobenzene) or surfactant-aided aqueous (such as sodium dodecyl sulfate or Triton X-100) dispersions, SWNTs are typically limited to low concentrations of nanotube bundles. If a surfactant is used to disperse the SWNTs, there is the added complication of removing the surfactant from the fiber during coagulation or after processing. In superacids (100+% sulfuric acid), SWNTs form charge-transfer complexes of individual positively charged nanotubes surrounded by a finite number of sulfuric acid anions (*19*). At very low concentration, such charged tube–anion complexes behave as Brownian rods (*20*). At higher concentration [>0.03 weight % (wt%)], a small amount of dissolved individual tubes coexists with a SWNT spaghetti phase consisting of seemingly endless "swollen" ropes of well-aligned positively charged SWNTs intercalated by sulfuric acid anions (*19*). The SWNTs in the spaghetti are mobile and at a high enough concentration (>4 wt%), they coalesce and form ordered domains (*20*), behaving similarly to nematic liquid crystalline rodlike polymers. The SWNT/acid system is very sensitive to water; the introduction of even minimal moisture causes phase separation and the precipitation of discrete needle-like crystal solvates,

[1]Center for Nanoscale Science and Technology, [2]Carbon Nanotechnology Laboratory, [3]Department of Chemical Engineering, [4]Department of Chemistry, Rice University, Houston, TX 77005, USA. [5]Department of Materials Science and Engineering, University of Pennsylvania, Philadelphia, PA 19104, USA. [6]Carbon Consultations, 15 Wellesley Road, Swarthmore, PA 19081, USA.

*To whom correspondence should be addressed. E-mail: whwang@rice.edu (W.F.H.); smalley@rice.edu (R.E.S.)

termed "SWNT alewives" (*19*, *20*). Using conventional fiber-spinning techniques, this ordered SWNT dispersion can be extruded and coagulated in a controlled fashion to produce continuous lengths of macroscopic neat SWNT fibers (*21*).

SWNTs used in this study were produced by high-pressure decomposition of CO (HiPco) (*22*, *23*) and were purified to remove excess metal catalyst (*24*–*26*). An 8 wt% dispersion of purified SWNTs in 102% sulfuric acid (2 wt% excess SO_3) was prepared in a nitrogen-purged dry box. The mixture was manually mixed and then transferred to the mixing apparatus via a stainless steel syringe. The mixture remained fastidiously dry during transfer and mixing to prevent the formation of SWNT alewives or changes in the acid's protonating ability. Extensive mixing was accomplished by two alternating pneumatic pistons, which pushed the SWNT dope back and forth through an actively rotating shear cell within an evacuated housing (*26*). The speed of the mixing pistons under a constant applied pneumatic pressure allowed for relative changes in dope viscosity to be monitored. When the viscosity reached a steady state, the SWNT material was extruded through a small capillary tube (<125 μm in diameter) into a coagulation bath (Fig. 1B). Fibers were produced under a variety of conditions, including different dope temperatures (0° to 100°C), coagulants (diethyl ether, 5 wt% aqueous sulfuric acid, or water), and coagulation bath temperatures (0°C and room temperature). In the case of aqueous coagulants, fibers were washed for several hours before collection onto a Teflon drum (Fig. 1C). To remove water and residual acid, water-coagulated fibers were dried in a vacuum oven at 100°C, followed by annealing in a flow of H_2/Ar (1:1) at 1 atm and 850°C for 1 hour. Fibers extruded into diethyl ether dried quickly in air. Before conductivity and x-ray diffraction (XRD) measurements, all fibers were further annealed in vacuum at ~1100°C.

Scanning electron micrograph (SEM) images show highly aligned macroscopic fibers consisting solely of SWNTs without any surface contaminants or impurities (Fig. 2, C and D). As in rodlike polymer spinning, the morphology of the fibers was strongly determined by their coagulation conditions. Fibers spun into diethyl ether possessed a collapsed structure (commonly referred to as "dog-bone") due to the rapid flux of sulfuric acid leaving the fiber during the coagulation process. A dense rigid skin formed, which collapsed upon evaporation of the ether, resulting in a fiber of density 0.87 ± 0.08 g/ml. When spun into dilute sulfuric acid or water, the fiber retained its circular shape and coagulated in a more uniform manner (Fig. 2C). These fibers possessed a density of 1.11 ± 0.07 g/ml, which is consistent with more uniform coagulation and fewer internal voids. The fact that the water-coagulated fibers had a density 77% that of the theoretical close-packing density for 1.0-nm nanotubes (1.5 g/ml) is encouraging. In addition to overall morphology, all of the neat fibers possessed an interesting substructure of nanotube super-ropes (Fig. 2D), approximately 200 to 600 nm in diameter. These super-ropes were typically well packed together and possessed connectivity between one another. A closer examination of these super-ropes shows that they are themselves composed of a dense packing of smaller ropes approximately 20 nm in diameter. Similar to the elemental microfibrils commonly observed in many rigid rod polymer fibers, they are believed to be formed during the coagulation of liquid crystalline samples during the extrusion process (*27*).

In addition to the qualitative alignment information that SEM analysis provided, polarized Raman spectroscopy and XRD have been used to probe the degree of alignment (*28*). Because of the anisotropic polarization of SWNTs, the ratio of a SWNT sample's G-band intensity (parallel versus perpendicular) provides a useful probe of the relative degree of alignment and has been used to probe other SWNT objects (*16*, *29*). The neat SWNT fibers possess a Raman ratio greater than 20:1. XRD analysis reveals that both ether-coagulated and water-coagulated fibers are highly aligned, with a full width at half maximum (FWHM) mosaic angle of $\phi = 31°$ and an unaligned fraction less than 10%. In comparison, Fischer *et al.*'s SWNT magnetic assemblies possessed FWHM of $\phi = 33°$, a Raman ratio of 4:1, and an unaligned fraction of 21% (*30*); Wei *et al.*'s vapor-grown SWNT fibers had a $\phi = 75°$ (*31*) and Vigolo *et al.*'s polymer-assisted SWNT fibers possessed FWHM of $\phi = 50°$ (*32*).

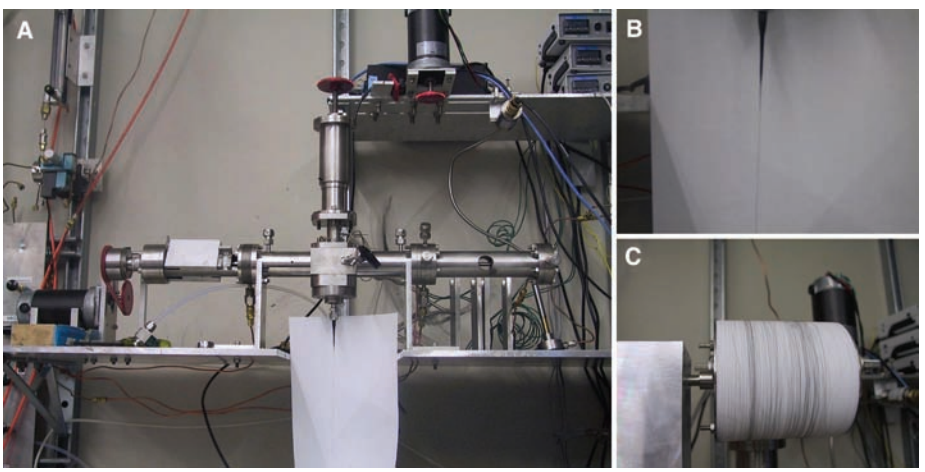

Fig. 1. The spinning process for SWNTs in 102% sulfuric acids. (**A**) The custom-built apparatus used for mixing and extruding neat SWNT fibers. (**B**) A jet of SWNT dispersion being extruded from a capillary tube. (**C**) A 30-m spool of water-coagulated fiber.

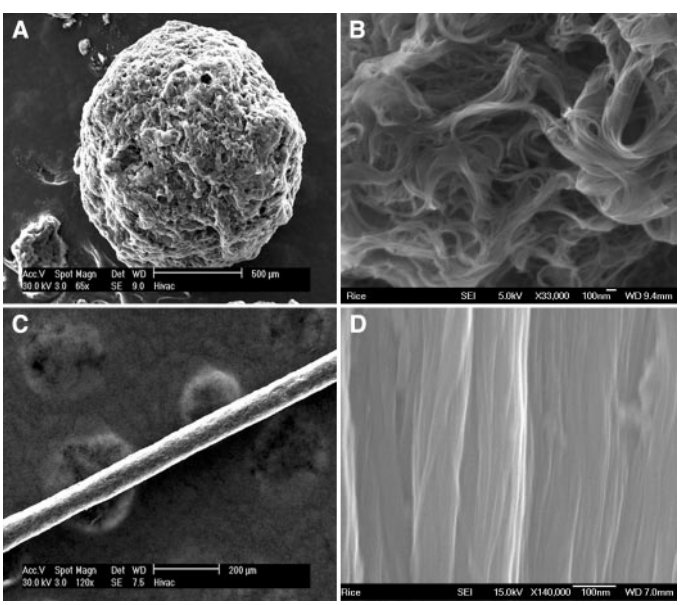

Fig. 2. SEM images showing the evolution of purified SWNTs into continuous fiber. (**A**) SWNTs after the purification process (*24*). (**B**) View inside the purified SWNTs shows a tangled mass of SWNT ropes that are 20 to 30 nm in diameter. (**C**) An annealed neat SWNT fiber spun from 8 wt% dispersion in 102% sulfuric acid and coagulated in water. (**D**) Higher magnification of the neat fiber surface shows that all the ropes have coalesced into aligned super-ropes that are 200 nm or larger in diameter.

The neat SWNT fibers possess good mechanical properties, with a Young's modulus of 120 ± 10 GPa and a tensile strength of 116 ± 10 MPa. The modulus is a good indicator of mechanical performance, because the strength is limited by the presence of localized defects and voids. In comparison, laboratory-grade PBO fibers possess a Young's modulus of 138 GPa and a tensile strength of 2.6 GPa (*11*). The electrical resistivity of the fibers is around ρ = 0.2 milliohm·cm, with an order of magnitude increase upon high-temperature annealing, which removes residual acid and the initial doping (*33*). The thermal conductivity of ether-coagulated fibers is κ = 21 W/K·m. Both conductivities are two orders of magnitude higher than those of SWNT fibers that involve polymers in their production process (*12*), but are similar to those of randomly oriented (*34*) and aligned mats of SWNTs (*30*). Given that the connectivity between SWNTs within a fiber is critical for transport properties and the presence of more than 20% voids, these values are not unexpected.

The success of this fiber-spinning process is predicated on the formation of SWNT/acid charge-transfer complexes (Fig. 3, A and B), which are highly mobile, highly dispersible, and easily align into ordered mesophases in SWNT dopes. This model is further supported by the swelling behavior of SWNT fibers in sulfuric acids. Inside a dry glove box, lengths of neat SWNT fiber were sealed in a quartz cell with sulfuric acid of varying concentrations and observed under an optical microscope. Fibers reexposed at room temperature to 102% or 120% sulfuric acid quickly swelled and sank to the bottom of the cell, whereas fibers exposed to 96% sulfuric acid (that is, concentrated) floated at the top. However, upon heating to 60°C, the fiber in concentrated sulfuric acid swelled and sank to the bottom. The ratio (R) of diameters before and after exposure to sulfuric acid was used to quantify the degree of swelling. In 102% sulfuric acid, ether-coagulated fiber was found to swell to $R = 1.9 \pm 0.1$, whereas the denser, water-coagulated, dried and annealed fibers swelled to $R = 1.66 \pm 0.11$ and 1.33 ± 0.1, respectively (Fig. 3, C and D). In 120% sulfuric acid, $R = 1.96 \pm 0.11$ and 1.44 ± 0.09 for the water-coagulated, dried and annealed fibers, respectively. Because the swelling ratios were less than two, there were probably fewer than three acid layers between adjacent nanotubes.

Given the considerable difference in density between SWNT fibers (< 1.11 g/ml), a close-packed triangular lattice of empty SWNTs (~1.5 g/ml), and sulfuric acid (~1.9 g/ml), the sinking behavior cannot be explained by the idea that sulfuric acid simply fills accessible nanotube voids and swells the fiber. Instead, the sulfuric acid within the fiber must form a dense phase. Sulfuric acid molecules intercalate nanotube ropes within

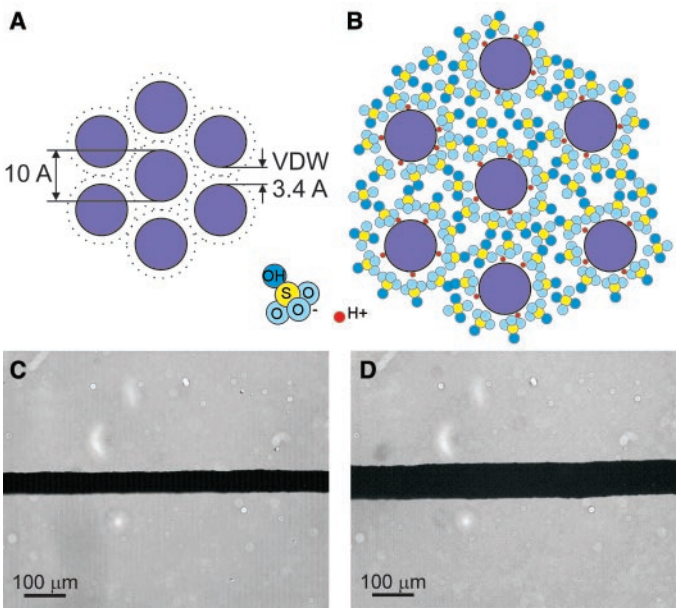

Fig. 3. A model illustrating the swelling of SWNT ropes in sulfuric acid. (**A**) A cartoon of SWNTs in van der Waals (VDW) contact within a neat fiber. (**B**) The same SWNT fiber after reexposure to sulfuric acid. A dense layer of sulfuric acid anions surrounds the individual nanotubes, forming an energetically favorable charge-transfer complex; additional acid molecules fill available voids. The chemical and structural character of the model is meant to be highly schematic. One possible mechanism that generates the repulsive interaction of SWNTs is direct protonation. (**C**) A neat fiber (52.7 μm in diameter) within a quartz cell (**D**) swells to 87.4 μm in diameter ($R = 1.66$) upon exposure to 102% sulfuric acid.

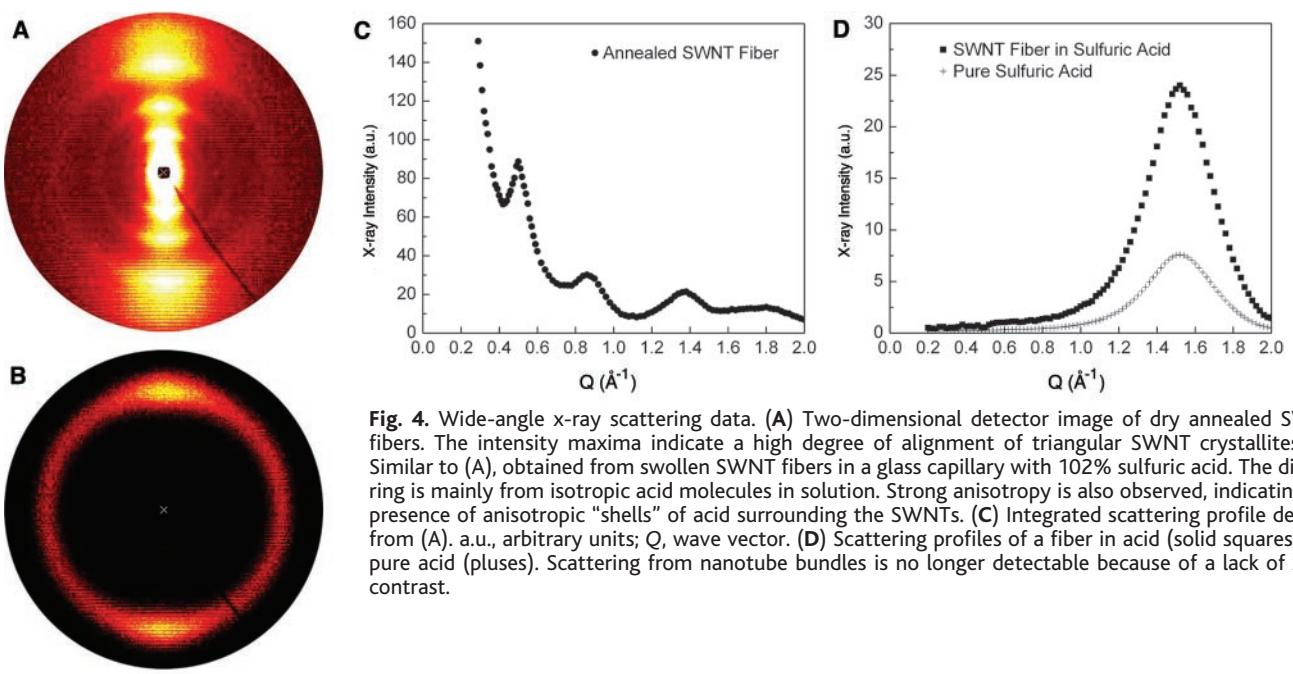

Fig. 4. Wide-angle x-ray scattering data. (**A**) Two-dimensional detector image of dry annealed SWNT fibers. The intensity maxima indicate a high degree of alignment of triangular SWNT crystallites. (**B**) Similar to (A), obtained from swollen SWNT fibers in a glass capillary with 102% sulfuric acid. The diffuse ring is mainly from isotropic acid molecules in solution. Strong anisotropy is also observed, indicating the presence of anisotropic "shells" of acid surrounding the SWNTs. (**C**) Integrated scattering profile derived from (A). a.u., arbitrary units; Q, wave vector. (**D**) Scattering profiles of a fiber in acid (solid squares) and pure acid (pluses). Scattering from nanotube bundles is no longer detectable because of a lack of x-ray contrast.

the fiber and possibly fill the SWNTs, forming charge-transfer complexes with individual nanotubes. The fact that solid sulfuric acid has a density of 2.13 g/ml (*35*) suggests that there is a similar increase in density for the ordered layer of sulfuric acid molecules surrounding the nanotubes (Fig. 3B). XRD data further support this interpretation.

In addition to XRD performed on dry fiber samples, data were also collected on a swollen SWNT fiber sample sealed in a glass capillary with 102% sulfuric acid. The pattern no longer showed the distinct Bragg reflections associated with SWNTs (*4*) in the neat fibers, and the scattering intensity at small angles diminished (Fig. 4), indicating that (i) the intercalation of SWNTs by sulfuric acid smears out the triangular lattice, and (ii) the density, and therefore the electron density, of the acid-swollen fibers has become similar to that of the superacid. Instead, the scattering profile shows only highly anisotropic scattering from the pure 102% sulfuric acid (Fig. 4D) but with about the same degree of orientation (FWHM = 32.1°) as the dry fibers. This means that some of the acid molecules must be aligned with respect to the fiber axis and that the anisotropic scattering is from a cylindrical shell of perhaps three acid monolayers in which the mass density is somewhat enhanced with respect to the bulk liquid because of interactions with the nanotubes. These results further affirm our model of acid-intercalated SWNT ropes in superacids, with individual nanotubes surrounded by ordered layers of sulfuric acid.

References and Notes

1. A. Krishnan, E. Dujardin, T. W. Ebbesen, *Phys. Rev. B* **58**, 14013 (1998).
2. D. A. Walters *et al.*, *Appl. Phys. Lett.* **74**, 3803 (1999).
3. M. F. Yu, B. S. Files, S. Arepalli, R. S. Ruoff, *Phys. Rev. Lett.* **84**, 5552 (2000).
4. A. Thess *et al.*, *Science* **273**, 483 (1996).
5. S. J. Tans *et al.*, *Nature* **386**, 474 (1997).
6. P. L. McEuen, M. S. Fuhrer, H. K. Park, *IEEE Trans. Nanotech.* **1**, 78 (2002).
7. J. Hone, M. Whitney, C. Piskoti, A. Zettl, *Phys. Rev. B* **59**, R2514 (1999).
8. J. Che, T. Cagin, W. A. Goddard, *Nanotechnology* **11**, 65 (2000).
9. R. Seidel *et al.*, *Nano Lett.* **4**, 831 (2004).
10. K. Besteman, J. Lee, F. G. M. Wiertz, H. A. Heering, C. Dekker, *Nano Lett.* **3**, 727 (2003).
11. S. Kumar *et al.*, *Macromolecules* **35**, 9039 (2003).
12. B. Vigolo *et al.*, *Science* **290**, 1331 (2000).
13. A. B. Dalton *et al.*, *Nature* **423**, 703 (2003).
14. R. Andrews *et al.*, *Appl. Phys. Lett.* **75**, 1329 (1999).
15. H. W. Zhu *et al.*, *Science* **296**, 884 (2002).
16. H. H. Gommans *et al.*, *J. Appl. Phys.* **88**, 2509 (2000).
17. K. Jiang, Q. Li, S. Fan, *Nature* **419**, 801 (2002).
18. Y. Li, I. A. Kinloch, A. H. Windle, *Science* **304**, 274 (2004).
19. S. Ramesh *et al.*, *J. Phys. Chem. B* **108**, 8794 (2004).
20. V. A. Davis *et al.*, *Macromolecules* **37**, 154 (2004).
21. R. E. Smalley *et al.*, U.S. Patent Application 20030170166 (2003).
22. P. Nikolaev *et al.*, *Chem. Phys. Lett.* **313**, 91 (1999).
23. M. J. Bronikowski, P. A. Willis, D. T. Colbert, K. A. Smith, R. E. Smalley, *J. Vac. Sci. Technol.* **19**, 1800 (2001).
24. The SWNTs were purified using a protocol based on Chiang *et al.*'s work (*25*). The process involved soft-baking followed by HCl extraction of the metal catalyst. During neutralization of the acid, the nanotube slurry was exchanged multiple times with hexanes in a separation flask. The SWNTs were found to readily move to the hexane layer, leaving aqueous HCl with extracted metal catalyst that was easily drained off. The purified SWNTs possessed less than 1.2 atom % residual metal catalyst, as determined by thermogravimetric analysis. The resulting purified material was a light porous powder with high surface area that could be easily handled (Fig. 1A).
25. I. W. Chiang, B. E. Brinson, R. E. Smalley, J. L. Margrave, R. H. Hauge, *J. Phys. Chem. B* **105**, 1157 (2001).
26. L. M. Ericson, thesis, Rice University, Houston, TX (2003).
27. Y. Tsabba, D. M. Rein, Y. Cohen, *J. Poly. Sci. B* **40**, 1087 (2002).
28. A Renishaw MicroRaman System 1000 with a 780-nm diode laser was used to collect Raman spectra. A multiangle diffractometer equipped with a Cu rotating anode, double-focusing optics, evacuated flight path, and two-dimensional wire detector was used for XRD measurements.
29. G. S. Duesberg, I. Loa, M. Burghard, K. Syassen, S. Roth, *Phys. Rev. Lett.* **85**, 5436 (2000).
30. J. E. Fischer *et al.*, *J. Appl. Phys.* **93**, 2157 (2003).
31. B. Q. Wei *et al.*, *Nano Lett.* **2**, 1105 (2002).
32. B. Vigolo, P. Poulin, M. Lucas, P. Launois, P. Bernier, *Appl. Phys. Lett.* **81**, 1210 (2002).
33. W. Zhou *et al.*, *J. Appl. Phys.* **95**, 649 (2004).
34. J. E. Fischer *et al.*, *Phys. Rev. B* **55**, R4921 (1997).
35. D. R. Allan, S. J. Clark, A. Dawson, P. A. McGregor, S. Parsons, *J. Chem. Soc. Dalton Trans.* **8**, 1867 (2002).

36. This work was supported by the Office of Naval Research (ONR) under the DURINT program, grant N00014-01-1-0789; by ONR N00014-03-1-0890; by U.S. Department of Energy grant DE-FG02-98ER45701; and by the Robert A. Welch Foundation. We thank S. Kumar, K. Winey, and R. Baughman for valuable conversations.

14 June 2004; accepted 30 July 2004

External and Internal Morphology of the BAR 1002′00 *Orrorin tugenensis* Femur

K. Galik,[1] B. Senut,[2] M. Pickford,[3] D. Gommery,[4] J. Treil,[5] A. J. Kuperavage,[6] R. B. Eckhardt[6]*

Late Miocene fossils from the Lukeino Formation in Kenya's Tugen Hills are assigned to *Orrorin tugenensis*. Of 20 fossils recovered there to date, 3 are proximal femurs. One of these, BAR 1002′00, preserves an intact head connected to the proximal shaft by an elongated neck. Although this fossil is comparable in size to *Pan troglodytes*, computerized tomography scans of the neck-shaft junction of BAR 1002′00 reveal that the cortex is markedly thinner superiorly than inferiorly, differing from the approximately equal cortical thicknesses observed in extant African apes, approaching the condition in later hominids, and indicating that *O. tugenensis* was bipedal.

Orrorin tugenensis is thought to represent some of the earliest known hominids, securely dated biostratigraphically, geologically, and radiometrically, as well as by paleomagnetism, to the Late Miocene, approximately 6 million years ago (Ma) (*1*, *2*). Samples (*1*) are derived from four localities in the Lukeino Formation (Aragai, Cheboit, Kapcheberek, and Kapsomin), along the eastern approach to the Tugen Hills in Baringo District, Kenya. Twenty fossils representing at least five individuals have been discovered there. Of these, three are portions of femurs critical for determining posture. BAR 1215′00 is a small fragment consisting of the proximal portion of a right femur lacking neck and head and preserving only about 20 mm of the upper shaft below the base of the greater trochanter, which also is missing. BAR 1003′00 comprises approximately half of a proximal left femur, including the entire lesser trochanter but lacking both the greater trochanter and the femoral head. The third partial femur, BAR 1002′00, is more complete, including about 200 mm of shaft plus an intact head that is connected to the shaft by a somewhat elongated neck; its anatomical features have been described fully and compared in detail with extant African apes and humans, as well as with Plio-Pleistocene hominids (*1*, *3*, *4*).

The Tugen Hills material apparently is younger than the Chad cranium (*Sahelanthropus tchadensis*) from the Toros-Menalla locality (*5*), the age of which is estimated to be in the range of 6 to 7 million years from faunal correlations with East African sites

[1]Orthopedic Biomechanics Laboratory, Allegheny General Hospital, Pittsburgh, PA 15212, USA. [2]Département Histoire de la Terre, Muséum national d'Histoire naturelle, UMR 5143 du CNRS, Case Postale 38, 57, rue Cuvier, 75231 Paris Cedex 05, France. [3]Chaire de Paléoanthropologie et de Préhistoire, Collège de France, et UMR 5143 du CNRS, Département Histoire de la Terre, Muséum national d'Histoire naturelle, UMR 5143 du CNRS, Case Postale 38, 57, rue Cuvier, 75231 Paris Cedex 05, France. [4]UPR 2147 CNRS, 44, rue de l'Amiral-Mouchez, 75014 Paris & GDR 983 du CNRS, 8, rue Buffon, 75005 Paris, France. [5]Service du Radiologie, UMR 8555 du CNRS et Service de Radiologie, Clinique Pasteur, 45, Avenue de Lombez, 31300 Toulouse, France. [6]Laboratory of Comparative Morphology and Mechanics, Department of Kinesiology, Pennsylvania State University, University Park, PA 16802, USA.

*To whom correspondence should be addressed. E-mail: eyl@psu.edu

(mainly Lothagam in Kenya), moderately older than the remains from Ethiopia's Middle Awash valley, which are dated more securely than those from Chad by techniques including biostratigraphic, paleomagnetic, and radioisotopic data to a narrower range of 5.2 to 5.8 Ma (*6*). Beyond the different geographic and temporal relations, comparisons among the earliest putative hominids are exacerbated by the paucity of cranial elements in the Tugen material, absence of postcrania associated with the Chad cranium (*5*), and the inclusion of just one proximal pedal phalanx among the Middle Awash remains, along with dental elements that are said to display a suite of hominid features (*6*).

Despite their temporally intermediate position between the other two early sites that have yielded putative hominids, the Tugen Hills fossils sometimes still are characterized as ambiguous in the features of lower-limb anatomy shared with later members of our lineage (*7*). Here, we address this phylogenetic question directly through functional morphology. With upright posture and habitual or obligate bipedal locomotion accepted as critical adaptive signatures of our lineage, documenting anatomical correlates of these behaviors in BAR 1002′00 would support its hominid status. We used computerized tomography (CT) to quantify the internal distribution of cortical bone in the most ancient femora pertinent to reconstructing hominid origins.

BAR 1002′00 has several external morphological attributes that are characteristic of Plio-Pleistocene through later hominids and that distinguish them from African apes: a shallow trochanteric fossa, an obturator externus groove, and a long femoral neck (*3*, *8*). The trochanteric fossa demarcates chimpanzee femurs from those of most past and present hominids, although its developmental genesis and functional consequences are as yet incompletely understood. In chimpanzees, the central portion of the trochanteric fossa commonly includes a cavity that extends deeply into the diaphyseal shaft, approaching the medullary canal in some specimens (*8*). In BAR 1002′00 as well as the other two partial femurs attributed to *Orrorin tugenensis*, in common with South African Plio-Pleistocene hominids, there is no evidence of deep penetration by the trochanteric fossa into the shaft, in contrast with the usual morphology observed in *Pan*.

The obturator externus muscle is an adductor, flexor, and external rotator of the thigh. One of its primary functions is to shorten the distance between the pelvis and the femur, and consequently to stabilize the hip joint. The obturator externus groove, present in BAR 1002′00, is believed to result from bone remodeling to accommodate the direct, although passive, contact of the obturator

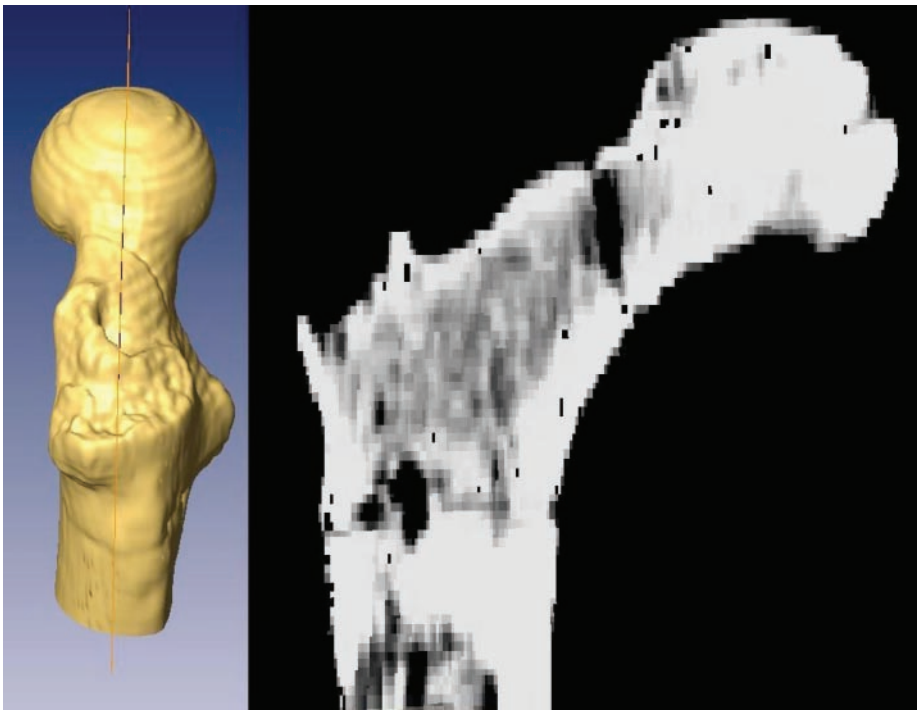

Fig. 1. 3-D model of BAR 1002′00 showing probe line along which BAR 1002′00 was sectioned (**left**), and the anterior-posterior section itself (**right**).

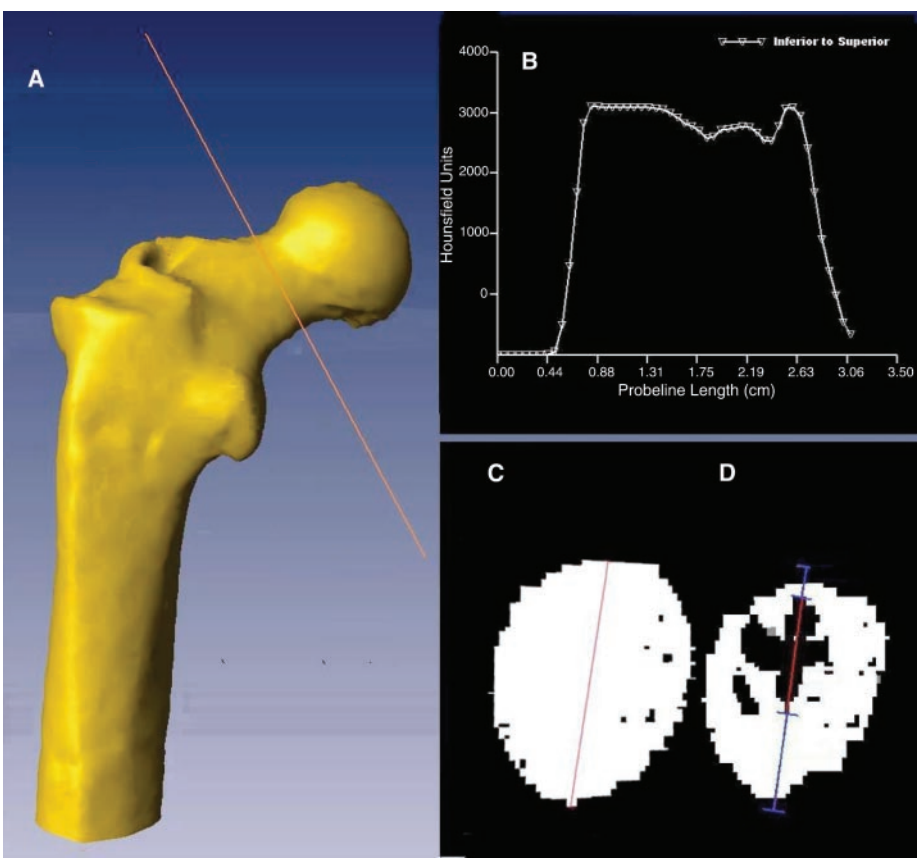

Fig. 2. (**A**) 3-D model of BAR 1002′00 reconstructed from CT sections. Probe line shows location of more proximal section. (**B**) Hounsfield plot with plateau at left indicates presence of some "white overflow," which occurs when all pixels have the maximum CT number (*10*). (**C**) Outline of section at interface of air to cortical bone. (**D**) Outline of section at interface of cortical to trabecular bone. Inferior cortical thickness (ICT) = 8.6 mm; superior cortical thickness (SCT) = 2.8 mm. Refer to Fig. 3 for notes regarding possible complicating effects of white overflow.

externus tendon with the dorsal surface of the femoral neck at full extension of the femur. A sample of 155 African hominoids did not include a single example of an obturator externus groove (*8*), whereas this feature is present in OH 20 from Tanzania, SK 82 and SK 97 from South Africa, and AL-333-95, AL 288-1, and MAK-VP-1/1 from Ethiopia (*3*, *8*). Femoral neck length establishes the moment arm of the anterior gluteal muscles (gluteus minimus, gluteus medius, and tensor fasciae) in the pelvic-support phase of bipedal locomotion. Therefore, a long femoral neck, which implies a reorientation of the line of action of the anterior gluteals, is strongly indicative of habitual hominid locomotor function (*8*). In BAR 1002′00, the femoral neck length exceeds that of Miocene hominoid fossils attributed to *Afropithecus*, *Dryopithecus*, *Kenyapithecus*, *Nacholapithecus*, *Oreopithecus*, and *Ugandapithecus* (*3*). Among Plio-Pleistocene hominids, a long femoral neck recently has been reconstructed for the partial MAK-VP-1/1 femur (*8*).

The external attributes of bipedal locomotion summarized here, and more extensively elsewhere for the Tugen Hills femurs (*3*), have developmentally determined internal structural correlates. In particular, femoral neck length has functional importance due to the force-transmission pattern through the hip joint resulting from the mass of the trunk and head superior to it. Biomechanically, the structure of the femoral neck approximates a cantilevered beam. Among apes that assume a variety of postures during locomotion but are primarily quadrupedal, the femoral neck is relatively short. A cross section in the region of the neck-shaft junction (which biomechanically is the most relevant section) includes a central marrow cavity surrounded by trabecular bone extending outward toward the surface, which in turn is characterized by a relatively uniform dense ring of cortical bone. The outer cortical bone is thickened inferiorly due to compressive forces. Also, because cortical bone is weaker under tension than under compression, bone in the superior margin of the femoral neck is thickened as well, attaining dimensions that actually exceed those of the inferior margin in more than half (52%) of *Pan troglodytes* observed (*9*).

In contrast, among past and present hominids the femoral neck exhibits cortical bone that is much thinner superiorly than inferiorly (*8*, *9*). This reduction in superior cortical thickness is chiefly due to the altered functional demands of hominid bipedal locomotion, which over time has modified the action of the abductor muscles (gluteus medius and minimus). In hominids, these muscles are aligned approximately parallel to the femoral neck so that their contraction compresses the bone, balancing the tension that produced the thickening of the superior cortex in apes. The result is that in hominids, cortical thickening is greatest along the inferior margin of the neck-shaft junction. At this point of highest bending stress, in extant humans, superior cortical thickness approximates one-quarter of inferior cortical thickness or less; in extant African apes, superior and inferior cortical thicknesses approximate a 1:1 ratio (*9*, *10*).

We used CT scanning to display the interior structure of the more complete Tugen left femur, BAR 1002′00, which comprises the head, neck, and proximal shaft; an anterior-posterior CT scan of this fossil is shown in Fig. 1.

Overall, despite the presence of cracks and matrix in some regions, superior cortical bone consistently appears thinner than inferior cortical bone along the entire femoral neck from the head to the neck-shaft junction. We examined slices from the base of the femoral head to the trochanteric line; two are shown here (Figs. 2 and 3), and the remaining sections are in fig. S1. Each cortical thickness was calculated by the standard approach of using two thresholds (*11*, *12*), the first at the air-bone interface (Fig. 2C and Fig. 3C) and the second at the cortical-trabecular bone interface (Fig. 2D and Fig. 3D) (*13*).

For measurements of cortical bone thicknesses in Figs. 2 and 3, the infero-superior (IS) axis was defined conventionally as a line connecting the most inferior and superior points on the outer cortex (*9*), measured where the axis transected the specimen's cortical bone boundaries. In Fig. 2, C and D, although the probe is oriented to transect the thinnest portion of the inferior cortical bone, along the IS axis the ratio of inferior to superior cortical bone thickness is 3:1. In Fig. 3, C and D, because of the complex outlines of the cross section, three lines are shown: IS to the left is as previously defined, while IS to the right gauges cortical bone thicknesses at the midline of the medullary cavity. For both, the IS ratio is approximately

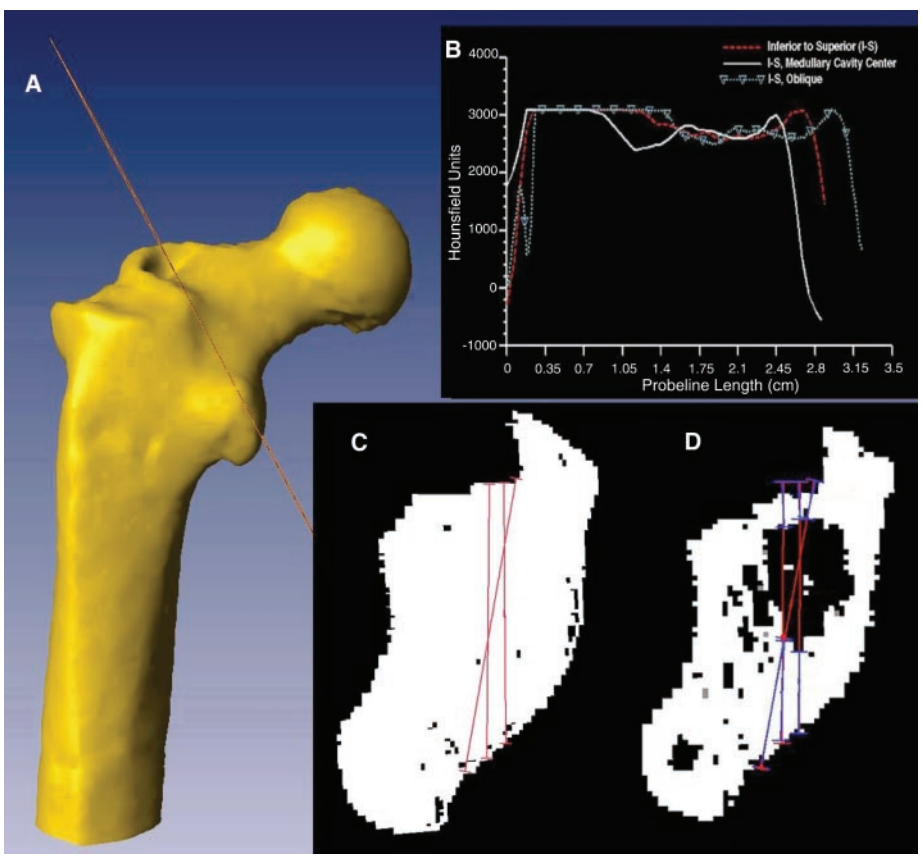

Fig. 3. (**A**) 3-D model of BAR 1002′00 with probe at neck-shaft junction. (**B**) Corresponding Hounsfield plot. (**C**) Outline of section at interface of air to cortical bone. Projection at upper right is superior margin of the trochanteric fossa. Mass with circular outline at lower left is the lesser trochanter. (**D**) Outline of section at interface of cortical to trabecular bone. As defined conventionally, ICT = 11.0 mm and SCT = 5.0 mm; in center of medullary cavity, ICT = 8.6 mm and SCT = 4.0 mm; oblique, ICT = 14.0 mm and SCT = 4.0 mm. Inferiorly there is some "black overflow," which occurs when CT numbers drop sharply and then rise again, as well as "white overflow," which could arise from mineralization of trabecular bone. One study comparing scans with and without white overflow showed an average thickness overestimation of 23% (*11*). Unless mineralization occurred selectively in the inferior cortex, it is unlikely that mineralized cortical bone accounts for the observed ratio of ICT to SCT, particularly because BAR 1002′00 absolute ICT values are nearly equaled by some extant (i.e., unmineralized) *Gorilla* and *Homo* specimens (*9*), and BAR 1002′00 absolute SCT values are less than half many SCT values in *Pan* and *Gorilla*.

2:1. The third line (IS oblique), connecting the minimum and maximum points, exclusive of the lesser trochanter (lower left) and superior margin of the trochanteric fossa (upper right), shows a ratio of 3:1. All of these values for both slices diverge markedly from the ≤1:1 ratio at the femoral neck-shaft junction for chimpanzees and gorillas (*9*) in the direction of extant human cortical bone proportions of ≥4:1. Although some nonhominoid primates exhibit superior cortex that is moderately thinner than the inferior cortex, published values (*10*) were averaged along the femoral neck and are not directly comparable to the most diagnostic point at the neck-shaft interface (*8*, *9*) reported here, where the IS ratio for the BAR 1002′00 femur is clearly distinguished from extant apes, particularly from *Pan troglodytes,* which is a close match in overall size for preserved portions of the fossil.

Our results show that the internal distribution of cortical bone in its femoral neck constitutes direct evidence for frequent bipedal posture and locomotion in this Late Miocene ancestor. In known features, external and internal, BAR1002′00 exhibits a total morphological pattern distinct from African apes, diagnostic of bipedal locomotion, and appropriate for a population standing at the dawn of the human lineage.

References and Notes

1. B. Senut *et al*., *C. R. Acad. Sci. Paris, Ser. IIa* **332**, 137 (2001).
2. Y. Sawada *et al*., *C. R. Palevol.* **1**, 293 (2002).
3. M. Pickford, B. Senut, D. Gommery, J. Treil, *C. R. Palevol.* **1**, 1 (2002).
4. M. Pickford, B. Senut, *C. R. Acad. Sci. Paris, Ser. IIa* **332**, 137 (2001).
5. M. Brunet *et al*., *Nature* **418**, 145 (2002).
6. Y. Haile-Selassie, G. Suwa, T. D. White, *Science* **303**, 1478 (2004).
7. D. Begun, *Science* **303**, 1503 (2004).
8. C. O. Lovejoy, R. S. Meindl, J. C. Ohman, K. G. Heiple, T. D. White, *Am. J. Phys. Anthropol.* **119**, 97 (2002).
9. J. C. Ohman, T. J. Krochta, C. O. Lovejoy, R. P. Mensforth, B. Latimer, *Am. J. Phys. Anthropol.* **104**, 117 (1997).
10. K. L. Rafferty, *J. Hum. Evol.* **34**, 361 (1998).
11. C. F. Spoor, F. W. Zonneveld, G. A. Macho, *Am. J. Phys. Anthropol.* **91**, 469 (1993).
12. E. H. W. Meijering, W. J. Nissen, M. A. Viergever, *Med. Image Anal.* **5**, 111 (2001).
13. Materials and methods are available as supporting material on *Science* Online.

14. We thank the Clinique Pasteur in Toulouse, France for the CT scans, D. A. Eckhardt at the Carnegie Mellon School of Computer Science for technical assistance, and J. C. Ohman and C. O. Lovejoy for access to their original data previously summarized (*9*), along with several helpful discussions. The American Philosophical Society and Sigma Xi provided support for collection of comparative CT scans at the U.S. National Museum of Natural History (Smithsonian) by R. Thorington and B. Frolich. We thank the Collège de France (Y. Coppens), the CNRS (UMR 8569, GDR 983, and PICS 1048), the Ministry of Foreign Affairs (Commission des Fouilles à l'Etranger), and the Community Museums of Kenya (E. Gitonga) for their help and support, and we thank all members of our team. The comments of three anonymous referees are acknowledged with great appreciation.

Supporting Online Material

www.sciencemag.org/cgi/content/full/305/5689/1450/DC1
Materials and Methods
Fig. S1

6 April 2004; accepted 2 August 2004

Testing Predator-Driven Evolution with Paleozoic Crinoid Arm Regeneration

Tomasz K. Baumiller[1]* and Forest J. Gahn[2]*

Regenerating arms of crinoids represent direct evidence of nonlethal attacks by predators and provide an opportunity for exploring the importance of predation through geologic time. Analysis of 11 Paleozoic crinoid Lagerstätten revealed a significant increase in arm regeneration during the Siluro-Devonian. During this interval, referred to as the Middle Paleozoic Marine Revolution, the diversity of shell-crushing predators increased, and antipredatory morphologies among invertebrate prey, such as crinoids, became more common. Crinoid arm-regeneration data suggest an increase in nonlethal attacks at this time and represent a causal link between those patterns, which implies an important role for predator-driven evolution.

Predation has been used to explain numerous macroevolutionary trends. For example, the hypothesis of escalation posits that prey evolve escape strategies (morphological, behavioral, or otherwise) as a consequence of interactions with their enemies. Vermeij (*1*, *2*) has argued that biological hazards, including predation, have increased through geologic time and, as a consequence, so have prey responses. This general trend has not been uniform: Several intervals of intensified escalation have been suggested, including the early Cenozoic (*2*), the Mesozoic (*3*), and the middle Paleozoic (*4*, *5*).

During the middle Paleozoic, the diversity of shell-crushing predators, especially arthropods and fishes, increased sharply and concomitantly with defensive features among mollusks, brachiopods, and crinoids, an event known as the Middle Paleozoic Marine Revolution (MPMR) (*4*, *5*). Crinoids, which developed more spines, thicker calyx plates, and reduced viscera through this interval (Siluro-Devonian), provide an important test of escalation because the high abundance and sessile, stalked life-habit of Paleozoic crinoids made them easily accessible to predators. Escalation implies a pronounced increase in nonlethal predation during the MPMR, a hypothesis that we test here by measuring the frequency of crinoids with regenerated arms from Paleozoic Lagerstätten, or fossil deposits of exceptional preservation.

Crinoids, like all echinoderms, exhibit exceptional regenerative abilities. In addition, they possess articulations in the arms and stalk specialized for autotomy, or active shedding of body parts (*6*–*8*). Years of observations have revealed that a variety of organisms, including starfish (*9*), crabs (*9*), sea urchins (*10*), and especially fishes (*11*–*13*), attack extant crinoids, which often leads to injuries. Although abiotic stimuli may also lead to trauma and subsequent regeneration, experiments, in situ observations, and functional morphology (*7*, *8*) suggest that predation is the predominant cause of autotomy and regeneration. Thus, arm-regeneration frequencies represent a measure of nonlethal predatory encounters (*14*–*17*). We examined well-preserved crinoids, that is, those with arms largely intact. For each individual, we recorded the number of visible arms and the number of regenerating arms. Regeneration was recognized by an abrupt change in arm diameter (Fig. 1).

Our data (Fig. 2 and table S1) show that the percentage of individuals with regenerating arms (i.e., regeneration frequency) in the early Paleozoic (Ordovician and Silurian) was <5% but increased in the middle to late Paleozoic (Devonian to Pennsylvanian) to >10%. The increase spanning the Siluro-Devonian is the only statistically significant change in the entire time series (χ^2, $P < 0.001$). The increase in regeneration frequency across the Siluro-Devonian remains statistically significant (χ^2, $P < 0.001$) even when (i) data are grouped by period (table S2), (ii) data are separated into two intervals by the Siluro-Devonian, and (iii) individual Lagerstätten are removed one at a time ("jackknife") (*18*).

Paleozoic crinoids are a morphologically heterogeneous clade—size, arm number, branching patterns of the arms, and arm-

[1]University of Michigan Museum of Paleontology, Ann Arbor, MI 48105, USA. [2]Department of Paleobiology, National Museum of Natural History, Smithsonian Institution, P.O. Box 37012, NHB MRC 121, Washington, DC 20013–7012, USA.

*To whom correspondence should be addressed. E-mail: tomaszb@umich.edu (T.K.B.); gahn.forest@nmnh.si.edu (F.J.G.)

articulation types can vary dramatically among groups. Because these factors may influence predation, regeneration, and preservation, we analyzed a morphologically more homogenous subsample, camerate crinoids (*19*, *20*). Camerates are the most diverse and abundant crinoids found at 10 of the 11 Lagerstätten. Their absence from the Pennsylvanian sample is explained by elevated extinction in the Late Mississippian (*21*, *22*). Camerates show the same pattern of increase in arm-regeneration frequency across the Siluro-Devonian as does the data for all crinoids combined (Fig. 2, C and D, and tables S3 and S4).

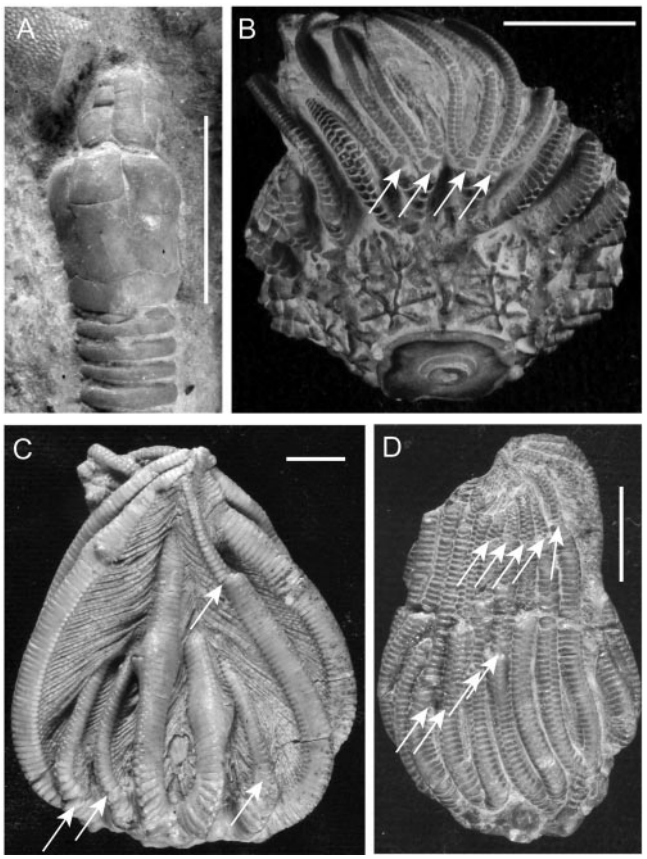

Fig. 1. Examples of regenerating arms in Paleozoic crinoids. (**A**) *Dystactocrinus constrictus*, Hall 1871, Late Ordovician, USA, USNM 93223, all arms regenerating. (**B**) *Gennaeocrinus mourantae*, Goldring 1934, Middle Devonian, Canada, USNM S4533. (**C**) *Agaricocrinus splendens*, Miller and Gurley 1890, Early Mississippian, USA, USNM S8856. (**D**) *Dimerocrinites icosidactylus*, Phillips in Murchison 1839, Middle Silurian, England, USNM S8857. White arrows point to regenerating arms. Note nine regenerating arms in (D). Scale bars, 1.0 cm.

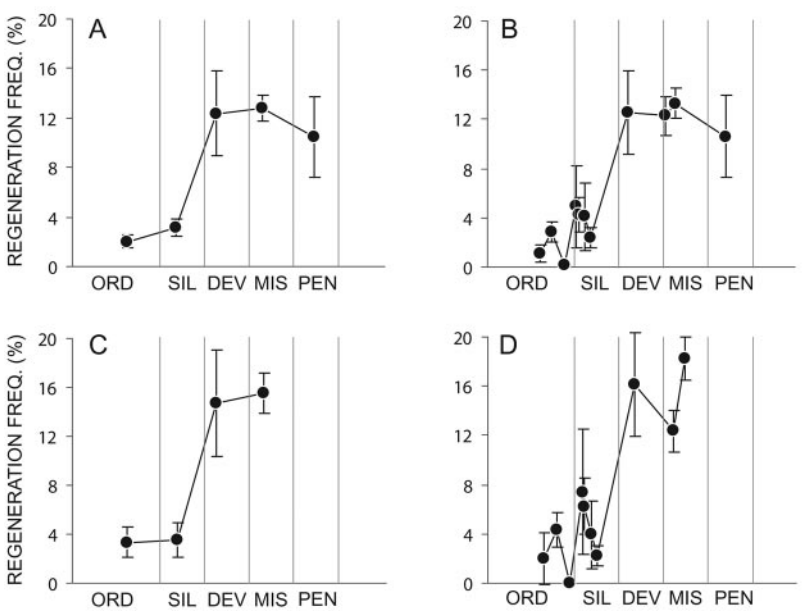

Fig. 2. Arm-regeneration frequencies in Paleozoic crinoids. Regeneration frequencies (%) = 100 × number of regenerating/total individuals at a locality. (**A**) Data for all crinoids from the 11 localities grouped into periods. (**B**) Data for all crinoids for each of the 11 localities. (**C**) Data for camerate crinoids from the 11 localities grouped by period. (**D**) Data for camerate crinoids for 10 of the 11 localities (the Pennsylvanian locality contained no camerate crinoids). Error bars correspond to 1 SE.

Although our data are relatively coarse and contain temporal gaps, the timing of the Siluro-Devonian increase in arm-regeneration frequency is roughly coincident with the increased diversity of shell-crushing predators as predicted by the MPMR (*4*, *5*). Although most of our data are from eastern North America, a global extrapolation may be justified by the low variability in regeneration frequencies for a single time interval, the Silurian, when regeneration data from eastern Canada, Sweden, Great Britain, and the central United States are compared.

All crinoids used in this study inhabited the paleotropics (*23*) (table S1); thus, known latitudinal gradients in predation intensity (*2*) cannot explain the observed pattern. Although the 11 Lagerstätten do not represent a single depositional environment, the observed temporal pattern is unlikely to be an artifact of environmental differences in predator abundance and diversity, because the 4 Silurian Lagerstätten represent the full spectrum of environments yet exhibit a narrow range of regeneration frequencies (mean, 3.8%; SD, 1.1%), and the same temporal pattern emerges when comparing Lagerstätten of a single depositional type (storm-dominated shelf/ramp) (table S1).

Although regeneration frequency is only a measure of nonlethal encounters, it is nonlethal encounters with predators that lead to escalation, because selection for antipredatory traits "can occur only if individuals in a population reproduce after they have suffered. . .attacks" (*24*–*26*). Thus, the observed trend in crinoid arm-regeneration frequency implies a considerable increase in predator-driven evolution, or escalation, in the Siluro-Devonian.

References and Notes

1. G. J. Vermeij, *Paleobiology* **3**, 245 (1977).
2. G. J. Vermeij, *Evolution and Escalation* (Princeton University Press, Princeton, NJ, 1987).
3. W. D. Allmon, J. C. Nieh, R. D. Norris, *Palaeontology* **33**, 595 (1990).
4. P. W. Signor III, C. E. Brett, *Paleobiology* **10**, 229 (1984).
5. C. E. Brett, in *Predator-Prey Interactions in the Fossil Record*, P. H. Kelley, M. Kowalewski, T. A. Hansen, Eds. (Kluwer Academic/Plenum Publishers, New York, 2003), pp. 401–432.
6. N. D. Holland, J. C. Grimmer, *Zoomorphology* **98**, 169 (1981).
7. T. Oji, T. Okamoto, *Paleobiology* **20**, 27 (1994).
8. T. K. Baumiller, in *Echinoderm Research*, J.-P. F. Feral and B. David, Eds. (Balkema, Rotterdam, 2003), pp. 243–248.
9. P. V. Mladenov, *Can. J. Zool.* **61**, 2873 (1983).
10. T. K. Baumiller, R. Mooi, C. G. Messing, in *Echinoderms 2000*, M. Barker, Ed. (Balkema, Lisse, 2001), pp. 3.
11. L. Fishelson, *Mar. Biol.* **26**, 183 (1974).

12. D. L. Meyer, C. A. LaHaye, N. D. Holland, A. C. Arenson, J. R. Strickler, *Mar. Biol.* **78**, 179 (1984).
13. D. L. Meyer, *Paleobiology* **11**, 154 (1985).
14. T. Oji, *Paleobiology* **22**, 339 (1996).
15. J. A. Schneider, in *Echinoderm Biology*, R. D. Burke, P. V. Mladenov, P. Lambert, and R. Parsley, Eds. (Balkema, Rotterdam, 1988), pp. 531–538.
16. D. L. Meyer, T. Oji, *J. Paleontol.* **67**, 250 (1993).
17. C. Neumann, R. Kohring, *Fossilien* **1998**, 175 (1998).
18. B. Efron, *Biometrika* **63**, 589 (1981).
19. M. J. Simms, G. D. Sevastopulo, *Palaeontology* **36**, 91 (1993).
20. M. Foote, *Paleobiology* **21**, 272 (1995).
21. J. A. Waters, C. G. Maples, *Paleobiology* **17**, 400 (1991).
22. T. K. Baumiller, in *Echinoderms Through Time (Echinoderms Dijon)*, B. David, A. Guille, J.P. Feral, M. Roux, Eds. (Balkema, Rotterdam, 1994), pp. 193–198.
23. C. R. Scotese, W. S. McKerrow, *Geol. Soc. London, Memoir* **12**, 1 (1990).
24. G. J. Vermeij, D. E. Schindel, E. Zipser, *Science* **214**, 1024 (1981).
25. G. J. Vermeij, *Annu. Rev. Ecol. Syst.* **25**, 219 (1994).
26. G. J. Vermeij, *Am. Nat.* **125**, 470 (1985).
27. We thank W. I. Ausich, C. Franzen, T. Huizman, K. Karns, J. Koniecki, C. Mendelson, D. Miller, J. Topor, M. Topor, and B. Miljour for assistance and three anonymous reviewers for constructive comments. This work was supported by a Fulbright Research Fellowship (T.K.B.) and grants from the Geological Society of America, The Turner Fund (University of Michigan), and the American Chemical Society (ACS-PRF 37737-AC).

Supporting Online Material
www.sciencemag.org/cgi/content/full/305/5689/1453/DC1
Tables S1 to S4

2 June 2004; accepted 28 July 2004

Polymorphism in Presolar Al_2O_3 Grains from Asymptotic Giant Branch Stars

Rhonda M. Stroud,[1]* Larry R. Nittler,[2] Conel M. O'D. Alexander[2]

We report microstructural and isotopic analyses of two presolar Al_2O_3 grains. Aluminum oxide is important cosmically, because its presence has been detected in the infrared spectra of the circumstellar envelopes of O-rich asymptotic giant branch stars and because it is predicted to be the first solid to condense in these stellar environments. The two grain structures, one corundum and the other amorphous, confirm that asymptotic giant branch stars produce both phases. The variation in structure and Ti content demonstrates that Al_2O_3 can condense in the absence of TiO_2 seed clusters but that Ti may be important in determining the crystal structure.

The molecular cloud from which the solar system formed contained the dusty ejecta of ancient stars, including red giant branch (RGB) stars, asymptotic giant branch (AGB) stars, and supernovae. The majority of this presolar circumstellar dust was extensively processed and destroyed during solar system formation. However, some presolar dust grains escaped processing, retain the isotopic signatures of extrasolar stellar origins, and are found in primitive meteorites and interplanetary dust particles (*1*–*3*).

In addition to providing information about nucleosynthesis in the progenitor stars, presolar grains provide physical data that can be used to constrain circumstellar dust condensation models (*4*) and aid in the interpretation of infrared (IR) spectra of remote stars. Circumstellar dust condensation models (*5*–*7*) have predicted that Al_2O_3 is the first solid phase to condense as the gaseous outflows from O-rich giant stars cool from high temperatures. The simplest models are equilibrium thermodynamic calculations that assume homogeneous nucleation. In principle, these models can be improved upon by allowing for heterogeneous nucleation and kinetically driven reactions (*8*–*11*), but eventually the accuracy of the models must be weighed against physical data from actual stellar dust. The best source of this data has historically been IR spectra obtained from the circumstellar envelopes of RGB and AGB stars, both of which have features that indicate a mixture of amorphous and crystalline dust phases. However, the level of detail that these spectra provide does not rigorously constrain the dust formation models; for instance, it has not allowed researchers to determine whether Al_2O_3 condenses directly or by adsorption onto TiO_2 seeds (*9*, *10*). Laboratory analyses of presolar Al_2O_3 grains bridge this information gap by providing complete chemical, isotopic, and structural profiles of individual dust grains.

Although several C-rich presolar grain types—including nanodiamonds, SiC, and graphite—have been well studied by transmission electron microscopy (TEM) (*4*, *12*–*14*), there have been no previous structural studies of presolar oxide grains, despite more than a decade of isotopic analyses (*15*). This is because of the rarity of the grains (~1% of micrometer-sized refractory oxides in meteorites) and the difficulty of extracting ultrathin TEM sections of particular grains of submicrometer-to-micrometer size among thousands of others. The former problem is alleviated by the use of automated search techniques, which have led to the identification and isotopic analysis of ~200 presolar Al_2O_3 grains (*16*, *17*). The latter problem was solved by the adaptation of focused ion beam (FIB) lift-out techniques (*18*–*20*). We report correlated structural and isotopic data for two presolar Al_2O_3 grains found in an acid-resistant residue of the Tieschitz ordinary chondrite (*21*).

The grains, named T96 and T103, were identified by automated O isotope measurements by means of a Cameca ims-6F ion microprobe (*18*, *21*, *22*). After the O analyses, the grains were manually analyzed for Al-Mg isotope systematics (Table 1). The oxygen isotopic ratios place the grains within the majority Group 1 defined for presolar oxide grains (*16*) (Fig. 1), consistent with an origin in the outflows of O-rich RGB or AGB stars. An AGB origin is indicated by large enrichments of ^{26}Mg, resulting from the decay of the now extinct ^{26}Al. The inferred $^{26}Al/^{27}Al$ ratios for the two grains are within the range expected for O-rich AGB stars. Comparison with nucleosynthesis models (*23*) indicates that the parent stars of the grains had masses about two times the mass of the Sun and near solar metallicity.

After isotopic analysis, sections of these grains were prepared for TEM studies with the use of an FIB lift-out (*18*, *21*). Despite the similar isotopic signatures, the structures of the grains are radically different. Grain T103 is a single crystal of corundum (α-Al_2O_3), which exhibits sharp Bragg diffraction (Fig. 2) and strong diffraction contrast. The other grain, T96, is amorphous, or very finely nanocrystalline, and exhibits only diffuse diffraction with no diffraction contrast when tilted. The grains also have different chemical compositions, as determined by energy-dispersive x-ray spectroscopy: T103 shows trace amounts [~0.1 weight percent (wt %)] of Ti, whereas T96 shows only Al_2O_3, to a detection limit of ~0.05 wt % for Ti. The Ti appears to be distributed in T103 as a solid solution. No subgrains were observed in either Al_2O_3 grain (*24*).

The structures of presolar grains reflect both the circumstellar dust condensation conditions and subsequent processing histories. It is important to consider how processing in the interstellar medium (ISM), solar system, or laboratory may have affected the structures. The grains retain their stellar isotopic

[1]Code 6360, Naval Research Laboratory, Washington, DC 20375, USA. [2]Department of Terrestrial Magnetism, Carnegie Institution of Washington, Washington, DC 20015, USA.

*To whom correspondence should be addressed. E-mail: stroud@nrl.navy.mil

signatures, which indicates that they experienced little chemical or isotopic processing after their formation. The effects of laboratory processing are limited to the removal of grain surfaces during the acid dissolution of the parent meteorite, and surface amorphization (depth of <20 nm) by the Cs^+ and O^- ion sources of the ion probe and the Ga^+ source of the FIB.

In principle, processing in the ISM by supernova shock waves or cosmic rays could alter the microstructure of Al_2O_3 grains without changing the isotopic composition. Supernova shocks can vaporize, sputter, or fragment dust grains (*25*, *26*); the survival of the presolar Al_2O_3 grains studied indicates that they did not experience many such shocks. A heating event would be required to recrystallize T103 to corundum from a previous amorphous or metastable crystalline structure. In terrestrial studies, the transformation of the metastable phases of Al_2O_3 to corundum begins at 700 K (*27*), well above typical interstellar grain temperatures of ~15 K (*28*). It is possible to heat interstellar dust by absorption of starlight (*28*) and/or by gas-grain collisions in supernova shocks (*29*), but it is not efficient for large grains such as those studied here. Heating by grain-to-grain collisions in shocks would be more likely to vaporize or fragment the grains than to anneal them (*26*). Moreover, interstellar silicates are exclusively amorphous (*30*), showing no evidence of thermal annealing.

Intense radiation damage of a previously crystalline grain is a possible explanation for the amorphous structure of T96. The radiation dose required for amorphization depends on radiation parameters (ion energy, ion mass, and incident angle), grain size, materials-specific atomic displacement energies, crystallinity, and ambient temperature. For single-crystal silicates with a grain size of 10 to 100 nm, experimental studies show that amorphization doses are within the realm achievable in the ISM, and this has been suggested as an explanation for the lack of detected crystalline silicates (*30*). However, T96 is one to two orders of magnitude larger than those silicates, and even for grains of comparable size, corundum has a higher amorphization dose than silicates (*31*). Moreover, Daulton *et al.* conducted a TEM analysis of several hundred presolar SiC grains (*12*) that were comparable in size to our Al_2O_3 grains but more susceptible to radiation-induced disorder (*32*), and their analysis revealed that most of them were crystalline. This result indicates that micrometer-sized presolar dust grains from AGB stars, at least those grains that survive in meteorites, were not significantly processed by radiation in the ISM. Thus, although some processing in the ISM cannot be ruled out, it is most likely that the observed structures of T96 and T103 are essentially the original structures into which the grains condensed around their parent AGB stars.

The differences in the structure and composition of the two grains have important consequences for dust condensation models and interpretation of IR spectra from circumstellar dust envelopes of O-rich AGB stars. Although it is agreed that Al_2O_3 will condense in these stars, there is long-standing disagreement, in both the condensation modeling and the IR spectroscopy communities, as to what form(s) the condensates take.

Equilibrium thermodynamic calculations predict that Al_2O_3 will be the first dust phase to condense in the circumstellar environment of O-rich AGB stars (*5*, *33*). However, there is a kinetic barrier to the homogeneous nucleation of Al_2O_3; that is, the concentration of molecular species with an Al_2O_3 stoichiometry in the stellar gas is very low (*9*). For this reason, some models assume heterogeneous nucleation of Al_2O_3 on TiO_2 seed clusters (*9*, *10*). The lack of any observed subgrains in T103 and T96 indicates that Al_2O_3 is indeed the first solid species to condense and argues against the TiO_2 seed models. To constitute 0.1 wt % of the ~1-μm T103 grain, a single TiO_2 seed would form a 60-nm TiO_2 subgrain that would have been observed by TEM. If, instead, the Ti were present as multiple seeds that were too small to produce significant imaging contrast, a polycrystalline grain structure would be expected rather than the observed single-crystal microstructure. The Ti appears to have been incorporated into T103 as a solid solution during the growth of the corundum grain rather than as the initial nucleation source. However, Ti may still be important for determining the crystal structure of the condensate. Terrestrial studies of synthetic Al_2O_3 show that trace amounts of Ti in solid solution can stabilize corundum relative to other structures (*27*). T96, which has no detectable Ti, is amorphous. Given the similar masses and metallicities of the progenitor stars indicated by the isotope data, the differences in the grains' Ti content and structure likely reflect a local difference in the condensation environments, such as pressure, temperature, cooling rate, or inhomogeneous Ti distributions.

That we find direct evidence for both crystalline and amorphous Al_2O_3 dust originating from O-rich AGB stars is directly relevant to an ongoing controversy among observational astronomers over the interpretation of features in the IR spectra of this class of stars. A narrow feature at 13 μm and a broad feature peaking close to 12 μm appear in spectra from some of these stars (*34*) and have been attributed to crystalline and amorphous Al_2O_3, respectively. The 13-μm feature was first reported in 1986 (*35*) and has been variously attributed to corundum or other crystalline Al_2O_3 (*36*, *37*), polymerized silicates (*34*), and spinel (*38*). As yet, none of these assignments has been definitively ruled out because of the complexity of the spectra and the uncertainty in obtaining reference spectra from appropriate laboratory dust analogs. It is plausible that two or more of these phases contribute to the feature to varying degrees. An objection to the assignment of this fea-

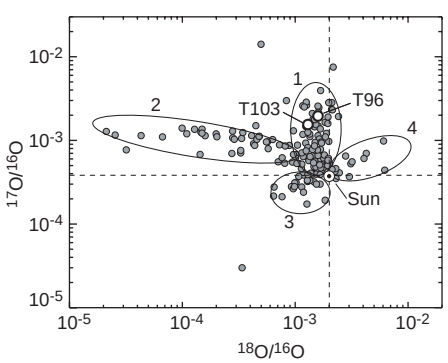

Fig. 1. Oxygen isotope plot of presolar Al_2O_3 grains. Grains from Groups 1 (including T96 and T103), 2, and 3 are all believed to have originated in O-rich RGB and AGB stars (*16*). The origin of the Group 4 grains is enigmatic.

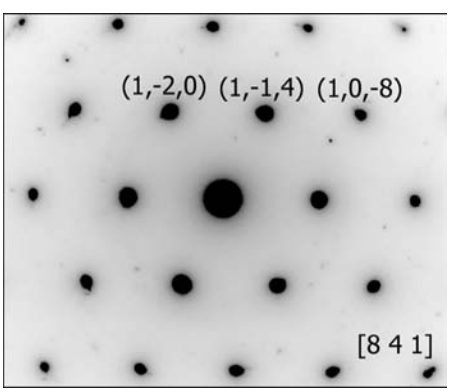

Fig. 2. Electron diffraction pattern from T103 indexed to the corundum structure.

Table 1. Isotopic and physical data for presolar Al_2O_3 grains. For comparison, solar isotopic ratios are $^{17}O/^{16}O = 3.83 \times 10^{-4}$ and $^{18}O/^{16}O = 2.005 \times 10^{-3}$.

Grain	Size (μm)	Structure	$^{17}O/^{16}O^a \pm 1\sigma$	$^{18}O/^{16}O \pm 1\sigma$	$^{26}Al/^{27}Al \pm 1\sigma$
T96	0.7 × 1.2	Amorphous	$1.96 \times 10^{-3} \pm 0.04 \times 10^{-3}$	$1.59 \times 10^{-3} \pm 0.05 \times 10^{-3}$	$6.4 \times 10^{-5} \pm 0.7 \times 10^{-5}$
T103	0.5 × 1.0	Corundum	$1.55 \times 10^{-3} \pm 0.07 \times 10^{-3}$	$1.30 \times 10^{-3} \pm 0.11 \times 10^{-3}$	$28.2 \times 10^{-5} \pm 0.6 \times 10^{-5}$

ture to corundum has been that a corresponding feature expected at 22 μm is not observed. However, the amplitude of the 22-μm feature is known to vary with grain shape (*37*) and is much lower in intensity than the 13-μm feature, and thus it may be too weak to resolve. Based on the structure and oblong shape of T103, crystalline corundum appears to be a likely contributor to the 13-μm feature. The assignment of the broad asymmetric feature peaking near 12 μm to amorphous Al_2O_3 is less debated, and this assignment gains further support from the amorphous nature of T96.

References and Notes

1. L. R. Nittler, *Earth Planet. Sci. Lett.* **209**, 259 (2003).
2. E. Zinner, *Annu. Rev. Earth Planet. Sci.* **26**, 147 (1998).
3. D. D. Clayton, L. R. Nittler, *Annu. Rev. Astron. Astrophys.*, **42**, 39 (2004).
4. T. J. Bernatowicz *et al.*, *Astrophys. J.* **472**, 760 (1996).
5. E. E. Salpeter, *Annu. Rev. Astron. Astrophys.* **15**, 267 (1977).
6. K. Lodders, B. Fegley, in *Astrophysical Implications of the Laboratory Study of Presolar Materials*, E. K. Zinner, Ed. (American Institute of Physics, Woodbury, NY, 1997), vol. 402, pp. 391–450.
7. A. G. G. M. Tielens, in *From Miras to Planetary Nebulae: Which Path for Stellar Evolution?*, M. O. Mennessier, A. Omont, Eds. (Editions Frontières, Gir-sur-Yvette, France, 1990), pp. 186–200.
8. H.-P. Gail, in *Astromineralogy*, T. K. Henning, Ed. (Springer-Verlag, Heidelberg, Germany, 2003), vol. 609, pp. 55–120.
9. H.-P. Gail, E. Sedlmayr, *Faraday Discussions*, **109**, 303 (1998).
10. K. S. Jeong, J. M. Winters, E. Sedlmayr, in *Asymptotic Giant Branch Stars*, A. Lebre, C. Waelkens, T. Le Bertre, Eds. (Astronomical Society of the Pacific, San Francisco, CA, 1999), pp. 233–238.
11. H. Sogawa, T. Kozasa, *Astrophys. J.* **516**, L33 (1999).
12. T. L. Daulton *et al.*, *Science* **296**, 1852 (2002).
13. T. L. Daulton, D. D. Eisenhour, T. J. Bernatowicz, R. S. Lewis, P. Buseck, *Geochim. Cosmochim. Acta* **60**, 4853 (1996).
14. T. K. Croat, T. Bernatowicz, S. Amari, S. Messenger, F. Stadermann, *Geochim. Cosmochim. Acta* **67**, 4705 (2003).
15. The term corundum refers to only rhombohedral Al_2O_3. Several forms of Al_2O_3 can be produced synthetically, but corundum is the only natural terrestrial form. All previously reported mineral classifications of presolar oxides, including corundum, spinel, and hibonite, were based on composition measurements and an assumption of the stable crystal structure. Our data demonstrate the danger of this historic assumption and argue for a return to the stricter terminology.
16. L. Nittler, C. M. O'D. Alexander, X. Gao, R. M. Walker, E. Zinner, *Astrophys. J.* **483**, 475 (1997).
17. B.-G. Choi, G. R. Huss, G. J. Wasserburg, *Science* **282**, 1282 (1998).
18. R. M. Stroud, C. M. O'D. Alexander, L. R. Nittler, *Meteoritics* **37**, A137 (2002).
19. M. R. Lee, P. A. Bland, G. Graham, *Mineral. Mag.* **67**, 581 (2003).
20. P. J. Heaney, E. P. Vicenzi, L. A. Giannuzzi, K. J. T. Livi, *Am. Mineral.* **86**, 1094 (2001).
21. Materials and methods are available as supporting material on *Science* Online.
22. L. R. Nittler, C. M. O'D. Alexander, F. Tera, *Meteor. Planet. Sci. Supp.* **36**, A149 (2001).
23. A. I. Boothroyd, I.-J. Sackmann, *Astrophys. J.* **510**, 232 (1999).
24. Subgrains in the portion of the grains destroyed by the FIB process, and thus not observed by TEM, are unlikely (*21*).
25. A. G. G. M. Tielens, C. F. McKee, C. G. Seab, D. J. Hollenbach, *Astrophys. J.* **431**, 321 (1994).
26. A. P. Jones, A. G. G. M. Tielens, D. J. Hollenbach, *Astrophys. J.* **469**, 740 (1996).
27. I. Levin, D. Brandon, *J. Am. Ceram. Soc.* **81**, 1995 (1998).
28. B. T. Draine, *Annu. Rev. Astron. Astrophys.* **41**, 241 (2003).
29. E. Dwek, S. M. Foster, O. Vancura, *Astrophys. J.* **457**, 244 (1996).
30. C. Jäger *et al.*, *Astron. Astrophys.* **401**, 57 (2003).
31. S. X. Wang, L. M. Wang, R. C. Ewing, R. H. Doremus, *J. Appl. Phys.* **81**, 587 (1997).
32. S. J. Zinkle, L. L. Snead, *Nucl. Instrum. Methods* **B116**, 92 (1996).
33. K. Lodders, B. Fegley, in *Asymptotic Giant Branch Stars*, A. Lebre, C. Waelkens, T. Le Bertre, Eds. (Astronomical Society of the Pacific, San Francisco, CA, 1999), pp. 279–289.
34. A. K. Speck, M. J. Barlow, R. J. Sylvester, A. M. Hofmeister, *Astron. Astrophys. Suppl. Ser.* **146**, 437 (2000).
35. I. R. Little-Marenin, S. D. Price, "The shapes of silicate features," *NASA Tech. Memo. 88342* (1986) pp. 137–138.
36. W. Glaccum, in *Airborne Astronomy Symposium on the Galactic Ecosystem: From Gas to Stars to Dust*, M. R. Haas, J. A. Davidson, E. F. Erickson, Eds. (Astronomical Society of the Pacific, San Francisco, CA, 1995), vol. 73, pp. 395–396.
37. G. C. Sloan, K. E. Kraemer, J. H. Goebel, S. D. Price, *Astrophys. J.* **594**, 483 (2003).
38. T. Posch *et al.*, *Astron. Astrophys.* **352**, 609 (1999).

39. This paper is dedicated to the memory of Dr. Robert M. Walker, without whom presolar oxide grains might not have been discovered. We acknowledge funding from the Office of Naval Research and NASA.

Supporting Online Material

www.sciencemag.org/cgi/content/full/305/5689/1455/DC1

Materials and Methods

References and Notes

4 June 2004; accepted 27 July 2004

Reverse Methanogenesis: Testing the Hypothesis with Environmental Genomics

Steven J. Hallam,[1] Nik Putnam,[2] Christina M. Preston,[1] John C. Detter,[2] Daniel Rokhsar,[2] Paul M. Richardson,[2] Edward F. DeLong[1]*†

Microbial methane consumption in anoxic sediments significantly impacts the global environment by reducing the flux of greenhouse gases from ocean to atmosphere. Despite its significance, the biological mechanisms controlling anaerobic methane oxidation are not well characterized. One current model suggests that relatives of methane-producing *Archaea* developed the capacity to reverse methanogenesis and thereby to consume methane to produce cellular carbon and energy. We report here a test of the "reverse-methanogenesis" hypothesis by genomic analyses of methane-oxidizing *Archaea* from deep-sea sediments. Our results show that nearly all genes typically associated with methane production are present in one specific group of archaeal methanotrophs. These genome-based observations support previous hypotheses and provide an informed foundation for metabolic modeling of anaerobic methane oxidation.

Anaerobic oxidation of methane (AOM) in marine sediments has been estimated to consume more than 70 billion kilograms of methane annually (*1*). Analyses of pore waters from methane-oxidizing sediments along continental margins have mapped extensive zones of sulfate and methane depletion, which define the geographic and geochemical boundary conditions for AOM (*2–4*). Combined geochemical and biological evidence indicate that microbial consortia, largely composed of archaea and sulfate-reducing bacteria (SRB), can couple methane oxidation to sulfate reduction (*5*, *6*). Current models suggest that methane is converted by methanotrophic archaea to carbon dioxide and reduced by-products (possibly including molecular hydrogen), which are subsequently consumed by sulfate-reducing bacteria (*6*). In anoxic deep-sea sediments, AOM catalyzes the formation of authigenic carbonates with highly depleted ^{13}C content, thereby providing an enduring geochemical signature for past and present methane oxidation (*7–9*). Microbial mediation of AOM significantly influences both local and global biological and biogeochemical processes. The process reduces methane flux to the water column, stimulates subsurface microbial metabolism, and also supports vigorous deep-sea chemolithotrophic communities that derive energy from one of its by-products, hydrogen sulfide.

Although no archaeal methanotrophs have yet been isolated in pure culture, phylogenetic, isotopic, and biochemical analyses indicate that several different methanogen-related archaeal groups are involved in AOM (*10–13*). Two groups of putative anaerobic methane-oxidizing *Archaea* (ANME-1 and

[1]Monterey Bay Aquarium Research Institute, Moss Landing, CA 95064, USA. [2]Joint Genome Institute, Walnut Creek, CA 94598, USA.

*Present address: Massachusetts Institute of Technology, Cambridge, MA 02139, USA.

†To whom correspondence should be addressed. E-mail: delong@mit.edu

ANME-2) (*10*, *11*) and several SRB groups typically occur together in methane-rich marine sediments, although environmental surveys and incubation studies have identified distinct population structures and distributions associated with specific habitats (*10*, *14*–*17*). The extent to which ANME and SRB groups cooperate in AOM is uncertain, but specific physical associations between them have been observed (*11*, *15*).

To better define the process of AOM, we used environmental genomic techniques (*18*) to analyze methane-oxidizing archaeal populations found in deep-sea methane seeps. Our samples originated from a 6- to 9-cm-deep sediment pushcore interval (PC45) obtained from the Eel River Basin off the Mendocino California coastline (*19*). Previous geochemical and chemotaxonomic analyses of the sampling site determined that ANME and SRB groups represent active and abundant members of a microbial community associated with AOM in Eel River sediments (*14*, *15*, *17*). Microbial cells, including ANME-1, ANME-2, and associated SRB, were enriched from the sediment using density centrifugation and size selection (*19*). High-molecular-weight DNA purified from this cell enrichment was used to construct several 3000– to 4000–base pair (3- to 4-kbp) insert whole-genome shotgun (WGS) libraries, and one 32- to 45-kbp insert fosmid library (*19*). A total of 111.3 million base pairs (Mbp) of DNA sequence generated from 224,736 reads (averaging 732 bp per read) was derived from the WGS libraries. Paired-end sequencing of the fosmid library generated 4.6 Mbp of DNA sequence from 7104 reads (averaging 700 bp per read). Then, 191 fosmids encompassing 7.4 Mbp of DNA were selected for subcloning and sequencing on the basis of the results of paired-end sequencing, small-subunit ribosomal RNA (SSU rRNA), and functional gene screening (*19*). Fosmid-sequencing efforts focused on archaeal clones to maximize large-insert coverage depth of ANME genomes.

The cell purification procedure used in sample preparation was intended to reduce the complexity in the original, diverse sediment-associated microbial community and to enrich for the AOM microbial consortia. Based on SSU rRNA gene representation in both the WGS and fosmid libraries, the microbial community structure was dominated by ANME-1, ANME-2, and SRB groups (Fig. 1). The dominance of ANME-1 in the purified cell population is also supported by the distribution and types of methane-oxidizing *Archaea* (MOA)–specific methyl coenzyme M reductase (MCR) subunit A (*mcrA*) genes present in the library (figs. S1 and S2) (*17*). This enrichment of ANME cells and genomic DNA facilitated detailed genomic analyses of this population subset.

ANME-1 and ANME-2 SSU rRNA and *mcrA* genes encoded on large genomic fragments formed distinct groups and subdivisions, each showing specific substitutions, transpositions, and indels. However, over the length of each fragment, gene content and operon organization were highly conserved within any given subdivision (Fig. 2 and fig. S1). In several instances, gene content was shared among fosmids from different groups containing SSU rRNA or *mcrA*, or between fosmids containing SSU rRNA and *mcrA* (Fig. 2). On average, the G+C content of ANME-1 fosmids containing SSU rRNA and *mcrA* was 45.1%, compared with 51.1% for those of ANME-2 (table S2). Subgroups of ANME-1 and ANME-2 fosmids containing SSU rRNA or *mcrA* harbored additional methanogenesis-associated genes (Figs. 2 and 3; table S2), providing linkage information used in determining the origin of related sequences in the WGS and fosmid libraries.

Surveys of the environmental libraries revealed the presence and relative abundance of many genes encoding enzymes typically associated with the methanogenic pathway (Table 1, Fig. 4, and fig. S2) (*19*–*21*). With the exception

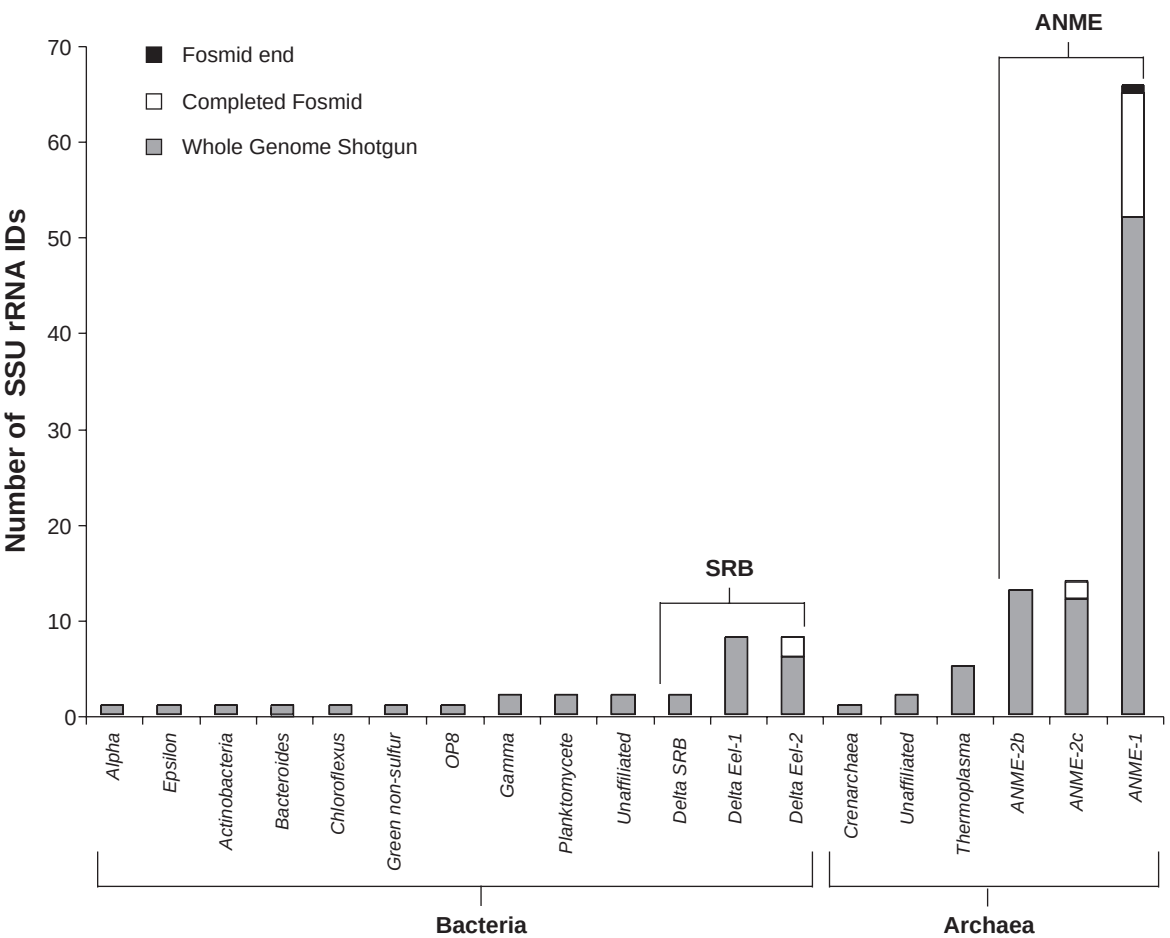

Fig. 1. Taxonomic distribution of SSU rRNA sequences identified in whole-genome shotgun sequencing (n = 114) and fosmid DNA libraries (n = 18).

of step 5, encoded by F_{420}-dependent N^5, N^{10}-methenyltetrahydromethanopterin (methylene-H4MPT) reductase (*mer*), components of all enzymatic steps (steps 1 to 4 and steps 6 to 7, Table 1) were represented in both WGS and fosmid library data sets (Table 1 and table S2). Four sequences encoding *mer* were encountered only in the WGS data set, but these probably reflect a low-level presence of bona fide methanogens in the sample. This observation is consistent with previous SSU rRNA surveys in Eel River sediments, where a few acetoclastic methanogen sequences occurred together with ANME-1 and/or ANME-2 ribotypes (*14*). Although no bona fide methanogen SSU rRNAs

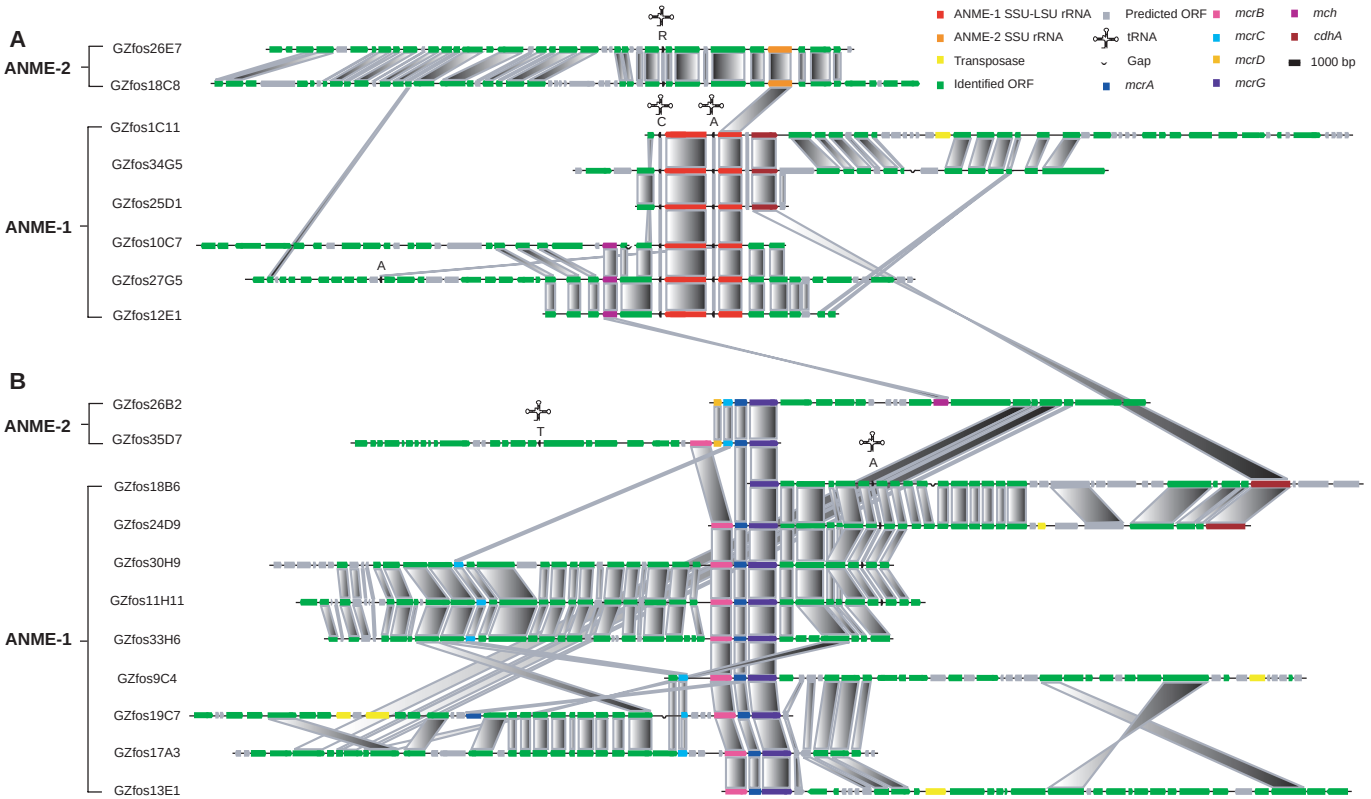

Fig. 2. Comparison of ANME-1 and ANME-2 fosmids containing SSU rRNA (**A**) or *mcrA* (**B**) based on predicted gene content and order. Genes shared in common among or between fosmids are connected by shaded boxes. ANME-1 *mcrBGA* subunits are separated from the *mcr*C component by a spacer region varying between ~1 and 14 kbp from the predicted *mcrB* start site. In every case, the *mcrC* component is linked to a tandem duplication of the *atw* locus, an adenosine 5′-triphosphate (ATP)–binding protein associated with activation of the MCR holoenzyme in vitro (*26*).

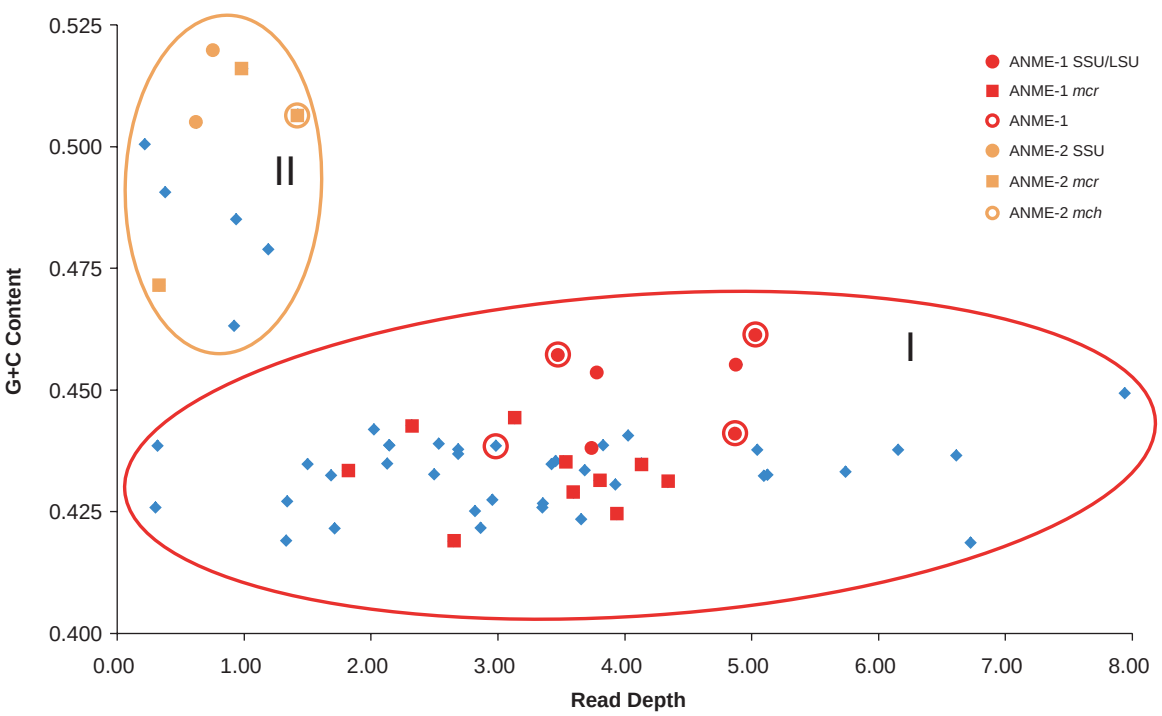

Fig. 3. Determination of ANME-1 or ANME-2 fosmid identity based on G+C content and depth of WGS coverage. Bin I bounded by red ellipse corresponds to ANME-1. Bin II bounded by orange ellipse corresponds to ANME-2. Fosmids containing SSU rRNA (filled circle), *mcr* (filled square), and *mch* (open circle) genes are highlighted in red (ANME-1) or orange (ANME-2). Read depth corresponds to the total number of WGS nucleotides aligning to a given fosmid, divided by the length (in bps) of that fosmid (*19*).

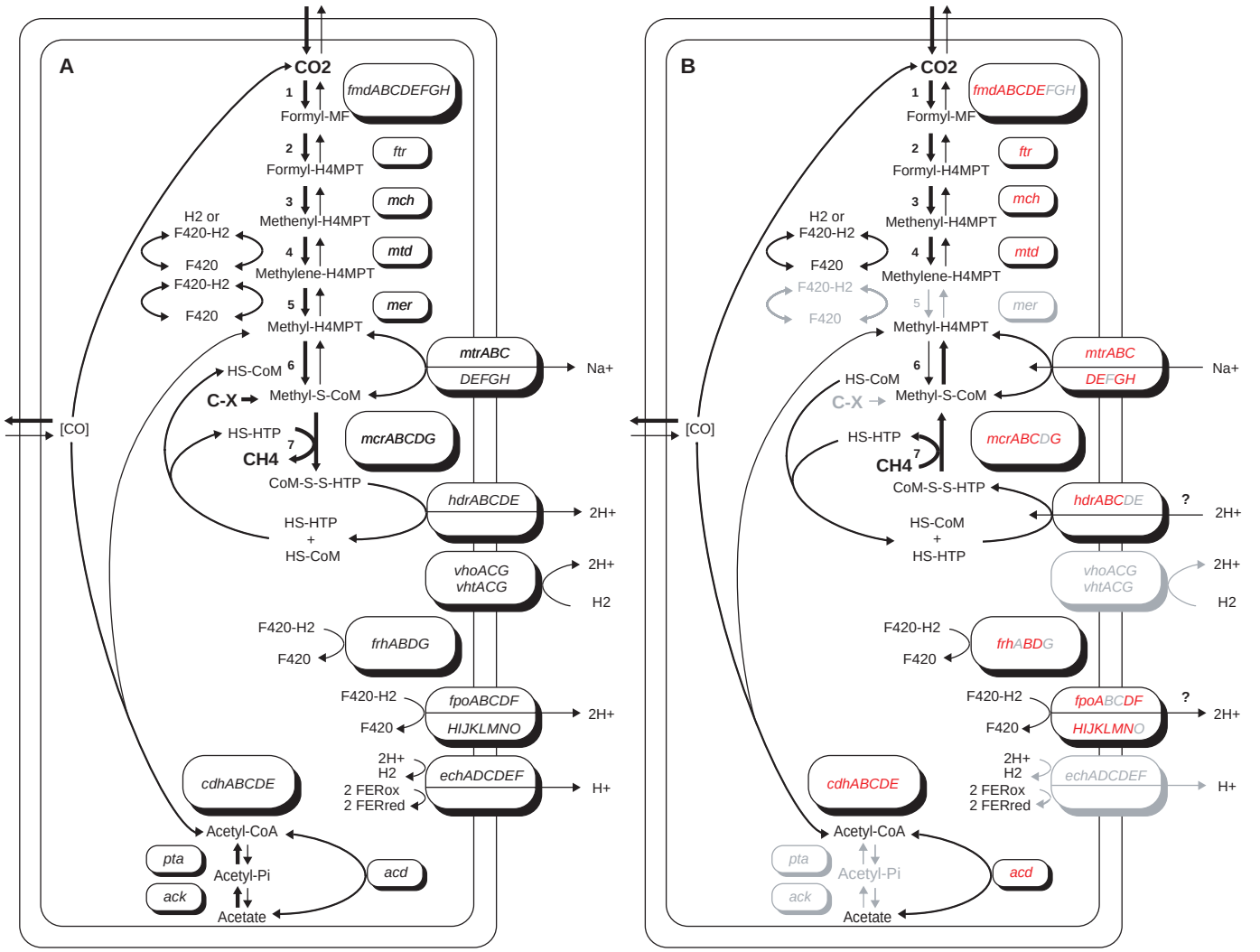

Fig. 4. Hypothetical model for reverse methanogenesis in ANME-1. (**A**) A combined pathway for methanogenesis. Gene identifications are shown in black. (**B**) A reconstructed pathway for ANME-1 based solely on predicted gene content of identified ANME-1 fosmids. Positive gene identifications are shown in red. Negative gene identifications are shown in gray.

were identified in either the WGS or fosmid library sequences, several *mcr* subunit sequences affiliated with the *Methanosarcinales* lineage were identified (fig. S2). These are readily distinguished from ANME gene fragments by both their phylogeny and WGS coverage.

Fosmid sequences were compared on the basis of their G+C content and WGS coverage (*19*). This approach was chosen on the basis of the clear G+C bias between ANME-1 and ANME-2, as well as the apparent high representation of ANME-1 genomic DNA (Fig. 1) in the WGS and fosmid libraries. Two bin distributions, I and II, were evident from using this approach (Fig. 3 and table S2). The depth of WGS coverage for bin I ranged between 0.3 and 7.9 × and between 0.4 and 1.4 × for bin II (Fig. 3). All ANME-1 fosmids containing SSU rRNA or *mcrA* mapped to bin I, and all ANME-2 fosmids containing SSU rRNA or *mcrA* mapped to bin II (Fig. 3 and table S2). Independent phylogenetic and linkage analyses clearly identified a total of 16 ANME-1 fosmids, all of which grouped in bin I (Fig. 3). Similarly, all five fosmids that could be unambiguously identified as ANME-2 grouped into bin II (Fig. 3). Assembly of binned fosmids generated 13 unique scaffolds from within bin I, and one from within bin II, with no cross-assembly between the bins (*22*). Together, these data provide strong support for the assignment of fosmids encoding methanogenesis-associated genes to ANME-1 or ANME-2 groups, according to their bin distribution. Specific identification of many ANME-1–derived genome fragments provided the framework necessary for modeling a presumptive pathway for methane consumption within this group.

The available data strongly suggest that the ANME-1 group contains all steps in the canonical seven-step methanogenic pathway with the exception of step 5, encoded by *mer* (Table 1 and Fig. 4). Although this gene is required for methanogenesis from CO_2 and one carbon (C1) compounds including methanol and methylamines, loss of *mer* activity in ANME-1 could promote AOM by increasing the activation barrier for conversion of methylene-H_4MPT to methyl-H_4MPT. Given this observation, identification of methanofuran (MF)/H_4MPT-dependent C1 transfer enzymes mediating steps 1 to 4 of methanogenesis in ANME-1 sequences is intriguing. It is possible that methylene-H_4MPT derived from reduced CO_2 becomes a substrate for assimilatory metabolism via the serine cycle (*23*). Alternatively, the C1 transfer module in ANME-1 could play a role in formaldehyde detoxification, analogous to the properties of other methylotrophic (*24*) or nonmethylotrophic bacteria (*25*).

An F_{420}-dependent quinone oxidoreductase (*fqo*) and numerous iron-sulfur cluster proteins were identified among the ANME-1

Table 1. Identification of methanogenesis-associated genes in Eel River sediment genomic DNA libraries. Step numbers indicate points in the H4MPT–dependent methanogenic pathway. Total number of gene ids among libraries: Identification based on tblastN results constrained to expectation cut-off $>E-10$. Positive identifications (ids) are indicated by numbers, and negative ids are indicated by (–) and underlined gene name and locus.

Step	Gene name	Locus	Total no. of gene ids among libraries: Shotgun	Fosmid ends	Completed fosmids
1	Formylmethanofuran dehydrogenase, subunit A	*fmdA*	55	12	4
	subunit B	*fmdB*	69	6	4
	subunit C	*fmdC*	50	1	4
	subunit D	*fmdD*	23	1	2
	subunit E	*fmdE*	26	2	2
	subunit F	*fmdF*	9*	2	–
	subunit G	*fmdG*	–	–	–
	subunit H	*fmdH*	–	–	–
2	Formylmethanofuran-tetrahydromethanopterin formyltransferase	*ftr*	67	7	3
3	N^5,N^{10}-methenyltetrahydromethanopterin cyclohydrolase	*mch*	29	1	5
4	F_{420}-dependent methylenetetrahydromethanopterin dehydrogenase	*mtd*	25	2	2
	H2-forming N^5,N^{10}-methylene-tetrahydromethanopterin cyclohydrolase	*hmd*	–	–	–
5	Coenzyme F_{420}-dependent N^5,N^{10}-methenyltetrahydromethanopterin reductase	*mer*‡	4	–	–
6	N^5-methyltetrahydromethanopterin-coenzyme M methyltransferase, subunit A	*mtrA*	9	–	8
	subunit B	*mtrB*	3	1	3
	subunit C	*mtrC*	10	1	3
	subunit D	*mtrD*	10	2	3
	subunit E	*mtrE*	11	–	3
	subunit F	*mtrF*	–	–	–
	subunit G	*mtrG*	7	–	4
	subunit H	*mtrH*	39	4	6
7	Methyl coenzyme M reductase, subunit α	*mcrA*	45	3	11
	subunit β	*mcrB*	28	9	11
	protein C	*mcr**C***	33	1	13
	protein D	*mcrD*	2	1	3
	subunit γ	*mcrG*	31	1	11
	Heterodisulfide reductase, subunit A	*hdrA*	319*	22	4
	subunit B	*hdrB*	80	3	8
	subunit C	*hdrC*	45	4	3
	subunit D	*hdrD*	67*	4	–
	subunit E	*hdrE*‡	7	–	–
	CO dehydrogenase/acetyl-CoA synthase, subunit α	*cdhA*	74	8	8
	subunit β	*cdhC*	52	1	3
	subunit γ	*cdhD*	38	3	1
	subunit δ	*cdhE*	56	3	4
	subunit ε	*cdhB*	16	–	4
	ADP-forming acetyl-CoA synthetase	*acd*	139†	9	4

*Includes related iron-sulfur [Fe-S] proteins. †Includes related coenzyme A-binding proteins. ‡Identified only in shotgun.

sequences (fig. S4, table S2). Moreover, electron input modules encoded by coenzyme F_{420}-reducing hydrogenase subunit B (*frhB)* were identified on 12 ANME-1 fosmids containing methanogenesis-associated genes (table S2), which suggested possible coupled expression and functioning of these enzymes, as well as the generation of a proton motive force derived from reduced F_{420} or ferredoxin. Given these observations, the "unfavorable" thermodynamics of methane activation in AOM might be overcome by metabolic coupling to the energy conservation reactions driven by the F_{420}-dependent respiratory chain. In ANME-1, *fqo* is most similar in operon structure and gene sequence to homologous genes in *Archaeoglobus fulgidus* (fig. S3), which indicates that ANME-1 contains genomic features of both sulfate-reducing and methanogenic *Archaea*.

The identification of most of the genes associated with methanogenesis in the ANME-1 group (and to a lesser extent, ANME-2) lends strong support to the reverse-methanogenesis hypothesis. The presence of genes that typify methane production in methanotrophic *Archaea* renders some of the classical molecular biomarkers of methanogenesis somewhat ambiguous. At the same time, these data provide new insight into the evolution, ecological roles, and diversity of methane-cycling *Archaea* and their unique metabolic machinery. The data also facilitate a more mechanistic biological understanding of the environmentally significant biogeochemical process of methane oxidation in anoxic marine habitats.

References and Notes

1. W. S. Reeburgh, in *Microbial Growth on C1 Compounds*, M. E. Lidstrom, F. R. Tabita, Eds. (Kluwer Academic, Dordrecht, Netherlands, 1996), pp. 334–342.
2. N. Iverson, B. B. Jorgensen, *Limnol. Oceanogr.* **30**, 944 (1985).
3. W. S. Borowski, C. K. Paull, W. Ussler III, *Mar. Geol.* **159**, 131 (1999).
4. S. D'Hondt, S. Rutherford, A. J. Spivack, *Science* **295**, 2067 (2002).
5. A. J. Zehnder, T. D. Brock, *J. Bacteriol.* **137**, 420 (1979).
6. T. M. Hoehler, M. J. Alperin, in *Microbial Growth on C1 Compounds*, M. E. Lidstrom, F. R. Tabita, Eds. (Kluwer Academic, Dordrecht, Netherlands, 1996), pp. 326–333.
7. L. D. Kulm *et al.*, *Science* **231**, 561 (1986).
8. C. K. Paull, J. P. Chanton, A. C. Neumann, J. A. Coston, C. S. Martens, *Palaios* **7** (1992).
9. G. Jiang, M. J. Kennedy, N. Christie-Blick, *Nature* **426**, 822 (2003).
10. K. U. Hinrichs, J. M. Hayes, S. P. Sylva, P. G. Brewer, E. F. DeLong, *Nature* **398**, 802 (1999).
11. A. Boetius *et al.*, *Nature* **407**, 623 (2000).
12. V. J. Orphan, C. H. House, K. U. Hinrichs, K. D. McKeegan, E. F. DeLong, *Science* **293**, 484 (2001).
13. M. Kruger *et al.*, *Nature* **426**, 878 (2003).
14. V. J. Orphan *et al.*, *Appl. Environ. Microbiol.* **67**, 1922 (2001).
15. V. J. Orphan, C. H. House, K. U. Hinrichs, K. D. McKeegan, E. F. DeLong, *Proc. Natl. Acad. Sci. U.S.A.* **99**, 7663 (2002).
16. W. Michaelis *et al.*, *Science* **297**, 1013 (2002).
17. S. J. Hallam, P. R. Girguis, C. M. Preston, P. M. Richardson, E. F. DeLong, *Appl. Environ. Microbiol.* **69**, 5483 (2003).
18. E. F. DeLong, *Curr. Opin. Microbiol.* **5**, 520 (2002).

19. Materials and methods are available as supporting material on *Science* Online.
20. J. N. Reeve, J. Nolling, R. M. Morgan, D. R. Smith, *J. Bacteriol.* **179**, 5975 (1997).
21. R. K. Thauer, *Microbiology* **144**, 2377 (1998).
22. S. J. Hallam *et al.*, data not shown.
23. S. Angelaccio *et al.*, *J. Biol. Chem.* **278**, 41789 (2003).
24. L. Chistoserdova *et al.*, *Microbiology* **146**, 233 (2000).
25. C. J. Marx, J. A. Miller, L. Chistoserdova, M. E. Lidstrom, *J. Bacteriol.* **186**, 2173 (2004).
26. C. H. Kuhner, B. D. Lindenbach, R. S. Wolfe, *J. Bacteriol.* **175**, 3195 (1993).
27. Special thanks to L. Christianson, P. Girguis, and V. Orphan at MBARI for technical assistance, and the pilots of the *ROV Tiburon* and the captain and crew of the *R/V Western Flyer*. We also thank S. Pitluck and the Joint Genome Institute staff for technical assistance, and W. Ussler and D. Graham, who provided insight and commentary. This study was supported by the David and Lucille Packard Foundation, NSF grant MCB-0236541, and the U.S. Department of Energy's Office of Science, Biological and Environmental Research Program, and the University of California, Lawrence Livermore National Laboratory, under contract W-7405-ENG-48, Lawrence Berkeley National Laboratory contract DE-AC03-765F00098, and Los Alamos National Laboratory contract W-7405-ENG-36. Sequences have been submitted to GenBank under accession numbers AY714814 to AY714873. Additional data are available at www.jgi.doe.gov/aom.

Supporting Online Material
www.science.org/cgi/content/full/305/5689/1457/DC1
Materials and Methods
Figs. S1 to S3
Tables S1 and S2
References and Notes

6 May 2004; accepted 23 July 2004

Bmp4 and Morphological Variation of Beaks in Darwin's Finches

Arhat Abzhanov,[1] Meredith Protas,[1] B. Rosemary Grant,[2] Peter R. Grant,[2] Clifford J. Tabin[1]*

Darwin's finches are a classic example of species diversification by natural selection. Their impressive variation in beak morphology is associated with the exploitation of a variety of ecological niches, but its developmental basis is unknown. We performed a comparative analysis of expression patterns of various growth factors in species comprising the genus *Geospiza*. We found that expression of *Bmp4* in the mesenchyme of the upper beaks strongly correlated with deep and broad beak morphology. When misexpressed in chicken embryos, *Bmp4* caused morphological transformations paralleling the beak morphology of the large ground finch *G. magnirostris*.

Darwin's finches are a group of 14 closely related songbird species on the Galápagos Islands and Cocos Island (*1*–*3*) collected by Charles Darwin and other members of the *Beagle* expedition in 1835 (*4*). Many biology textbooks use these birds to illustrate the history of evolutionary theory as well as adaptative radiation, natural selection, and niche partitioning (*5*–*7*). The diverse shapes and sizes of the finch beaks are believed to be maximally effective for exploiting particular types of food, including seeds, insects, and cactus flowers (*3*, *7*). The external differences in beak morphology reflect differences in their respective craniofacial skeletons (*3*, *8*). The specialized beak shapes are apparent at hatching (*3*, *8*) and thus are genetically determined.

To study the craniofacial development of Darwin's finches, we first developed a staging system by which we could compare them to each other and to the chicken, the existing avian model system (fig. S1) (*9*). We used this system to compare beak development in six species of Darwin's finches belonging to the monophyletic ground finch genus *Geospiza*. The sharp-beaked finch *G. difficilis*, with a small symmetrical beak, is the most basal species (Fig. 1A) (*10*). The other species fall into two groups: three species with broad and deep beaks used for crushing seeds (small, medium, and large ground finches—*G. fuliginosa*, *G. fortis*, and *G. magnirostris*) and cactus finches with long pointed beaks used for reaching into cactus flowers and fruits (cactus and large cactus finches—*G. scandens* and *G. conirostris*) (Fig. 1A) (*7*, *10*).

We compared beak development in embryos of all six species. Species-specific differences in the morphological shape of the beak prominence are first apparent by embryonic stage 26 (Fig. 1, B and C, and fig. S2). We therefore expected factors involved in directing the differential aspects of beak morphologies to be expressed at or before this time. We also expected such species-specific differences to reside in the mesenchyme on the basis of recent transplantation experiments between quail and duck embryos (*11*).

We analyzed expression patterns of a variety of growth factors, which are known to be expressed during avian craniofacial development (*12*–*14*), among the different *Geospiza* species, using in situ hybridizations on equivalent medial sections (as revealed by the presence of Rathke's pouch; fig. S3) of stage 26 and stage 29 embryos (Fig. 1, B and C, and fig. S4) (*15*). We looked for factors whose expression in the mesenchyme of the beak prominence correlated with the increasing depth and width of beaks seen as one compares *G. difficilis* to *G. fuliginosa*, *G. fortis*, and *G. magnirostris*. To eliminate changes in expression that were merely related to the overall size of the bird and not to changes in beak morphology, we also compared expression patterns in *G. scandens* and *G. conirostris,* which are similar in size to *G. fortis* and *G. magnirostris*, respectively, but share the more pointed beak morphology (Fig. 1A).

Most factors examined either showed no difference between Darwin's finches species (including *Shh* and *Fgf8*) (*15*) or, in the case of *Bmp2* and *Bmp7*, correlated with the size of the beak but not its shape (fig. S4). In contrast, we observed a striking correlation between beak morphology and the expression of *Bmp4* (Fig. 1, B and C). In *G. difficilis*, *Bmp4* expression is first seen at low levels in the subectodermal mesenchyme at stage 26 (Fig. 1B). Once the cartilage condensation has occurred at stage 29, *Bmp4* continues to be expressed in mesenchymal cells surrounding the most rostral part of the prenasal cartilage. When the embryos of the three ground finch species were examined, we noted a dramatic increase in the level of *Bmp4* expression in *G. magnirostris* at stage 26, whereas *Bmp4* expression in all the other species was more or less equivalent to that in *G. difficilis* (Fig. 1B). By stage 29, however, all three ground finch species displayed elevated levels of *Bmp4* expression, with *G. magnirostris* being the strongest and *G. fuliginosa* the weakest of these. *G. scandens*, a relatively pointed-beaked species of similar size to *G. fortis*, and *G. conirostris*, which is similar in size to *G. magnirostris*, did not show this increase in relative levels of *Bmp4* expression (Fig. 1C). The expression patterns of all factors were examined in three or four independent embryos for each species (except for *G. scandens*, for which two embryos were examined), and the results were consistent. Thus, the species with deeper, broader beaks relative to their length express *Bmp4* in the mesenchyme of their beak prominences at higher levels and at earlier stages (a heterochronic shift) than species with relatively narrow and shallow beak morphologies. Moreover, the differences in *Bmp4* expression are coincident with the appearance of species-

[1]Department of Genetics, Harvard Medical School, Boston, MA 02115, USA. [2]Department of Ecology and Evolutionary Biology, Princeton University, Princeton, NJ 08544, USA.

*To whom correspondence should be addressed.

specific differences in beak morphology. This observed correlation was specific to *Bmp4* expression in the upper beak, whereas expression of *Bmp4* in the lower beak remains constant in spite of the fact that lower beak morphology varies in concert with that of the upper beak (*15*).

We next tested whether the observed change in *Bmp4* expression could be partially responsible for the differences in beak morphology in ground finch species. *Bmp4* has been previously shown to be important for the production of skeletogenic cranial neural crest cells and capable of affecting patterning, growth and chondrogenesis in derivatives of the mandibular and maxillary prominences (*16*–*19*). However, the expression of *Bmp4* is quite dynamic during craniofacial development and might be expected to play different roles at various times.

During craniofacial development, *Bmp4* is first expressed in the epithelium of the maxillary and lateral frontonasal prominences in early embryos. The same factor is later expressed in the distal mesenchyme of the upper beak of embryos at stage 29 and later (Fig. 2, A and B). We took advantage of the ability to misexpress genes during chicken development with the RCAS replication-competent retroviral vector to test the effect of increasing BMP4 levels in both of these domains. Because the RCAS vector does not spread across basement membranes, we were able to confine misexpression to either the facial ectoderm or mesenchyme (Fig. 2, C and E). Infection of the facial ectoderm with the RCAS::*Bmp4* virus caused smaller and narrower upper beaks (fig. S5). Ectodermally infected beaks also showed a dramatic loss of chondrogenesis in the adjacent mesenchyme (Fig. 2, D and F, and fig. S5), indicating a role in epithelial–to-mesenchymal signaling early in head morphogenesis.

In a second set of misexpression experiments designed to mimic the elevated levels of *Bmp4* seen in *G. magnirostris*, we injected RCAS::*Bmp4* virus into the mesenchyme of the frontonasal process of chicken embryos at stage 23 to 24. Because of the time required for viral infection and spread, this results in robust misexpression in the distal frontonasal process around stage 26 (*15*), which is the time when elevated *Bmp4* levels are first seen in *G. magnirostris*. The phenotypes we obtained were quite different from those resulting from epithelial misexpression, showing that *Bmp4* expression has distinct functions in the epithelium and mesenchyme. Rather than diminished beaks, beaks resulting from infection of the mesenchyme were reminiscent of those of the ground finches with deep and broad beaks. These morphological changes in beak morphology were observed before the onset of skeletogenesis, as revealed by *Col II* expression (*15*). By stage 36, the infected beaks ($n = 13$) were on average about 2.5 times as wide (±21%) and 1.5 times (±16%) as deep as uninfected control beaks ($n = 11$; $P < 0.003$) (Fig. 3, A, B, D, and E). The more massive *Bmp4*-infected beaks had a corresponding increase in the size of the skeletal core (Fig. 3, G and H, and fig. S6), again in parallel to a larger beak skeleton of *G. magnirostris*. This skeletal phenotype was observed in the majority of the infected embryos ($n = 11$ out of 13). These data suggest that BMP4 may have a proliferating effect on skeletal progenitors in the upper jaw. Indeed, we find that cell proliferation, as assessed by bromodeoxyuridine (BrdU) labeling, is highest in a zone of the upper beak process where *Bmp4* is expressed (Fig. 3, J to L; marked with arrow in J, asterisks in L and O). Moreover, this zone of high cell proliferation expands and shows a higher level of proliferation after RCAS::*Bmp4* misexpression (Fig. 3, M to O). A similar phenotype was observed in a study reported in an accompanying paper, where *Bmp4* was misexpressed as part of a study comparing its role in the development of the beak in ducks and chickens (*20*). In contrast, mesenchymal injection of the RCAS::*Noggin* virus, which antagonizes BMP2/4/7 signaling, led to a dramatic decrease in the size of the upper beak and to much smaller skeletal elements inside the upper beak ($n = 7$ out of 9; $P < 0.002$) (Fig. 3, C, F, and I).

We have identified variation in the level and timing of *Bmp4* expression that correlates with variation in beak morphology in Darwin's finch species. We are tempted to speculate that differences in the cis-regulatory elements of *Bmp4* may underlie the distinct expression patterns, although alternatively they could be explained by differences in the timing or amounts of upstream inductive factors or differences in the transduction of such signals. Two such potential upstream signals are *Sonic hedgehog* (*Shh*) and *Fibroblast growth factor 8* (*Fgf8*), which are expressed in the beak epithelium. Beak outgrowth occurs at the location where their expression domains meet, and

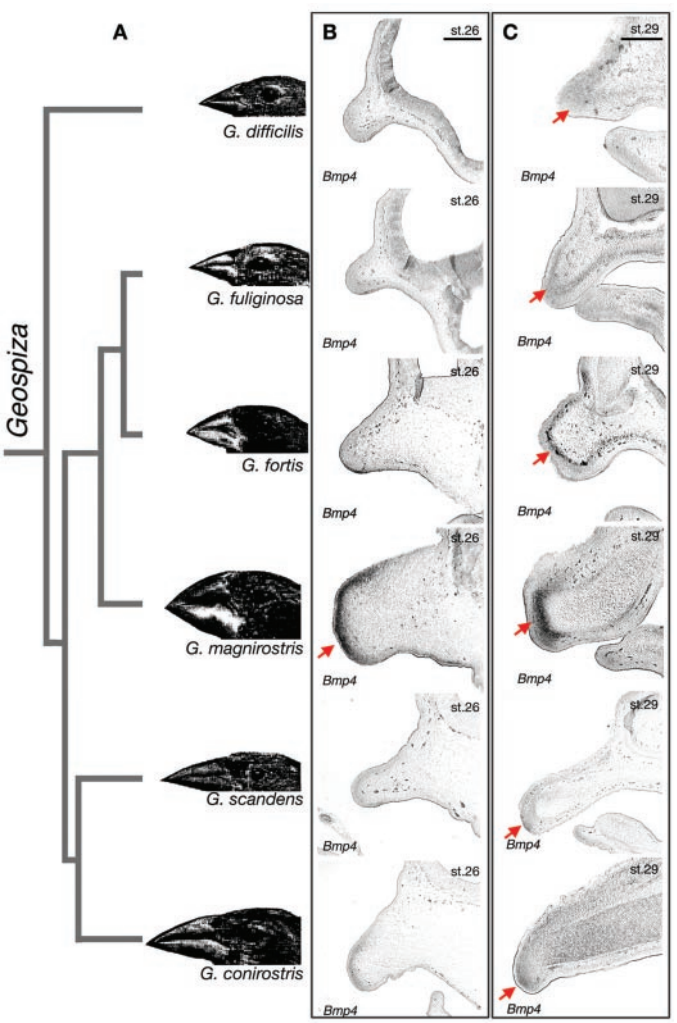

Fig. 1. (**A**) Previous studies suggest that *G. difficilis* is the most basal species of the genus *Geospiza*, and the rest of the species form two groups: ground and cactus finches, with distinct beak morphologies. (**B**) At stage (st.) 26, *Bmp4* is strongly expressed in a broad distal-dorsal domain in the mesenchyme of the upper beak prominence of *G. magnirostris* and at significantly lower levels in *G. fortis* and *G. conirostris*. No *Bmp4* was detected in the mesenchyme of *G. difficilis*, *G. fuliginosa*, and *G. scandens*. (**C**) At stage 29, *Bmp4* continues to be expressed at high levels in the distal beak mesenchyme of *G. magnirostris*. Broad domains of *Bmp4* expression are detectable around prenasal cartilages of *G. fuliginosa* and *G. fortis*. A small domain of strong *Bmp4* expression is also found in the most distal mesenchyme of *G. conirostris*, and weaker expression is seen in *G. scandens* and *G. fortis* (red arrows). Scale bars: 1 mm in (B) and 2 mm in (C).

SHH and FGF8 have been shown to synergistically drive outgrowth, and in the process to induce expression of *Bmp4* in subjacent mesenchyme (*21*, *22*). Also, we have not ruled out the possibility that genes expressed in other regions of the face are important for directing morphogenesis. In addition to the correlation between variation in *Bmp4* levels and the development of the beaks of Darwin's finches, we have also found that artificially increasing BMP4 levels in the beak mesenchyme is sufficient to alter beak morphology in the same direction as is seen in the larger ground finches. Thus, although polymorphism in other genes may also contribute to differences in beak morphology, we propose that variation in *Bmp4* regulation is one of the principal molecular variables that provided the quantitative morphological variation acted on by natural selection in the evolution of the beaks of the Darwin's finch species (*23*).

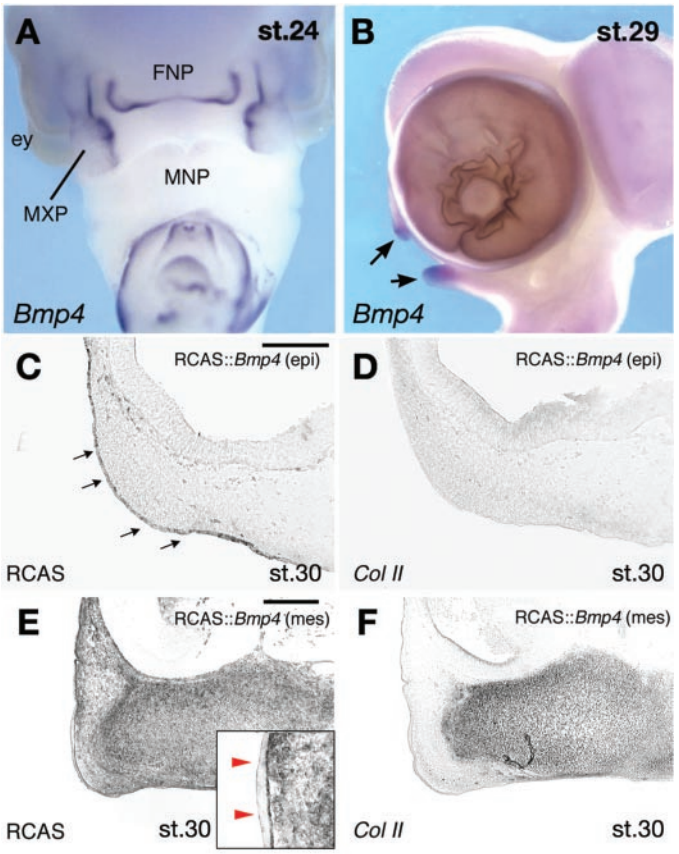

Fig. 2. (**A**) At stage 24, *Bmp4* is expressed in the ectoderm of the maxillary process (MXP) and lateral frontonasal process (FNP). (**B**) By stage 29, *Bmp4* expression expands into the distal mesenchyme of the upper and lower beaks (black arrows). (**C** and **E**) Misexpression of RCAS::*Bmp4* can be targeted to either the facial ectoderm [red arrowheads in inset in (E)] or the mesenchyme (mes) of the frontonasal process of a chicken embryo, as revealed with in-situ hybridization with a virus-specific probe. (**D**) No chondrogenesis is detected in the embryos whose epithelium (epi) was infected with RCAS::*Bmp4* virus. (**F**) In contrast, embryos whose FNP mesenchyme was infected with RCAS::*Bmp4* virus showed high levels of chondrogenesis as revealed with an anti–*Col II* riboprobe. MNP, mandibular process; ey, eye. Scale bars: 1 mm in (C) and (E).

References and Notes

1. D. Lack, *Darwin's Finches* (Cambridge Univ. Press, Cambridge, 1947).
2. R. I. Bowman, *Univ. Calif. Publ. Zool.* **58**, 1 (1961).
3. P. R. Grant, *The Ecology and Evolution of Darwin's Finches* (Princeton Univ. Press, Princeton, NJ, 1999).
4. C. Darwin, *The Voyage of the Beagle* (New American Library, New York, 1988).
5. D. J. Futuyma, *Evolutionary Biology, Third Edition* (Sinauer Associates, Sunderland, MA, 1998).
6. S. Freeman, J. C. Herron, *Evolutionary Analysis, Third Edition* (Prentice-Hall Inc., Upper Saddle River, NJ, 2003).
7. D. Schluter, *The Ecology of Adaptive Radiation* (Oxford Univ. Press, Oxford, 2000).
8. P. R. Grant, *Proc. R. Soc. London Ser. B* **B212**, 403 (1981).
9. Materials and methods are available as supporting material on *Science* Online.
10. K. Petren, B. R. Grant, P. R. Grant, *Proc. R. Soc. London Ser. B* **266**, 321 (1999).
11. R. A. Schneider, J. A. Helms, *Science* **299**, 565 (2003).

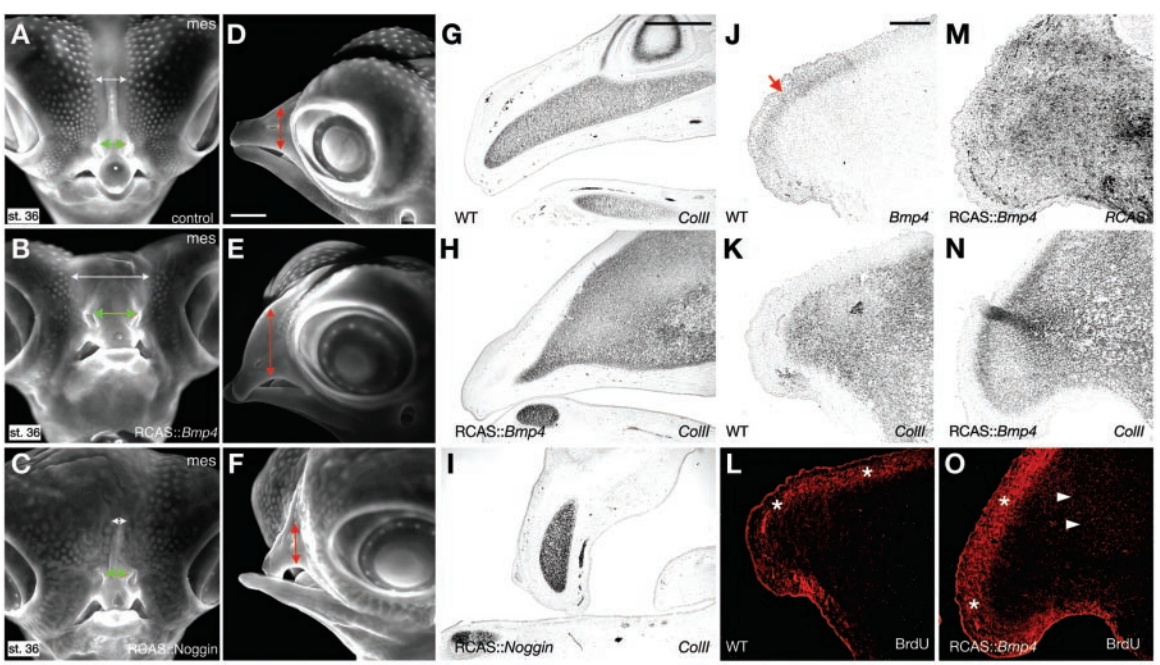

Fig. 3. (**A** and **D**) Ultraviolet pictures of wild-type stage 36 chicken embryonic heads. The width and depth of the beak are shown with white and red double-headed arrows, respectively. The width of the beak tip is indicated with a double-headed green arrow. (**G**) Prenasal cartilage in wild-type chickens forms a narrow protruding skeletal rod. (**B** and **E**) RCAS::*Bmp4* infection in the mesenchyme of the frontonasal process caused a significant increase in the width and depths of the beak. (**H**) These larger upper beaks contained more skeletogenic cells, as revealed with *Col II* in-situ hybridization. (**C** and **F**) In contrast, infection with RCAS::*Noggin* led to narrower and shallower upper beaks. (**I**) Ectopic *Noggin* produced smaller skeletal elements inside the upper beak. BrdU labeling reveals that the *Bmp4* expression domain [red arrow in (**J**)], which is rostral and dorsal to the developing prenasal cartilage (**K**), is closely associated with proliferating cells (**L**) of stage 30 chick embryos. The upper beaks of embryos infected with RCAS::*Bmp4* (**M**) by stage 30 develop larger cartilages (**N**), and there is an up-regulation of cell proliferation both around and within the developing cartilage (**O**). Scale bars: 2 mm in (D); 0.5 mm in (G); and 1 mm in (J).

12. R. A. Schneider, D. Hu, J. L. Rubenstein, M. Maden, J. A. Helms, *Development* **128**, 2755 (2001).
13. P. A. Trainor, K. R. Melton, M. Manzanares, *Int. J. Dev. Biol.* **47**, 541 (2003).
14. P. Kulesa, D. L. Ellies, P. A. Trainor, *Dev. Dyn.* **229**, 14 (2004).
15. A. Abzhanov, M. Protas, B. R. Grant, P. R. Grant, C. J. Tabin, data not shown.
16. B. Kanzler, R. K. Foreman, P. A. Labosky, M. Mallo, *Development* **127**, 1095 (2000).
17. S. Ohnemus *et al.*, *Mech. Dev.* **119**, 127 (2002).
18. A. J. Barlow, P. H. Francis-West, *Development* **124**, 391 (1997).
19. I. Semba *et al.*, *Dev. Dyn.* **217**, 401 (2000).
20. P. Wu *et al.*, *Science* **305**, 1465 (2004).
21. D. Hu, R. S. Marcucio, J. A. Helms, *Development* **130**, 1749 (2003).
22. A. Abzhanov, C. J. Tabin, *Dev. Biol.*, in press.
23. T. D. Price, P. R. Grant, *Am. Nat.* **125**, 169 (1985).
24. We thank field assistants J. Chavez, G. Castaneda, O. Perez, F. Brown, and A. Aitkhozhina; the Charles Darwin Research Station and The Galápagos National Park for permits and logistical support; M. Kirschner for discussions that led to the inception of this project; and P. Wu and C.-M. Chuong for sharing data before submission. A.A. was supported by the Cancer Research Fund of the Damon Runyon–Walter Winchell Foundation Fellowship, grant DRG1618. This project was funded by NIH grant PO1 DK56246 to C.J.T.

Supporting Online Material
www.sciencemag.org/cgi/content/full/305/5689/1462/DC1
Materials and Methods
Figs. S1 to S6
References

19 March 2004; accepted 14 July 2004

Molecular Shaping of the Beak

Ping Wu, Ting-Xin Jiang, Sanong Suksaweang, Randall Bruce Widelitz, Cheng-Ming Chuong*

Beak shape is a classic example of evolutionary diversification. Beak development in chicken and duck was used to examine morphological variations among avian species. There is only one proliferative zone in the frontonasal mass of chickens, but two in ducks. These growth zones are associated with bone morphogenetic protein 4 (BMP4) activity. By "tinkering" with BMP4 in beak prominences, the shapes of the chicken beak can be modulated.

During bird evolution, the beak emerged as the dominant avian facial feature, adapting birds to diverse eco-morphological opportunities (*1*, *2*). The beak is made up of multiple facial prominences: the frontonasal mass (FNM), maxillary prominences (MXP), lateral nasal prominences (LNP), and mandibular prominence (MDP) (fig. S1A). During development, these prominences are proportionally coordinated to compose a unique beak. Progress in molecular mechanisms underlying early beak morphogenesis has been reviewed recently (*3*, *4*). Here, we focus on later events that mold the shape of the FNM, by comparing proliferation zones of chickens and ducks that have distinct beak shapes (Fig. 1A, fig. S2A).

Temporal- and spatial-specific changes of proliferative zones occur within the FNM (Fig. 1B; fig. S1, C and D). In stage 26 chickens, labeling with short pulses of BrdU (5-bromo-2′-deoxyuridine) showed cell proliferation in both FNM lateral edges. At stage 27, the two growth zones shifted toward the rostral margin, flanking the midline. At stage 28, these growth zones gradually converged into one centrally localized zone. In ducks, the two bilaterally positioned growth zones persisted in the lateral edges, widening the developing FNM. These changes precede morphological changes of the

Department of Pathology, Keck School of Medicine, University of Southern California, Los Angeles, CA 90033, USA.

*To whom correspondence should be addressed at Department of Pathology, University of Southern California, 2011 Zonal Avenue, HMR 315B, Los Angeles, CA 90033, USA. E-mail: chuong@pathfinder.usc.edu

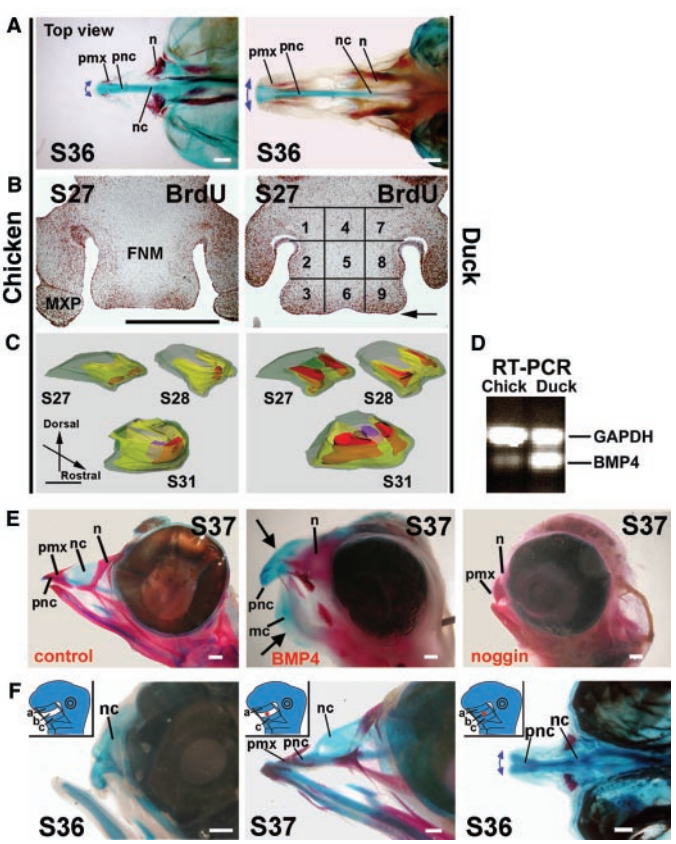

Fig. 1. Cell proliferation and BMP4 function in chicken and duck beak morphogenesis. (**A**) Stage 36 chicken and duck beaks, top view. Blue, cartilage; red, bones. Double-headed arrows indicate beak tip width (fig. S2E). (**B**) Stage 27 frontal sections after 1.5 hours of BrdU labeling. See fig. S1C for stages 26, 28, 29, and 31 BrdU labeling. The percentage of BrdU-positive cells was quantified in nine regions using the grid overlay (*12*) shown in table S1. Arrow indicates the rostral margin. (**C**) Three-dimensional reconstruction of the percentage of BrdU-positive cells in the FNM. Red indicates >20% BrdU-positive cells, yellow 10 to 20%, and green <10%. Viewing the inner red zone through the yellow zone appears orange. Purple indicates proliferation in the cartilage region. (**D**) BMP4 RT-PCR from stage 25 FNMs showed a higher BMP4/GAPDH ratio in ducks than in chickens. (**E**) (Left) Stage 37 control. (Middle and right) RCAS-BMP4 or RCAS-noggin was injected into all beak prominences of chicken embryos and harvested at stage 37. Arrows indicate enlarged skeletal elements. (**F**) (Left) Stage 20 chicken FNM was divided into three regions (a to c, defined in fig. S2B). Excision of region b containing the frontonasal ectodermal zone and subjacent mesenchyme (inset) truncated the upper beak with distal cartilage elements missing as observed at stage 36. Ablation of region a or c showed normal growth (not shown). (Middle) BMP4 beads (inset, red circle) can rescue most growth and cartilage elements from region b–ablated specimens (stage 37). (Right) Addition of BMP4 beads to nonablated FNM resulted in wider upper beaks (stage 36). FNM, frontonasal mass; mc, Meckel's cartilage; MXP, maxillary prominence; n, nasal bone; nc, nasal chonchae; pmx, premaxilla bone; pnc, prenasal cartilage. Scale bars, 1 mm.

FNM. After stage 31, the basic beak structures were determined. The percentage of BrdU-positive cells was quantified in nine separate FNM regions (Fig. 1B and table S1). A growth zone shift is clearly seen in the three-dimensional reconstruction (Fig. 1C).

Bone morphogenetic protein 2 (BMP2), BMP4, and BMP receptors are expressed in chicken beak prominences (*5*–*7*). We observed higher expression of BMP4 transcripts in ducks than in chickens, using reverse transcription polymerase chain reaction (RT-PCR) with primers conserved between chickens and ducks (Fig. 1D). Furthermore, BMP4 in the mesenchyme was closely associated with the shifting growth zones (fig. S1, C and E). Comparisons showed more diffuse BMP4 expression in the duck than in the chicken, and duck MXPs were larger than chicken MXPs (fig. S1F).

We examined the roles of BMP4 in shaping beaks with two different strategies. To test whether BMP4 drives beak growth, we injected replication-competent avian sarcoma retrovirus (RCAS)-BMP4 into all beak prominences of stage 22 and stage 23 chicken embryos. This treatment resulted in larger beaks with significant increases in length, width, and depth (Fig. 1E, middle; percentage of experiments showing indicated phenotypes = 100%; total number of experiments $n = 15$, $P < 0.001$) compared with controls (Fig. 1E, left). To determine whether BMP is physiologically involved, we misexpressed noggin, the BMP antagonist. Treatment with RCAS-noggin resulted in miniaturized beaks (Fig. 1E, right, 100%; $n = 9$, $P < 0.001$). Analysis of histological sections showed that BMP4 caused enhanced cell proliferation and skeletal differentiation as seen by hematoxylin and eosin, BrdU, and collagen-I staining (fig. S3, A to D), consistent with results obtained using RCAS-BMP receptors (*7*). Noggin had the opposite effect, causing reduced cell proliferation and skeletal differentiation (fig. S3, A and C).

The "frontonasal ectodermal zone" flanked by fibroblast growth factor 8 (FGF8) and Sonic hedgehog (Shh) was shown to direct beak outgrowth (*8*) (fig. S1B). We microsurgically ablated this region (including the epithelium and mesenchyme; region b in fig. S2B), and growth was arrested, with the distal cartilage elements missing (Fig. 1F, left, 70%; $n = 20$). BMP4-coated beads could partially restore growth even when this mesenchymal zone was deleted (Fig. 1F, middle, 62%; $n = 13$). Implanting a BMP4 bead in the nonablated FNM region induced a new growth zone, resulting in a wider beak (Fig. 1F, right, 33%; $n = 12$). The moderate percentage of unablated beak samples responding to BMP beads may be due to a slight shift of bead positions in ovo, because the BMP bead effect appears to be highly location specific (*6*). The width of the upper beak tip was significantly increased ($P < 0.01$) and resembled that of the duck (fig. S2F). Albumin-coated beads did not produce this effect (fig. S2C). Within 24 hours, BMP4-coated beads induced surrounding mesenchymal cell proliferation (*9*).

Our results show that BMP4 is one of the major driving forces building beak mass. The number and activity of localized growth zones in the prominence confer the specific beak shape. Darwin's finches in the Galapagos Islands exhibit different-sized and -shaped beaks (*1*), as a result of a process regulated in part by BMP4 (*10*). We produced beaks that phenocopy those in nature by modulating BMP activities. It is likely that beak shape diversity is achieved by modulating prototypical molecular modules (*11*), and proteins of the BMP pathway may mediate a spectrum of morphological designs for selection.

References and Notes

1. P. R. Grant, B. R. Grant, *Science* **296**, 707 (2002).
2. A. Feduccia, *The Origin and Evolution of Birds*, A. Feducia, Ed. (Yale Univ. Press, New Haven, CT, ed. 2, 1999), pp. 93–137.
3. J. A. Helms, R. A. Schneider, *Nature* **423**, 326 (2003).
4. J. M. Richman, S. H. Lee, *Bioessays* **25**, 554 (2003).
5. P. H. Francis-West, T. Tatla, P. M. Brickell, *Dev. Dyn.* **201**, 168 (1994).
6. A. M. Ashique, K. Fu, J. M. Richman, *Development* **129**, 4647 (2002).
7. A. M. Ashique, K. Fu, J. M. Richman, *Int. J. Dev. Biol.* **46**, 243 (2002).
8. D. Hu, R. S. Marcucio, J. A. Helms, *Development* **130**, 1749 (2003).
9. P. Wu *et al.*, data not shown.
10. A. Abzhanov, M. Protas, B. R. Grant, P. R. Grant, C. J. Tabin, *Science* **305**, 1462 (2004).
11. G. von Dassow, E. Munro, *J. Exp. Zool.* **285**, 307 (1999).
12. M. E. MacDonald, U. K. Abbott, J. M. Richman, *Dev. Dyn.* **230**, 335 (2004).

13. We thank C. J. Tabin and A. Abzhanov for discussion, and B. R. Grant for comments. This work is supported by NIH grants AR42177 and AR47364 (C.-M.C.), and CA83716 (R.B.W.).

Supporting Online Material

www.sciencemag.org/cgi/content/full/305/5689/1465/DC1
Materials and Methods
Figs. S1 to S3
Table S1
References

19 March 2004; accepted 23 July 2004

Activation of Apoptosis in Vivo by a Hydrocarbon-Stapled BH3 Helix

Loren D. Walensky,[1,2] Andrew L. Kung,[2,3] Iris Escher,[4] Thomas J. Malia,[5,6] Scott Barbuto,[1] Renee D. Wright,[3] Gerhard Wagner,[5] Gregory L. Verdine,[4]* Stanley J. Korsmeyer[1]*

BCL-2 family proteins constitute a critical control point for the regulation of apoptosis. Protein interaction between BCL-2 members is a prominent mechanism of control and is mediated through the amphipathic α-helical BH3 segment, an essential death domain. We used a chemical strategy, termed hydrocarbon stapling, to generate BH3 peptides with improved pharmacologic properties. The stapled peptides, called "stabilized alpha-helix of BCL-2 domains" (SAHBs), proved to be helical, protease-resistant, and cell-permeable molecules that bound with increased affinity to multidomain BCL-2 member pockets. A SAHB of the BH3 domain from the BID protein specifically activated the apoptotic pathway to kill leukemia cells. In addition, SAHB effectively inhibited the growth of human leukemia xenografts in vivo. Hydrocarbon stapling of native peptides may provide a useful strategy for experimental and therapeutic modulation of protein-protein interactions in many signaling pathways.

BCL-2 is the founding member of a protein family (*1*–*3*) composed of pro- and anti-apoptotic molecules that serve as an essential control point in apoptosis, governing susceptibility to cell death (*4*–*6*). The BCL-2 family is defined by the presence of up to four conserved BCL-2 homology (BH) domains, all of which include α-helical segments. Anti-apoptotic proteins (for example, BCL-2 and BCL-X_L) display sequence conservation in all BH domains, whereas pro-apoptotic proteins are divided into multidomain members (such as BAX and BAK), and BH3-only members (such as BID and BAD) that display sequence similarity only to the BH3 α-helical domain. The amphipathic α-helical BH3 segment of pro-

[1]Howard Hughes Medical Institute, [2]Department of Pediatric Hematology/Oncology and Children's Hospital Boston, [3]Department of Cancer Biology, Dana-Farber Cancer Institute, Boston, MA 02115, USA. [4]Department of Chemistry and Chemical Biology, Harvard University, Cambridge, MA 02138, USA. [5]Department of Biological Chemistry and Molecular Pharmacology, Harvard Medical School, Boston, MA 02115, USA. [6]Department of Chemistry, Massachusetts Institute of Technology, Cambridge, MA 02139, USA.

*To whom correspondence should be addressed. E-mail: stanley_korsmeyer@dfci.harvard.edu (S.J.K.) and verdine@chemistry.harvard.edu (G.L.V.)

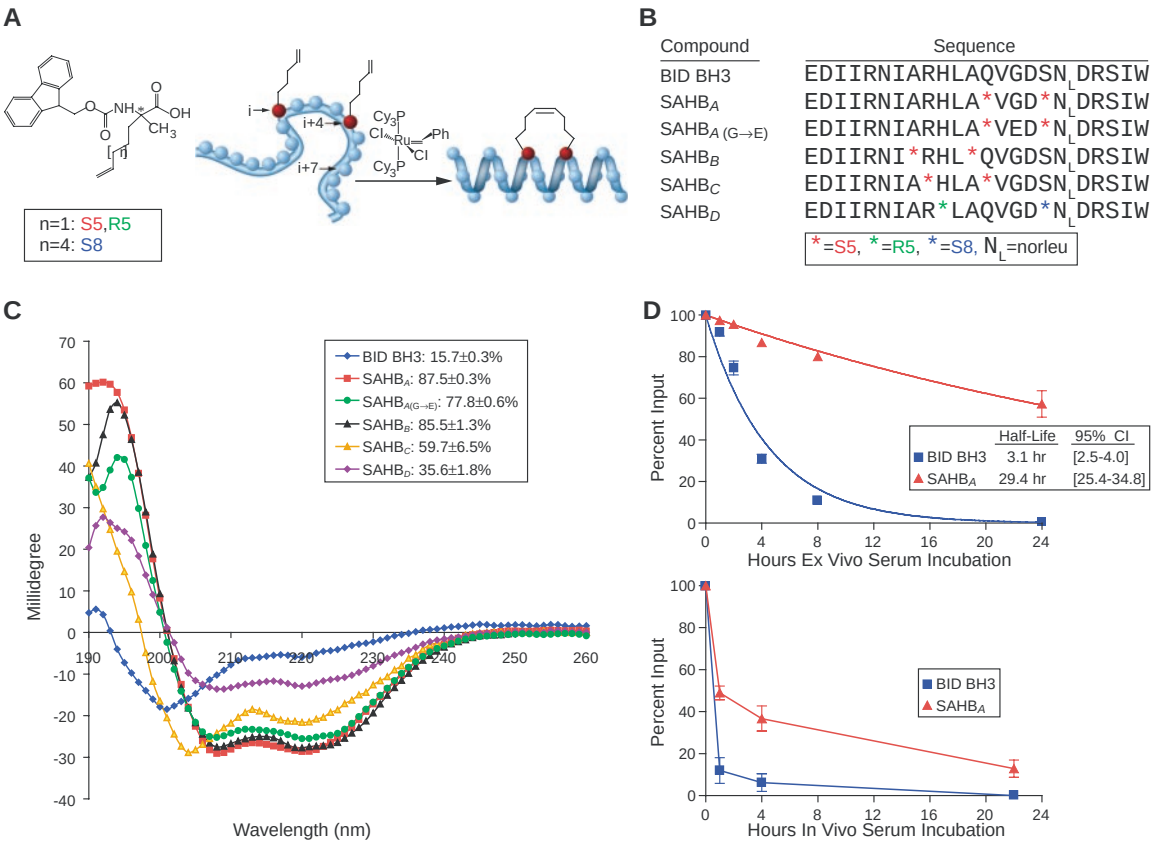

Fig. 1. Enhanced helicity, protease resistance, and serum stability of hydrocarbon-stapled BID BH3 compounds. (**A** and **B**) α,α-disubstituted nonnatural amino acids containing olefinic side chains of varying length were synthesized as previously reported (*16*, *31*, *32*). Nonnatural amino acid substitutions were made to flank three (substitution positions i and i+4) or six (i and i+7) amino acids within the BID BH3 peptide, so that reactive olefinic residues would reside on the same face of the α helix. (**C**) Circular dichroism was used to measure the percentages of SAHB maintained in helical configuration when dissolved in aqueous potassium phosphate solution (pH 7) (supporting online material). (**D**) Fluoresceinated $SAHB_A$ and BID BH3 peptide were incubated at 37°C in mouse serum or injected intravenously (10 mg/kg) into NOD SCID mice. Serum concentrations of $SAHB_A$ and BID BH3 peptide were measured at the indicated time points with a fluorescence-based high-performance liquid chromatography detection assay. Both assays demonstrated enhanced serum stability of $SAHB_A$.

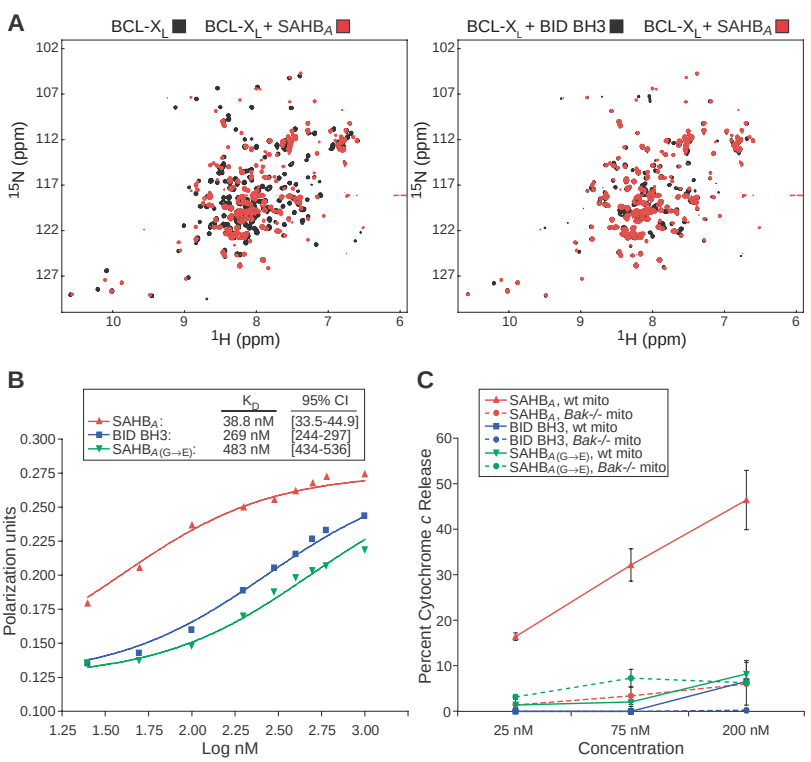

Fig. 2. $SAHB_A$ targets the binding pocket of BCL-X_L, displays enhanced BCL-2 binding affinity, and specifically activates cytochrome c release from mitochondria in vitro. (**A**) HSQC experiments show similar spectral changes in ^{15}N-BCL-X_L upon binding $SAHB_A$ or BID BH3 peptide. (**B**) K_d's for binding of individual peptides to glutathione *S*-transferase–BCL-2 were determined by fluorescence polarization. (**C**) Mouse liver mitochondria (wild-type or Bak$^{-/-}$, 0.5 mg/ml) were incubated for 40 min with 25 to 200 nM concentrations of BID BH3 peptide, $SAHB_A$, or $SAHB_{A(G\rightarrow E)}$, and cytochrome c was measured in the supernatant and sedimented mitochondria by an enzyme-linked immunosorbent assay.

apoptotic family members is a required death domain (*7*, *8*) that binds to the hydrophobic groove formed by the juxtaposition of BH1, BH2, and BH3 domains of anti-apoptotic multidomain members (*9*, *10*).

The α helix, a major structural motif of proteins, frequently mediates intracellular protein-protein interactions that govern

many biological pathways (*7*, *11*). Theoretically, helical peptides, such as the BH3 helix, could be used to selectively interfere with or stabilize protein-protein interactions and thereby manipulate physiological processes. However, biologically active helical motifs within proteins typically have little structure when taken out of context and placed in solution. Although peptides are attractive candidates for stabilizing or disrupting protein-protein interactions, their efficacy as in vivo reagents is severely compromised by their loss of secondary structure, susceptibility to proteolytic degradation, and difficulty in penetrating intact cells.

Most approaches to covalent helix stabilization involve polar or labile cross-links (*12*–*15*), which leave the peptides vulnerable to decomposition or unable to penetrate cells, if not both. We have developed an alternative strategy in which we use α,α-disubstituted non-natural amino acids containing olefin-bearing tethers to generate an all-hydrocarbon "staple" by ruthenium-catalyzed olefin metathesis (*16*, *17*) (Fig. 1A). A panel of hydrocarbon-stapled peptides, referred to as stabilized alpha-helix of BCL-2 domains (SAHBs), was designed to mimic the BH3 domain of BID (Fig. 1B). BID is a pro-apoptotic BH3-only protein that, in response to death receptor signaling, interconnects the extrinsic and core intrinsic apoptotic pathways. Activated BID (tBID) can be bound and sequestered by anti-apoptotic proteins (such as BCL-2 and BCL-X_L), but also triggers activation of the multidomain pro-apoptotic proteins BAX and BAK, resulting in cytochrome c release and a mitochondrial program of apoptosis (*4*–*6*, *8*, *18*, *19*).

Circular dichroism revealed that a 23–amino acid BID BH3 peptide displays only 16% helicity in solution and thus predominantly exists as a random coil (Fig. 1C). SAHBs, however, demonstrated helical stabilization, with helical content ranging from 35 to 87%. In addition to reinforcing

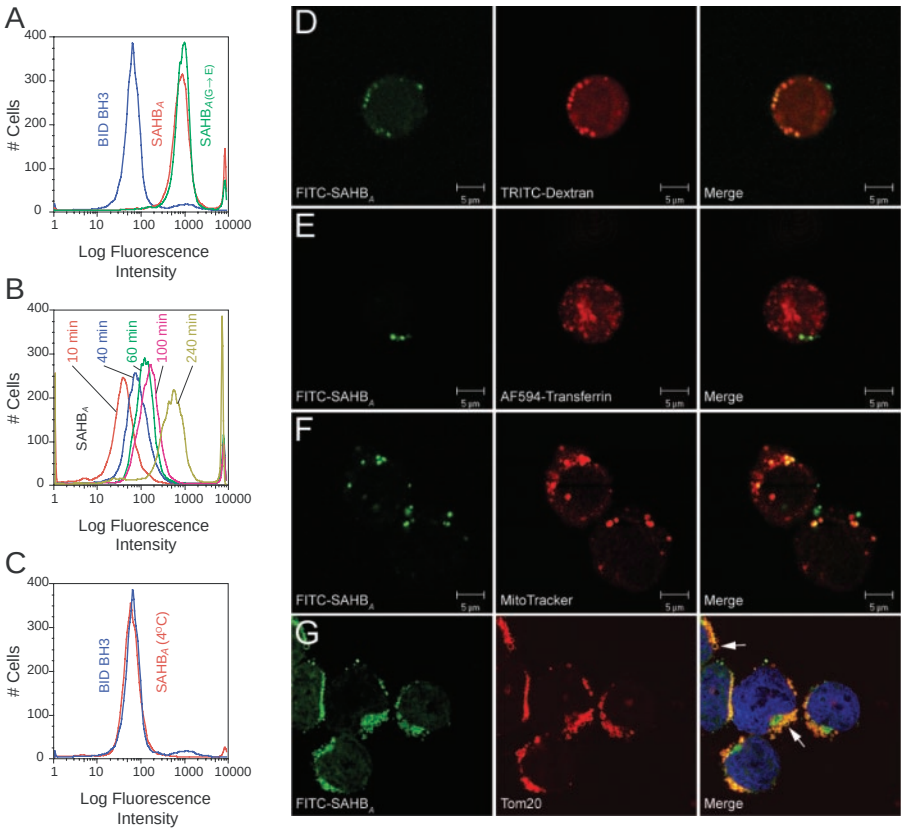

Fig. 3. SAHB$_A$ penetrates Jurkat leukemia cells by fluid-phase endocytosis and localizes to the mitochondrial membrane. Jurkat leukemia cells were incubated with FITC-labeled peptides for 4 hours at 37°C, followed by FACS analysis (**A**). FITC-SAHB$_A$ uptake occurred in a time-dependent manner at 37°C (**B**), but no FITC-SAHB$_A$ labeling was evident by 4 hours, when the experiment was performed at 4°C (**C**). Live confocal images demonstrated a colocalization of FITC-SAHB$_A$ with 4.4-kD dextran-labeled endosomes (**D**) but not transferrin-labeled endosomes (**E**) at 4 hours. A mitochondrial colocalization was evident by 24 hours, as demonstrated by the merged images of FITC-SAHB$_A$ and MitoTracker in live cells (**F**) and those of FITC-SAHB$_A$ and Tom20 (a mitochondrial outer-membrane marker) in fixed cells (**G**). Arrows highlight sites of colocalization corresponding to the surface of mitochondria cut in cross section (G).

Fig. 4. SAHB$_A$ triggers apoptosis in Jurkat cells and inhibits a panel of human leukemia cells. FACS analysis of annexin V–treated cells was used to monitor apoptosis of Jurkat cells treated with 0.5 to 5 μM concentrations of BID BH3 peptide, SAHB$_A$, or SAHB$_{A(G\rightarrow E)}$ for 20 hours (**A**). Jurkat, REH, MV4;11, SEMK2, and RS4;11 leukemia cells were treated with serial dilutions of SAHB$_A$ (**B**), BID BH3 peptide (**C**), or SAHB$_{A(G\rightarrow E)}$ (**D**), and MTT assays were performed at 48 hours to measure viability.

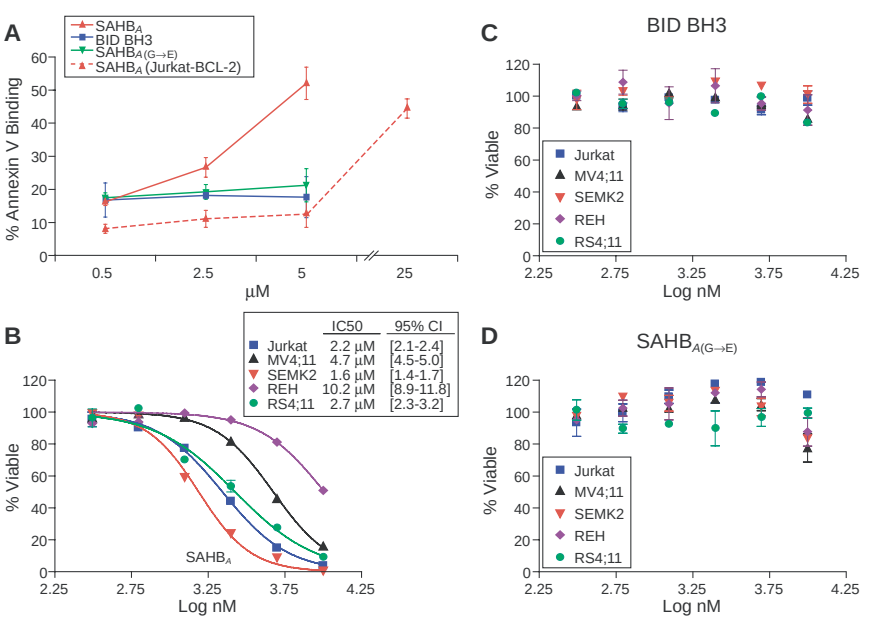

the biologically active secondary structure of the BID BH3 domain, peptide helix stabilization is expected to bury the amide backbone, shielding it from proteolysis. Insertion of the hydrocarbon staple did endow SAHBs with protease resistance and serum stability in vitro and in vivo, as exemplified by comparing $SAHB_A$ to the unmodified BID BH3 peptide in three distinct degradation assays (Fig. 1D and fig. S1).

To determine whether $SAHB_A$ specifically interacts with the defined binding groove of an anti-apoptotic multidomain protein, we recorded a two-dimensional ^{15}N-^{1}H heteronuclear single-quantum correlation (HSQC) spectrum of ^{15}N-labeled BCL-X_L before and after the addition of $SAHB_A$ and compared the profile with the corresponding spectrum derived from addition of unmodified BID BH3 peptide (Fig. 2A). The overall similarity of the HSQC spectra indicates that the structural changes occurring in BCL-X_L after the addition of $SAHB_A$ are nearly identical to those observed with BID BH3 peptide. A BCL-2 fluorescence polarization binding assay demonstrated more than sixfold enhancement in binding affinity of $SAHB_A$ (K_d, 38.8 nM) compared to that of unmodified BID BH3 peptide (K_d, 269 nM) (Fig. 2B). A Gly-to-Glu mutation (*8*) [$SAHB_{A(G\rightarrow E)}$] (K_d, 483 nM), reduced high-affinity binding and served as a useful control.

The in vitro biological activity of $SAHB_A$ was investigated by assaying peptide-induced cytochrome c release from purified mouse liver mitochondria. Measured at equilibrium, $SAHB_A$ caused a dose-dependent increase in cytochrome c release, in contrast to the negligible effects of BID BH3 peptide and the $SAHB_{A(G\rightarrow E)}$ point mutant in the dose range from 25 to 200 nM (Fig. 2C). The identical experiment was performed on isolated *Bak*$^{-/-}$ mouse liver mitochondria, which lack both BAK and cytosolic BAX and do not release cytochrome c in response to tBID (*5*, *18*). The inability of $SAHB_A$ to induce cytochrome c release from *Bak*$^{-/-}$ mitochondria confirms that it functions through the defined pathway of apoptosis.

With the exception of select positively charged peptides (*20*–*22*), the electrostatic charge of amino acid side chains and the polarity of the peptide backbone generally impede the transduction of peptides across cellular membranes. We tested whether our approach to stabilizing helical structure by the insertion of a hydrocarbon staple would confer lipophilic and potentially membrane-penetrating properties on SAHB compounds. We incubated Jurkat T cell leukemia cells in culture with fluorescein isothiocyanate (FITC)–labeled BID BH3 peptide, $SAHB_A$, or $SAHB_{A(G\rightarrow E)}$, followed by confocal microscopy and fluorescence-activated cell sorting (FACS) analyses. Whereas FITC was not detected in BID BH3–treated cells, $SAHB_A$-treated cells displayed fluorescent labeling, with a discrete cytoplasmic localization evident within the cells on confocal images (Fig. 3 and fig. S2). FITC-labeled Jurkat cells initially excluded propidium iodide (as determined by FACS analysis), indicating that $SAHB_A$ compounds do not function as nonspecific permeabilizing agents. The cellular uptake of FITC-$SAHB_A$ was time-dependent (Fig. 3B) and was inhibited at 4°C (Fig. 3C) and by a combination treatment with sodium azide and deoxyglucose

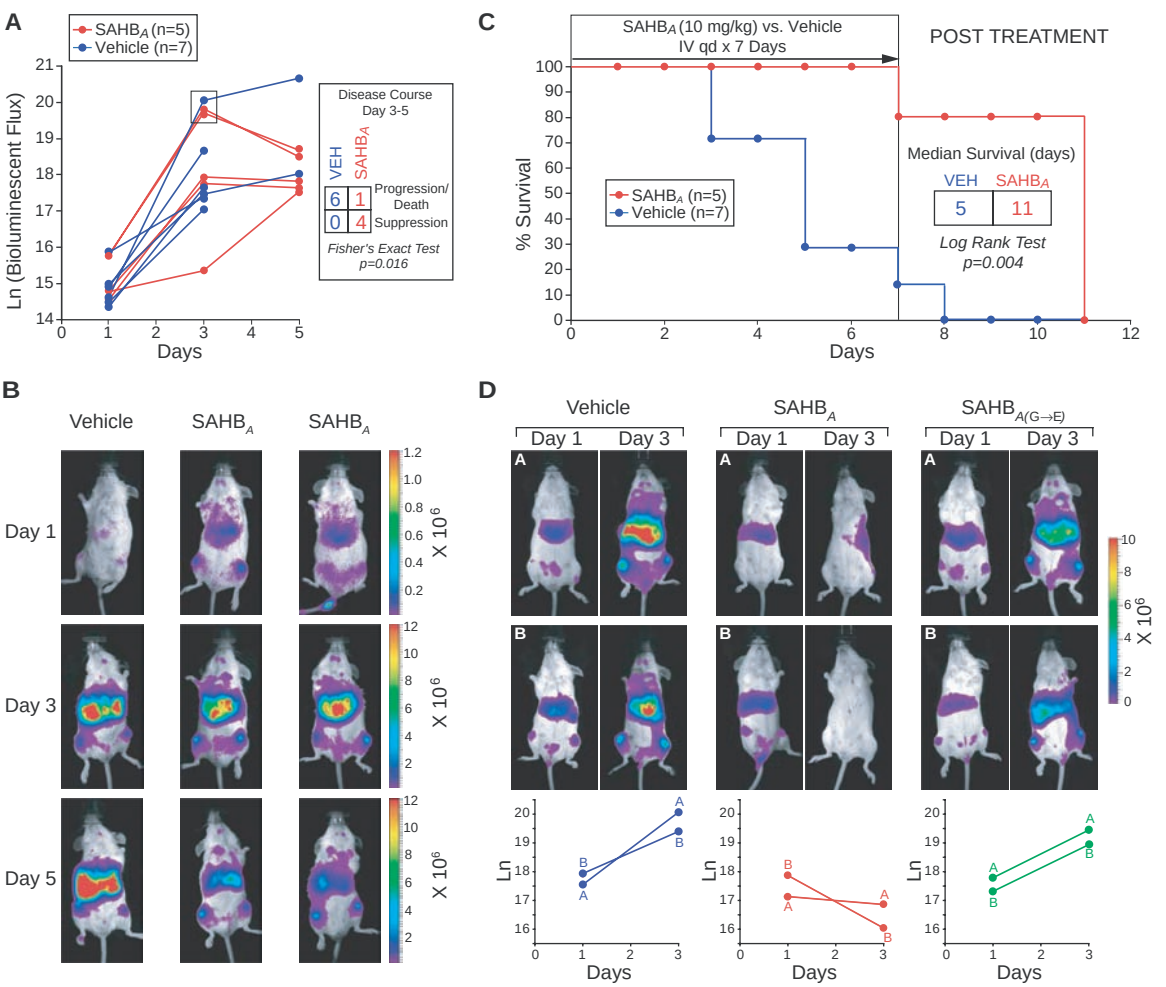

Fig. 5. $SAHB_A$ suppresses growth of human leukemia cells in vivo, prolonging the survival of leukemic mice. (**A**) Leukemic SCID beige mice [with a day-1 natural logarithm (ln) bioluminescence range of 14.4 to 15.9] were treated with intravenous injections of 10 mg/kg $SAHB_A$ or vehicle (5% DMSO in D5W) daily for 7 days and were monitored for survival; leukemia burden was quantified by total body luminescence (photons/s/mouse) on days 1, 3, and 5. The disease course from days 3 to 5 differed between $SAHB_A$-treated animals and controls ($P = 0.016$, Fisher's exact test [box in (A)], as illustrated by representative Xenogen images of bioluminescent leukemic mice (**B**); red signal represents the highest level of leukemia on the colorimetric scale. (**C**) Median survival was prolonged in $SAHB_A$-treated animals as compared to controls ($P = 0.004$, log rank test). (**D**) To compare $SAHB_A$ with $SAHB_{A(G\rightarrow E)}$, leukemic mice (with a day 1 ln bioluminescence range of 17.1 to 17.9) were treated daily with SAHB (10 mg/kg) or vehicle, and animals were imaged on days 1 and 3 to measure total body luminescence.

(*23*), suggesting an energy-dependent endocytosis mechanism for cellular import. Whereas binding to cell surface glycosaminoglycans, such as heparin, has been implicated in the targeting and import mechanism of positively charged cell penetrating peptides such as human immunodeficiency virus transactivator of transcription (TAT) and Antennapedia (Antp) (*24–26*), cellular uptake of $SAHB_A$ was not inhibited in a dose-responsive manner by soluble heparin (fig. S3). Live cell confocal microscopy performed 4 hours after SAHB treatment demonstrated an initial colocalization of FITC-$SAHB_A$ with 4.4- or 70-kD dextran-labeled endosomes (Fig. 3D) but not transferrin-labeled endosomes (Fig. 3E), which is consistent with cellular uptake by fluid-phase pinocytosis (*27*), the endocytic pathway determined for TAT and Antp peptides (*28*). At a 24-hour time point, intracellular FITC-$SAHB_A$ showed increased colocalization with MitoTracker-labeled mitochondria in live cells (Fig. 3F), consistent with the mitochondrial colocalization observed in fixed cells when an antibody to Tom20 (*29*), a mitochondrial outer membrane protein, was used (Fig. 3G).

The ability of $SAHB_A$ to activate apoptosis was assessed in Jurkat T cell leukemia cells. Fifty percent of cells treated with 5 μM $SAHB_A$ demonstrated staining for annexin V after 20 hours, whereas cells treated with BID BH3 peptide or $SAHB_{A(G\rightarrow E)}$ showed no increase in apoptosis in this dose range (Fig. 4A). Jurkat cells overexpressing BCL-2 were resistant to 5 μM $SAHB_A$. However, the protective effect of BCL-2 could be overcome at higher concentrations of $SAHB_A$; the rightward shift in dose response is consistent with $SAHB_A$ functioning at the BCL-2 control point in intact cells. In concert, these data indicate that $SAHB_A$ can penetrate leukemia cells and selectively trigger the apoptotic pathway.

To investigate whether $SAHB_A$ would inhibit a wider panel of leukemia cells, 3-(4,5-dimethylthiazol-2-yl)2,5-diphenyl tetrazolium bromide (MTT) assays were performed on T cell (Jurkat), B cell (REH), and mixed lineage leukemia (MLL) cells (cell lines MV4;11, SEMK2, and RS4;11) in culture. $SAHB_A$ inhibited the proliferation of leukemia cells at median inhibitory concentrations of 2.2 (Jurkat), 10.2 (REH), 4.7 (MV4;11), 1.6 (SEMK2), and 2.7 (RS4;11) μM (Fig. 4B). Neither the BID BH3 peptide nor the $SAHB_{A(G\rightarrow E)}$ point mutant had an effect in this dose range (Fig. 4, C and D).

In four cohorts of immunodeficient mice bearing established human leukemia xenografts, $SAHB_A$ treatment consistently suppressed leukemia growth in vivo. On day –3 of experimentation, severe combined immunodeficient (SCID) beige mice were subjected to 300 cGy of total body irradiation, followed by intravenous injection of 5×10^6 RS4;11 leukemia cells that stably expressed luciferase. Leukemia burden was monitored using the In Vivo Imaging System (IVIS, Xenogen), which quantitates total body luminescence after intraperitoneal injection of D-luciferin (*30*). On day 1, leukemic mice were treated intravenously with $SAHB_A$ [10 mg per kg of body weight (mg/kg)] or with vehicle [5% dimethyl sulfoxide (DMSO) in 5% dextrose water] daily for 7 days. Mice were monitored daily for survival and were imaged on days 1, 3, and 5 to measure leukemia burden. Control mice demonstrated progressive leukemic growth as quantitated by increased luminescence from days 1 through 5 (Fig. 5A). In this cohort, $SAHB_A$ treatment usually suppressed the leukemic expansion after day 3, and tumor regression was frequently observed by day 5. Imaging showed progressive leukemic infiltration of the spleen and liver in control mice, but often showed regression of disease at these anatomical sites in $SAHB_A$-treated mice by day 5 of treatment (Fig. 5B). The median time to death in this cohort was 5 days for control animals, but 11 days for $SAHB_A$-treated animals (Fig. 5C). In a similar experiment comparing the effects of $SAHB_A$ and $SAHB_{A(G\rightarrow E)}$, animals receiving the point mutant SAHB did not exhibit regression of leukemia (Fig. 5D). Histologic examination of $SAHB_A$-treated mice showed no obvious toxicity of the compound to normal tissue.

Insertion of an all-hydrocarbon staple into the BID BH3 peptide yielded a marked enhancement of peptide α-helicity, stability, and in vitro and in vivo biological activity. SAHBs that engage the pocket of multidomain BCL-2 members could serve as prototypes for the development of therapeutics for cancer and perhaps other diseases. Intracellular protein-protein interactions constitute major control points in many signaling pathways, yet have frequently proven a difficult target for small-molecule chemistry, often reflecting a protein interface that is extensive, shallow, and hydrophobic. Such endogenous control points are typically regulated by other protein domains or their modifications. Synthetic approaches such as hydrocarbon stapling that reinforce native peptide sequences provide an alternative strategy to probe protein-protein interactions and manipulate biological pathways.

References and Notes

1. A. Bakhshi *et al*., *Cell* **41**, 899 (1985).
2. M. L. Cleary, J. Sklar, *Proc. Natl. Acad. Sci. U.S.A.* **82**, 7439 (1985).
3. Y. Tsujimoto, J. Cossman, E. Jaffe, C. M. Croce, *Science* **228**, 1440 (1985).
4. N. N. Danial, S. J. Korsmeyer, *Cell* **116**, 205 (2004).
5. M. C. Wei *et al*., *Science* **292**, 727 (2001).
6. L. Scorrano *et al*., *Science* **300**, 135 (2003).
7. T. Chittenden *et al*., *EMBO J.* **14**, 5589 (1995).
8. K. Wang, X. M. Yin, D. T. Chao, C. L. Milliman, S. J. Korsmeyer, *Genes Dev.* **10**, 2859 (1996).
9. S. W. Muchmore *et al*., *Nature* **381**, 335 (1996).
10. M. Sattler *et al*., *Science* **275**, 983 (1997).
11. P. H. Kussie *et al*., *Science* **274**, 948 (1996).
12. J. C. Phelan, N. J. Skelton, A. C. Braisted, R. S. McDowell, *J. Am. Chem. Soc.* **119**, 455 (1997).
13. A. Leuc *et al*., *Proc. Natl. Acad. Sci. U.S.A.* **100**, 11273 (2003).
14. C. Bracken, J. Gulyas, J. W. Taylor, J. Baum, *J. Am. Chem. Soc.* **116**, 6431 (1994).
15. B. Yan, D. Liu, Z. Huang, *Bioorg. Med. Chem. Lett.* **14**, 1403 (2004).
16. C. Schafmeister, J. Po, G. Verdine, *J. Am. Chem. Soc.* **122**, 5891 (2000).
17. H. E. Blackwell, R. H. Grubbs, *Angew. Chem. Int. Ed. Engl.* **37**, 3281 (1994).
18. M. C. Wei *et al*., *Genes Dev.* **14**, 2060 (2000).
19. X. Luo, I. Budihardjo, H. Zou, C. Slaughter, X. Wang, *Cell* **94**, 481 (1998).
20. S. Fawell *et al*., *Proc. Natl. Acad. Sci. U.S.A.* **91**, 664 (1994).
21. D. Derossi, A. H. Joliot, G. Chassaing, A. Prochiantz, *J. Biol. Chem.* **269**, 10444 (1994).
22. S. R. Schwarze, A. Ho, A. Vocero-Akbani, S. F. Dowdy, *Science* **285**, 1569 (1999).
23. L. D. Walensky, S. J. Korsmeyer, unpublished data.
24. G. Drin, S. Cottin, E. Blanc, A. R. Rees, J. Temsamani, *J. Biol. Chem.* **278**, 31192 (2003).
25. S. Console, C. Marty, C. Garcia-Echeverria, R. Schwendener, K. Ballmer-Hofer, *J. Biol. Chem.* **278**, 35109 (2003).
26. J. P. Richard *et al*., *J. Biol. Chem.* **278**, 585 (2003).
27. N. Araki, M. T. Johnson, J. A. Swanson, *J. Cell Biol.* **135**, 1249 (1996).
28. J. S. Wadia, R. V. Stan, S. F. Dowdy, *Nature Med.* **10**, 310 (2004).
29. E. Schleiff, G. C. Shore, I. S. Goping, *J. Biol. Chem.* **272**, 17784 (1997).
30. S. A. Armstrong *et al*., *Cancer Cell* **3**, 173 (2003).
31. R. M. Williams, M. N. Im, *J. Am. Chem. Soc.* **113**, 9276 (1991).
32. Single-letter abbreviations for the amino acid residues are as follows: A, Ala; D, Asp; E, Glu; G, Gly; H, His; I, Ile; L, Leu; Q, Gln; R, Arg; S, Ser; V, Val; and W, Trp.

33. We thank D. Brown and M. Salanga for assistance with confocal microscopy; D. Neuberg and M. Goldwasser for biostatistics support; E. Gillespie and W. Beavers for assistance with automated peptide synthesis and amino acid analysis; S. Armstrong for providing leukemia cell lines; R. Bronson for rodent necropsy evaluation; Q. Liao for assistance with mass spectrometry; S. Lux, B. Malynn, and F. Bernal for helpful discussions; and E. Smith for editorial and computer graphics assistance. L.D.W. is a Lymphoma Research Foundation Fellow and is also supported by National Heart, Lung, and Blood Institute grant no. K08HL074049, an American Society of Hematology Scholar Award, and the Lauri Strauss Leukemia Foundation. This work is supported in part by NIH grant no. R37CA50239, a Leukemia and Lymphoma Society deVilliers International Achievement Award to S.J.K., a grant from the Virginia and D.K. Ludwig Fund for Cancer Research to G.W., and a gift from Enanta Pharmaceuticals to G.L.V. Molecular interaction data have been deposited in the Biomolecular Interaction Network Database with accession codes 151034 and 151035.

Supporting Online Material

www.sciencemag.org/cgi/content/full/305/5689/1466/DC1
SOM Text
Figs. S1 to S3
References and Notes

15 April 2004; accepted 15 July 2004

A Small Molecule Smac Mimic Potentiates TRAIL- and TNFα-Mediated Cell Death

Lin Li,[1]* Ranny Mathew Thomas,[1]* Hidetaka Suzuki,[1]*
Jef K. De Brabander,[1]† Xiaodong Wang,[1,2]† Patrick G. Harran[1]†

We describe the synthesis and properties of a small molecule mimic of Smac, a pro-apoptotic protein that functions by relieving inhibitor-of-apoptosis protein (IAP)–mediated suppression of caspase activity. The compound binds to X chromosome–encoded IAP (XIAP), cellular IAP 1 (cIAP-1), and cellular IAP 2 (cIAP-2) and synergizes with both tumor necrosis factor α (TNFα) and TNF-related apoptosis-inducing ligand (TRAIL) to potently induce caspase activation and apoptosis in human cancer cells. The molecule has allowed a temporal, unbiased evaluation of the roles that IAP proteins play during signaling from TRAIL and TNF receptors. The compound is also a lead structure for the development of IAP antagonists potentially useful as therapy for cancer and inflammatory diseases.

Inhibitor-of-apoptosis proteins (IAPs) inhibit the enzymatic activity of caspases, cysteine proteases that execute the cell death program (*1*). IAPs bind directly to caspases with the use of a characteristic ~70-residue zinc-containing domain termed the baculovirus inhibitory repeat (Bir). Human X chromosome–encoded IAP (XIAP), cellular IAP 1 (cIAP-1), and cellular IAP 2 (cIAP-2) have three tandem repeats of the Bir domain in their N-terminal region, whereas other mammalian IAPs have a single Bir domain (*2*). XIAP is the most potent caspase inhibitor among IAPs, and it interacts with initiator caspase 9 and executioner caspases 3 and 7 through its Bir3 and Bir2 domains, respectively (*3*, *4*). The role of cIAP 1 and 2 in apoptosis is less defined, although both are associated with the TNFα receptor 1 signaling complex (*5*, *6*). XIAP potently inhibits activated caspases, those generated in situ from a corresponding zymogen after the stimulation of death receptors on the cell surface or after the release of pro-apoptotic factors from the intermembrane space of mitochondria into the cytosol (*3*). Because effector caspase activity is both necessary and sufficient for irrevocable programmed cell death, XIAP functions as a gatekeeper to this final stage of the process. IAP gene amplifications and protein overexpression have been found in many human cancers, suggesting a means by which these cells evade apoptosis during tumorigenesis and become resistant to chemotherapy and radiation treatments (*7*–*9*).

IAP-mediated inhibition of apoptosis is countered by the second mitochondria-derived activator of caspases (Smac) (*10*, *11*). Smac protein is secreted from mitochondria into the cytosol during apoptosis. There it interacts with Bir domains in IAPs with the use of four amino acid residues [AVPI (*12*)] at its N terminus (*13*, *14*). Synthetic Smac N-terminal peptides fused to cell-permeablizing peptides have been found to bypass mitochondrial regulation and sensitize both human cancer cells in culture and tumor xenographs in mice to apoptosis when combined with TNF-related apoptosis-inducing ligand (TRAIL) or chemotherapeutic drug treatments (*15*–*18*). Here, we describe a small molecule that functions similarly at 10^5- to 10^6-fold lower concentrations. The compound penetrates cell membranes and binds XIAP with an affinity equal to that of Smac itself. Moroever, as a true Smac mimetic, the molecule also binds and eliminates cIAP-1 and cIAP-2 activities and promotes both TRAIL- and TNFα-induced apoptosis at low nanomolar concentrations in cancer cell culture.

The co-crystal structure of Smac in complex with the XIAP Bir3 domain shows the Smac N terminus interacts with a groove formed on the Bir3 surface (*13*). The four Smac residues (AVPI) that contact Bir3 do so by docking a fourth strand onto an existent three-stranded antiparallel β sheet. Structural variations in the C-terminal end of the tetrapeptide are tolerated, and AVPF (*12*) actually outperforms AVPI as a Smac mimetic in vitro. We therefore used computer-simulated conformations of AVPF as a guide to design nonpeptidyl replacements for its C-terminal half (PF). Each was synthesized in optically active form, immobilized onto the surface of polystyrene beads, and used to generate a set of compounds having variable amino acids at position two and L-alanine at position one (*19*). The resultant hybrid mimetics (180 compounds) were released from solid support, purified, and evaluated for their ability to compete at the Smac binding site on recombinant XIAP-Bir3 (*14*). In this format, oxazoline **1** was the most potent competitor (Fig. 1, A and B). However, a number of its relatives had comparable affinity for the Bir3 domain, and no compound performed better than AVPF. When **1** was tested for stimulation of deoxyadenosine triphosphate (dATP)–dependent caspase 3 activation in soluble HeLa extracts, its potency exceeded that of synthetic AVPF but was orders of magnitude less than recombinant Smac. This troubling situation remained unchanged until modifications of **1** reached tetrazoyl thioethers of type **2**. Attempts at a particular manipulation of the alkyne in **2** produced a by-product eventually characterized as C_2-symmetric diyne **3**, the endpoint of an oxidative homodimerization known as a Glaser coupling (*20*). Dimer **3** and its corresponding monomer **2** have comparable affinity for an isolated XIAP Bir3 domain (Fig. 1B). However, in a caspase 3 activation assay that measures neutralization of endogenous IAP activity in HeLa cell extract, diyne **3** is much more active as a Smac mimetic (Fig. 1D). The reason for this large discrepancy is likely attributable to bivalency. In particular, that compound **3** may interact simultaneously with adjacent Bir domains in XIAP. The resultant two-point bound complex may be considerably more stable than single-site affinities would predict (*21*). Recent evidence suggests that Smac, a native homodimer, binds XIAP similarly (*22*).

Complexes of Smac and full-length XIAP can be visualized by Coomassie Blue staining after nondenaturing gel electrophoresis. Incubation of XIAP with Smac (1:1.6 molar ratio) produces a high molecular weight complex that is completely disrupted by inclusion of a twofold molar excess of compound **3** (Fig. 1C). In fact, equal molar amounts of **3** disrupt more than half of the XIAP/Smac complex (lane 8). To the extent that equilibrium is reached under these conditions, the data suggest that compound **3** has a higher affinity for XIAP than does Smac. The latter interaction has $K_D \sim 300$ pM when measured with full-length Smac and a Bir2+Bir3-containing segment of XIAP (*22*). Monomer **2** and control **4** (both alanine residues carbamoylated) have no effect on the Smac/XIAP complex, even when present in fivefold excess (lanes 11 and 13). Like Smac, compound **3** also competitively blocks the interaction of XIAP with active caspase 9 in vitro (Fig. 1F) (*23*).

To test the activity of compound **3** in vivo, we added it in varying amounts to T98G cells. T98G is a human glioblastoma cell line resistant to DNA damage–induced apoptosis. Compound **3** alone at high concentrations (>1 μM) does not induce apoptosis (Fig. 2A) or caspase 8 activation (Fig. 2B). However,

[1]Department of Biochemistry and [2]Howard Hughes Medical Institute, University of Texas Southwestern Medical Center at Dallas, 5323 Harry Hines Boulevard, Dallas, TX 75390–9038, USA.

*These authors contributed equally to the work.
†To whom correspondence should be addressed. E-mail: pharra@biochem.swmed.edu (P.G.H.), xwang@biochem.swmed.edu (X.W.), jdebra@biochem.swmed.edu (J.K.D.)

when used in combination with TRAIL (50 ng/mL), 100 nM of **3** causes extensive cell death (Fig. 2A). In fact, caspase 8 activation and apoptosis are observed at concentrations of **3** as low as 100 pM when combined with 50 ng/mL TRAIL (Fig. 2B). TRAIL alone at 50 ng/mL induces neither caspase 8 activation nor apoptosis in this cell line. Downstream caspase 3 activity in response to **3** plus TRAIL was monitored by Western blot analysis of cleaved poly(adenosine diphosphate–ribose)polymerase (PARP), a caspase 3 substrate (Fig. 2B). Endogenous PARP begins to be cleaved in the presence of 30 pM of **3** and 50 ng/mL TRAIL (lane 10, fig. S3). Control compound **4** has no effect in this assay. Importantly, unlike the situation in cancer cells, compound **3** alone (10 μM) or in combination with TRAIL had no detectable effects on primary cultures of human skin fibroblasts (*23*).

To verify that dimer **3** targets IAPs in cells, we synthesized a biotinylated variant. Although the display and spacing of monomers within this construct differs slightly

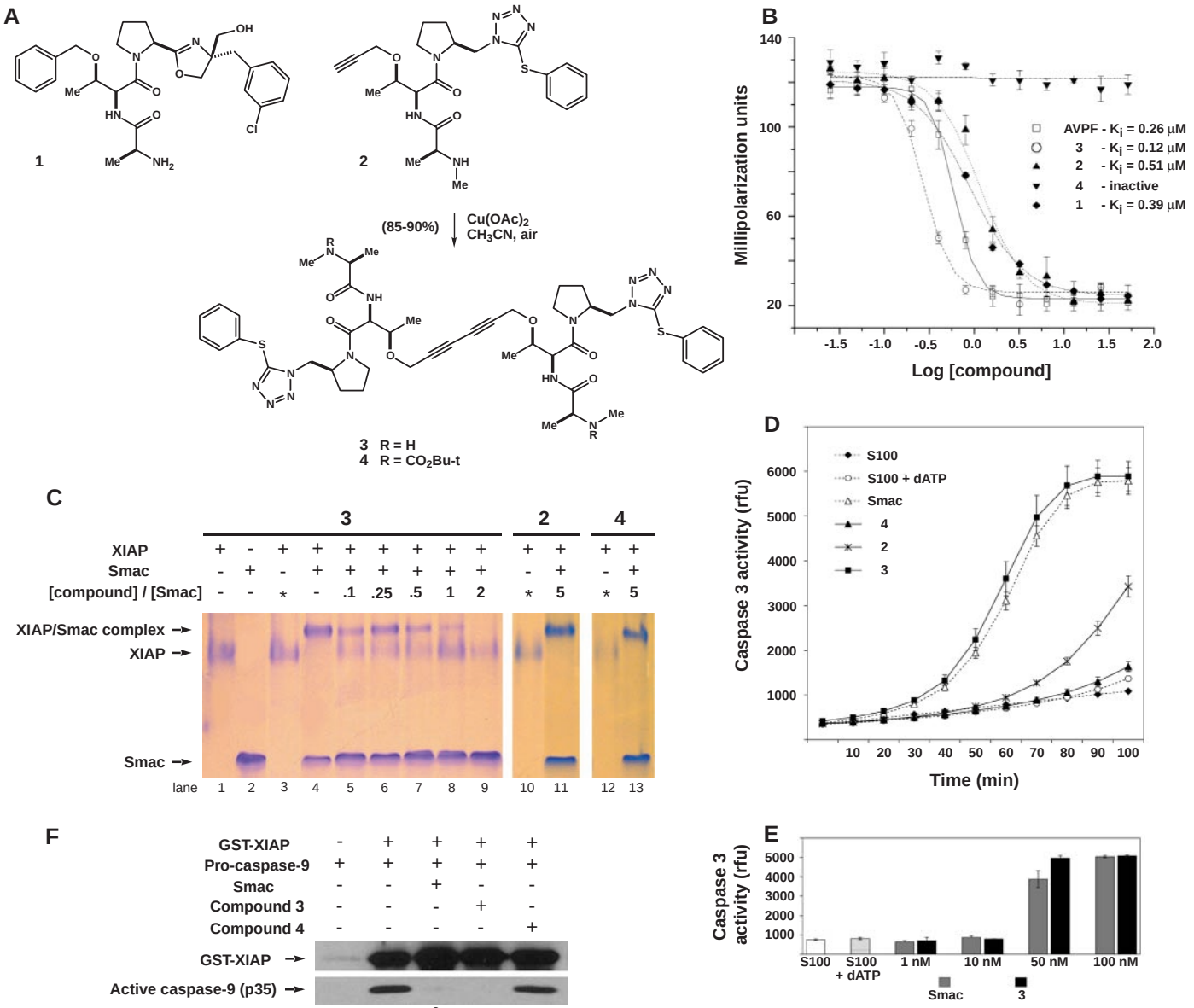

Fig. 1. C_2-symmetric compound **3** is a potent Smac mimetic in vitro. (**A**) Chemical structures of the small molecules described in this study. (**B**) Fluorescence polarization assay for the interaction of Smac and mimetics with the Bir3 domain of human XIAP. A synthetic Smac peptide [AVPIAQKSEK (*12*)] was C-terminally labeled with Alexafluor488 (Molecular Probes), and its complex with recombinant XIAP Bir3 (residues 241 to 356) was used to evaluate competitive Bir3 domain binding by synthetic small molecules (*14*). (**C**) Polyacrylamide gel electrophoresis under nondenaturing conditions and Coomassie Blue staining were used to evaluate the binding of **3** to recombinant full-length human XIAP. XIAP (5 μM) and Smac (8 μM) were incubated for 30 min at 37°C with or without prior treatment with varying amounts of **3**. Asterisks indicate that compound alone (40 μM) was present along with XIAP in lanes 3, 10, and 12. (**D**) Time course comparison of caspase 3 activation by recombinant Smac and small molecule mimetics. HeLa S100 was activated with 1 mM dATP. Either Smac (100 nM) or a small molecule (100 nM) was then added. The onset of caspase 3 activity was monitored as a fluorogenic substrate (Ac-DEVD-AMC, CalBiochem) was cleaved in situ (rfu, relative fluorescence units). (**E**) Bar graph representation of the same experiment performed in (D) except with varying concentrations of Smac and compound **3**. (**F**) Smac and compound **3** compete with glutathione *S*-transferase (GST)–tagged human XIAP for active caspase 9 binding. Procaspase 9 (0.9 μM) was activated with 20 nM Apaf-1, 100 nM cytochrome C, and 1 mM dATP and then incubated with recombinant GST-XIAP for 3 hours at 30°C either in the absence (lane 2) or presence (lane 3) of Smac (1 μM), compound **3** (1 μM, lane 4), or compound **4** (1 μM, lane 5). Western blots for active caspase 9 that subsequently associates with added glutathione-coated beads are shown.

from compound **3**, the molecule functions equally well to relieve IAP inhibition of caspase 3 in HeLa cell extracts (fig. S2). When biotinylated **3** was added to T98G cell extracts and recovered with streptavidin-coated beads, Western blots of associated proteins showed the presence of XIAP, cIAP-1, and cIAP-2 (Fig. 2C). Pre-incubating T98G cells with excess **3** blocked these affinity purifications, and a biotinylated control had no detectable IAP affinity in this format. These results suggest that compound **3** facilitates TRAIL-induced apoptosis by neutralizing the effects of multi-Bir domain–containing IAPs.

Related observations have been made with the use of Smac peptides. However, these experiments focused on XIAP as a mediator of their effects (*15*–*18*). The finding that **3** binds to cIAP 1 and 2 suggested the additional opportunity to probe the role of these proteins in TNFα signaling. Both are present in TNFα receptor-1 signaling complexes (*5*, *6*), but whether they inhibit caspase 8 or promote nuclear factor κB (NF-κB) and c-Jun N-terminal kinase (JNK) signaling (*24*), or both, was not clear. Treatment of HeLa cells with compound **3** (100 nM) in combination with TNFα causes extensive apoptosis (Fig. 3A). Caspase 8 activation was observed within 2 hours (Fig. 3C), and cleavage of endogenous PARP, indicative of caspase 3 activity, was detected after 4 hours. The effect of compound **3** in this case was comparable to that of 10 μM cycloheximide (Fig. 3B). TNFα treatment, either alone or in combination with monomer **2** or control compound **4** (Fig. 3A), had no such effect. These data indicate that the long-mysterious requirement for a translation inhibitor (cycloheximide) in TNFα-mediated apoptosis can be explained through lowered cIAP protein amounts. Likewise, lower XIAP levels would promote caspase 3 activation, the latter being observed 2 hours after caspase 8 activation (Fig. 3C). Interestingly, compound **3** has little if any effect on TNFα-induced activation of NF-κB and JNK signaling pathways (fig. S4).

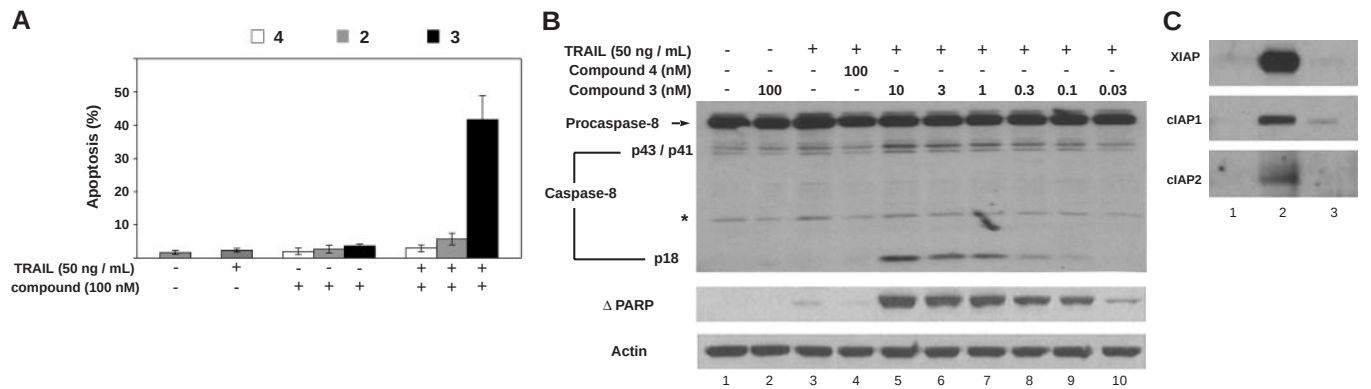

Fig. 2. Compound **3** and TRAIL act synergistically to induce apoptosis in cell culture. (**A**) Human glioblastoma (T98G) cells were cultured in Dulbecco's minimum essential medium (DMEM) containing fetal calf serum (10%) and treated with TRAIL (50 ng/mL) alone or compound (100 nM) alone for 15 and 19 hours, respectively. When used together, the small molecule was added 4 hours before TRAIL (total incubation time, 19 hours). Cell death (% of total population) was quantified by trypan blue staining. Values represent the average of three independent experiments (error bars indicate 1 standard derivation). (**B**) Activation of caspase 8 and caspase 3 by **3** in combination with TRAIL. T98G cells were treated with TRAIL (50 ng/ml) alone or **3** (100 nM) alone (for 8 and 12 hours, respectively) or were treated first with various concentrations of **3** for 4 hours and then with TRAIL for 8 hours. Cell extracts were prepared and subjected to Western blot analysis with the use of antibodies specific for caspase 8 and proteolyzed PARP. Asterisk indicates cross-reactive band. (**C**) Affinity purification of IAP proteins using a biotinylated form of compound **3** (fig. S2). Biotinylated **3** was immobilized onto streptavidin-conjugated beads and incubated with T98G cell extracts. The recovered beads were boiled, and released proteins were resolved by gel electrophoresis. The gel was probed with antibodies to XIAP, cIAP1 and cIAP2: Lane 1, precipitation using a negative control compound. Lane 2, precipitation using biotinylated **3**. Lane 3, same as lane 2, except the cell extract was treated first with **3** (5 μM) for 4 hours.

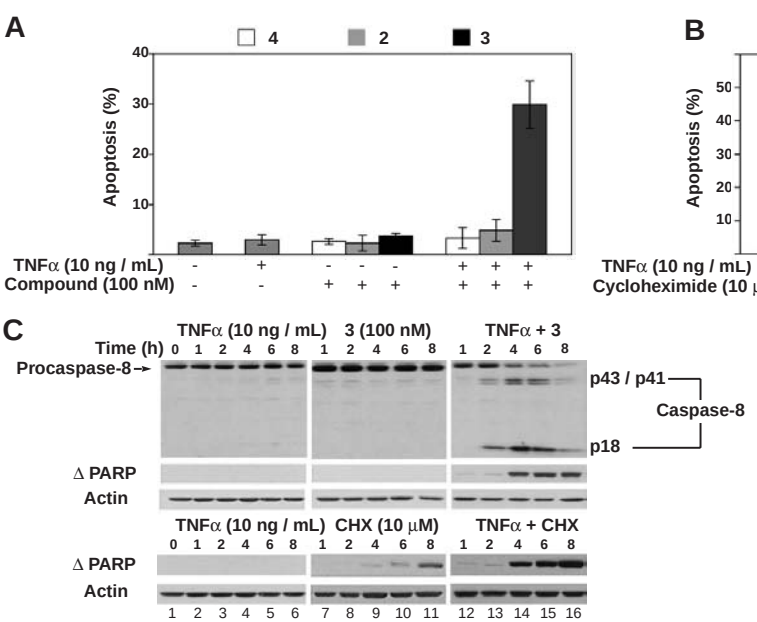

Fig. 3. Compound **3** and TNFα act synergistically to induce apoptosis in cell culture. (**A**) HeLa cells were cultured in DMEM containing fetal calf serum (10%) and treated with TNFα (10 ng/mL) alone or compound (100 nM) alone for 15 and 19 hours, respectively. When used together, the small molecule was added 4 hours before TNFα (total incubation time, 19 hours). Cell death (% of total population) was quantified by trypan blue staining. Values represent the average of three independent experiments (error bars, 1 standard derivation). (**B**) Hela cells were treated with TNFα (10 ng/ml) alone, cycloheximide (CHX, 10 μM) alone, or a combination of TNFα and CHX for 15 hours. (**C**) (Top) Time course of caspase 8 and caspase 3 activation in Hela cells treated with TNFα and/or **3**. Hela cells were treated with TNFα (10 ng/ml) alone, **3** (100 nM) alone, or treated with **3** for 4 hours and then with TNFα. Cell extracts were made at indicated times and subjected to Western blot analysis with antibodies to caspase 8 or proteolyzed PARP. (Bottom) Time course of caspase 3 activation in Hela cells treated with TNFα, CHX, or both.

This suggests that the primary role for cIAP-1 and cIAP-2 is to block caspase 8 activation. It also verifies a previous proposal that cIAPs act downstream of NF-κB during its cell survival pathway (*25*, *26*). NF-κB signaling is insufficient to block the onset of apoptosis in the presence of Smac or compound **3**. The ability of compound **3** to potentiate apoptosis in TNFα-treated cells, despite NF-κB activation, suggests a strategy for treating inflammatory disease such as rheumatoid arthritis (RA). TNFα functions in RA by inducing secretion of matrix-degrading proteases and multiple inflammatory cytokines and chemokines and increased expression of class I major histocompatibility molecules by synovial fibroblasts (leading to cartilage and bone erosion) and synovial neoangiogenesis (*27*). Moreover, it stimulates adhesion molecules on the surface of vascular endothelial cells to recruit circulating leukocytes to the endothelium and activates multinucleated osteoclasts to form a seal around bone, where they cause erosion by acidic secretions and protease activity (*28*). If the original TNFα signal terminated in cell death, it is possible that these downstream events would be avoided.

References and Notes

1. N. A. Thornberry, Y. Lazebnik, *Science* **281**, 1312 (1998).
2. Q. L. Deveraux, J. C. Reed, *Genes Dev.* **13**, 239 (1999).
3. X. Wang, *Genes Dev.* **15**, 2922 (2001).
4. J. Chai *et al.*, *Nature* **406**, 855 (2000).
5. A. G. Uren, M. Pakusch, C. J. Hawkins, K. L. Puls, D. L. Vaux, *Proc. Natl. Acad. Sci. U.S.A.* **93**, 4974 (1996).
6. M. Rothe, M. G. Pan, W. J. Henzel, T. M. Ayres, D. V. Goeddel, *Cell* **83**, 1243 (1995).
7. I. Imoto *et al.*, *Cancer Res.* **61**, 6629 (2001).
8. T. Hasegawa *et al.*, *Blood* **101**, 1164 (2003).
9. M. Krajewska *et al.*, *Clin. Cancer Res.* **9**, 4914 (2003).
10. C. Du, M. Fang, Y. Li, L. Li, X. Wang, *Cell* **102**, 33 (2000).
11. A. M. Verhagen *et al.*, *Cell* **102**, 43 (2000).
12. Single-letter abbreviations for the amino acid residues are as follows: A, Ala; E, Glu; F, Phe; I, Ile; K, Lys; P, Pro; Q, Gln; and V, Val.
13. G. Wu *et al.*, *Nature* **408**, 1008 (2000).
14. Z. Liu *et al.*, *Nature* **408**, 1004 (2000).
15. S. Fulda, W. Wick, M. Weller, K. M. Debatin, *Nat. Med.* **8**, 808 (2002).
16. O. E. Pardo *et al.*, *Mol. Cell. Biol.* **23**, 7600 (2003).
17. L. Yang *et al.*, *Cancer Res.* **63**, 831 (2003).
18. C. R. Arnt, M. V. Chiorean, M. P. Heldebrant, G. J. Gores, S. H. Kaufmann, *J. Biol. Chem.* **277**, 44236 (2002).
19. This nomenclature refers to the AVPF prototype where the N-terminal L-alanine is position 1 and L-phenylalanine is position 4. Ten surrogates for a proline-phenylalanine dipeptide and 18 variable amino acid residues at position two were combined for a total of 180 compounds.
20. The conversion of **2** to **3** shown in Fig. 1A is an optimized version (*29*) of an oxidation first observed as a minor competing pathway during Cu^{I}-catalyzed cycloadditions of **2** to alkyl azides.
21. M. Mammen, S.-K. Choi, G. M. Whitesides, *Angew. Chem. Int. Ed. Engl.* **37**, 2754 (1998).
22. Y. Huang, R. L. Rich, D. G. Myszka, H. Wu, *J. Biol. Chem.* **278**, 49517 (2003).
23. Under conditions identical to those used in Fig. 1F, neither Smac nor compound **3** block the interaction of XIAP with activated caspases 3. However, both relieve XIAP suppression of caspase 3 activity (fig. S5).
24. Y. Deng, X. Ren, L. Yang, Y. Lin, X. Wu, *Cell* **115**, 61 (2003).
25. C. Y. Wang, M. W. Mayo, R. G. Korneluk, D. V. Goeddel, A. S. Baldwin Jr., *Science* **281**, 1680 (1998).
26. Z. L. Chu *et al.*, *Proc. Natl. Acad. Sci. U.S.A.* **94**, 10057 (1997).
27. D. A. Fox, *Arch. Intern. Med.* **160**, 437 (2000).
28. J. Lam *et al.*, *J. Clin. Invest.* **106**, 1481 (2000).
29. R Berscheid, F Vögtle, *Synthesis* **1992**, 58 (1992).

30. We thank O. Guryev for invaluable technical assistance, J. Chen for helpful discussions, N. Williams for preliminary toxicological data, and M. S. Brown and S. L. McKnight for helpful suggestions. Funding provided by a program project grant from the National Cancer Institute (PO1 CA95471). J.K.D. and P.G.H. are fellows of the Alfred P. Sloan Foundation. P.G.H. acknowledges unrestricted research awards from Eli Lilly, Pfizer, and AstraZeneca. Molecular interaction data have been deposited in the Biomolecular Interaction Network Database with accession codes 150999 to 151001.

Supporting Online Material

www.sciencemag.org/cgi/content/full/305/5689/1471/DC1

Figs. S1 to S6

23 March 2004; accepted 15 June 2004

The Emergence of Competition Between Model Protocells

Irene A. Chen,[1,2] Richard W. Roberts,[3] Jack W. Szostak[1]*

The transition from independent molecular entities to cellular structures with integrated behaviors was a crucial aspect of the origin of life. We show that simple physical principles can mediate a coordinated interaction between genome and compartment boundary, independent of any genomic functions beyond self-replication. RNA, encapsulated in fatty acid vesicles, exerts an osmotic pressure on the vesicle membrane that drives the uptake of additional membrane components, leading to membrane growth at the expense of relaxed vesicles, which shrink. Thus, more efficient RNA replication could cause faster cell growth, leading to the emergence of Darwinian evolution at the cellular level.

A simple model of a primitive cell involves a self-replicating genome, such as an RNA polymerase ribozyme (a "replicase"), and an encapsulating membrane that can grow and divide (*1*) (supporting online text). Genomic influence over vesicle growth has been assumed to require a second RNA function, such as a ribozyme that would synthesize membrane components (*2*). Although such molecules presumably evolved at some point, we wondered whether the transition to a unified cell might have been facilitated by simpler physical mechanisms for coupling genomic properties and membrane behavior.

We sought to detect the emergence of an adaptive cellular-level trait based on the physical properties of a model prebiotic vesicle system containing encapsulated nucleic acids. Counterions associated with RNA encapsulated by a semipermeable membrane exert osmotic pressure on the membrane, which is counterbalanced by membrane tension. RNA replication would convert freely diffusing nucleic acid monomers into large impermeable macromolecules, increasing the concentration of trapped counterions. The resulting increase in osmotic pressure and membrane tension would create a driving force for an increase in membrane area, thereby coupling RNA replication to membrane growth (supporting online text).

We tested whether fatty acid vesicles (*3*–*5*) (supporting online text) osmotically stressed by encapsulated contents would increase in membrane area at the expense of unstressed vesicles. An initial concern was that fatty acid membranes might be too structurally weak to maintain a substantial osmotic gradient. We therefore determined the maximum sustainable membrane tension of oleate (C18:1) vesicles under osmotic stress. Oleate vesicles (100-nm diameter) encapsulating 1 M sucrose were diluted into hypotonic buffers (*6*). Applied gradients $\geq$0.7 M caused transient membrane rupture and release of solutes, detectable by size-exclusion chromatography, followed by membrane resealing at a maximal sustainable membrane tension (τ^*_{oleate}). After accounting for vesicle swelling from the extruded nonspherical shape to a spherical shape (*7*, *8*) and the partial loss of encapsulated solutes, we estimate that τ^*_{oleate} is 10 dyn/cm, or 4 atm. A similar experiment with 100 nm POPC (1-palmitoyl-2-oleoyl-*sn*-glycero-3-phosphocholine) vesicles showed that τ^*_{POPC} is 25 dyn/cm (supporting online text). These measurements fall within the range previously reported for phospholipid membranes (3 to 40 dyn/cm) (*9*–*11*). Thus, fatty acids, though chemically simple, can indeed form surprisingly strong membranes under osmotic stress.

[1]Department of Genetics, Harvard Medical School, and Howard Hughes Medical Institute, Department of Molecular Biology, Massachusetts General Hospital, Boston, MA 02114, USA. [2]Program in Biophysics, Harvard University, Cambridge, MA 02138, USA. [3]Division of Chemistry and Chemical Engineering, California Institute of Technology, Pasadena, CA 91125, USA.

*To whom correspondence may be addressed. E-mail: szostak@molbio.mgh.harvard.edu

We then performed competition experiments between swollen and isotonic vesicles. Low-osmolarity (isotonic) oleate vesicles were prepared in buffer without sucrose. High-osmolarity (swollen) vesicles were prepared by encapsulating sufficient osmolyte (e.g., 1 M sucrose) to generate the maximal sustainable membrane tension upon dilution into buffer. The two vesicle preparations were mixed in a stopped-flow device, and membrane surface areas of the swollen and isotonic vesicles were monitored in separate experiments using a fluorescence resonance energy transfer (FRET)–based assay (*6*). We observed that the membrane area of swollen oleate vesicles increased and the membrane area of isotonic vesicles decreased in parallel by ~25% when mixed in a 1:1 ratio (Fig. 1, A to D), following first-order kinetics ($k_{oleate} \sim 0.1\ s^{-1}$). Vesicle fusion, which would result in FRET decreases for both vesicle populations, does not explain the observed changes. No pronounced changes in FRET were seen upon mixing vesicles of equal osmolarity or mixing vesicles with buffer alone. Similar experiments with POPC vesicles showed no changes in FRET over several hours (Fig. 1, E and F), as expected from the very low vesicle-vesicle exchange rates of phospholipids (*12*, *13*).

The above results show that vesicles with high internal osmotic pressure can acquire membrane from isotonic vesicles. These isotonic vesicles can lose membrane until they become spherical, but further membrane loss requires a volume decrease and concomitant concentration of their impermeable contents. The resulting osmotic gradient should eventually limit the redistribution of fatty acid. Indeed, as more swollen vesicles were added to a fixed number of initially isotonic vesicles, membrane loss reached a plateau (Fig. 2A). The maximum observed membrane loss from initially isotonic vesicles (~35%) was somewhat larger than the estimated membrane loss necessary to adopt a spherical shape (~27%; supporting online text), indicating that initially isotonic vesicles lost membrane until they also built up some osmotic gradient. Conversely, swollen vesicles, in the presence of excess isotonic vesicles, should grow until the membrane tension reaches zero, which we calculated should occur after a 35% surface area increase; the maximum observed increase was ~35%.

To examine the mechanism of fatty acid transfer among vesicles, we tested the role of vesicle-vesicle collisions by varying the concentration of vesicles, but no rate changes were observed. Because the initial rate of uptake of fatty acid from micelles into vesicles can be quite fast compared with the observed rate of exchange (*14*), fatty acid adsorption is unlikely to be rate-limiting. We also tested the role of fatty acid desorption from vesicles, which becomes faster as chain length decreases (*15*). Myristoleate vesicles (C14:1) showed faster exchange ($k_{myristoleate} \sim 0.6\ s^{-1}$). Exchange rates were also slower than fatty acid flip-flop rates (*16*). These observations indicate that exchange may be rate-limited by desorption, consistent with previous results on phospholipid transfer among liposomes (*12*, *17*).

Having established that encapsulated osmolytes could drive vesicle growth at the expense of isotonic vesicles, we turned to vesicles that were osmotically swollen by encapsulated nucleic acids. Efforts to encapsulate high concentrations of nucleic acids (>0.1 M nucleotide monophosphate equivalents) in pure fatty acid vesicles caused visible aggregation and contents leakage. Because the addition of glycerol monoesters to fatty acid membranes has been reported to increase vesicle stability in the presence of high salt concentrations

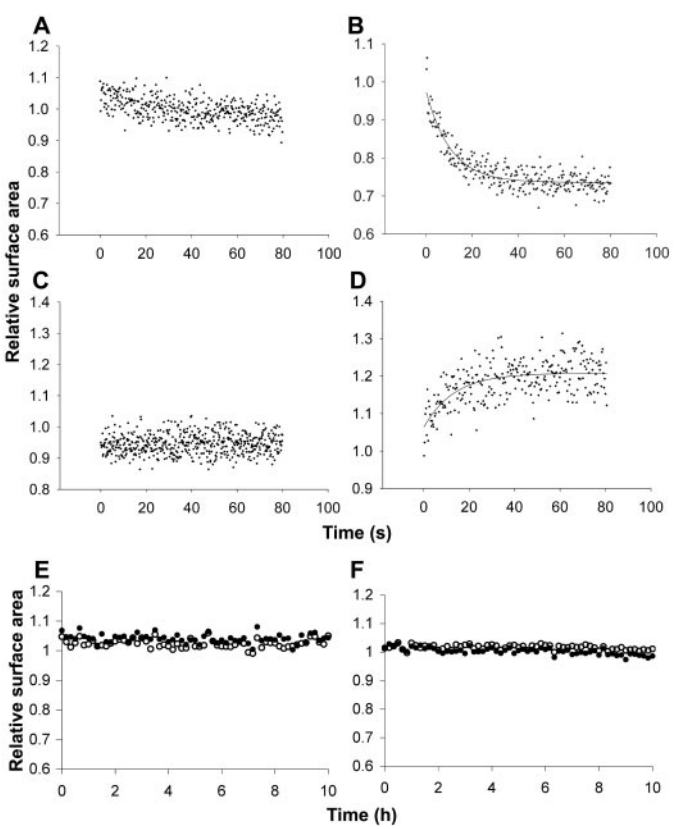

Fig. 1. Stopped-flow mixing of isotonic and swollen oleate vesicles (1:1 molar ratio) in 0.2 M bicine, pH 8.5. Relative surface area was measured by the FRET assay; membrane growth decreases probe density, causing the FRET signal to decrease. Isotonic vesicles, labeled with FRET dyes, were mixed with unlabeled isotonic (**A**) or swollen (**B**) vesicles. The solid line indicates a single exponential decay curve fit with rate constant $k = 0.09\ s^{-1}$. Swollen vesicles, labeled with FRET dyes, were mixed with unlabeled swollen (**C**) or isotonic (**D**) vesicles. The solid line indicates the single exponential curve fit ($k = 0.08\ s^{-1}$). Isotonic (**E**) or swollen (**F**) POPC vesicles, labeled with FRET dyes, were mixed with unlabeled isotonic (open circles) or swollen (solid circles) POPC vesicles.

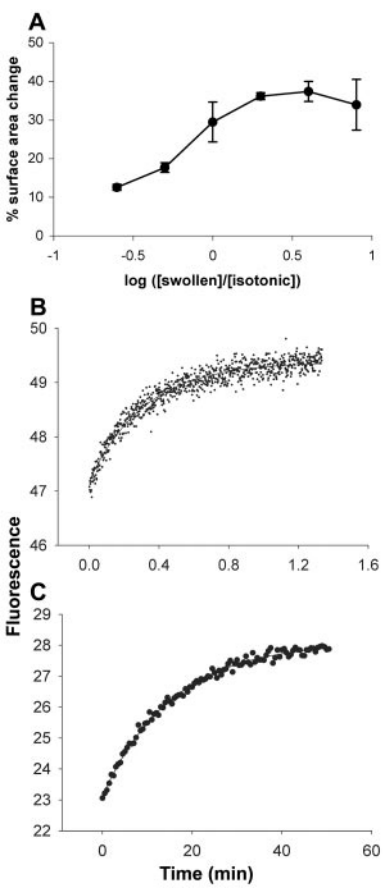

Fig. 2. (**A**) Change in surface area of isotonic vesicles mixed with different ratios of swollen vesicles, measured by FRET assay. Error bars indicate 95% confidence intervals for at least three trials. Time scale of intervesicular exchange of R18 in oleate (**B**) or MA:GMM (**C**) vesicles, measured by fluorescence dequenching. (B) Solid line indicates the single exponential curve fit ($k = 3.1\ min^{-1}$). (C) Solid line indicates a single exponential curve fit ($k = 0.06\ min^{-1}$).

(*18*), we encapsulated nucleic acids in myristoleate:glycerol monomyristoleate (MA:GMM = 2:1) vesicles, which were stable (supporting online text).

Initial competition experiments with MA:GMM vesicles were done using vesicles containing 0.2 M uridine 5′-monophosphate (5′-UMP) (~0.6 osmolar) (supporting online text). Growth of swollen vesicles and shrinkage of isotonic vesicles were observed as before (Table 1). The rate of exchange was substantially slower ($k_{MA:GMM} \sim 0.1\ min^{-1}$), consistent with the expected slower desorption rate from the more stable membranes. We confirmed that the difference between k_{oleate} and $k_{MA:GMM}$ quantitatively reflected the difference between the rate of lipid exchange in oleate versus that in MA:GMM vesicles using a self-quenching fluorescent fatty acid, octadecyl rhodamine B (R18) (*6*). Dilution of R18 among vesicles was detected as an increase in fluorescence (Fig. 2, B and C). The rate constant of R18 transfer in oleate vesicles (k^{R18}_{oleate}) was 3.0 min^{-1}, whereas $k^{R18}_{MA:GMM}$ was 0.06 min^{-1} (supporting online text). The fluorescence of R18-labeled vesicles did not change after mixing with buffer alone. These rate constants are in good agreement with the corresponding rate constants of osmotically driven lipid exchange.

Table 1. Intervesicle competition reactions using RNA osmolytes.

Osmolyte	FRET-labeled vesicles (low or high osmolarity)	% surface area change	k (min^{-1})
5′-UMP	Low	−45	0.05
	High	+36	0.02
Oligoribo-nucleotides*	Low	−64	0.03
	High	+51	0.02
tRNA	Low	−23	0.1
	High	+21	0.1

* Vesicles swollen by oligomers appeared to exchange more membrane than vesicles swollen by other osmolytes, an effect possibly due to salts or other minor components of bulk yeast RNA.

Membrane transfer to swollen vesicles was also observed when the osmolyte was a heterogeneous mixture of RNA oligomers obtained by alkaline hydrolysis of bulk RNA (93 mg/ml; ~0.29 M nucleotide equivalents), which were 1 to 40 nucleotides in length as estimated by high-performance liquid chromatography. Finally, we observed membrane transfer using vesicles osmotically swollen by tRNA (83 mg/ml; ~0.26 M nucleotide equivalents), which has a length (72 to 95 bases) comparable to that of many ribozymes (*19*) (Fig. 3) (supporting online text).

The concentrations of nucleic acids that produce this effect are biologically reasonable. In general, the concentration of genomic nucleic acid in a unicellular organism increases as the size of the organism decreases. For one of the smallest bacteria, *Mycoplasma genitalium* (~300 nm in diameter), the concentration of DNA alone is 100 mg/ml (0.32 M nucleotide equivalents) (*20*). In a larger bacterium, *Escherichia coli*, the concentration of DNA is 13 mg/ml, and the combined concentration of DNA and RNA is ~130 mg/ml (0.4 M nucleotide equivalents) (*21*). The RNA concentrations used in our osmotically driven growth experiments fell within this range.

Our results show that osmotically swollen fatty acid vesicles can grow at the expense of relaxed (isotonic) vesicles. We have attempted to model the behavior of a primitive cell in which an RNA genome encodes functional RNA, but the same principles would apply given any other charged genetic polymer. In contrast, a neutral polymer such as PNA (peptide nucleic acid), having no associated counterions, would be a much less effective osmolyte, a difference that may have influenced the natural selection of the genetic material itself. We suggest that the phenomenon of osmotically driven, competitive vesicle growth could have played an important role in the emergence of Darwinian evolution during the origin of cellular life (supporting online text). The present results suggest that simple physical principles may allow a direct connection between genome and membrane. RNA replicating within vesicles could confer a substantial growth advantage to the membrane by creating internal osmotic pressure. The faster replication of a superior replicase would therefore lead to faster vesicle growth, at the expense of cells lacking RNA or containing less efficient replicases. A faster replicase genotype would thus produce the higher-level phenotype of faster cellular growth, a prerequisite of cellular replication (supporting online text). Darwinian evolution at the organismal level might therefore have emerged earlier than previously thought—at the level of a one-gene cell.

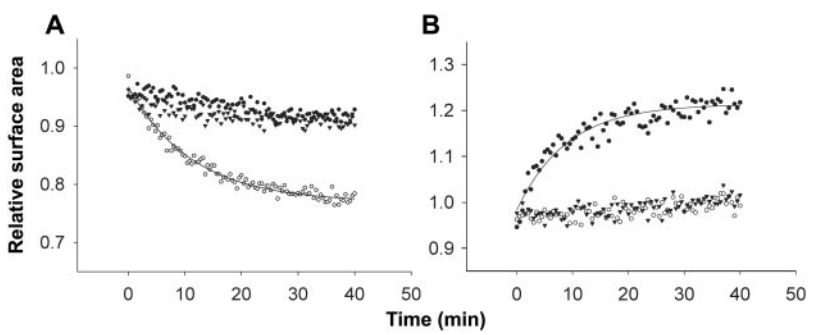

Fig. 3. Intervesicle competition using tRNA to swell MA:GMM vesicles. Isotonic (**A**) or swollen (**B**) vesicles were labeled with FRET dyes and mixed with unlabeled swollen vesicles pressurized by tRNA (open circles), isotonic vesicles (solid circles), or buffer only (triangles). (A) Solid line indicates a single exponential curve fit ($k = 0.09\ min^{-1}$). (B) Solid line indicates a single exponential curve fit ($k = 0.1\ min^{-1}$).

References and Notes

1. J. W. Szostak, D. P. Bartel, P. L. Luisi, *Nature* **409**, 387 (2001).
2. D. P. Bartel, P. J. Unrau, *Trends Cell Biol.* **9**, M9 (1999).
3. M. M. Hanczyc, S. M. Fujikawa, J. W. Szostak, *Science* **302**, 618 (2003).
4. J. M. Gebicki, M. Hicks, *Nature* **243**, 232 (1973).
5. P. Walde, R. Wick, M. Fresta, A. Mangone, P. L. Luisi, *J. Am. Chem. Soc.* **116**, 11649 (1994).
6. Materials and methods are available as supporting material on *Science* Online.
7. B. L. Mui, P. R. Cullis, E. A. Evans, T. D. Madden, *Biophys. J.* **64**, 443 (1993).
8. A. J. Jin, D. Huster, K. Gawrisch, R. Nossal, *Eur. Biophys. J.* **28**, 187 (1999).
9. S. D. Shoemaker, T. K. Vanderlick, *Ind. Eng. Chem. Res.* **41**, 324 (2002).
10. D. Needham, R. S. Nunn, *Biophys. J.* **58**, 997 (1990).
11. K. Olbrich, W. Rawicz, D. Needham, E. Evans, *Biophys. J.* **79**, 321 (2000).
12. L. R. McLean, M. C. Phillips, *Biochemistry* **20**, 2893 (1981).
13. J. D. Jones, T. E. Thompson, *Biochemistry* **28**, 129 (1989).
14. I. A. Chen, J. W. Szostak, *Biophys. J.* **87**, 988 (2004).
15. F. Zhang, F. Kamp, J. A. Hamilton, *Biochemistry* **35**, 16055 (1996).
16. I. A. Chen, J. W. Szostak, *Proc. Natl. Acad. Sci. U.S.A.* **101**, 7965 (2004).
17. J. E. Ferrell Jr., K. J. Lee, W. H. Huestis, *Biochemistry* **24**, 2857 (1985).
18. P. A. Monnard, C. L. Apel, A. Kanavarioti, D. W. Deamer, *Astrobiology* **2**, 139 (2002).
19. L. F. Landweber, P. J. Simon, T. A. Wagner, *Bioscience* **48**, 94 (1998).
20. H. J. Morowitz, *Beginnings of Cellular Life* (Yale Univ. Press, New Haven, CT, 1992).
21. J. D. Watson, *Molecular Biology of the Gene* (Benjamin, New York, ed. 1, 1965).
22. We are grateful to S. M. Fujikawa, M. M. Hanczyc, P.-A. Monnard, J. Carothers, and A. Luptak for helpful discussions. J.W.S. is an investigator of the Howard Hughes Medical Institute. I.A.C. was supported by the NIH Medical Scientist Training Program (T32-GM07753) and an NIH Molecular Biophysics Training Grant (T32-GM08313). This work was supported in part by a grant from the NASA Exobiology Program (EXB02-0031-0018).

Supporting Online Material

www.sciencemag.org/cgi/content/full/305/5689/1474/DC1
Materials and Methods
SOM Text
References

26 May 2004; accepted 26 July 2004

New Products

Bruker Daltronics
For more information
978-663-3660
www.bruker-biosciences.com
www.scienceproductlink.org

Antibody Magnetic Bead Assays

The MagAB nanoparticle, a key addition to the ClinPlot product line, allows researchers to attach antibodies, antibody fragments, peptides, DNA, or ligands to the magnetic bead surface. The beads are useful for researchers looking for specific proteins or binding partners and for biologically selective and sensitive specific clinical assays. The MagAB beads are also useful as a more generally applicable tool for research and discovery in interaction proteomics. The flexibility of the MagAB beads allows ClinProt users to capture specific populations of proteins and peptides based on the specificity of the antibody interaction. In the case of antibody cross-reactivity, researchers can take advantage of the compound-specific readout by mass spectrometry to identify multiple antibody-binding partners, such as isoforms.

Kendro Laboratory Products
For more information
828-658-2856
www.kendro.com
www.scienceproductlink.org

Copper Interior Incubator

Available with a fungicidal and bactericidal solid copper interior, the Heraeus HERAcell 240 carbon dioxide incubator provides a stable, precisely controlled growing environment and offers unsurpassed contamination protection for cell and tissue cultures. The 8.4-cubic-foot capacity HERAcell 240 incorporates the ContraCon 90°C automatic decontamination routine for thorough chamber decontamination without the need to remove and subsequently re-fit shelves and sensors. Proven to totally eliminate mycoplasma, bacteria, fungi, and spores, the ContraCon routine complements a number of contamination prevention measures designed to protect valuable cultures. Reduced internal surface area minimizes contamination-prone surfaces, while a smooth interior with rounded corners simplifies cleaning procedures. The instrument incorporates a large, directly heated water reservoir and a water level alarm. Direct humidification ensures optimal growth conditions and improves humidity recovery times.

Eppendorf
For more information
+49 40-5 38 01-0
www.eppendorf.com
www.scienceproductlink.org

PCR System

The Eppendorf PCR System includes devices and reagents designed to harmonize with one another. The epMotion 5070 Liquid Handling Workstation enables a contamination-free and reproducible set-up of polymerase chain reaction (PCR) reactions in 96- and 384-well formats. With its modular construction and its comprehensive system accessories, the instrument can aspirate and dispense reagents from a great variety of tubes. Another component of the system is the Mastercycler ep gradient thermocycler. The twin.tec PCR plates in 96- and 384-well formats are manufactured using "twin-shot" technology, which combines a polycarbonate plate frame for high mechanical stability and a precise seal that prevents evaporation with polypropylene wells for maximum sample recovery. The ultra-thin wells provide improved heat transfer, a secure fit in the thermal block, and minimal binding of biological molecules. The stable frames make them usable with robots. Also available are reagents for the novel Hot Start PCR technology, which is based on an inert ligand that reversibly and temperature-dependently blocks the polymerase, thus making a long initial activation phase superfluous.

Takara
For more information
888-251-6618
www.takaramirusbio.com
www.scienceproductlink.org

Adenovirus Expression Vector Kit

A new Adenovirus Expression Vector Kit offers two methods for recombinant adenovirus production using the same stable cosmid vector. The Full-Length DNA Transfer Method produces recombinant adenoviruses using recombinant cosmids that have been created by direct insertion of the target gene into the cosmid, with no shuttle vector required. Alternatively, the COS-TPC method makes use of an adenovirus DNA fragment associated with a terminal protein complex in a co-transfection with a cosmid carrying the target into 293 cells. This method can be used when, due to the characteristics of the gene, the Full-Length DNA Transfer Method may not result in desired recombinant virus production and offers increased efficiency of recombinant adenovirus production (up to two orders of magnitude) compared with conventional methods.

ISI ResearchSoft
For more information
760-438-5526
www.isiresearchsoft.com
www.scienceproductlink.org

Bibliographic Software

EndNote 8 is an upgrade of bibliographic management software that features the ability to search online bibliographic databases, organize references and images, and create instant bibliographies. The new version is now Unicode compliant, so it can import, organize, and cite references in any language. Users can now create EndNote libraries of unlimited size, and store longer abstracts and notes of up to 50 KB in each field. It features new reference types and fields. An EndNote library can now be transferred to any device running Palm OS 4.1 or higher. A new "find reference" function makes it easier to locate references.

Alexis Biochemicals
For more information
800-900-0065
www.alexis-e.biz
www.scienceproductlink.org

Literature

Caspases: Executioner of Apoptosis & Judges of Inflammation is a 16-page product guide with technical, application, and product information on more than 240 enzymes, antibodies, inhibitors, assay kits, and other products for life scientists studying the role of caspases in apoptosis and inflammation. A family of proteases best known as executioners of apoptotic cell death, caspases are either activated through oligomerization (initiator/apical caspases) or require cleavage by an initiator caspase (effector caspases). Caspases are also involved in immune reactions that culminate in cytokine production rather than apoptosis.

Newly offered instrumentation, apparatus, and laboratory materials of interest to researchers in all disciplines in academic, industrial, and government organizations are featured in this space. Emphasis is given to purpose, chief characteristics, and availability of products and materials. Endorsement by *Science* or AAAS of any products or materials mentioned is not implied. Additional information may be obtained from the manufacturer or supplier by visiting www.scienceproductlink.org on the Web, where you can request that the information be sent to you by e-mail, fax, mail, or telephone.

Published by AAAS